

Journal of the National Science Foundation of Sri Lanka





**JOURNAL OF THE
NATIONAL SCIENCE FOUNDATION
OF SRI LANKA**

Editorial Board

Ajit Abeysekera (Editor in Chief)
A. Atputharajah
J.K.D.S. Jayanetti
L.P. Jayatissa
P. Prasad M. Jayaweera
Jagath Manatunge
S.S.N. Perera
Rohini de A. Seneviratne
Saman Seneweera
P. Wijekoon
M.J.S. Wijeyaratne

Language Editor

R.D. Guneratne

Editorial Office

Nadeeja Wickramarachchi (Principal Scientific Officer)
Uthpala T. Karunaratne (Senior Scientific Officer)
Upuli Ratnayake (Scientific Officer)

International Editorial Advisory Board

Chamil Abeykoon, UK
Dilanthi Amaratunga, UK
Dilantha Fernando, Canada
Leslie Gunatilaka, USA
Saman K. Halgamuge, Australia
Kithsiri W. Jayasena, Australia
Vassilios Kapaklis, Sweden
Wah Yun Low, Malaysia
Thomas Mathew, USA
Shanthi Mendis, Switzerland
Javier Francisco Ortega, USA
Malik Peiris, Hong Kong
Kamal Premaratne, USA
Nalin Samarasingha, USA
Ravi Silva, UK
Christopher C. Steel, Australia

Impact Factor : 0.682

Publication : Published quarterly (March, June, September and December) by the National Science Foundation of Sri Lanka.

Subscription : Foreign : US \$ 75 (SAARC countries)
US \$ 150 (other countries) } inclusive of airmail postage
Local : Rs. 2000

Accepted as standing orders or on a calendar year basis.
Single issues - Available on request;
Rs. 600 per copy

Payment must accompany all orders. Remittances in favour of the National Science Foundation of Sri Lanka.

Manuscripts : Research Articles, Research Communications, Reviews and Correspondence in all fields of Science and Technology may be submitted for consideration for publication. A guide to the preparation of manuscripts is provided in each issue. The guidelines may also be obtained by visiting the NSF website.

No responsibility is assumed by the National Science Foundation of Sri Lanka for statements and opinions expressed by contributors to this Journal.

Manuscripts and all correspondence relating to them should be sent to the Editorial Office, National Science Foundation, 47/5, Maitland Place, Colombo 07, Sri Lanka.

Fax: 94-11- 2694754

E-mail: jnsf@nsf.gov.lk

JNSF home page: <https://www.nsf.gov.lk/index.php/science-for-all/jnsf>

Publication : A publication fee of US\$ 150 will be levied for each manuscript except when the corresponding author is affiliated to a Sri Lankan institution.

Copyright : © National Science Foundation of Sri Lanka

Articles in the Journal of the National Science Foundation of Sri Lanka are Open Access articles published under the Creative Commons CC-BY-ND License (<http://creativecommons.org/licenses/by/4.0/>). This license permits use, distribution and reproduction, commercial and non-commercial, provided that the original work is properly cited and is not changed anyway.

Indexing : **The JNSF is indexed in Science Citation Index Expanded, Journal Citation Reports/Science Edition, BIOSIS Previews, Zoological Record, Biological Abstracts, Chemical Abstracts, Scopus, TEEAL, Ulrich's, AGRICOLA and EBSCOhost**

**JOURNAL OF THE
NATIONAL SCIENCE FOUNDATION
OF SRI LANKA**

Volume 50 Number 2

June 2022

C O N T E N T S

EDITORIAL

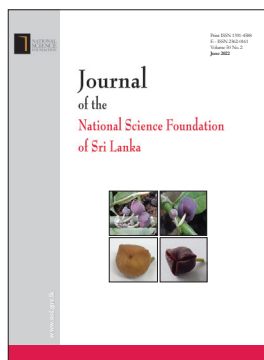
- 345 **Competition encourages exaggerated claims**
Ajit Abeyssekera
-

RESEARCH ARTICLES

- 347 **An approach to develop bioremediation by isolation and characterization of microorganisms from soil contaminated with used lubricating oil**
MM Wijesooriya, K Masakorala, SMK Widana Gamage and SS Walakulu Gamage
- 361 **Screening and quantitative analysis of antibiotic resistance genes in hospital and aquaculture effluent in Sri Lanka as an emerging environmental contaminant**
GY Liyanage, MM Weerasekera and PM Manage
- 371 **Combined use of non-destructive tests, visual inspection and service life prediction to ensure the reliability of reinforced concrete water tanks**
K Ranasinghe and S De Silva
- 387 **Application of Benford's law in agricultural production statistics**
F Hanci
- 395 **Implementation of adaptive lasso regression based on multiple Theil-Sen Estimators using differential evolution algorithm with heavy tailed errors**
E Dündar, T Zaman, MA Cengiz and K Alakuş
- 405 **Stability analysis of a partially saturated layered soil formation associated with shallow landslides**
SC Walpita, P Ratnaweera and G WAR Fernando
- 417 **Comparison of radioactive iodine therapy outcome and the duration of pretreatment discontinuation of carbimazole among hyperthyroid patients: a prospective study**
S Raheem and DKK Nanayakkara
- 425 **The odd modified Burr-III exponential distribution: properties, estimation and application**
H Rasheed, IS Dar, M Saqib, N Abbas and M Suhail
- 441 **First record of *Thottea duchartrei* Sivar., A. Babu & Balach. (Aristolochiaceae) in Sri Lanka**
TMSG Tennakoon, R Borosova, C Suraweera, S Herath, T De Silva, C Padumadasa, J Weerasena, N Gunaratna, N Gunasekera, S Edwards and S Wijesundara

- 453 **Seismic performance of stiffened steel box column with different corner stiffener arrangements: a numerical approach**
T Thevega, JASC Jayasinghe and KAS Susantha
- 467 **Effect of PEGylated gold nanorods on the circulating vascular endothelial growth factor, platelet-derived growth factor, and miR-29a in CD-1 mice**
AM Gamal-Eldeen, BM Raafat, CA Fahmy, MT Abo-Elfadl, SM El-Daly and MRK Ali
- 477 **Effects of dietary lead exposure on the call of Japanese quail (*Coturnix japonica*) hatchlings**
RPTI Ranasinghe, TSP Fernando and MR Wijesinghe
- 489 **Development of vacuum-dried powder and drinking yoghurt from soursop fruit (*Annona muricata L.*) and evaluation of their physico-chemical and functional properties**
NI Ranaweera, RC Pitipanaarachchi, HMT Herath and DVP Chandramali
- 503 **Development of wind energy prediction models using statistical, machine learning and hybrid techniques: a case study**
P Ekanayake, O Panahatipola and J Jayasinghe

Guidelines for Contributors



Cover: Floral and inflorescence morphology of *Thottea duchartrei*
See *J.Natn.Sci. Foundation Sri Lanka* 2022 50(2): 441 - 452

EDITORIAL

Competition encourages exaggerated claims

Science like most other professional activities is competitive. The days of the purely curiosity driven amateur scientist is long past. While healthy competition is a spur to achievement, the adverse effects of the current intensely competitive environment on scientists' work and behaviour is increasingly drawing the attention of commentators on the sociological aspects of science.

Scientists compete for many things during their careers including tangibles such as research funding and faculty positions, as well as intangibles such as influence and prestige. When competition assumes an overriding influence on a scientist's actions, ethics seems to lose its importance. It is recognized that competition among scientists have in certain instances resulted in questionable research practices as evidenced by the increasing rate of retractions of published research taking place today.

The incorporation of business management concepts in the management of academic and

research activities, have also resulted in increasing the competition amongst scientists. Many senior scientists today are compelled to spend a larger proportion of their time on writing grant proposals and endless reports for funding agencies of their existing grants, than on actual science. Those managing the award of research funds favour research output with palpable economic outcomes over creation of knowledge, thus stifling the emotional drive which lead most people to take up science as a career.

One of the insidious effects of competition and the emphasis on so called 'relevant science' is the exaggerated claims made for the importance of the results of a study. Authors are tending to shift from the established practice of reporting a significant finding which is supported by several different lines of evidence, consolidated by adequate control experiments, towards making a multitude of exaggerated claims based on a limited set of observations. Only humility and fidelity to truth, can prevent such excesses.

Ajit Abeysekera

RESEARCH ARTICLE

Bioremediation

An approach to develop bioremediation by isolation and characterization of microorganisms from soil contaminated with used lubricating oil

MM Wijesooriya, K Masakorala*, SMK Widana Gamage and SS Walakulu Gamage

Department of Botany, Faculty of Science, University of Ruhuna, Matara, Sri Lanka.

Submitted: 25 May 2021; Revised: 11 October 2021; Accepted: 22 October 2021

Abstract: Soil contamination with used lubricating oil (ULO) is an emerging environmental threat in many parts of the world. Bioremediation is a cost-effective and green, technological approach with the potential to remediate soil contaminated with ULO. Therefore, as an attempt to develop a bioremediation technique, the present study aimed to isolate and characterize microorganisms from soil contaminated with ULO. Bacteria and fungi were isolated from soil exposed to ULO for a long period, by enrichment culture in a mineral salt medium (MSM). Biodegradation assays and total microbial activity (TMA) studies were carried out for the microbial isolates in laboratory-scale microcosms with 1–4% w/w contamination levels of ULO. The initial screening experiment confirmed that two novel strains, RUH-K01 and RUH-F07 were efficient ULO degraders. They were identified as *Pseudomonas aeruginosa* RUH-K01 and *Aspergillus fumigatus* RUH-F07 with respect to their morphological characteristics and 16S rRNA gene sequences. Microcosm experiments revealed the biodegradation percentage in soil with 1% w/w ULO was 82.27% and 70.09% for *P. aeruginosa* and *A. fumigatus*, respectively. A slight reduction in ULO degradation was observed by both strains when the ULO contamination level increased. At 4% w/w ULO contamination level, the degradation was 56.91% for RUH-K01 and 50.25% for RUH-F07. The potential to produce bio-surfactants and other species-specific metabolic activities may be reasons for the efficient biodegradation of ULO by *P. aeruginosa*. The resulting significant negative correlation ($p < 0.05$) between the residual total petroleum hydrocarbon (TPH) content and TMA of both strains confirmed the applicability of the FDA assay as an appropriate method to characterize the ULO degradation efficiency of microorganisms. In conclusion, the overall

results indicate the potential of *P. aeruginosa* RUH-K01 and *A. fumigatus* RUH-F07 to be used in bioremediation of ULO contaminated soils.

Keywords: *Aspergillus fumigatus*, biodegradation, *Pseudomonas aeruginosa*, species-specific, total microbial activity, used lubricating oil.

INTRODUCTION

Soil is a complex natural ecosystem that is vitally important for the survival of life on earth. Soil contamination with used lubricating oil (ULO) has become a global environmental issue (Glibovytska *et al.*, 2019). Parallel to the increasing demand for lubricating oil (LO) from automobiles and industry, a large amount of ULO is generated as LO needs to be replaced from time to time due to the alteration of its chemical and physical properties during utilization (Yash, 2015). Accidental spills, careless handling, and illegal dumping that occur during routing oil replacement operations at mechanical workshops and automobile service stations have been identified as significant sources of environmental contamination by ULO (Ogunbayo *et al.*, 2012). ULO is a complex mixture of different types of hydrocarbon compounds including aliphatic (73–80%), mono-aromatic (11–15%), poly-aromatic (4–8%), di-aromatic (2–5%), and heavy metals (Vazquez-Duhalt, 1989). Further, degradation of ULO in the environment is very

* Corresponding author (mas@bot.ruh.ac.lk;  <https://orcid.org/0000-0003-4648-1738>)



This article is published under the Creative Commons CC-BY-ND License (<http://creativecommons.org/licenses/by-nd/4.0/>). This license permits use, distribution and reproduction, commercial and non-commercial, provided that the original work is properly cited and is not changed in any way.

slow (Tang *et al.*, 2012) and the aliphatic and aromatic hydrocarbons, chlorodibenzofurans, additives, heavy metals, and decomposition products in ULO are known to be toxic, carcinogenic, and mutagenic (ATSDR, 1997; Wu *et al.*, 2008). Therefore, soil contamination with ULO may adversely affect not only soil quality (Abioye *et al.*, 2012; Tiwari & Saraf, 2017) but also environmental and human wellbeing. Hence, the application of sustainable remediation methods is vitally important to reclaim ULO contaminated soils.

At present, bioremediation is considered to be a promising, cost-effective, and green technological approach compared to conventional physical and chemical soil remediation strategies (Agarry & Ogunleye, 2012; Shahsavari *et al.*, 2017). Microorganisms such as bacteria, filamentous fungi, algae, and yeast (Margesin & Schinner, 2001), and higher plant species can be used as biological agents in the biodegradation of contaminants (Sardrood *et al.*, 2013). Microorganisms with the potential to degrade contaminants are widely applied to environments contaminated with a variety of organic compounds (Chang *et al.*, 2011) and heavy metals (Alisi *et al.*, 2009).

The application of microorganisms in the bioremediation of contaminated sites is considered as an efficient strategy due to their adaptability to a wide range of environmental conditions, rapid population growth, highly efficient metabolism, and production of biosurfactants (Tyagi *et al.*, 2011). Since screening and identification of efficient strains of microorganisms are crucial steps in the development of bioremediation techniques, many researchers have focused on the isolation and characterization of microorganisms capable of degrading hydrocarbons (Batista *et al.*, 2006; Mandri & Lin, 2007; Zhao *et al.*, 2008; Ling *et al.*, 2011; Masakorala *et al.*, 2013; Yuan *et al.*, 2014; Tiwari & Saraf, 2017). Although the biodegradation potential of petroleum pollutants by bacteria and fungi has been extensively studied (Tyagi *et al.*, 2011; Ghoreishi *et al.*, 2017), only a few studies indicate the degradation of ULO by bacteria and fungi. Umar *et al.* (2013) have identified that bacterial species *Pseudomonas fluorescens*, *Bacillus mycoides*, and *Acinetobacter* sp. and fungal genera such as *Aspergillus* and *Penicillium* (Jesunmi, 2014) are capable of degrading ULO. The success of a bioremediation strategy is largely determined by the ability of inoculants to adapt to new environmental conditions, degradation efficiency, microbial activity, and their diversity (Wu *et al.*, 2016). Therefore, isolation and identification of effective and efficient ULO degraders from the environment are challenging.

Although contamination of soil by ULO is an emerging environmental issue in Sri Lanka, enough attention has not been paid on the management of contaminated soils. Though a few studies have been conducted to develop phytoremediation techniques for ULO contaminated soil (Gamage *et al.*, 2020), studies on the microorganism-mediated bioremediation have not been carried out up to date. Therefore, conducting a pilot-scale study is a prerequisite for establishing effective and efficient bioremediation using native microorganisms. Moreover, it would be beneficial for planning management strategies to restore ULO contaminated sites surrounding industrial areas and automobile service stations. Therefore, the present study aimed to isolate, identify, and characterize bacteria and fungi from ULO contaminated sites, with a capacity to degrade ULO and to determine their biodegradation efficiency at different levels of ULO contamination.

MATERIALS AND METHODS

Soil and ULO sample collection and preparation

Soil samples were collected from the Service Station of Sri Lanka Transportation Board (SLTB) bus depot in Matara, Sri Lanka. This has a long history as a service station and is known to be contaminated with ULO. After carefully scraping off the surface soil layer, soil samples were obtained at a depth of 5–10 cm. The collected samples were homogenized and sieved through a 2 × 2 mm mesh to remove large particles and other debris. Samples were then stored in polythene bags at 4°C to be used for further analyses. Total petroleum hydrocarbon (TPH) content was determined according to the method followed by Tang *et al.* (2012) with slight modifications as described in section 'Determination of biodegradation of ULO'. Uncontaminated soil was collected from the surface layer of an undisturbed site of the University of Ruhuna, Sri Lanka, at a depth of 5–10 cm, to carry out microcosm experiments as mentioned in section 'Biodegradation of ULO in microcosms'. Homogenized soil samples were obtained following air drying and sieving. An ULO sample, collected from an automobile service station at Kekanadura, Matara, Sri Lanka was filter-sterilized using Whatman® membrane filter (pore size 0.45 µm) before being used in the experiments.

Reagents and culture media

Several media were used for the isolation and maintenance of potential ULO degrading microorganisms. The mineral salt agar (MSA) medium used in the experiment was composed of (L⁻¹): NaCl 10 g; MgSO₄·7H₂O 0.42 g;

KCl 0.29 g; KH_2PO_4 0.85 g; Na_2HPO_4 1.25 g; NaNO_3 0.42 g; and 20 g of bacteriological agar. The nutrient agar (NA) medium used in the experiment was composed of (L^{-1}): NaCl 8 g; peptone 5 g; beef extract 3 g and 14 g of bacteriological agar. The nutrient broth (NB) was composed of (L^{-1}): pepton 5 g; beef extract 1 g; yeast extract 2 g; NaCl 5 g. The potato dextrose agar (PDA) medium was prepared by dissolving 35 g of PDA powder in 1 L of distilled water. The pH of the media was adjusted to 7.4 ± 0.2 . Prepared culture media were sterilized by autoclaving at 121°C for 30 min.

Isolation of ULO degrading microorganisms

An enrichment isolation technique was used to isolate potential ULO degrading microorganisms (Zhao *et al.*, 2008; Masakorala *et al.*, 2013; Thenmozhi *et al.*, 2013) from ULO contaminated soil. Briefly, 1 g of ULO contaminated soil was suspended in 100 mL of MS broth in a 250 mL Erlenmeyer flask. As an enrichment substrate, 1 mL of filter-sterilized ULO (1% v/v) was added as the sole carbon source and incubated at 30°C in a horizontal orbital shaker (Lab Companion SK 300) at 180 rpm. Following 14 days of incubation, a 1 mL aliquot from the enriched culture was transferred weekly for a period of 4 weeks to 100 mL MS broth supplemented with 1% v/v ULO, and incubated under the same conditions. Bacterial cultures were obtained by uniform spreading of 100 μL aliquots of cultures at seven days of incubation on MSA medium coated with 100 μL 1% w/v ULO in dichloromethane. For the isolation of ULO degrading fungi, MSA supplemented with tetracycline (10 $\mu\text{g}/\text{mL}$) was used. Morphologically distinct bacterial and fungal colonies, which appeared following seven days of incubation at 30°C , were further purified. Pure cultures were obtained after three consecutive sub-cultures on NA and PDA. Stock cultures of bacteria were stored in 20% v/v glycerol at -20°C and fungi were stored in sterilized distilled water and PDA at 4°C (Zhao *et al.*, 2008; Masakorala *et al.*, 2013; Thenmozhi *et al.*, 2013).

Screening bacterial and fungal isolates for ULO degradability

The ULO degradability of pure isolates of bacteria and fungi were further screened on MSA medium coated with 100 μL 1% w/v ULO. Streak lines of similar lengths were drawn for all three bacterial isolates. Fungal isolates were inoculated by actively growing a mycelium plug (5×5 mm) in the middle of the Petri dish. Inoculated culture plates were incubated for 10 days at 30°C (Ibrahim *et al.*, 2018). The capacity of bacteria for biodegradability was estimated by measuring the area of

clear zone surrounding the bacterial growth, while that of fungi was determined by visual observation of mycelial growth, sporulation, and distinct clear zone (Thenmozhi *et al.*, 2013). Un-inoculated ULO coated MSA plates were used as controls. The experiments were carried out in triplicate and repeated three times to confirm the reproducibility of the results.

Characterization of ULO degrading bacteria and fungi

Morphological and biochemical characterization

The bacterial isolate RUH-K01, which showed the highest degradation potential, was identified and characterized based on colony morphology and pigmentation on NA medium and Gram staining. The biochemical properties of the isolate were determined by conducting a series of biochemical tests, such as triple sugar fermentation, methyl red, citrate, nitrate reduction, oxidation and fermentation, urease, indole, starch hydrolysis, catalase, and Voges-Proskauer. The results were analyzed following Bergey's Manual of Determinative Bacteriology (Breed & Bergey, 1948). The fungal isolate RUH-F07, with the highest degradation potential, was identified based on macroscopic and microscopic colony characters on the PDA medium. Macroscopic colony characters such as pigmentation, visible surface texture, and growth rate (time taken to cover a 90 mm Petri plate) were recorded. In addition, features of hyphae, arrangement of conidiophores, and conidia were examined on slide cultures (Riddell, 1950) under high power ($\times 400$) of the phase-contrast microscope (OLYMPUS DP 21). High-resolution images were captured using an in-built camera to the microscope.

Molecular characterization

Genomic DNA was extracted from RUH-K01 and RUH-F07 isolates using commercial extraction kits (Qiagen). Bacterial genomic DNA from RUH-K01 was amplified by Polymerase Chain Reaction (PCR) with universal primers for the 16S rRNA gene; 785F (5'GGATTAGATACCCTGGTA3') and 907R (5'CCGTCAATTCMTTGTGAGTTT3'). Fungal genomic DNA from RUH-F07 was amplified by universal primers for the ITS1, 5.8S rRNA, and ITS2 regions of the fungal genome, ITS1 (forward primer, 5'TCCGTAGGTGAACCTGCGG3') and ITS4 (reverse primer, 5'TCCTCCGCTTATTGATATGC3'). Amplicons were sequenced (Macrogen, Korea). Sequences were assembled using the software, Geneious R11 (Kearse *et al.*, 2012), and searched for nucleotide identities in NCBI/GenBank (<https://blast.ncbi.nlm.nih.gov/Blast>).

cgi) using the non-redundant database. Sequences of RUH-K01 and RUH-F07 were deposited in the NCBI/GenBank database under the accession numbers MH828325 and MK949124, respectively.

Biosurfactant production

Oil displacement assay was conducted to determine the ability of bacteria to produce biosurfactants as described by Rodrigues *et al.* (2006). In this assay, a thin smear of ULO was formed by spreading 20 μ L of ULO (1% w/v) on 25 mL of sterilized distilled water in a Petriplate. Subsequently, 15 μ L of cell-free supernatant obtained from the saturated culture of RUH-K01 was placed on the center of the oil-water surface and the formation of a distinct clear zone was observed. Sodium dodecyl sulphate (SDS) was used as the positive control. The experiment was carried out in triplicate and repeated three times to confirm the reproducibility of the results.

Biodegradation of ULO in microcosms

Experimental setup

Soil samples obtained from an undisturbed site of the University of Ruhuna, sterilized by autoclaving at 121°C for 30 min, were mixed with ULO at 1–4% w/w levels in laboratory-scale microcosms prepared in 250 mL Erlenmeyer flasks. The water holding capacity was adjusted to 70%. Three replicates were used for the treatments and control at each contamination level. All replicates of the treatments were allowed to stand for three days before adding 5 mL of RUH-K01 bacteria

suspension (at $OD_{600nm} \sim 0.4$) and mycelia-free spore suspension of RUH-F07 (at $OD_{600nm} \sim 0.4$) separately. The control setup was not inoculated, while 5 mL of sterilized distilled water was added. The microcosms were incubated at 30°C. After every 10, 20, and 30 days, total petroleum hydrocarbon (TPH) content and total microbial activity were measured using standard procedures as follows.

Determination of biodegradation of ULO

TPH content in ULO contaminated soil was estimated gravimetrically according to the method described by Tang *et al.* (2012) with slight modifications. Five grams of ULO contaminated soil from the microcosms were extracted into 10 mL of dichloromethane. The mixture of soil and dichloromethane was sonicated for 15 min and the supernatant was collected by repeating the extraction procedure three times. The collected supernatants were centrifuged at $996 \times g$ for 10 min, and the dichloromethane was evaporated in a water bath at 40°C (Tang *et al.*, 2012). Finally, the residual TPH content was determined according to equation number 1.

$$TPH \text{ Content} = \left(\begin{array}{l} \text{Final weight of the crucible} \\ \text{containing residual oil} \end{array} \right) - \left(\begin{array}{l} \text{Weight of the empty} \\ \text{dried crucible} \end{array} \right) \quad \dots(1)$$

The percentage biodegradation of ULO was determined according to the weight loss method using equation 2 (Bartha & Bossert, 1984).

$$Biodegradation = \frac{\text{Average weight of oil}(\text{Control}) - \text{Average weight of oil}(\text{Treatment})}{\text{Average weight of oil}(\text{Control})} \times 100 \quad \dots(2)$$

Total Microbial Activity

Changes in the inoculated microbial population or their enzymatic activity during the process of biodegradation of ULO were determined by the fluorescein di-acetate (FDA) hydrolysis method described by Adam & Duncan (2001). The amount of fluorescein released after 10, 20, and 30 days of incubation of microcosms containing 1–4% w/w ULO contaminations at 30°C was quantified at a wavelength of 490 nm using UV/Visible spectrophotometer (Evolution 260 Bio, Thermo Fisher Scientific Inc. Germany). A standard concentration series of 1–5 μ g/mL was prepared by diluting 20 μ g/mL of fluorescein stock solution in 60 mM potassium phosphate buffer at pH 7.6 (Adam & Duncan, 2001).

Statistical Analysis

Data were analyzed statistically using the MINITAB (version 17) statistical software package. Results of the measured parameters were given as arithmetic means of three independent replicates. Two-way ANOVA was conducted to determine the significant differences between percentage level of contamination, time, and the effect of both contamination level and time on reduction of residual TPH content and total microbial activity. The correlation between the residual TPH content and total microbial activity was determined using the Pearson product correlation coefficient (*r*). The statistical significance in all analyses was defined at $p < 0.05$.

RESULTS AND DISCUSSION

The amount of petroleum hydrocarbon content in the ULO contaminated soil of the composite sample was determined before the isolation of the microorganism. Results showed the presence of 100,500 mg/kg \pm 200 mg/kg or 10.5% (w/w) of TPH in the analyzed soil implying a high level of ULO contamination.

Isolation of potential ULO degrading microorganisms

ULO degrading bacteria

Through the enrichment isolation of potential ULO degrading bacteria, three morphologically distinct bacteria (RUH-K01, RUH-J01, and RUH-I01) were isolated in MSA medium supplemented with 1% (w/v)

ULO as the sole source of carbon. In the literature, it has been reported that the formation of a clear zone and considerable growth of bacteria along the streaked path are indications of the biodegradation potential of bacteria (Vinothini *et al.*, 2015). Therefore, isolates were further screened on ULO coated MSA medium to confirm and differentiate their ULO degradation potentials. At the end of 10 days of incubation, a clear zone and bacterial growth were visible along the streaked path of each bacterial isolate on MSA medium coated with ULO. The mean of the measured area of the clear zones from the isolates RUH-K01, RUH-J01, and RUH-I01 in three trials were 403 mm², 229 mm², and 394 mm², respectively. Therefore, the results infer the difference in the potential of the isolates to degrade ULO, and the RUH-K01 (Figure 1) was identified as the isolate with the highest potential.

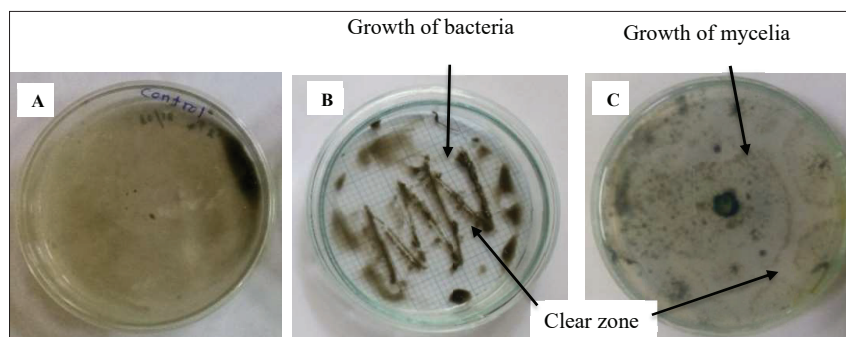


Figure 1: ULO degradation by bacteria and fungi. (A) Un-inoculated control; (B) growth and clear zone formation of bacterial isolate RUH-K01 and (C) growth and spore formation of fungal isolate RUH-F07 on MSA coated with 100 μ L 1% w/v ULO after 10 days of incubation at 30°C

ULO degrading fungi

Two morphologically distinct fungal colonies (RUH-F06 and RUH-F07) were isolated in MSA medium supplemented with 1% w/v ULO as the sole source of carbon. The mycelium of the fungal isolate RUH-F07 proliferated and sporulated rapidly on MSA coated with ULO and formed a clear zone surrounding colonies (Figure 1). Thenmozhi *et al.* (2013) have reported that the large colony diameter, abundant mycelial growth, and heavy sporulation of fungal isolate are characteristic morphological features of efficient hydrocarbon degraders. Thus, the reported visual observations of the present study infer that the isolate RUH-F07 is likely to have the capability of utilizing ULO as the sole source of carbon for its growth and reproduction, and the potential to degrade ULO.

Morphological and biochemical characterization of ULO degrading bacteria and fungi

Morphological characterization and Gram's staining indicated that the RUH-K01 is a rod-shaped Gram-negative bacterium. The colonies were pale brown, circular-shaped with an entire margin, and had a convex elevation on NA medium (Figure 2). Biochemically, the RUH-K01 isolate gave positive results for citrate, catalase, nitrate reduction, and oxidase tests, produced acids by the fermentation of D-glucose and was negative for sucrose, lactose, starch hydrolysis, Indole, Voges-Proskauer (VP), methyl red, and urease tests. Based on the morphological and biochemical characteristics, the novel isolate RUH-K01 was provisionally identified as a member belonging to genus *Pseudomonas* (Breed & Bergey, 1948), and was confirmed by the sequencing

of 16s rRNA. The analysis of the partial sequence (1486 nucleotides) of the 16s rRNA showed that the strain RUH-K01 was 99% identical to *Pseudomonas aeruginosa*. Therefore, the novel strain RUH-K01 with the GeneBank accession number MH828325 was tentatively nominated as a *Pseudomonas aeruginosa* RUH-K01.

The features of colonies and microscopic examination of the fungal isolate RUH-F07 showed conidiophore and conidia characters similar to that of genus *Aspergillus* (Figure 2). Conidiophores were hyaline, short and simple. Conidia were unicellular, smooth-walled, green, spherical in shape and formed as chains. A partial

sequence (593 nucleotides) of the ITS region confirmed that the strain RUH-F07 was 99% identical to *Aspergillus fumigatus*. Therefore, the novel strain RUH-F07 with the GeneBank accession number MK949124 was tentatively named as *Aspergillus fumigatus* RUH-F07.

The phylogenetic trees constructed using neighbour-joining method to illustrate the relationships of RUH-K01 and RUH-F07 with nearest phylogenetic relatives are given in Figure 3 (A) and (B) respectively. All the accession numbers of the reference sequences are given in Figure 3. According to the phylogenetic trees, strains RUH-K01 and RUH-F07 cluster with the largest clades

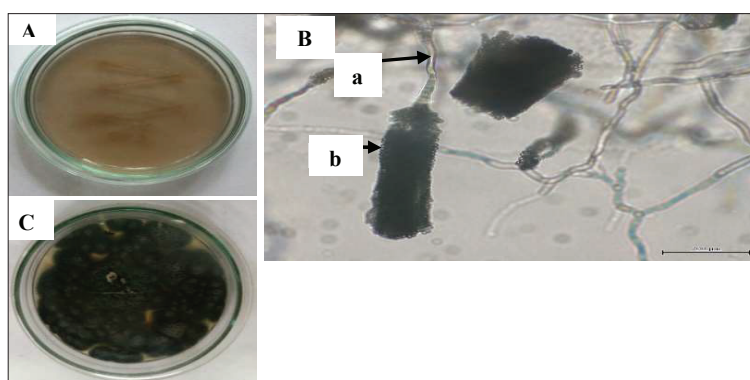


Figure 2: A pure culture of RUH-K01 on NA (A), RUH-F07 observed under the high power ($\times 400$) of the microscope (a-Conidiophore, b-Conidia) (B) and a pure culture of RUH-F07 on PDA (C).

Biosurfactant Production

Biosurfactants are amphiphilic molecules produced by microorganisms. Depending on the origin of biosurfactants, chemical composition may comprise different structural components such as glycolipids, phospholipids, peptides and glycopeptides (Gautam & Tyagi, 2006). Bioavailability of hydrocarbons for microbial degradation is less, due to their hydrophobic nature (Das et al., 2014). Biosurfactants enhance the bioavailability of hydrocarbons for hydrocarbon-degrading bacteria by reducing surface tension and increasing contact surface and solubility in the aqueous phase (Gautam & Tyagi, 2006; Masakorala et al., 2013). Therefore, much attention has been paid towards the potential of microorganisms to produce surfactants in planning bioremediation or bio-augmentation strategies for decontamination of hydrocarbon contaminated sites. Although the biosurfactant production potential

of *Aspergillus* spp. is well documented (Sperb et al., 2018), there is limited information on biosurfactant production by bacteria (Ghazala et al., 2019). Therefore, the biosurfactant production ability of the isolated ULO degrading bacteria was studied in this research. Our results showed that *P. aeruginosa* RUH-K01 has a potential to synthesize biosurfactants (Figure 4). Since the biodegradability of ULO by *P. aeruginosa* RUH-K01 has been shown to be significantly efficient, this strain may have utilized alternative mechanisms such as microbial mobilization and microbial attachment (Ortega-Calvo, 2017) to enhance the bioavailability of ULO during the biodegradation process, in addition to the biosurfactant production.

Biodegradation of ULO

Previous studies have revealed the potential of microorganisms isolated from hydrocarbon-

contaminated sites to degrade hydrocarbon compounds (Husaini *et al.*, 2008; Wu *et al.*, 2008; Das & Chandran, 2011; Liu *et al.*, 2011). Further, genes responsible for the hydrocarbon degradation process have been identified in

indigenous microorganisms isolated from hydrocarbon-contaminated soils (Zhang *et al.*, 2016). Furthermore, some studies have revealed that the monitoring of residual TPH content with time is a direct measurement

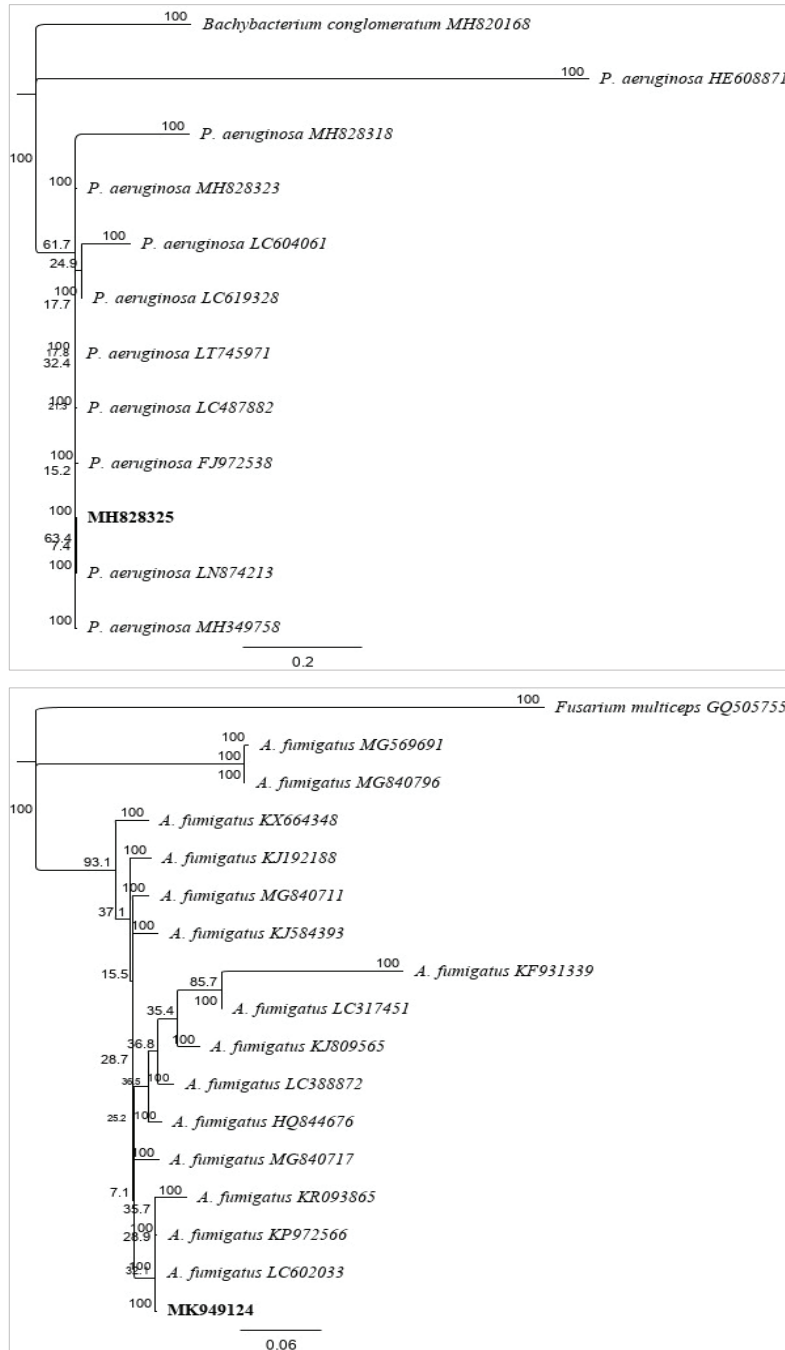


Figure 3: Phylogenetic trees of the novel strain RUH-K01 (A) and novel strain RUH-F07 (B). Bootstrap values, expressed as percentages of 1000 replications, are given at branch points. NCBI/GeneBank accession numbers are given after the scientific name.

of biodegradation which reflects the efficiency of bioremediation (Margesin & Schinner, 2001; Tang et al., 2012; McIntosh et al., 2017; Zeneli et al., 2019). Hence the characterization of the degradation potential of

microorganisms isolated from ULO contaminated soil is vitally important prior to implementing bioremediation. Therefore, the ULO degradation potential of isolated microorganisms was evaluated.

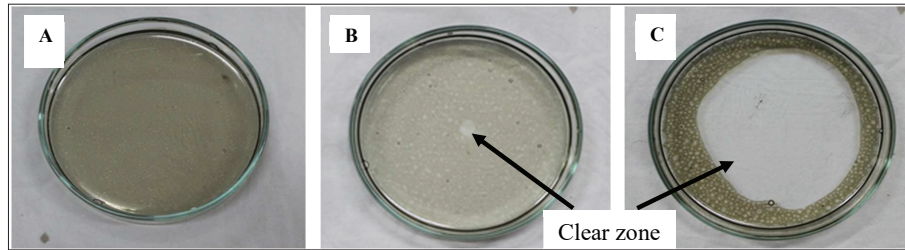


Figure 4: Biosurfactant production of *P. aeruginosa* RUH-K01. Negative control (A), oil spreading test for cell-free supernatant taken from the saturated culture of RUH-K01 (B), positive control SDS (C).

Results obtained from microcosm experiments showed an obvious degradation of ULO at all the tested contamination levels 1-4% (w/w) of ULO after inoculation with novel strains *P. aeruginosa* RUH-K01 and *A. fumigatus* RUH-F07 (Figure 5 (a)). However, *P. aeruginosa* RUH-K01 seems to be more efficient in degrading ULO compared to RUH-F07, at all the tested contamination levels. At the end of the first 10 days at 1% (w/w) ULO levels of contamination, RUH-K01 and RUH-F07 reached 70% and 45% degradation, respectively. The highest degradation was recorded in *P. aeruginosa* RUH-K01 inoculated soil at 1% (w/w) contamination level with a degradation efficiency of 82.27% after 30 days of incubation. At the end of 30 days, the recorded degradation efficiency of *A. fumigatus* RUH-F07 inoculated soil at 1% (w/w) ULO was 70.09%.

It is stated that the activity of microorganisms is a result of the expression of specific genes responsible for a certain function (Yu et al., 2013). Therefore, the recorded ULO degradation efficiencies by the novel bacterial isolate *P. aeruginosa* RUH-K01 and novel fungal isolate *A. fumigatus* RUH-F07 could be due to species-specific reasons.

Members of the genus *Pseudomonas* are well-known bacteria with the potential of utilizing different types of hydrocarbons as the sources of energy and carbon (Das & Chandran, 2011; Kadali et al., 2012; Puškárová et al., 2013; Pacwa-Płociniczak et al., 2014). Safdari et al. (2017) have reported 62% diesel removal from contaminated water by *P. aeruginosa* during 20 days, highlighting a strong diesel degradation capacity.

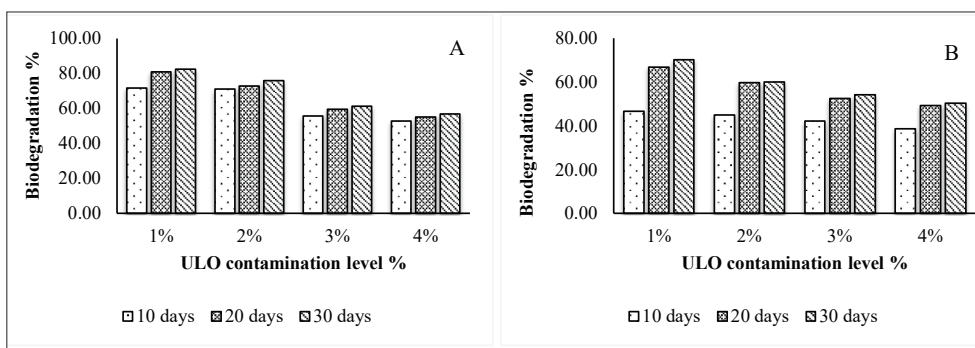


Figure 5 (a): Percentage biodegradation of ULO at 1–4 % (w/w) contamination levels over 30 days of incubation inoculated with *P. aeruginosa* RUH-K01 (A) and *A. fumigatus* RUH-F07 (B).

Similarly, it has been shown that *P. aeruginosa* was able to reduce TPH concentration in crude petroleum-contaminated soil from 84 to 21 g/kg within 60 days (Das & Mukherjee, 2007). Results obtained for *A. fumigatus* RUH-F07 in the present study and results of similar studies available in the literature indicates that *A. fumigatus* is known to be a frequent fungal species in soils polluted with petroleum, emphasizing its tolerance and ability to grow and survive in such soils (Al-Jawhari, 2014). Further, 78% degradation of crude oil by *A. fumigatus* at 2% (v/v) contamination level during 28 days has been reported, highlighting its suitability for remediation of hydrocarbon polluted soil at low contamination levels (Al-Jawhari, 2014). Moreover, Tiwari and Saraf (2017) have showed 71.1% of crude oil degradation at a 1% (v/v) contamination level within seven days by *A. fumigatus* isolated from ULO contaminated soil. Therefore, the results of the present study are in agreement with the previous findings. However, the observed decrease in the degradation efficiency at the ULO contamination levels higher than 1% (w/w) and the resulting degradation plateau after 20 days of incubation indicate dependency of ULO degradation rate on both ULO contamination levels and time. However, even at a higher contamination level such as 4% (w/w) ULO, the recorded 56.91%, and 50.25% biodegradation from the microcosm inoculated with RUH-K01 and RUH-F07, respectively, at the end of 30 days indicate the higher ULO degradation potential of both novel strains, highlighting their suitability to be used in bioaugmentation or bioremediation.

The results of Two-way ANOVA revealed significantly higher ($p < 0.05$) residual TPH content (mg/g) with respect to the contamination level and time, in treatments inoculated by both strains. However, the interactive effect between ULO contamination level and incubation time on the residual TPH content (mg/g) in both strains were not significant ($p > 0.05$). Wu *et al.* (2017) have observed a similar pattern of degradation in soils contaminated with TPH and alkane following three weeks of incubation.

This type of degradation pattern may be due to the inhibition of the degradation as a result of the accumulation of toxic metabolites produced early in the degradation process (Chaineau *et al.*, 2003). In addition, accumulation of high molecular weight aromatic hydrocarbons that are resistant to microbial degradation in the soil matrix can also be a reason for limited biodegradation after 35-40 days of incubation (Lee *et al.*, 2007). Therefore, the observed limitations in the degradation following the initial phase in the microcosms inoculated with both RUH-K01 and RUH-

F07 might be due to accumulation of toxic intermediate metabolites along with residual high molecular weight aromatic hydrocarbons, or the limitation of carbon source for microbes, or due to the combined effect of both.

Total microbial activity

Microbial activity is an important parameter to understand the capability of microbial degradation of xenobiotic compounds. Previous studies have reported the possible negative impacts of hydrocarbons on the metabolic pathways of soil microorganisms, through changes in the activities of enzymes such as dehydrogenase, lipase, urease, and catalase (Margesin *et al.*, 2000). Most such enzymes produced by microorganisms have the potential to hydrolyze colorless fluorescein di-acetate (FDA) into a colored end product called fluorescein (Patle *et al.*, 2018). Since the rate of fluorescein production indicates the total microbial activity (TMA), FDA assay was employed as a tool to assess the changes in TMA during the degradation of ULO in the microcosms inoculated by RUH-K01 and RUH-F07. FDA assay revealed the decreasing trend in the production of fluorescein in both *P. aeruginosa* and *A. fumigatus* inoculated soils when the ULO contamination level increased (1–4% w/w) (Figure 5 (b)). The highest fluorescein concentrations reached were 6.825 $\mu\text{g/mL}$ and 6.124 $\mu\text{g/mL}$ at 1% ULO contamination level following 10 days of incubation with *P. aeruginosa* and *A. fumigatus* respectively. Therefore, results indicate the contamination level and time-dependent decrease in TMA with increasing ULO contamination level and incubation time. Abioye *et al.* (2012) have reported that low levels of ULO in soil may not have a negative impact on the metabolic activities of the microbial population in microcosms. In a previous study, a concentration-dependent reduction has been reported in microbial biomass which was exposed to increasing crude oil concentration (Vanishree *et al.*, 2014). Thus the possible reasons for the observed trend in the current study might be due to the inhibition of the growth and proliferation of microorganisms as a result of direct toxic effects (Tshikantwa *et al.*, 2018) or indirect toxicity caused by the secondary metabolites generated during the biodegradation process. The resulting differences in the decreasing trend in the production of fluorescein by *P. aeruginosa* and *A. fumigatus* with respect to the ULO contamination level and incubation time reflect the species-specific differences of the microorganisms employed in the microcosms. The bioavailability of contaminants in the soil environment affects microbial activity (Antizar-Ladislao, 2010). Therefore, a larger reduction of the bioavailable fraction of ULO in the microcosm inoculated by *P. aeruginosa*

compared to that of *A. fumigatus* inoculated soil might be another reason for the observed disparity in TMA reflected by FDA hydrolysis due to RUH-K01 and RUH-F07. Results of the Two-way ANOVA revealed that there was a significantly higher ($p < 0.05$) interactive effect between ULO contamination level and incubation time on the TMA of *P. aeruginosa* inoculated soil.

The observed decrease in TMA might be the reason for the reduction of the percentage of biodegradation at higher levels of ULO contamination. According to Ramos *et al.* (1991), the population density of microorganisms present in a hydrocarbon-contaminated medium after inoculation with a potential microbial degrader is one of the main criteria that determines the efficiency of biodegradation. Therefore, in the present study, the bioremediation process was monitored by estimating residual TPH content and total microbial activity. At the end of 30 days, a significant negative correlation ($p < 0.05$) of -0.636, and -0.929 between

residual TPH content and TMA were observed in both the strains, RUH-K01 and RUH-F07, respectively. Margesin *et al.* (2000) reported that the effects caused to the microbial population by organic compounds can be positive, negative, or indifferent, and the degree of the effect on the microbial population may vary with the level of the contamination or the concentration, and with the period of exposure of microbes. Limited studies have been conducted so far to explore the relationship between degradation of hydrocarbons and microbial populations and their activity. According to the study of Tang *et al.* (2012), a significant negative correlation was observed between TPH content and bacterial population. Another study has shown a negative correlation for the biodegradation of polycyclic aromatic hydrocarbons (PAHs), due to the reduction of organic pollutants causing less bioavailability for microorganisms with time (Sverdrup *et al.*, 2002). Therefore, the results of the present study are consistent with the finding of similar studies available in the literature.

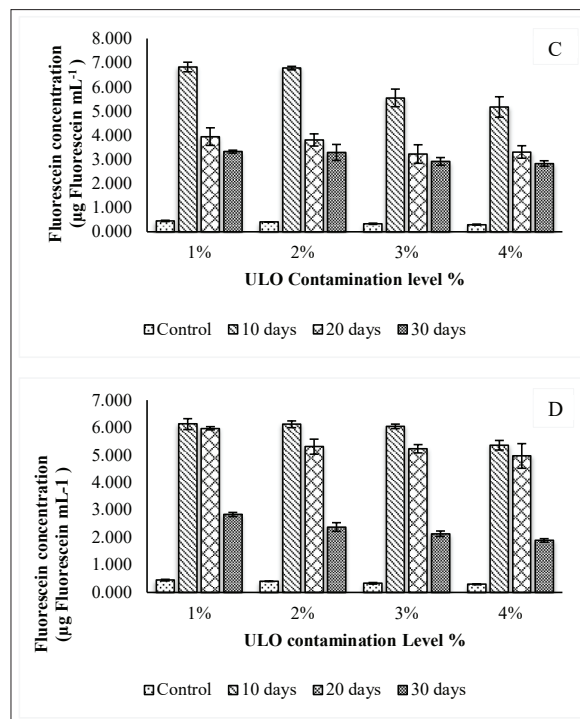


Figure 5 (b): Concentration of Fluorescein produced at 1–4 % (w/w) contamination levels over 30 days of incubation inoculated with *P. aeruginosa* RUH-K01 (C) and *A. fumigatus* RUH-F07 (D). Error bars represent the standard deviation of three independent measurements.

CONCLUSION

Two novel strains, bacterium RUH-K01 and fungi RUH-F07, with the potential to degrade ULO efficiently were isolated from soil with prolonged exposure to ULO contamination. Subsequent phylogenetic analysis following initial morphological characterization confirmed the novel strains as *P. aeruginosa* RUH-K01 and *A. fumigatus* RUH-F07. Therefore, the present study contributed to upgrading features of *Pseudomonas aeruginosa* and *Aspergillus fumigatus* with a potential to degrade ULO. While the increase in the level of contamination (1–4% w/w) showed a slight reduction in the degradation of ULO, *P. aeruginosa* RUH-K01 was found to be more efficient in ULO degradation than *A. fumigatus* RUH-F07. The FDA assay revealed the possibility of assessing TMA as an appropriate method to characterize ULO degradation efficiency of microorganisms. The positive results for the oil spreading test confirmed the potential of *P. aeruginosa* RUH-K01 to produce biosurfactants. The metabolic activities of both strains would make them promising agents for bioremediation of ULO contaminated soil. Therefore, findings of this study provide important information for establishing bioremediation by *P. aeruginosa* and *A. fumigatus*. However, it is recommended to carry out small scale field trials using the two strains in order to further confirm the laboratory derived data.

Acknowledgement

Financial assistance received from the Faculty of Science, University of Ruhuna (Grant No. RU/SF/RP/2018-09) is gratefully acknowledged.

REFERENCES

- Abioye O., Agamuthu P. & Abdul Aziz A. (2012). Biodegradation of used motor oil in soil using organic waste amendments. *Biotechnology Research International* **2012**: 1–8.
DOI: <https://doi.org/10.1155/2012/587041>
- Adam G. & Duncan H. (2001). Development of a sensitive and rapid method for the measurement of total microbial activity using fluorescein diacetate (FDA) in a range of soils. *Soil Biology and Biochemistry* **33**: 943–951.
DOI: [https://doi.org/10.1016/S0038-0717\(00\)00244-3](https://doi.org/10.1016/S0038-0717(00)00244-3)
- Agarry S.E. & Ogunleye O.O. (2012). Box-Behnken design application to study enhanced bioremediation of soil artificially contaminated with spent engine oil using biostimulation strategy. *International Journal of Energy and Environmental Engineering* **1**(3): 1–14.
DOI: <https://doi.org/10.1186/2251-6832-3-31>
- Al-Jawhari I.F.H. (2014). Ability of some soil fungi in biodegradation of petroleum hydrocarbon. *Journal of Applied & Environmental Microbiology* **2**(2): 46–52.
DOI: <https://doi.org/10.12691/jaem-2-2-3>
- Alisi C., Musella R., Tasso F., Ubaldi C., Manzo S., Cremisini C. & Sprocati A.R. (2009). Bioremediation of diesel oil in a co-contaminated soil by bioaugmentation with a microbial formula tailored with native strains selected for heavy metals resistance. *Science of the Total Environment* **407**(8): 3024–3032.
DOI: [10.1016/j.scitotenv.2009.01.011](https://doi.org/10.1016/j.scitotenv.2009.01.011)
- Antizar-Ladislao B. (2010). Bioremediation: working with bacteria. *Elements* **6**(6): 389–394.
DOI: <https://doi.org/10.2113/gselements.6.6.389>
- ATSDR (1997). Toxicology: Profile for used mineral base crankcase oil. Atlanta: ATSDR (Agency for Toxic Substances and Disease Registry)
- Bartha R. & Bossert I. (1984). The treatment and disposal of petroleum wastes. In: *Petroleum Microbiology*, pp. 553–577. Macmillan Publ Co, New York, USA.
DOI: <https://doi.org/10.4491/ceer.2018.134>
- Batista S., Mounteer A., Amorim F. & Totola M. (2006). Isolation and characterization of biosurfactant/bioemulsifier-producing bacteria from petroleum contaminated sites. *Bioresource Technology* **97**(6): 868–875.
DOI: <https://doi.org/10.1016/j.biortech.2005.04.020>
- Breed R.S. & Bergey D.H. (1948). Manual of determinative bacteriology. In: *Manual of Determinative Bacteriology*. Williams & Wilkins, USA.
- Chaineau C., Yepremian C., Vidalie J., Ducreux J. & Ballerini D. (2003). Bioremediation of a crude oil-polluted soil: biodegradation, leaching and toxicity assessments. *Water, Air, and Soil Pollution* **144**(1): 419–440.
DOI: <https://doi.org/10.1023/A:1022935600698>
- Chang L.K., Ibrahim D. & Omar I.C. (2011). A laboratory scale bioremediation of Tapis crude oil contaminated soil by bioaugmentation of *Acinetobacter baumannii* T30C. *African Journal of Microbiology Research* **5**(18): 2609–2615.
DOI: <https://doi.org/10.5897/AJMR11.185>
- Das K. & Mukherjee A.K. (2007). Crude petroleum-oil biodegradation efficiency of *Bacillus subtilis* and *Pseudomonas aeruginosa* strains isolated from a petroleum-oil contaminated soil from North-East India. *Bioresource Technology* **98**(7): 1339–1345.
DOI: <https://doi.org/10.1016/j.biortech.2006.05.032>
- Das N. & Chandran P. (2011). Microbial degradation of petroleum hydrocarbon contaminants: an overview. *Biotechnology Research International* **2011**: 1–13.
DOI: <https://doi.org/10.4061/2011/941810>
- Das P., Yang X.P. & Ma L.Z. (2014). Analysis of biosurfactants from industrially viable *Pseudomonas* strain isolated from crude oil suggests how rhamnolipids congeners affect emulsification property and antimicrobial activity. *Frontiers in Microbiology* **5**: 696.
DOI: <https://doi.org/10.3389/fmicb.2014.00696>
- Gamage S.S.W., Masakorala K., Brown M.T. & Gamage S.M.K.W. (2020). Tolerance of *Impatiens balsamina* L.,

- and *Crotalaria retusa* L. to grow on soil contaminated by used lubricating oil: A comparative study. *Ecotoxicology and Environmental Safety* **188**: 109911.
DOI: <https://doi.org/10.1016/j.ecoenv.2019.109911>
- Gautam K. & Tyagi V. (2006). Microbial surfactants: a review. *Journal of Oleo Science* **55**(4): 155–166.
DOI: <https://doi.org/10.5650/jos.55.155>
- Ghazala I., Bouallegue A., Haddar A. & Ellouz-Chaabouni S. (2019). Characterization and production optimization of biosurfactants by *Bacillus mojavensis* I4 with biotechnological potential for microbial enhanced oil recovery. *Biodegradation* **30**(4): 235–245.
DOI: <https://doi.org/10.1007/s10532-018-9844-y>
- Ghoreishi G., Alemzadeh A., Mojarrad M. & Djavaheri M. (2017). Bioremediation capability and characterization of bacteria isolated from petroleum contaminated soils in Iran. *Sustainable Environment Research* **27**(4): 195–202.
DOI: <https://doi.org/10.1016/j.serj.2017.05.002>
- Glibovytska N.I., Karavanovych K.B. & Kachala T.B. (2019). Prospects of phytoremediation and phytoindication of oil-contaminated soils with the help of energy plants. *Journal of Ecological Engineering* **20**(7): 147–154.
DOI: <https://doi.org/10.12911/22998993/109875>
- Husaini A., Roslan H., Hii K. & Ang C. (2008). Biodegradation of aliphatic hydrocarbon by indigenous fungi isolated from used motor oil contaminated sites. *World Journal of Microbiology and Biotechnology* **24**(12): 2789–2797.
DOI: <https://doi.org/10.1007/s11274-008-9806-3>
- Ibrahim M., Makky E.A., Azmi N.S. & Ismail J. (2018). Impact of incubation period on biodegradation of petroleum hydrocarbons from refinery wastewater in Kuantan, Malaysia by indigenous bacteria. *Bioremediation Journal* **22**(1–2): 10–19.
DOI: <https://doi.org/10.1080/10889868.2018.1476453>
- Jesubunmi C.O. (2014). Isolation of oil-degrading microorganisms in spent engine oil-contaminated soil. *Journal of Biology, Agriculture and Healthcare* **4**(24): 191–195.
- Kadali K.K., Simons K.L., Skuza P.P., Moore R.B. & Ball A.S. (2012). A complementary approach to identifying and assessing the remediation potential of hydrocarbonoclastic bacteria. *Journal of Microbiological Methods* **88**(3): 348–355.
DOI: <https://doi.org/10.1016/j.mimet.2011.12.006>
- Kearse M., Moir R., Wilson A., Stones-Havas S., Cheung M., Sturrock S., Buxton S., Cooper A., Markowitz S. & Duran C. (2012). Geneious Basic: an integrated and extendable desktop software platform for the organization and analysis of sequence data. *Bioinformatics* **28**(12): 1647–1649.
DOI: <https://doi.org/10.1093/bioinformatics/bts199>
- Lee S.H., Lee S., Kim D.Y. & Kim J.G. (2007). Degradation characteristics of waste lubricants under different nutrient conditions. *Journal of Hazardous Materials* **143**(1–2): 65–72.
DOI: <https://doi.org/10.1016/j.jhazmat.2006.08.059>
- Ling J., Zhang G., Sun H., Fan Y., Ju J. & Zhang C. (2011). Isolation and characterization of a novel pyrene-degrading *Bacillus vallismortis* strain JY3A. *Science of the Total Environment* **409**(10): 1994–2000.
DOI: <https://doi.org/10.1016/j.scitotenv.2011.02.020>
- Liu P.W.G., Chang T.C., Whang L.M., Kao C.H., Pan P.T. & Cheng S.S. (2011). Bioremediation of petroleum hydrocarbon contaminated soil: effects of strategies and microbial community shift. *International Biodeterioration & Biodegradation* **65**(8): 1119–1127.
DOI: <https://doi.org/10.1016/j.ibiod.2011.09.002>
- Mandri T. & Lin J. (2007). Isolation and characterization of engine oil degrading indigenous microorganisms in Kwazulu-Natal, South Africa. *African Journal of Biotechnology* **6**(1): 23–27.
DOI: <https://doi.org/10.5897/AJB07.728>
- Margesin R. & Schinner F. (2001). Bioremediation (natural attenuation and biostimulation) of diesel-oil-contaminated soil in an alpine glacier skiing area. *Applied Environmental Microbiology* **67**(7): 3127–3133.
DOI: <https://doi.org/10.1128/AEM.67.7.3127-3133.2001>
- Margesin R., Zimmerbauer A. & Schinner F. (2000). Monitoring of bioremediation by soil biological activities. *Chemosphere* **40**(4): 339–346.
DOI: [https://doi.org/10.1016/S0045-6535\(99\)00218-0](https://doi.org/10.1016/S0045-6535(99)00218-0)
- Masakorala K., Yao J., Cai M., Chandankere R., Yuan H. & Chen H. (2013). Isolation and characterization of a novel phenanthrene (PHE) degrading strain *Psuedomonas* sp. USTB-RU from petroleum contaminated soil. *Journal of Hazardous Materials* **263**: 493–500.
DOI: <https://doi.org/10.1016/j.jhazmat.2013.10.007>
- McIntosh P., Schulthess C.P., Kuzovkina Y.A. & Guillard K. (2017). Bioremediation and phytoremediation of total petroleum hydrocarbons (TPH) under various conditions. *International Journal of Phytoremediation* **19**(8): 755–764.
DOI: <https://doi.org/10.1080/15226514.2017.1284753>
- Ogunbayo A., Bello R. & Nwagbara U. (2012). Bioremediation of engine oil contaminated site. *Journal of Emerging Trends in Engineering and Applied Sciences* **3**(3): 483–489.
DOI: <https://doi.org/10.7717/peerj.7389>
- Ortega-Calvo J. (2017). Strategies to increase bioavailability and uptake of hydrocarbons. In: *Cellular Ecophysiology of Microbe: Hydrocarbon and Lipid Interactions* (ed. T. Krell), pp. 303–314. Springer, USA.
DOI: https://doi.org/10.1007/978-3-319-20796-4_10-1
- Pacwa-Płociniczak M., Plaza G. A., Poliwoda A. & Piotrowska-Seget Z. (2014). Characterization of hydrocarbon-degrading and biosurfactant-producing *Pseudomonas* sp. P-1 strain as a potential tool for bioremediation of petroleum-contaminated soil. *Environmental Science and Pollution Research* **21**: 9385–9395.
DOI: <https://doi.org/10.1007/s11356-014-2872-1>
- Pušárová A., Bučková M., Chovanová K., Harichová J., Karelová E., Godočiková J., Polek B., Ferienc P. & Pangallo D. (2013). Diversity and PAH growth abilities of bacterial strains isolated from a contaminated soil in Slovakia. *Biologia* **68**(4): 587–591.
DOI: <https://doi.org/10.2478/s11756-013-0193-3>
- Ramos J., Duque E. & Ramos-Gonzalez M. (1991). Survival in soils of an herbicide-resistant *Pseudomonas putida* strain bearing a recombinant TOL plasmid. *Applied Environmental Microbiology* **57**(1): 260–266.
DOI: <https://doi.org/10.1128/aem.57.1.260-266.1991>

- Riddell R.W. (1950). Permanent stained mycological preparations obtained by slide culture. *Mycologia* **42**(2): 265–270.
DOI: <https://doi.org/10.2307/3755439>
- Safdari M.S., Kariminia H.R., Nejad Z.G. & Fletcher T.H. (2017). Study potential of indigenous *Pseudomonas aeruginosa* and *Bacillus subtilis* in bioremediation of diesel-contaminated water. *Water, Air, & Soil Pollution* **228**(1): 1–7.
DOI: <https://doi.org/10.1007/s11270-016-3220-5>
- Sardrood B.P., Goltapeh E.M. & Varma A. (2013). An introduction to bioremediation. In: *Fungi as Bioremediators*, pp. 3–27. Springer, USA.
DOI: https://doi.org/10.1007/978-3-642-33811-3_1
- Shahsavari E., Poi G., Aburto-Medina A., Haleyur N. & Ball A.S. (2017). Bioremediation approaches for petroleum hydrocarbon-contaminated environments. In: *Enhancing Cleanup of Environmental Pollutants*, pp. 21–41. Springer, USA.
DOI: https://doi.org/10.1007/978-3-319-55426-6_3
- Sperb J.G.C., Costa T.M., Bertoli S.L. & Tavares L.B.B. (2018). Simultaneous production of biosurfactants and lipases from *Aspergillus niger* and optimization by response surface methodology and desirability functions. *Brazilian Journal of Chemical Engineering* **35**: 857–868.
DOI: <https://doi.org/10.1590/0104-6632.20180353s20160400>
- Sverdrup L.E., Nielsen T. & Krogh P.H. (2002). Soil ecotoxicity of polycyclic aromatic hydrocarbons in relation to soil sorption, lipophilicity, and water solubility. *Environmental Science & Technology* **36**(11): 2429–2435.
DOI: <https://doi.org/10.1021/es010180s>
- Tang J., Lu X., Sun Q. & Zhu W. (2012). Aging effect of petroleum hydrocarbons in soil under different attenuation conditions. *Agriculture, Ecosystems & Environment* **149**: 109–117.
DOI: <https://doi.org/10.1016/j.agee.2011.12.020>
- Thenmozhi R., Arumugam K., Nagasathya A., Thajuddin N. & Paneerselvam A. (2013). Studies on mycoremediation of used engine oil contaminated soil samples. *Advanced in Applied Science Research* **4**(2): 110–118.
- Tiwari M. & Saraf A. (2017). Isolation, screening and identification of hydrocarbon degrading potential of indigenous fungus from oil contaminated soil of modha Para automobile Shop of Raipur, CG. *International Journal of Advance Research in Science and Engineering* **6**(10): 782–795.
- Tshikantwa T.S., Ullah M.W., He F. & Yang G. (2018). Current trends and potential applications of microbial interactions for human welfare. *Frontiers in Microbiology* **9**: 1156.
DOI: <https://doi.org/10.3389/fmicb.2018.01156>
- Tyagi M., da Fonseca, M.M.R. & de Carvalho C.C. (2011). Bioaugmentation and biostimulation strategies to improve the effectiveness of bioremediation processes. *Biodegradation* **22**(2): 231–241.
DOI: <https://doi.org/10.1007/s10532-010-9394-4>
- Umar A., Ujah U., Hauwa B., Sumayya B., Shuaibu M., Yakubu M. & Mina F. (2013). Biodegradation of waste lubricating oil by bacteria isolated from the soil. *Journal of Environmental Science, Toxicology and Food Technology* **3**(6): 32–37.
DOI: <https://doi.org/10.9790/2402-0366267>
- Vanishree M., Thatheyus A. & Ramya D. (2014). Biodegradation of petrol using the fungus *Penicillium* sp. *Science International* **2**(1): 26–31.
DOI: <https://doi.org/10.17311/sciintl.2014.26.31>
- Vazquez-Duhalt R. (1989). Environmental impact of used motor oil. *Science of the Total Environment* **79**(1): 1–23.
DOI: [https://doi.org/10.1016/0048-9697\(89\)90049-1](https://doi.org/10.1016/0048-9697(89)90049-1)
- Vinothini C., Sudhakar S. & Ravikumar R. (2015). Biodegradation of petroleum and crude oil by *Pseudomonas putida* and *Bacillus cereus*. *International Journal of Current Microbiology and Applied Sciences* **4**(1): 318–329.
- Wu M., Dick W.A., Li W., Wang X., Yang Q., Wang T., Xu L., Zhang M. & Chen L. (2016). Bioaugmentation and biostimulation of hydrocarbon degradation and the microbial community in a petroleum-contaminated soil. *International Biodeterioration & Biodegradation* **107**: 158–164.
DOI: <https://doi.org/10.1016/j.ibiod.2015.11.019>
- Wu M., Li W., Dick W.A., Ye X., Chen K., Kost D. & Chen L. (2017). Bioremediation of hydrocarbon degradation in a petroleum-contaminated soil and microbial population and activity determination. *Chemosphere* **169**: 124–130.
DOI: <https://doi.org/10.1016/j.chemosphere.2016.11.059>
- Wu Y., Luo Y., Zou D., Ni J., Liu W., Teng Y. & Li Z. (2008). Bioremediation of polycyclic aromatic hydrocarbons contaminated soil with *Monilinia* sp.: degradation and microbial community analysis. *Biodegradation* **19**(2): 247–257.
DOI: <https://doi.org/10.1007/s10532-007-9131-9>
- Yash M.P. (2015). Re-refining of used lubricating oil. *International Journal of Scientific & Engineering Research* **6**(3): 329–332.
- Yu C., Yao J., Cai M., Wang F., Masakorala K., Liu H., Blake R.E., Doni S. & Ceccanti B. (2013). Functional gene expression of oil-degrading bacteria resistant to hexadecane toxicity. *Chemosphere* **93**(7): 1424–1429.
DOI: <https://doi.org/10.1016/j.chemosphere.2013.07.035>
- Yuan H., Yao J., Masakorala K., Wang F., Cai M. & Yu C. (2014). Isolation and characterization of a newly isolated pyrene-degrading *Acinetobacter* strain USTB-X. *Environmental Science and Pollution Research* **21**(4): 2724–2732.
DOI: <https://doi.org/10.1007/s11356-013-2221-9>
- Zeneli A., Kastanaki E., Simantiraki F. & Gidaracos E. (2019). Monitoring the biodegradation of TPH and PAHs in refinery solid waste by biostimulation and bioaugmentation. *Journal of Environmental Chemical Engineering* **7**(3): 103054.
DOI: <https://doi.org/10.1016/j.jece.2019.103054>
- Zhang H., Tang J., Wang L., Liu J., Gurav R.G. & Sun K. (2016). A novel bioremediation strategy for petroleum hydrocarbon pollutants using salt tolerant *Corynebacterium variabile* HRJ4 and biochar. *Journal of Environmental Sciences* **47**: 7–13.

DOI: <https://doi.org/10.1016/j.jes.2015.12.023>
Zhao H.P., Wang L., Ren J.R., Li Z., Li M. & Gao H.W. (2008).
Isolation and characterization of phenanthrene-degrading

strains *Sphingomonas* sp. ZP1 and *Tistrella* sp. ZP5.
Journal of Hazardous Materials **152**(3): 1293–1300.
DOI: <https://doi.org/10.1016/j.jhazmat.2007.08.008>

RESEARCH ARTICLE

Environmental pollution

Screening and quantitative analysis of antibiotic resistance genes in hospital and aquaculture effluent in Sri Lanka as an emerging environmental contaminant

GY Liyanage^{1,4}, MM Weerasekera² and PM Manage^{1,3*}

¹ Centre for Water Quality and Algae Research, Department of Zoology, Faculty of Applied Sciences, University of Sri Jayewardenepura, Gangodawila, Nugegoda, Sri Lanka.

² Department of Microbiology, Faculty of Medical Sciences, University of Sri Jayewardenepura, Gangodawila, Nugegoda, Sri Lanka.

³ Faculty of Graduate Studies, University of Sri Jayewardenepura, Gangodawila, Nugegoda, Sri Lanka.

⁴ Department of Aquatic Bioresources, Faculty of Urban and Aquatic Bioresources, University of Sri Jayewardenepura, Gangodawila, Nugegoda, Sri Lanka.

Submitted: 09 April 2021; Revised: 11 October 2021; Accepted: 22 October 2021

Abstract: Hospital and aquaculture wastewaters play an important role in the evolution and spread of antibiotic resistance genes. In the present study, nine Antibiotic Resistance Genes (ARGs) were screened, which belong to two common groups of antibiotics: penicillin – *OPR D*, *bla TEM*, *bla OXA*, *amp a*, and *amp b*, and tetracycline – *tet A*, *tet M*, *tet B*, and *tet S*. The highest number of positive hospital wastewater sample locations were for *bla TEM* (51%) gene, followed in descending order by *amp a* (15%), *bla OXA* (14%), *OPR D* (5%) and *amp b* (1%). The highest number of positive sample locations for *tet (M)* genes was detected in aquaculture sampling sites (82%), followed by *tet (A)*, *tet (S)*, and *tet (B)* were 53%, 35%, and 18% respectively. A significant positive correlation ($p = 0.001$) between the concentrations of penicillin (0.001 – 0.006 $\mu\text{g/mL}$) and *bla TEM* gene (7.56×10^5 – 9.8×10^5 copies/mL) was found. The average concentrations of the *OPR D* and *amp a* was in the range 1.2×10^2 – 1.56×10^2 copies/mL, 1.2×10^5 – 6.56×10^5 copies/mL in hospital wastewater, whereas *tet M* and *tet A* in aquaculture effluent water was in the range 1.1×10^5 – 9.23×10^5 copies/mL and 1.3×10^4 – 4.56×10^4 copies/mL, respectively. The penicillin group (AMX, AMP, CLOX) in hospital wastewater effluent and tetracycline (TET, OTC) in aquaculture wastewater effluent were found to be important point sources of antibiotic pollution in their respective environments.

Keywords: Antibiotic-resistant genes, tetracycline, penicillin, *bla TEM*, *tet A*, *tet M*.

INTRODUCTION

The unregulated use of antibiotics in health care, livestock farming, and agriculture, has resulted in large amounts of such compounds being discharged directly into the natural ecosystem (Hernandes *et al.*, 2013). Wastewater effluent from hospitals, intensive livestock, and aquaculture are the major sources of Antibiotic Resistance Genes (ARGs). According to the reports of World Health Organization (WHO) ARGs are one of the most critical human health challenges in the next century. ARGs serve as pathways of carrying out genetic manipulation and generate pressure for the development of antibiotic resistance in a susceptible microbial strain through horizontal gene transfer (Rodríguez-Mozaz *et al.*, 2014; Liyanage & Manage, 2016a). The spread of antibiotic resistance is frequently associated with the high adaptive capacity of microorganisms.

Tetracycline and penicillin are widely used in livestock farming and healthcare. The major mechanisms for tetracycline resistance is prevention of drug uptake (efflux) into the cells, ribosomal protection, and enzyme inactivation (Ansari *et al.*, 2009). Efflux genes are *tet A*, *tet B*, *tet C*, *tet D*, *tet K*, and *tet L* (Ansari *et*

* Corresponding author (pathmalal@sjp.ac.lk;  <https://orcid.org/0000-0002-2014-2060>)



This article is published under the Creative Commons CC-BY-ND License (<http://creativecommons.org/licenses/by-nd/4.0/>). This license permits use, distribution and reproduction, commercial and non-commercial, provided that the original work is properly cited and is not changed in any way.

al., 2009). The *tet M* and *tet O* are common genes for ribosomal protection proteins (Huddleston, 2014; Ansari et al., 2009) while only *tet S*, *tetX*, *tet 34*, and *tet 37* are coding for a protein capable of enzymatic inactivation of tetracycline (Ansari et al., 2009). Penicillin is one of the common antibiotics, and major penicillin resistance mechanisms are antibiotic hydrolysis mediated by the bacterial enzyme *beta-lactamase (bla TEM)*, changes in Penicillin Binding Proteins (PBP) (*amp a*), and decreasing of porin channel formation (*OPR D*). Among the penicillin resistance genes, *bla TEM* gene is one of the most frequently detected plasmid-borne antimicrobial resistance genes, which confers resistance to penicillin and extended-spectrum cephalosporin (Mroczkowska & Barlow, 2008).

Current EU legislation does not include specific regulations, neither the potential presence of antibiotic-resistant bacteria and ARGs in these waters nor their concentration thresholds. The evaluation of ARGs in clinical and environmental settings would therefore be the first step in tackling the rapidly growing resistance to antibiotics (Huddleston, 2014). Although the knowledge of antibiotic resistance in hospital wastewaters has largely depended on data provided by culture-based methods, the analysis of ARGs is limited in developing countries (Duong et al., 2008; Finley et al., 2013; Fekadu et al., 2015; Hocquet et al., 2016).

Because of the complexity of the processes and the relative scarcity of studies done, knowledge regarding ARGs and their role in the environment is still poor, and therefore environmental studies are given priority.

Documented evidence related to ARG levels and resistant bacteria in hospitals and aquaculture wastewater effluent is limited in Sri Lanka (Liyanage et al., 2015; Liyanage & Manage, 2016a). This is the first report on screening and quantification of ARGs in hospital and aquaculture effluents in Sri Lanka. As an outcome, the study aimed to quantify ARGs for penicillin and tetracycline, as well as the level of antibiotic contamination in some selected hospital and aquaculture effluent water.

MATERIALS AND METHODS

Sampling sites and sample collection

Effluent water samples were collected in triplicate from 80 hospitals including the National Hospital Sri Lanka, 11 Teaching Hospitals, 15 General Hospitals, 30

Base Hospitals, 18 Divisional Hospitals, 2 Regional hospitals and 3 Private Hospitals (Table 1, Figure 1) and 16 aquaculture farms (food fish farms, ornamental fish farms, and shrimp farms) in different districts in Sri Lanka. Water samples were filtered through 150 µm plankton nets to remove debris and collected to sterile amber colour glass bottles (2 L). Then the samples were stored in ice boxes at 4°C during transportation and kept in refrigerated conditions for subsequent analysis.

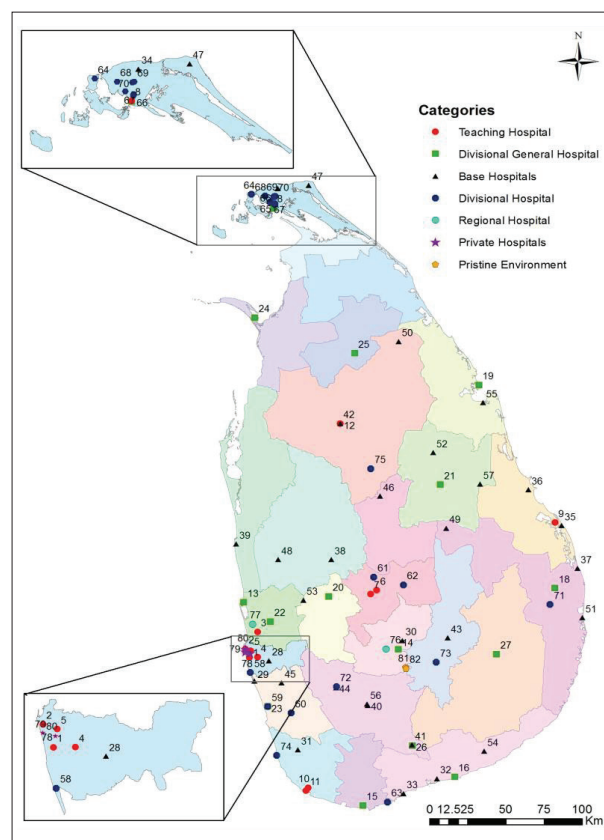


Figure 1: Hospital wastewater effluent sampling locations in the study

Quantification of tetracycline and penicillin in water samples

A 1L sample of wastewater was adjusted to pH 3 and filtered through a 0.22 µm Millipore filter. The filtered samples were spiked with antibiotic at a final concentration of 100 ppm and loaded onto a Sep-Pak Plus C18 cartridge after conditioning with 5ml of 100% HPLC grade methanol and following with 5 mL of deionized water (Liyanage et al., 2015). Pre-prepared

samples were then passed through the C18 cartridges set up with SPE unit at a flow rate of approximately 1–2 mL/min and then rinsed with 5 mL of deionized water. The analytes were eluted with HPLC grade 80% methanol (Liyanage & Manage, 2014; 2016b). The

target antibiotics were quantified by using an Agilent 1200 series HPLC equipped with a diode array and fluorescence detector (Fernandez-Torres *et al.*, 2010; Liyanage & Manage, 2016b). The injected volume was 20 µL and chromatography was performed at 30 °C.

Table 1: Hospital wastewater effluent sampling locations screened in the study

No	Location	No	Location	No	Location	No	Location
1.	Colombo-NHSL	21.	Polonnaruwa-GH	41.	Ambilipitiya- BH	61.	Akurana- -DH
2.	Colombo South Teaching Hospital (CSTH)	22.	Gampaha-GH	42.	Anuradhapura- BH	62.	Madadumbara -DH
3.	Colombo Northern Teaching Hospital (CNTH)	23.	Kalutara-GH	43.	Badulla -BH	63.	Dickwella -DH
4.	J'pura hospital – TH	24.	Mannar-GH	44.	Awissawella –BH	64.	Karainagar -DH
5.	Castle Street Hospital for Women (CSHW)- TH	25.	Vauniya-GH	45.	Horana-BH	65.	Konadavil -DH
6.	Kandy- TH	26.	Embilipitiya –GH	46.	Dambulla-BH	66.	Kokuvil -DH
7.	Peradeniya- TH	27.	Monaragala-GH	47.	Point pedro-BH	67.	Manipay-DH
8.	Jaffna- TH	28.	Homagama -BH	48.	Kuliyapitiya-BH	68.	Vaddukkodai -DH
9.	Batticaloa- TH	29.	Panadura- BH	49.	Dehiattakandiya-BH	69.	Chunnakam -DH
10.	Karapitiya- TH	30.	Ambewala - BH	50.	Padaviya-BH	70.	Uduvil -DH
11.	Mahamodara- TH	31.	Alpitiya- BH	51.	Thirukkivil-BH	71.	Damana -DH
12.	Anuradhapura- TH	32.	Ambalanthota- BH	52.	Medirigiriya-BH	72.	Rathnapura-DH
13.	Negombo-GH	33.	Tangalle- BH	53.	Warakapola-BH	73.	Bandarawela-DH
14.	Nuwaraeliya-GH	34.	Tellippalai- BH	54.	Tissamaharama-BH	74.	Ambalangoda-DH
15.	Matara-GH	35.	Kattankudy- BH	55.	Muthur-BH	75.	Kekirawa-DH
16.	Hambanthota-GH	36.	Valaichchenai- BH	56.	Kahawatta-BH	76.	Lindula-RH
17.	Jaffna-GH	37.	Kalmunai- BH	57.	Welikanda-BH	77.	Jae la-RH
18.	Ampara-GH	38.	Kurunegala -BH	58.	Moratuwa -DH	78.	Asiri hospital-Colombo
19.	Trincomalee-GH	39.	Puttalam- BH	59.	Kalutara -DH	79.	Durdans Hospital-Colombo
20.	Kegalle-GH	40.	Kahawatta- BH	60.	Mathugama -DH	80.	Nawaloka hospital-Colombo

TH; Teaching Hospitals, GH; General Hospitals, BH; Base Hospitals, DH; Divisional Hospitals, RH; Regional Hospitals.

Extraction of environmental DNA from wastewater effluent

For DNA extraction, a 250 mL sample of water was collected and filtered through a 47 mm polycarbonate filter (0.22 µm pore size, Millipore). Each filter paper was soaked in 10 mL of 70% methanol and stored at -20°C until use. Extraction of DNA from the filter paper was carried out according to a modified version of Kim *et al.* (2012). Purified DNA was subjected to PCR analysis.

Detection of ARGs by PCR

PCR was performed to detect antibiotic resistance genes and the PCR mixtures contained 0.5 µL of target primer (10 µM), 5 µL of Go taq reaction buffer, 0.5 µL of dNTPs, 2.0 µL of 25 mM MgCl₂ and 0.1 µL of Gotaq DNA polymerase, adjusted to a total volume of 25 µL. Purified DNA (5 µL) was used as the PCR template. Optimized conditions used for the primers are shown in Table 1. PCR amplification was performed using the BIOLAB PCR system thermal cycler (BYQ6078E-757, China)

and utilized 35 cycles (denaturation at 95 °C for 30 s, annealing for 30 s, and extension at 72°C for 1 min). The final extension was performed at 72 °C for 5 min. The amplified products were analysed by electrophoresis on a 1.5% agarose gel stained with ethidium bromide.

Quantification of Antibiotic Resistance Genes (ARGs)

Real-time PCR (qPCR) assays were employed to quantify five ARGs: *bla TEM*, *bla OXA*, *amp a*, *tet A*, and *tet M*, which confer resistance to the main antibiotic

families' penicillin and tetracycline. Quantitative PCR (qPCR) assays were performed using the SYBR Green chemistry (Applied Bio systems) using an Applied Bio system 7500 real-time machine (Martí *et al.*, 2013). Each gene was amplified using specific primer sets (Table 2) and the PCR conditions included an initial denaturation at 95 °C for 3 min, followed by 40 cycles at 95 °C for 15 s and at the annealing temperatures are given in the Table 2 for 20 s. After each qPCR assay, a dissociation curve was constructed by increasing the temperature from 65 to 95 °C to confirm the specificity of the amplified products.

Table 2: Primers, primer sequences and annealing temperatures used to amplify selected resistant genes of the two antibiotics, *i.e.*, Tetracycline and Penicillin

Antibiotic group	Resistance gene	Primer pair	Nucleotide sequence 5' – 3'	Annealing temperature (°C)
Tetracycline	tet (A)	tet A-F	GCGCGATCTGGTCACTCG	56
		tet A-R	AGTCGACAGYRGC GCCGGC	
	tet (M)	tet M - F	GTAAATAGTGTCTTGGAG	48
		tet M- R	CTAAGATATGGCTCTAACAA	
	ORP (D)	ORP- F	TTGGTTAGGGGCAAGTTTTG	64
		ORP- R	GTAATGGGCCAATAACACCG	
Penicillin	TEM-1	TEM-1- F	CATAGACAAGCCGTTGACC	57
		TEM-1- R	ATGTTTTTGG AACGACAGAG	
	amp a	amp a -F	CATAGACAAGCCGTTGACC	32
		amp a -R	ATGTTTTTGG AACGACAGAG	

Development of standard curves

Standard curves were generated by cloning the amplicon from positive controls into the PBR322 vector (Invitrogen, USA), and the corresponding copy number was calculated as follows: copy number $\mu\text{L}^{-1} = (A \times 6.022 \times 10^{23}) (660 \times B)^{-1}$, where A is the plasmid DNA concentration ($\text{g } \mu\text{L}^{-1}$), B is the plasmid length (bp) containing the cloned sequence, 6.022×10^{23} is Avogadro's number and 660 is the average molecular weight of one base pair (Perini *et al.*, 2011). A ten-fold

serial dilution was used to construct the standard curve for each ARG, which was run in parallel with the samples to obtain absolute quantification.

Statistical analysis

Comparisons of average antibiotic and ARG concentrations among different sampling points were carried out using ANOVA tests. Correlation between antibiotic and ARG values was made using Pearson's test (all variables satisfied the normality assumption).

Differences were considered significant at $p < 0.05$. All statistical analysis was performed using Minitab 17 software.

RESULTS AND DISCUSSION

At present great attention has been paid to the heavy use of antibiotics in hospitals and the aquaculture industry by national and international health agencies due to the development of antibiotic resistance (Aminov & Mackie, 2007; WHO, 2015).

The most abundantly use antibiotic classes in the worldwide are β -lactams, glycopeptides, sulphonamides, quinolones and trimethoprim (Kümmerer, 2001; Kimosop *et al.*, 2016). β -Lactams and tetracycline are the most intensively used antibiotic classes for human therapies in Sri Lanka (Ministry of Health, 2015). However, the same antibiotics which are used for human infections are used for different diseases and as growth hormones in the aquaculture industry (NAQDA, 2015). Despite Sri Lanka's lengthy history of antibiotic use, information on antibiotic manufacturing and usage trends is scarce due to a lack of publicly available information, systematic monitoring, and documentation efforts.

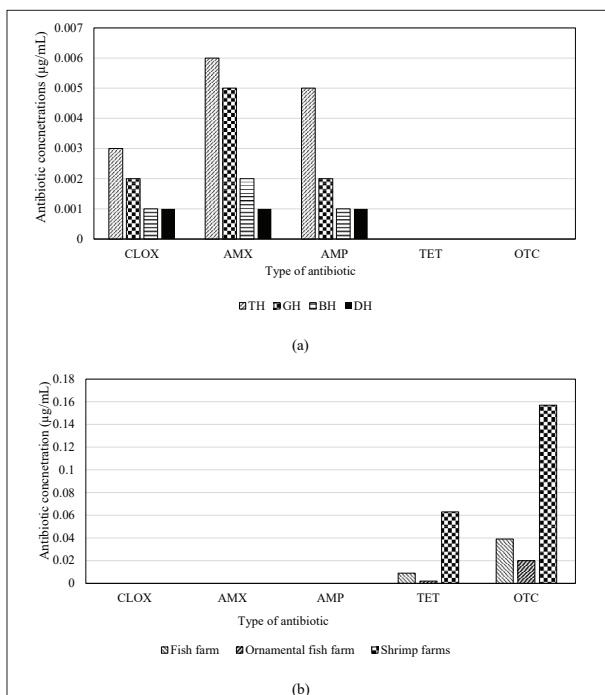


Figure 2: Mean antibiotic contamination in (a) Hospital effluent (TH: Teaching Hospitals, GH; General Hospitals, BH; Base Hospitals, DH; Divisional Hospitals) and (b) Aquaculture effluent ($n = 3$)

Antibiotic concentrations in hospital and aquaculture wastewater

The mean concentrations of antibiotics in the penicillin (AMX, AMP, CLOX) group ranged from 0.001 $\mu\text{g/mL}$ to 0.006 $\mu\text{g/mL}$ for hospital effluent water. However, OTC and TET were not recorded in hospital effluent during the study period (Figure 2 a).

The detected mean OTC concentration ($0.157 \pm 0.001 \mu\text{g/mL}$) in shrimp hatcheries was comparatively higher than OTC concentrations ($0.039 \pm 0.012 \mu\text{g/mL}$) recorded in food fish farms and ornamental fish farms ($0.020 \pm 0.011 \mu\text{g/mL}$). Similarly, a high mean TET concentration was detected in shrimp hatcheries ($0.063 \pm 0.019 \mu\text{g/mL}$) compared to ornamental ($0.002 \pm 0.001 \mu\text{g/mL}$) and food fish farms ($0.009 \pm 0.001 \mu\text{g/mL}$) (Figure 2b). Antibiotics in the penicillin group were not detected in any aquaculture wastewater effluent during the period.

Screening of Antibiotic Resistance Genes (ARGs)

Many researchers have reported the potential presence of ARGs in environmental samples worldwide (Hsieh *et al.*, 2011; Pruden *et al.*, 2013), including in the pristine environment (Hsieh *et al.*, 2011; Pruden *et al.*, 2013; Liyanage & Manage, 2016a). According to the authors' knowledge, so far, no records are available regarding ARGs (*tet M*, *tet S*, *tet A*, *amp a*, *amp b*, *amp c*, *bla TEM*, and *bla OXA*) in environmental samples in Sri Lanka (Liyanage & Manage, 2015). Thus, the present study is the first report of screening at more than 90 sampling locations including hospital effluents and aquaculture farms for the potential of ARGs in Sri Lanka.

The percentage of positive sampling locations for penicillin resistance genes (*bla TEM*, *bla OXA*, *OPR D*, *amp a*, *amp b*) detected ranged from 5% to 51%, which is higher than the percentage of positive sampling locations of tetracycline resistance genes (*tet A*, *tet M*, *tet S* and *tet B*) in hospital wastewater samples (Figure 3). The highest number of positive hospital wastewater sample locations were for *bla TEM* (51%) gene, followed in descending order by *amp a* (15%), *bla OXA* (14%), *OPR D* (5%) and *amp b* (1%) [Figure 3(a)].

By contrast, the resistance genes *tet A*, *tet M*, *tet B*, and *tet S* belonging to the tetracycline group (OTC and TET) was detected in aquaculture sites with high frequency, ranging from 17% to 82%, compared with hospital wastewater effluents (0.5% to 11%), suggesting that the usage of specific antibiotics in

particular applications cause ARGs development in the environment [Figure 3(b)].

It should be noted that in the present study, a pristine reference sample was collected from the Horton plains, which is situated 2100 m above sea level and was declared a World Heritage Site (WHS) by UNESCO (UNESCO, 2010). The investigators of the study assumed that the Horton plains are free of antibiotic contamination due to minimum anthropological impact and strict regulations for human entry into the Horton plains. Interestingly, none of the antibiotics was detected in the Horton

plains, supporting the assumption that it is a pristine environment for the study. However, AMX and TET resistance bacteria were detected in Horton plains water samples and one sample was even positive for the *bla TEM* gene. The presence of ARGs in such environments may be the result of Horizontal Gene Transfer (Hsieh et al., 2011; Liyanage & Manage, 2017), which can facilitate the development of new resistance bacteria. Thus, further studies are needed to investigate how the level of antibiotic resistance has developed and spread, and also how these levels vary in different environments with different bacterial communities.

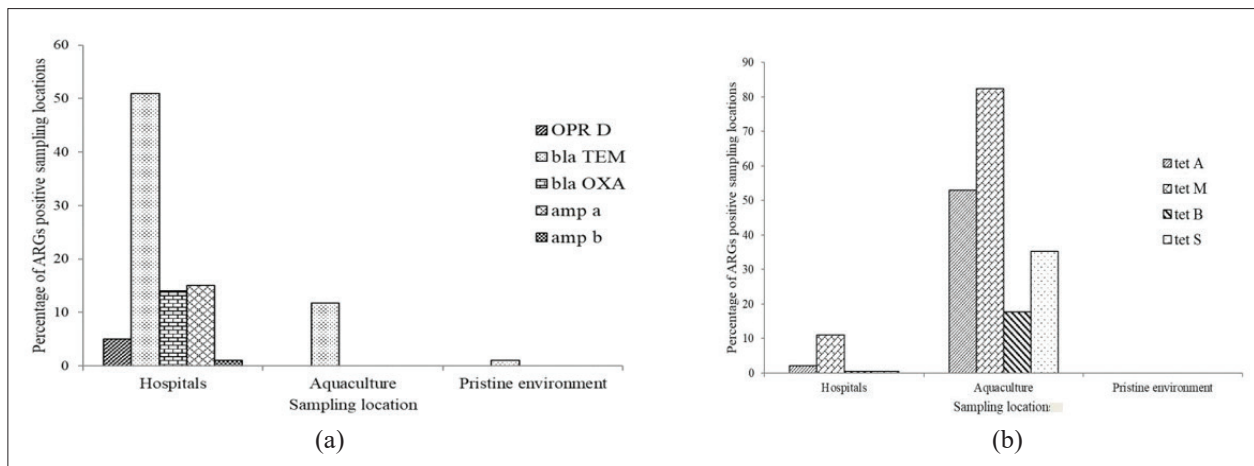


Figure 3: - Penicillin (a) (*bla TEM*, *bla OXA*, *OPR D*, *amp a*, *amp b*) and tetracycline (b) (*tet M*, *tet S*, *tet A*, *tet B*) resistance gene percentages at the wastewater effluent in hospitals, aquaculture farms and pristine environment

Quantification of Antibiotic Resistance Genes (ARGs)

In the present study, culture-independent approaches were used to determine the occurrence and abundance of ARGs. Out of five 5 genes which were initially investigated during the pre-screening process in the wastewater of 80 hospitals, three genes were selected from each resistance mechanism (changes in penicillin-binding protein, secretion of b-lactamases, and decreasing porin channel formation) with high abundance in hospital wastewater samples. In aquaculture wastewater samples two genes were selected for further analysis based on detection frequency and responsible mechanism. Subsequently, these selected genes were quantified using qPCR assays. All qPCR assays showed high R^2 values (> 0.99) and high efficiencies from 96.84% to 107.71%. ARG quantification overestimates the actual gene-carrying bacteria in a sample as an indicator of environmental impact and the possibility of further dissemination of

ARGs, and it may be a superior indicator compared to an accurate measure of the number of resistant bacteria (Mao et al., 2015).

Among the detected ARGs, the most ARGs, ranging from 7.68×10^5 copy/mL to 1.572×10^2 copy/mL, were recorded in teaching hospitals, where 7.26×10^5 – 1.24×10^2 copy/mL, 7.0057×10^4 – 8.00 copy/mL and 37.2 – 3.4 copy/mL were detected in General Hospitals, Base Hospitals, and Divisional hospitals respectively [Figure 4(a)].

A higher absolute copy number of b-lactam resistance genes ($p < 0.05$) was recorded in Teaching Hospital (TH) effluent than in effluent water from other types of hospitals [Figure 4(b)]. According to previously published literature, the *bla TEM* gene is one of the most frequently detected plasmid-borne antimicrobial resistance genes, which confers resistance to penicillin

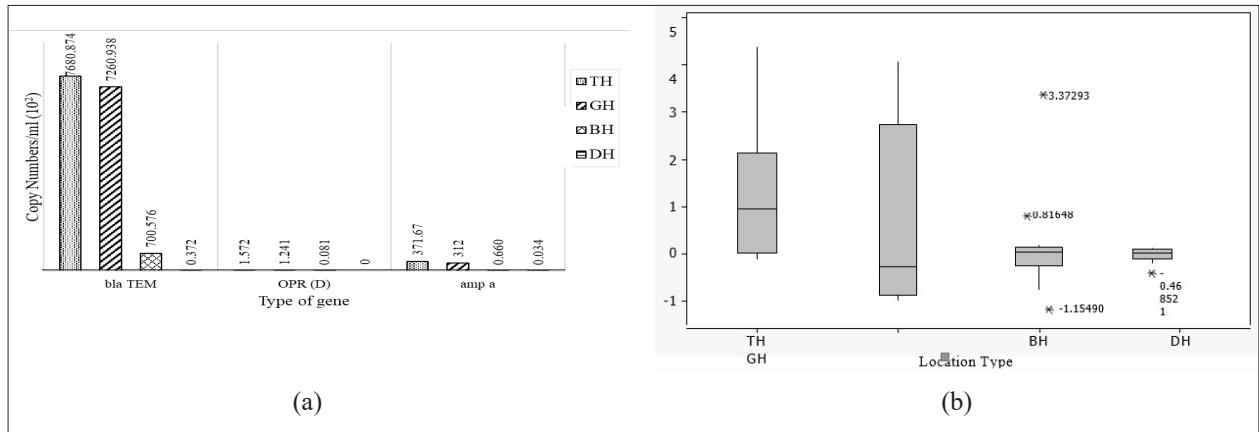


Figure 4: (a) Variations of total copy numbers of antibiotic resistance genes with hospital categories; (b) Absolute concentration of b-lactam resistance genes in the hospital effluent water samples. Within the box plot chart, the crosspieces of each box plot represent (from top to bottom) maximum, upper-quartile, median (black bar), lower quartile and minimum values, when error bars are not shown, standard deviation was less than the width of symbol.

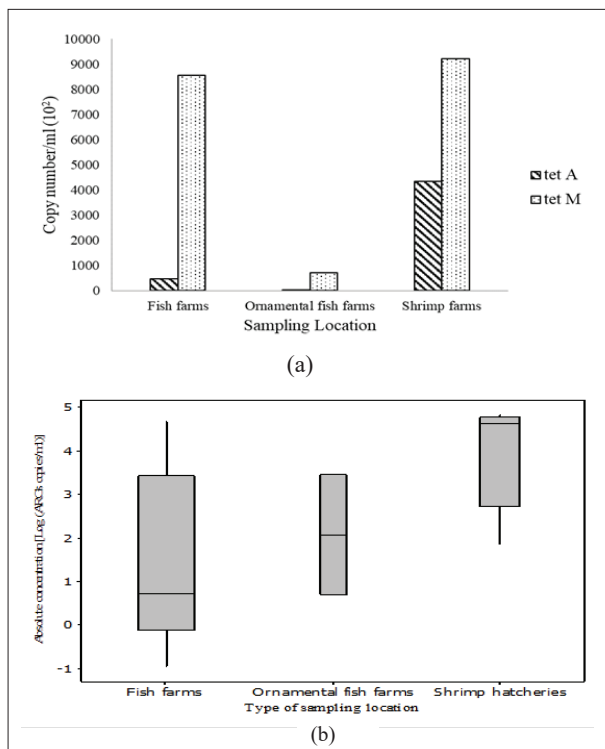


Figure 5: (a) Variations of total copy numbers of antibiotic resistance genes with farm categories (b) Absolute concentration of tetracycline resistance genes in the hospital effluent water samples. Within the box plot chart, the crosspieces of each box plot represent (from top to bottom) maximum, upper-quartile, median (black bar), lower quartile and minimum values, When error bars are not shown, the standard deviation was less than the width of the symbol

and extended-spectrum cephalosporin (Zhang & Li., 2011). The present results agree with previous studies suggesting that hospital discharges could contribute to the spread of ARGs into the aquatic environment. McCoy *et al.* (2011) observed that the abundance of *bla TEM* gene in hospitals was higher in populated urban areas than in rural areas. Czekalski *et al.* (2015) recently demonstrated that the abundance of *bla TEM* in hospital effluent was an indicator for high penicillin contamination in water. In the case of penicillin resistance genes (*bla TEM*, *OPR D*, *amp a*), detected concentrations in effluent water from hospitals may become severe, due to detecting the respective gene without detecting any of the selected penicillin (AMX, AMP, CLOX) in the water samples (Figure 4). Thus, it will be confirmed that the spreading of ARGs and ARB is not dependent on antibiotic concentration. Altogether, these observations undoubtedly demonstrate the contribution of hospital effluent water discharges to the spread of antibiotic resistance in the natural environment.

Among genes conferring resistance to tetracycline, both *tet M* and *tet A* genes were detected in shrimp farms ranging from 7.93×10^4 to 9.23×10^5 copy/mL and from 1.23×10^2 to 4.39×10^5 copy/mL respectively. The recorded concentrations were greater than the values recorded in fish farms (*tet M*- 1.1 – 8.560×10^5 copy/mL; *tet A*- 1.3 – 4.56×10^4 copy/mL) and ornamental fish farms (*tet M*- 2.2×10^2 – 7.23×10^4 copy/mL; *tet A*~ 3.2×10^3 copy/mL) [Figure 5 (a)].

A significant difference ($p < 0.05$) was also observed in the concentration of ARGs between resistance genes

detected in each hospital category [Figure 5 (b)]. Further, the genes; effect size estimate showed that 90–95% (χ^2) of the variability in rank scores is accounted for by location and it was not due to random events. Recorded values ($1.1\text{--}9.23 \times 10^5$ copies/mL) were greater than the aquaculture farms ($2.3\text{--}4.32 \times 10^3$ copies/mL) in the Philippines (Suzuki *et al.*, 2013) and in Finnish sediment ($3.0\text{--}2.35 \times 10^3$ copies/mL) (Muziasari *et al.*, 2014), but are comparable to values ($\sim 7.93 \times 10^4$ copies/mL) reported for aquaculture farms in Thailand (McKinney *et al.*, 2010). Thus, the present results suggest that tetracycline resistance genes are persistent even in the absence of tetracycline contamination in the water.

Relationship between antibiotic concentration vs antibiotic resistance genes

The abundance of types of ARGs (Figure 3) showed a similar pattern as the corresponding classes of antibiotics, where b-lactams had the highest concentration in the hospital effluent water and tetracycline in the aquaculture wastewater.

A correlation analysis was done to determine a potential link between the absolute concentration of b-lactam resistance genes and the penicillin concentration (Figure 6).

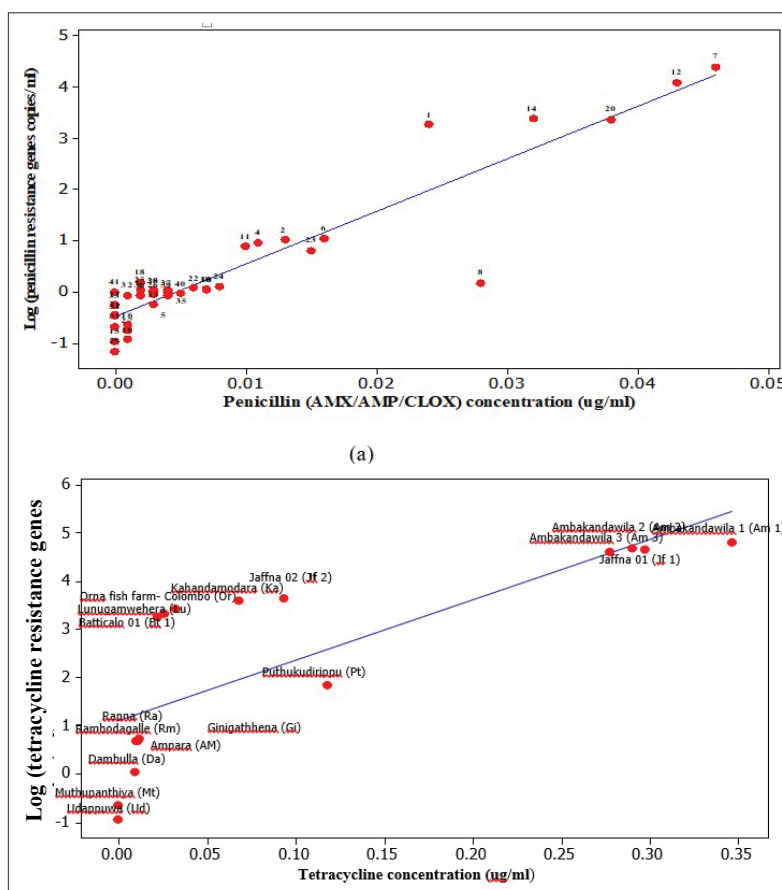


Figure 6: Correlation between the concentrations of antibiotics and antibiotic resistance genes (a) penicillin ($p < 0.05$, $R^2 = 0.889$); (b) tetracycline ($p > 0.05$, $R^2 = 0.776$). Sample locations were represented by red circles.

As a result, a significant positive correlation between penicillin concentrations and b-lactam resistance genes was found. In fact, there was a link between penicillin and b-lactamase resistance genes ($p = 0.001$, $R^2 = 0.889$). The correlations also revealed that ARGs increase with

antibiotic exposure concentration (Fig. 6). However, no significant ($p = 0.052$, $R^2 = 0.776$) differences in *tet M* and *tet A* gene concentrations were found in aquaculture samples.

Furthermore, it was found that tetracycline resistance genes could be detected in the absence of tetracycline in water. These findings suggest that the increase in the prevalence of tetracycline resistance genes is caused by their persistence in the absence of selection pressure (Kim *et al.*, 2012). However, the results discussed in this study are consistent with previous research indicating that antibiotic exposure may be a major factor leading to selective pressure for ARGs (Franje *et al.*, 2010).

In the future, the author suggests that more exploration be conducted to determine at what concentrations antibiotic resistance is developed and disseminated, as well as how these concentrations vary in different environments with different bacterial communities and ARGs.

CONCLUSION

The present study is the first in Sri Lanka to look at antibiotics and ARGs in hospital and aquaculture effluents. The results reveal that hospital effluents, fish farms, and shrimp hatcheries are ARG reservoirs, as well as showing the presence of potential resistant strains. It is also suggested that pathogen-associated taxonomic groups in fish farms have implications for human health. The study results highlighted the significant impact of heavy and unregulated antibiotic use, as well as the discharge of untreated wastewater into the aquatic environment, which could lead to significant contamination by both antibiotics and ARGs.

Acknowledgement

The authors would like to express their gratitude to the University of Sri Jayewardenepura in Sri Lanka for providing financial support for the study. The Centre for Water Quality and Algae Research, Department of Zoology, and Department of Microbiology, University of Sri Jayewardenepura provided technical assistance for the study.

REFERENCES

- Aminov R.I. & Mackie R.I. (2007). Evolution and ecology of antibiotic resistance genes. *FEMS Microbiology Letters* **271**(2): 147–161.
DOI: <https://doi.org/10.1111/j.1574-6968.2007.00757.x>
- Ansari F., Erntell M., Goossens H. & Davey P. (2009). The European surveillance of antimicrobial consumption (ESAC) point-prevalence survey of antibacterial use in 20 European hospitals in 2006. *Clinical Infectious Diseases*

- 49**(10): 1496–1504.
DOI: <https://doi.org/10.1086/644617>
- Czekalski N., Sigdel R., Birte I.J., Matthews B. & Bürgmann H. (2015). Does human activity impact the natural antibiotic resistance background? Abundance of antibiotic resistance genes in 21 Swiss lakes. *Environment International* **81**: 45–55.
DOI: <https://doi.org/10.1016/j.envint.2015.04.005>
- Duong H.A., Pham N.H., Nguyen H.T., Hoang T.T., Pham H.V., Pham V.C. & Alder A.C. (2008). Occurrence, fate and antibiotic resistance of fluoroquinolone antibacterials in hospital wastewaters in Hanoi, Vietnam. *Chemosphere* **72**(6): 968–973.
DOI: <https://doi.org/10.1016/j.chemosphere.2008.03.009>
- Fekadu S., Merid Y., Beyene H., Teshome W. & Gebre-Selassie S. (2015). Assessment of antibiotic-and disinfectant-resistant bacteria in hospital wastewater, south Ethiopia: a cross-sectional study. *The Journal of Infection in Developing Countries* **9**(02): 149–156.
DOI: <https://doi.org/10.3855/jidc.4808>
- Fernandez-Torres R., Consentino M.O., Lopez M.B. & Mochon M.C. (2010). Simultaneous determination of 11 antibiotics and their main metabolites from four different groups by reversed-phase high-performance liquid chromatography-diode array-fluorescence (HPLC–DAD–FLD) in human urine samples. *Talanta* **81**(3): 871–880.
DOI: <https://doi.org/10.1016/j.talanta.2010.01.031>
- Finley R.L., Collignon P., Larsson D.J., McEwen S.A., Li X.Z., Gaze W.H. & Topp E. (2013). The scourge of antibiotic resistance: the important role of the environment. *Clinical Infectious Diseases* **57**(5): 704–710.
DOI: <https://doi.org/10.1093/cid/cit355>
- Franje C.A., Chang S.K., Shyu C.L., Davis J.L., Lee Y.W., Lee R.J. & Chou C.C. (2010). Differential heat stability of amphenicols characterized by structural degradation, mass spectrometry and antimicrobial activity. *Journal of Pharmaceutical and Biomedical Analysis* **53**(4): 869–877.
DOI: <https://doi.org/10.1016/j.jpba.2010.06.013>
- Hernandes F., Henriques L., Pilz R., Bonifacio O., Boechat Salloto G., Oliveira Santoro D., Mandetta M. & Machado A. (2013). Antibiotic resistance in aquatic environments of Rio de Janeiro, Brazil. *Perspectives in Water Pollution* [Online]. Available at: <http://www.intechopen.com/books/perspectives-in-water-pollution/antibiotic-resistance-in-aquatic-environments-of-rio-de-janeiro-brazil>, Accessed October 2015.
DOI: <https://doi.org/10.5772/54638>
- Hocquet D., Muller A. & Bertrand X. (2016). What happens in hospitals does not stay in hospitals: antibiotic-resistant bacteria in hospital wastewater systems. *Journal of Hospital Infection* **93**(4): 395–402.
DOI: <https://doi.org/10.1016/j.jhin.2016.01.010>
- Hsieh M.K., Shyu C.L., Liao J.W., Franje C.A., Huang Y.J., Chang S.K. & Chou C.C. (2011). Correlation analysis of heat stability of veterinary antibiotics by structural degradation, changes in antimicrobial activity and genotoxicity. *Vet Med (Praha)* **56**: 274–285.
DOI: <https://doi.org/10.17221/1548-VETMED>

- Huddleston J.R. (2014). Horizontal gene transfer in the human gastrointestinal tract: potential spread of antibiotic resistance genes. *Infection and Drug Resistance* **7**: 167. DOI: <https://doi.org/10.2147/IDR.S48820>
- Kim S.J., Ogo M., Oh M.J. & Suzuki S. (2012). Occurrence of tetracycline resistant bacteria and tet (M) gene in seawater from Korean coast. Interdisciplinary studies on environmental chemistry—Environmental pollution and ecotoxicology. *TERRAPUB*: 367–375.
- Kimosop S.J., Getenga Z.M., Orata F., Okello V.A. & Cheruiyot J.K. (2016). Residue levels and discharge loads of antibiotics in wastewater treatment plants (WWTPs), hospital lagoons, and rivers within Lake Victoria Basin, Kenya. *Environmental Monitoring and Assessment* **188**(9): 532. DOI: <https://doi.org/10.1007/s10661-016-5534-6>
- Kümmerer K. (2001). Drugs in the environment: Emission of drugs, diagnostic aids and disinfectants into wastewater by hospitals in relation to other sources - A review. *Chemosphere* **45**(6–7): 957–969. DOI: [https://doi.org/10.1016/S0045-6535\(01\)00144-8](https://doi.org/10.1016/S0045-6535(01)00144-8)
- Liyanage G.Y. & Manage P.M. (2014). Quantification of oxytetracycline and ampicillin in two waste water discharging points in Colombo, Sri Lanka. *Journal of Environment and Natural Resources, Thailand*: 193–198.
- Liyanage G.Y. & Manage P.M. (2016a). Occurrence, fate and ecological risk of antibiotics in hospital effluent water and sediments in Sri Lanka. *International Journal of Agriculture and Environmental Research* **4**: 909–935.
- Liyanage G.Y. & Manage P.M. (2016b). Occurrence and distribution of tetracycline resistance determinants and their pollution status in the aquaculture environment of Sri Lanka. *3rd International Conference on Multidisciplinary Approaches Proceeding*, p. 8.
- Liyanage G.Y. & Manage P.M. (2017). Occurrence and abundance of multiple antibiotic resistance bacteria in hospital effluent water. *Asian Journal of Microbiology, Biotechnology and Environmental Sciences* **19**(4): 276–284.
- Liyanage G.Y., Manage P.M. & De Alwis A. (2015). Study on the occurrence of antibiotic contaminations in the aquatic environment, Sri Lanka. *International Conference on Multidisciplinary Approaches Proceeding*, p. 198.
- Mao W., Vu H., Xie Z., Chen W. & Tang S. (2015). Systematic review on irrational use of medicines in China and Vietnam. *PloS One* **10**(3): e0117710. DOI: <https://doi.org/10.1371/journal.pone.0117710>
- Marti E., Jofre J. & Balcazar J.L. (2013). Prevalence of antibiotic resistance genes and bacterial community composition in a river influenced by a wastewater treatment plant. *PLoS One* **8**(10): e78906. DOI: <https://doi.org/10.1371/journal.pone.0078906>
- Mccooy L.S., Xie Y. & Tor Y. (2011). Antibiotics that target protein synthesis. *Wiley Interdisciplinary Reviews: RNA* **2**(2): 209–232.
- McKinney E.F., Lyons P.A., Carr E.J., Hollis J.L., Jayne D.R., Willcocks L.C. & Pollard A.J. (2010). A CD8+ T cell transcription signature predicts prognosis in autoimmune disease. *Nature Medicine* **16**(5): 586–591. DOI: <https://doi.org/10.1038/nm.2130>
- Ministry of Health, Medicine and Indigenous Medicine, Available at http://www.health.gov.lk/moh_final/english/others.php?pid=101. Accessed October 2017.
- Mroczkowska J.E. & Barlow M. (2008). Fitness trade-offs in bla TEM evolution. *Antimicrobial Agents and Chemotherapy* **52**(7): 2340–2345. DOI: <https://doi.org/10.1128/AAC.00018-08>
- Muziasari W.I., Managaki S., Pärnänen K., Karkman A., Lyra C., Tamminen M. & Virta M. (2014). Sulphonamide and trimethoprim resistance genes persist in sediments at Baltic Sea aquaculture farms but are not detected in the surrounding environment. *PLoS One* **9**(3): e92702. DOI: <https://doi.org/10.1371/journal.pone.0092702>
- NAQDA (2015) Available at <http://www.fao.org/3/a-bp876e.pdf>. <http://www.naqda.gov.lk/our-centers/coastal-aquaculture-development-centers/>. Accessed November 2017.
- Perini F., Casabianca A., Battocchi C., Accoroni S., Totti C. & Penna A. (2011). New approach using the real-time PCR method for estimation of the toxic marine dinoflagellate *Ostreopsis* cf. *ovata* in marine environment. *PLoS One* **6**(3): e17699. DOI: <https://doi.org/10.1371/journal.pone.0017699>
- Pruden A., Larsson D.J., Amézquita A., Collignon P., Brandt K.K., Graham D.W. & Topp E. (2013). Management options for reducing the release of antibiotics and antibiotic resistance genes to the environment. *Environmental Health Perspectives* (Online) **121**(8): 878. DOI: <https://doi.org/10.1289/ehp.1206446>
- Ragan M.A. & Beiko R.G. (2009). Lateral genetic transfer: open issues. *Philosophical Transactions of the Royal Society B: Biological Sciences* **364**(1527): 2241–2251. DOI: <https://doi.org/10.1098/rstb.2009.0031>
- Rodriguez-Mozaz S., Marco M.P., De Alda M.J. & Damia, B. (2014) Biosensors for environmental applications: Future development trends. *Pure and Applied Chemistry* **76**(4): 723–752. DOI: <https://doi.org/10.1351/pac200476040723>
- Suzuki S., Ogo M., Miller T.W., Shimizu A., Takada H. & Siringan M.A. (2013). Who possesses drug resistance genes in the aquatic environment? sulfamethoxazole (SMX) resistance genes among the bacterial community in water environment of Metro-Manila, Philippines. *Frontiers in Microbiology* **4**: 207–216. DOI: <https://doi.org/10.3389/fmicb.2013.00102>
- UNESCO (2010). Available at <http://whc.unesco.org/en/list>. Accessed December 2014.
- World Health Organization (2015). Global action plan on antimicrobial resistance. Available at http://www.who.int/drugresistance/global_action_plan/en/. Accessed December 2017.
- Zhang T. & Li B. (2011). Occurrence, transformation, and fate of antibiotics in municipal wastewater treatment plants. *Critical Reviews in Environmental Science and Technology* **41**(11): 951–998. DOI: <https://doi.org/10.1080/10643380903392692>

RESEARCH ARTICLE

Structural engineering

Combined use of non-destructive tests, visual inspection and service life prediction to ensure the reliability of reinforced concrete water tanks

K Ranasinghe^{1*} and S De Silva²

¹ National Water Supply & Drainage Board, Galle Road, Ratmalana, Sri Lanka.

² Department of Civil and Environmental Engineering, Faculty of Engineering, University of Ruhuna, Hapugala, Wackwella, Sri Lanka.

Submitted: 24 March 2021; Revised: 03 September 2021; Accepted: 26 November 2021

Abstract: Corrosion of reinforcement is the most significant cause of premature deterioration of reinforced concrete structures. Many of the concrete structures have been exposed to aggressive environments, suffer from durability problems, and fail to fulfil their design service life requirements. Chloride-induced corrosion is one of the deterioration mechanisms that may reduce the service life of reinforced concrete structures. The condition assessment of a reinforced concrete structure over a period of time is useful with routine monitoring. The majority of water supply systems have some form of water storage tanks, most often constructed from reinforced concrete. These tanks are an integral part of the potable water distribution network. To ensure durability and sustainability, they should be adequately inspected and maintained. For effective and durable repairing or retrofitting of reinforced concrete tanks, the use of a suitable condition assessment system may give more sustainable results. This study aimed to propose a system to perform a condition assessment of existing reinforced concrete water retaining structures. The reinforced concrete tanks were selected in Galle, Matara, and Hambanthota districts in Sri Lanka, to perform visual inspections and non-destructive tests. The service life of reinforced concrete structures in marine environments depends on chloride-induced corrosion. Therefore, the development of the chloride penetration model is essential for its assessment. Fick's Second Law of diffusion provides a simple way to predict the chloride penetration in such situations. Therefore, an analytical method is introduced to predict the service life of reinforced concrete water retaining structures taking into account well-known corrosion models such as Fick's Second Law and the Bazant model. Both the predicted service life and the tank soundness score can be

used to develop a tank remediation plan more effectively. Therefore, the repair / retrofitting methods proposed based on such assessment will be cost-effective as well as more reliable in enhancing the service life of the water retaining structures. However, modelling the service life of reinforced concrete structures is a complex process as it includes many uncertainties.

Keywords: Aggressive environments, chloride induced corrosion, condition assessment, non-destructive test, service life prediction, visual inspections.

INTRODUCTION

Corrosion of steel embedded in concrete is a serious deterioration problem causing considerable losses to the nation due to maintenance and repair works. Corrosion-induced damage, such as concrete cracking, spalling, delamination, and cross-sectional reduction of the reinforcement, may dramatically affect the long-term performance of reinforced concrete structures, such as a decrease in the load-bearing capacity and, in the worst-case lead to fatal structural consequences, such as failure (ACI, 2008).

The corrosion level of the existing reinforced concrete bridges and buildings has been studied in many types of research. However, a comprehensive level of corrosion study on the water retaining structures in Sri Lanka is

* Corresponding author (sudhira@cee.ruh.ac.lk;  <https://orcid.org/0000-0003-0804-5097>)



This article is published under the Creative Commons CC-BY-ND License (<http://creativecommons.org/licenses/by-nd/4.0/>). This license permits use, distribution and reproduction, commercial and non-commercial, provided that the original work is properly cited and is not changed in anyway.

hardly found. The National Water Supply & Drainage Board in Sri Lanka has many water retaining structures close to the coastal belt. Some of them have been used in service for more than 30 years. Generally, the majority of them are continuously operating without adequate maintenance or any restoration. This investigation finds that they are subjected to spalling, cracks, water leakage, and vegetation on the concrete elements, apart from chloride-induced corrosion damage. Perhaps they hardly achieved the expected design service life of the structure.

The deterioration rate of reinforced concrete structures can be reduced by adopting suitable restoration methods based on continuous monitoring of such structures using visual examination and non-destructive testing. A condition assessment with

visual inspection and non-destructive test provides information on its structural performance. Further, to ensure its durable service and select the most appropriate repair method, it is essential to follow up a suitable condition assessment for reinforced concrete water retaining structures.

This study is focused on developing a mechanism to evaluate the current structural condition of existing water retaining structures, based on a visual inspection and non-destructive tests, as well as to predict the service life depending on prevailing mathematical models. For the study, selected reinforced concrete tanks located in the Southern Province in Sri Lanka were used. The locations of the selected water tanks are shown in Figure 1.

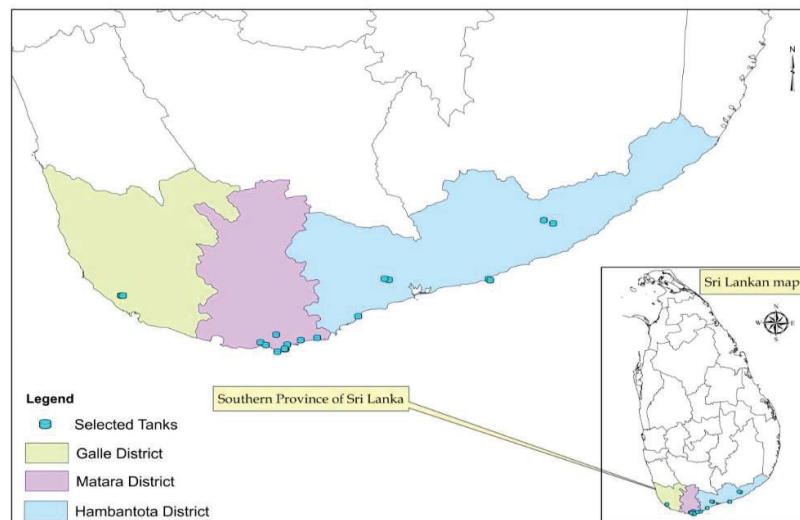


Figure 1: Location map of selected water tanks

MATERIALS AND METHODS

The condition assessment of reinforced concrete water retaining structures is mainly based on the data collected from visual inspection and non-destructive testing. The assessment methodology is developed based on ‘Synthesis of National and International Methodologies Used for Bridge Health Indices’, published by the Federal Highway Administration (FHWA), US Department of Transportation (Publication no. FHWA-HRT-15-081, 2016) in addition to the past research thesis and papers (Rashidi & Gibson, 2011; Pushpakumara, 2014).

Whether the structure should be repaired, rehabilitated, or replaced can be decided more technically based on remaining service life predictions (Bazant, 1979a; 1979b; Tuutti, 1982; Ming *et al.*, 2009). Thereby, the remaining service life is calculated. The structural repair, rehabilitation, or replacement can be selected more technically as well as economically based on the predicted remaining service life. The methodology used here is mainly based on the report, ‘ACI 365.1R-00’ published by American Concrete Institute (ACI, 2000). The current condition states of 30 existing reinforced concrete tanks were assessed to validate the proposed assessment procedure.

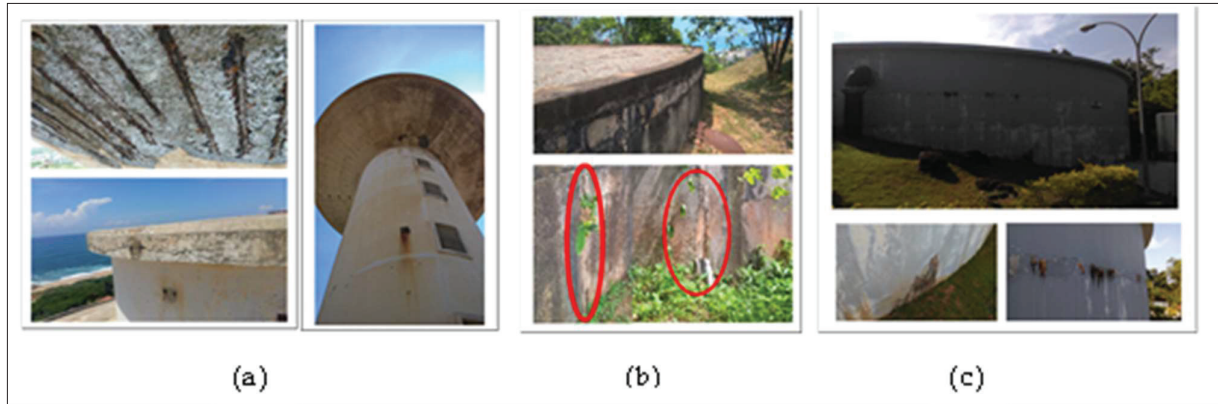


Figure 2: Existing reinforced concrete water tanks with corrosion effects: (a) structure no. 13 at Hambantota Sri Lanka; (b) structure no. 02 at Matara Sri Lanka; and (c) structure no. 19 at Galle Sri Lanka

Data collection from visual inspection

Each square meter of reinforced concrete structure was carefully scrutinized to identify the visual defects and failures. Crack details (i.e., crack type, length, and width), tank element details, vegetation cover (i.e., plant type and area), structural failures, spalling, delamination and reinforcement exposures, water leakages, distance from the coastal belt, the surrounding temperature, and humidity were measured and recorded into the visual inspection sheet. Temperature, humidity, and distance from the coastal belt were used to evaluate the environmental conditions. Apart from that, extra important data of the structures such as age, capacity, dimension, past maintenance details, and information about its past utilization were collected. Some reinforced concrete water tanks with corrosion effects that were observed during the data collection are shown in Figure 2. The formation of subsequent

testing programmes was done using non-destructive tests based on an initial indication, which was provided by the visual inspection of reinforced concrete water tanks (ACI, 2008).

Visual inspection factor (VIF)

A rating value for visual inspection parameters, such as vegetation cover, bleed marks with surface staining, spoiling with reinforcement exposures, surface cracks, surface voids, and honeycombing area was introduced.

Rating Values (RV) and priority weights for visual inspection data were used to determine the Visual Inspection Factor (VIF). Rating values were assigned to quantify tank conditions based on visual inspection data shown in Table 1. A higher rating value corresponds to a critical stage of the structure (Pushpakumara, 2014).

Table 1: Rating values for visual inspection data

Rating value (RV)	Vegetation cover (VC)	Bleed marks / water leakage (SB)	Spalling (SP)	Visibility of cracks (CK)	Surface voids and honeycombing area (%) (SH)
1	No	No	No	No	No
2	Moss and algae	Low	Initial stage	Hair cracks	0–5
3	Herbs	High	Concrete cover remove	< 2 mm	5–10
4	Plants	Very high	R/F exposed	>2 mm	>10

Table 2 shows the scales for relative importance value (i.e., importance intensity) for different criteria proposed by Saaty (1980). The Analytical Hierarchy Process (AHP) developed by Saaty (1980) can be used to find the priority vector of the visual inspection data (Saaty, 1980; 1988; 1994).

The importance of intensity values is assigned to equation (1). Vegetation Cover (VC) growth significantly influences the deterioration of tank elements compared to Surface Bleed marks (SB). Therefore, compared to VC, Surface Bleed marks (SB), Spalling (SP), and Crack (CK) have intermediate value (i.e., 4), Strong importance

(i.e., 5), and Moderate importance (i.e., 3) respectively. Besides, compared to surface voids and Honeycombs (SH), VC is of moderate importance (i.e., 3; refer to Table 2). Further, the Spoiling (SP) indicates the worst condition of an element, which causes failure, compared to VC. Therefore, SP has Strong importance (i.e., 5) compared to VC of elements (Table 2). On the other hand, SP was assessed as an intermediate value (i.e., 2) between two judgments (of equal importance, i.e., 1) to moderate importance (i.e., 3) compared to SB (Table 2). SP has moderate importance (i.e., 3) compared to SH. The results of the comparison of visual inspection data arrange as a comparison matrix.

Table 2: Relative importance values introduced by Saaty *et al.* (1980)

Importance intensity	Explanation
1	Equal importance
3	Moderate importance of one over another
5	Strong importance of one over another
7	Very strong importance of one over another
9	The absolute importance of one over another
2,4,6,8	Intermediate values between the two judgments
Reciprocals	Reciprocal for inverse comparison

The results of the comparison of visual inspection data may be categorized in a reciprocal comparison matrix, as shown in equation (1).

$$\begin{matrix} & \text{VC} & \text{SB} & \text{SP} & \text{CK} & \text{SH} \\ \text{VC} & \left[\begin{array}{ccccc} 1 & \frac{1}{4} & \frac{1}{5} & \frac{1}{3} & 3 \\ 4 & 1 & \frac{1}{2} & 2 & 5 \\ 5 & 2 & 1 & 4 & 3 \\ 3 & \frac{1}{2} & \frac{1}{4} & 1 & 2 \\ \frac{1}{3} & \frac{1}{5} & \frac{1}{3} & \frac{1}{2} & 1 \end{array} \right] & & & & \\ \text{SB} & & & & & & & & \\ \text{SP} & & & & & & & & \\ \text{CK} & & & & & & & & \\ \text{SH} & & & & & & & & \end{matrix} \dots(1)$$

The priority weights of visual inspection data categories were estimated as a normalized eigenvector by dividing each element by the sum of that column and then computing the average of each row. That gives the priority weight of the corresponding visual inspection data, and the results are tabulated in Table 3 (Ming *et al.*, 2009; Rashidi & Gibson, 2011).

Table 3: Priority weight of visual inspection data

Visual inspection parameters	Priority weight
Vegetation cover (VC)	0.097
Surface staining and bleed marks / water leakage (SB)	0.277
Spoiling (SP)	0.409
Crack (CK)	0.146
Surface voids and honeycombs (SH)	0.071

The priority weights of visual inspection data (Table 3) are used as coefficients in equation (2). The rating values assigned based on visual inspection data (Table 1) for equation (2) gives the Visual Inspection Factor (VIF) and it is then rounded off to the nearest whole number (VIF ∈ 1, 2, 3, 4).

$$\text{VIF} = 0.097 RV_{VC} + 0.277 RV_{SB} + 0.409 RV_{SP} + 0.146 RV_{CK} + 0.071 RV_{SH} \dots (2)$$

where RV_{VC} , RV_{SB} , RV_{SP} , RV_{CK} , and RV_{SH} are rating values (Table 1) of Vegetation Cover (VC), Surface Bleed marks (SB), Spoiling (SP), Differential movements or Crack (CK), and Surface voids and Honeycombing (SH) respectively. For example, if VC is found to be ‘moss and algae’, the value of RV_{VC} should be two. If SB is found to be ‘very high’, RV_{SB} should be four.

Crack detail factor (CDF)

The number of cracks, crack width (using a crack gauge) and crack length are recorded during visual inspection. Then based on the above-recorded data, the final rating values for crack width, number of cracks, crack length, and crack depth can be determined (Rashidi & Gibson, 2011; Pushpakumara, 2014).

Table 4: Rating values for crack details

Rating values (RV)	Crack details			
	Number of cracks (N)	Crack width (mm)(W)	Crack length (mm) (L)	Crack Depth (mm) (D)
1	No cracks			
2	1–2	0.25–1	< 100	< 10
3	2–3	1–2	100–300	10–20
4	> 3	> 2	> 300	> 20

The AHP is used to develop the reciprocal comparison matrix of crack details and priority weights of crack detail. The priority weights of crack detail are assigned as coefficients in equation (3). The rating values assigned to Equation 3 are based on collected data as shown in Table 4.

Then the equation gives the Crack Details Factor (CDF) and it is then rounded off to the nearest whole number (CDF ∈ 1, 2, 3, 4).

$$CDF = 0.489 RV_N + 0.138 RV_W + 0.235 RV_L + 0.138 RV_D \dots (3)$$

where RV_N , RV_W , RV_L , and RV_D are rating values for the number of cracks, crack width, crack length, and crack depth, respectively.

Element significant factor (ESF)

Based on the element significant factor used by the researchers for the analysis of concrete bridges (Rashidi

Table 5: Element significant factor

Element	(ESF)
Roof	1
Walls	2
Base slab	3
Shaft, columns, beams, foundation	4

& Gibson, 2011; Pushpakumara *et al.*, 2017), the new ESFs were introduced similarly for the main elements of reinforced concrete water tanks, as shown in Table 5. The lower rating value reflects the minor significant element, and higher rating values refer to the most significant element in the water tank.

Causal factor (CF)

Aggressive environmental conditions, age, and maintenance level may be directly involved with the overall condition of a water tank (Pushpakumara, 2014;

Table 6: Rating values for each parameter of the causal factor

Rating value	Age of the structure (A)	Type of exposure (E)	Maintenance level (M)	Quality of inspection (I)
1	Recently build	Mild	Satisfactory level	Very high
2	New	Moderate	Moderate satisfactory	High
3	Old	Severe	Poor level	Medium
4	Very Old	Very severe	Very poor level	Low

Pushpakumara *et al.*, 2017). Further, the standard of the inspection contributes to the condition assessment of water tanks. Therefore, the above factors are also considered during the calculation of overall tank condition and are commonly named the causal factor (CF). Table 6 shows the rating values for causal factors. The higher rating value reflects the worst situation (Ming *et al.*, 2009; Rashidi & Gibson, 2011).

The AHP is used to develop the reciprocal comparison matrix of causal factors and priority weights of causal factors are determined. The causal factor (CF) is calculated by using equation (4).

$$CF = 0.225 RV_A + 0.471 RV_E + 0.189 RV_M + 0.115 RV_I \dots (4)$$

RV_A , RV_E , RV_M , and RV_I represent the rating value for age, exposure condition, maintenance level, and quality of inspection, respectively ($CF \in 1, 2, 3, 4$).

Element construction type factor (ECTF)

The type which is used for the construction of the water tank is another important factor. Table 7 shows the construction type and their vulnerability for the tank condition assessment developed based on past research studies (Rashidi & Gibson, 2011; Pushpakumara,

2014). The higher construction type factor reflect more vulnerability.

Table 7: Element construction type factor (ECTF)

Construction type	ECTF
Precast concrete	1
Pre-stressed concrete	2
Steel	3
Reinforced concrete	4

Non-destructive test factor (NDF)

The non-destructive tests such as rebound hammer test, cover meter survey, concrete resistivity test, and crack gauge are used to investigate the structural condition of the reinforced concrete tanks. The rebound hammer is a surface hardness tester that indicates the quality and soundness of the concrete surface. The cover meter is used to investigate the precise concrete cover depth as well as pinpoint the exact location of the rebar in the reinforced concrete water tank. The corrosion resistivity meter is used to assess the possible rate of corrosion in embedded reinforcing steel. Figure 3 indicates a few photographs of data collection in the field.



Figure 3: Data collection by NDT: (a) record data from visual inspection; (b) rebound hammer test; (c) concrete resistivity test; and (d) cover meter survey

The past studies (Ming *et al.*, 2009; Rashidi & Gibson, 2011) indicate, the corrosion rate is a more critical parameter than the rebound number and concrete cover. The corrosion rate gives a hint about the corrosion status of the particular reinforced concrete structural element. The rebound number evaluates the compressive strength of the concrete surface. The minimum cover should be maintained to ensure the safe transmission of bond forces, durability, and fire resistance of the reinforced concrete members. Hence, the cover is one indicator of a durable structure. Therefore, from the above facts, as well as past studies (Pushpakumara, 2014), the priority weight for Corrosion Rate (CR), Rebound Number (RN), and Concrete Cover (CC) can be assigned as 0.5, 0.3, and 0.2, respectively. The Non-destructive Test Factor (NTF) is calculated from equation (5).

$$NDF = (0.5 \times \alpha) + (0.3 \times \beta) + (0.2 \times \gamma) \quad \dots (5)$$

where α is the rating value of concrete resistivity, β is the rating value corresponding to the rebound number, and γ is the rating value for concrete cover. NDF ranges from 1 to 4. The rating values were proposed for average concrete resistivity, quality of concrete surface related to average rebound number, and precise concrete cover depth, as shown in Tables 8, 9, and 10, respectively. The results of UNDP Disaster Risk Management Programme (2007), which have been developed for buildings, as well as past research papers and a thesis, were studied and assigned values accordingly for rating purposes (UNDP Disaster Risk Management Programme, 2007; Rashidi & Gibson, 2011; Pushpakumara, 2014; Pushpakumara *et al.*, 2017). The rating values from 1 to 4 in Table 8 indicate the possible rate of corrosion in the reinforced concrete element (NDT James Instrument Inc., 2021).

Table 8: Possible corrosion rates for resistivity and rating values

Resistivity (k Ohms cm)	Possible corrosion rate	Rating value (α)
> 20	Insignificant	1
10–20	Moderate to low	2
5–10	High	3
< 5	Very high	4

The rating values from 1 to 4 in Table 9 show the quality of the concrete surface related to the average rebound number (Pushpakumara, 2014; Pushpakumara *et al.*, 2017).

The rating values from 1 to 4 in Table 10 show the effect of the concrete surface relative to the precise concrete cover depth (Pushpakumara, 2014).

Table 9: Quality of concrete surface and rating value for average rebound number

Average rebound number	Quality of concrete surface	Rating value (β)
> 40	A very good hard layer	1
30–40	Good layer	
20–30	Fair	2
< 20	Poor concrete	3
0	Delaminated	4

Table 10: Proposed rating values for the cover of the concrete

Concrete cover (mm)	Rating value (γ)
> 50	1
30–50	2
10–30	3
< 10	4

Proposed reinforced concrete tank rating procedure

Every 1 m² of the elements of a tank was inspected separately. Then, using these visual and detailed inspection data and non-destructive test results, Visual Inspection Factor (VIF), Crack Details Factor (CDF), and Non-Destructive Test Factor (NDF) were calculated for each square meter of the elements.

The visual inspection provides a wide range of information (i.e., vegetation cover, surface staining and bleed marks, structural failures, different movements, surface voids and honey combing areas, and reinforcement exposures) compared to crack inspection (i.e., crack width, length, depth, and the number of cracks) and non-destructive tests (i.e., concrete strength and corrosion behaviour). Further, crack details are more critical than the non-destructive tests to identify the current condition of tanks. Therefore, it is considered that the VIF, CDF, and NDF have priority values of 0.5, 0.3, and 0.2, respectively (Pushpakumara, 2014; Pushpakumara *et al.*, 2017). Based on the above information, the Condition Index (CI) was calculated from equation (6) for all

the elements separately. Each calculated CI value was rounded off to the nearest whole number (CI ∈ 1, 2, 3, 4).

$$CI = (0.5 \times VIF) + (0.3 \times CDF) + (0.2 \times NDF) \quad \dots(6)$$

where,

VIF is the Visual Inspection Factor,

CDF is the Crack Detail Factor, and

NDF is the Non-Destructive Test Factor.

Areas with equal CI values are separately accumulated, and the element condition was calculated using Equation 7 as the Element Condition Index (ECI).

$$ECI = \frac{\sum(q_i \times CI)}{\sum q_i} \quad \dots(7)$$

where,

CI is the Condition Index of the selected area, and

q_i is the area of an element reported in the condition index (CI).

The overall condition of a water tank is calculated using equation (8) as the overall Tank Condition Index (OTCI). The higher OTCI value reflects the worst case of a reinforced concrete tank.

$$OTCI = \frac{CF \sum(ESF_i \times ECTF_i \times ECI_i)}{n} \quad \dots(8)$$

where,

ESF_i is the Element Significant Factor of i^{th} element,

CF is the Causal Factor,

$ECTF_i$ is the Element Construction Type Factor of the i^{th} element (ranging from 1 to 4),

ECI_i is the Element Condition Index of the i^{th} element, and n is the number of elements.

Table 11: Tank soundness score (TSS) ranges and physical condition of the tanks

TSS (%) range	Expected condition of reinforced concrete tank	Overall tank safety condition	Tank condition rating
$75 < TSS \leq 100$	The tank shows no deterioration. There may be discoloration, efflorescence, and/or superficial cracking but without effect on strength and/or serviceability.	Good condition	1
$50 < TSS \leq 75$	Minor cracks, spalls, bleeding marks, and algae may be present with moderate to low levels of corrosion of steel reinforcement and no deterioration of the system.	Satisfactory / fair condition	2
$25 < TSS \leq 50$	Some delamination and/or spalls may be present. Corrosion of steel reinforcement may be present with loss of bar sections and the strength may be lost and need repairing and retrofitting of element or tank.	Poor condition	3
$0 \leq TSS \leq 25$	Delamination, spalls, herbs and algae, and corrosion of steel reinforcement are prevalent. Element displacements and movements are present. The entire structure needs to be replaced.	Serious / failure condition	4

Tank Soundness Score (TSS) is calculated as a percentage by using equation (9).

$$TSS = \frac{(HOTCI - OTCI)}{HOTCI} \times 100 \quad \dots(9)$$

Lower TSS value reflects the worst case of a tank.

HOTCI is the highest OTCI valve (i.e., worst case) of any tank which is calculated by using equation (10).

In equation (10), it is considered that the ECI valves of all elements are equal to 4 (i.e., worst case) and CF is also equal to 4 (i.e., worst case).

$$HOTCI = \frac{16 \sum(ESF_i \times ECTF_i)}{n} \quad \dots(10)$$

Table 11 shows the TSS ranges and status relevant to the physical condition of a tank proposed based on similar studies that have been carried out for the Bridge Soundness Score (Pushpakumara, 2014; FHWA, 2016;).

Evaluation of current condition state of an existing reinforced concrete water tank

The structural condition of thirty existing reinforced concrete water tanks was assessed using both visual inspection and non-destructive tests. Figure 4 represents a flow diagram of the methodology of the assessment of reinforced concrete water tanks. The assessment methodology was developed based on ‘Synthesis

of National and International Methodologies Used for Bridge Health Indices’ published by the Federal Highway Administration (FHWA), US Department of Transportation (2016), the standard ACI 365.1R-08 published by the American Concrete Institute, and some past research studies (Rashidi & Gibson, 2011; Pushpakumara, 2014). Table 12 shows the calculation of TSS for a reinforced concrete water tank located in Hambantota (structure no. 13).

Table 12: Calculation of Tank Soundness Score (TSS) for a water tank (Structure no. 13)

Element	Total area ($\sum q_i$) (m ²)	ECI _i	ESF _i	ECTF _i	ECI _i × ESF _i × ECTF _i
Roof slab	152	2.88	1	4	11.54
Tank walls	295	2.90	2	4	23.23
Tank base slab	62	2.36	3	4	28.34
Shaft / column	245	2.13	4	4	34.13
Foundation	133	1.98	4	4	31.68
$\sum (ESF_i \times EMF_i \times ECI_i)$					128.92
Causal Factor (CF)	A 3	E 4	M 4	I 3	3.66
Number of elements (n)					5
Overall tank condition index (OTCI)					94.37
Highest overall tank condition index (HOTCI)					179.20
Tank soundness score (TSS)					47.34%

The tank is exposed to a very severe environment since it is located very close to a coastal belt (i.e., $RV_E = 4$). The tank could be considered an old structure since it is older than 30 years (i.e., $RV_A = 3$). Then, the causal factor was calculated from equation 4 by assigning rating values for maintenance level and quality of inspection as 4 and 3, respectively. VIF (Equation 2), CDF (Equation 3), and NDF (Equation 5) were calculated separately for each element of the tank, such as the roof, tank wall, base slab, tank shaft, and foundation. Similarly, CI was calculated by using Equation 6. The ECI values for each element were calculated by Equation 7. The product of ‘ $ECI_i \times ESF_i \times ECTF_i$ ’ was calculated for each tank element, and the sum was obtained. Next, the Overall Tank Condition Index (OTCI) was calculated by using Equation 8. These values were used to calculate the Highest Tank Condition Index (HOTCI) by using equation 10. Next, the Tank Soundness Score (TSS) was

calculated as a percentage by using Equation 9. Finally, the tank remediation actions can be proposed based on the TSS value. The calculations are listed in Table 12.

Prediction of the service life of reinforced concrete water tanks

Prediction of the service life of existing reinforced concrete water tanks would give an idea about the remaining service life period, deterioration rate, and the identification of the appropriate time to initiate the repairing and retrofitting. The corrosion process consists of three time periods: initiation time, de-passivation time, and propagation time (Tuutti, 1982). From the calculated corrosion initiation phase with the duration of de-passivation time and propagation phases, the overall service life of a reinforced concrete structure can be estimated. Such estimated values can be used to select an

optimum design service life for a new structure as well as optimum repair and rehabilitation solutions for existing structures. The rate of diffusion of chlorides through the concrete cover and the critical chloride threshold value of the embedded steel reinforcement significantly influence the duration of the corrosion initiation phase. Initiation time (t_c) can be predicted using equations 11 and 12 according to Fick's Second Law (Bazant, 1979a; 1979b; Ming *et al.*, 2009; Pillai, 2011).

$$C(x, t) = C_o \operatorname{erfc} \frac{x}{\sqrt{4D_c t_c}} \quad \dots(11)$$

where

$C(x, t)$ is the chloride concentration at depth x after time t ,
 C_o is the concentration of chloride ions in pores of concrete at the surface,
 erfc is the complementary error function,
 x is the concrete cover at various times t relevant to the required design life,
 t_c is the initiation time, and
 D_c is the diffusion coefficient.
 The diffusion coefficient (D_c) can be determined by using Equation 12

$$D_c = \beta \frac{kTLV \left(\frac{dc}{dt} \right)}{ZeECA} \quad \dots(12)$$

Where,

D_c is the diffusion coefficient (given in cm^2/s),
 β is the corrosion factor for ionic interaction (varies from 1.22 to 1.7 based on the chloride concentration from 0.1 M to 0.5 M NaCl),
 k is the Boltzmann constant,
 $(k = 1.38 \times 10^{-16} \text{ ergs/K/ion})$
 T is the temperature (K),
 Z is the chloride valence (Z is 1 for NaCl),
 e is the charge of the proton ($4.8 \times 10^{-10} \text{ e.s.u.}$),
 E is the applied electrical potential (V),
 L is the specimen thickness (cm),
 V is the volume of the chloride collection tank (cm^3),
 C is the initial chloride concentration in chloride source solution (mol/cm^3), and
 dc/dt is the steady-state migration rate of chloride ion ($\text{mol}/\text{cm}^3 \cdot \text{s}$).

Bazant *et al.* (1979a) established two classical formulas for calculating the de-passivation time (t_p) and propagation time (corrosion time, t_{corr}). The de-passivation time can be calculated by averaging the values of the Bazant method and Ming's proposed method (Bazant, 1979a; 1979b; Ming *et al.*, 2000).

When the de-passivation time is calculated from Ming's proposed method by using equation (14), the result is three times larger than the results from equation (13) according to the Bazant method. Ming *et al.* (2009) explained that this difference is caused by the different declined mechanisms of chloride ion concentration. Ming's proposed method, a declined straight line is used, while the Bazant method uses a declined parabolic curve. However, the real phenomenon may be a declined parabolic curve occurs and then, subsequently, a declined straight line (Ming *et al.* 2000, 2009). Therefore, to estimate a more precise value for de-passivation time, we get the average of the proposed Ming's and Bazant methods (Ming *et al.* 2000, 2009).

$$t_p = \frac{1}{12D_c} \left[\frac{L}{1 - \sqrt{\frac{C^*}{C_o}}} \right]^2 \quad \dots(13)$$

$$t_{p'} = \frac{1}{4D_c} \left[\frac{L}{1 - \sqrt{\frac{C^*}{C_o}}} \right]^2 \quad \dots(14)$$

where,

t_p is the de-passivation time,
 D_c is the diffusion coefficient,
 L is the cover thickness,
 C^* is the threshold value of the chloride concentration, and
 C_o is the concentration of chloride ions in pores of concrete at the surface.

Propagation time (t_{corr}) can be calculated by using the modified Bazant method (Bazant, 1979a; 1979b). Equations 15, 16, and 17 were used to calculate propagation time.

$$t_{\text{corr}} = \rho_{\text{cor}} \frac{D \Delta D^*}{s j_r} \quad \dots(15)$$

where ΔD^* is given by

$$\Delta D^* = f_t' \left[2 \left(\frac{L}{D} + 1 \right) \right] \delta_{pp} \quad \dots(16)$$

where δ_{pp} is given by

$$\delta_{pp} = \frac{D}{E_{ef}} (1 + \vartheta) + \frac{2D^3}{s^2 E_{ef}} \quad \dots(17)$$

where,

ρ_{cor} is the density of the corrosion product,

s is the space of the steel bar,
 D is the steel diameter,
 j_r is the rate of rust production per unit area of the plane,
 f_t' is the tensile strength,

L is the cover thickness,
 δ_{pp} is the bar hole flexibility,
 ν is Poisson's ratio (ν and, and
 E_{ef} is the effective elastic modulus.

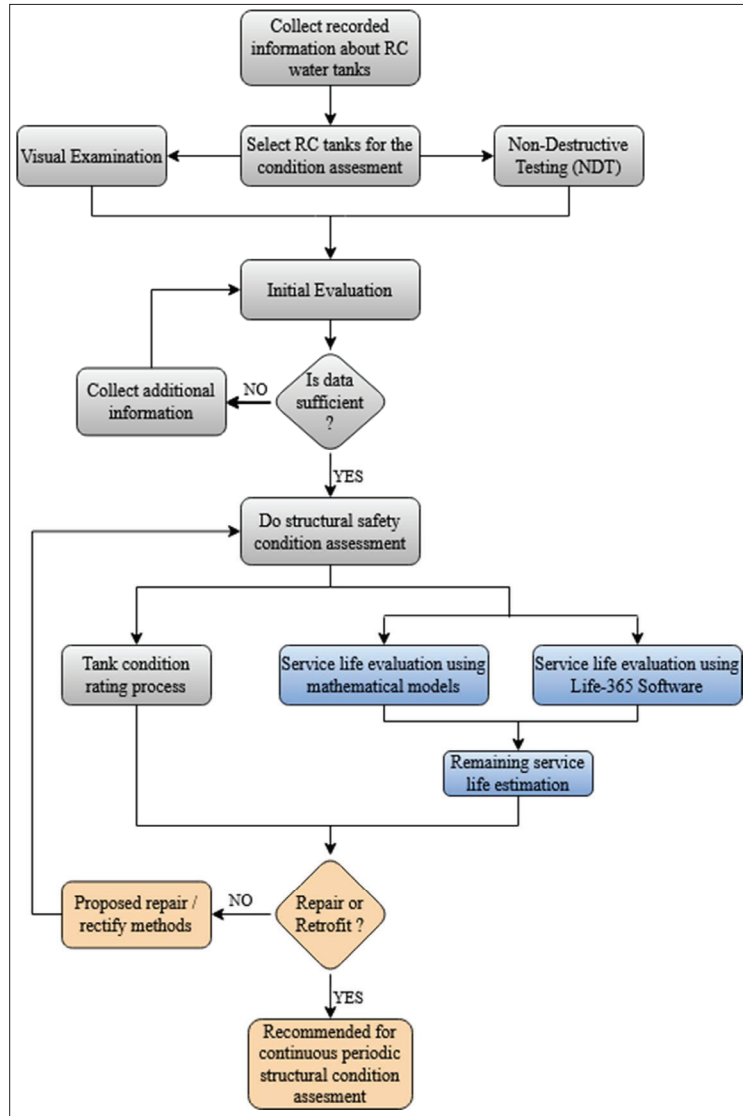


Figure 4: Flow diagram for assessment of the current condition of a reinforced concrete tank

The effective elastic modulus can be determined by using equation (18).

$$E_{ef} = \frac{E_c}{1 + \varphi_{cr}} \quad \dots(18)$$

where,
 φ_{cr} is the creep coefficient of concrete, and,
 E_c is the modulus of elasticity.
 The modulus of elasticity of concrete (E_c) can be determined by using equation (19).

$$E_c = 4700 \sqrt{f'_c} \quad \dots(19)$$

where, f'_c is the average compressive strength of concrete.

The total service life of reinforced concrete structure can be expressed as,

$$t = t_c + t_p + t_{corr} \quad \dots(20)$$

t_c and t_p are the initiation and de-passivation times, respectively,

t_{corr} is Propagation time, and $(t_p + t_{corr})$ can be considered as the propagation period.

Table 13: The assessment output of 30 structures

Structure No	Service life (years)			Predicted (total)		TSS %	Overall tank safety condition/rating
	From empirical formula			t_{emp}	$t_{life-365}$		
	Initiation time (t_c)	De-passivation time (t_p)	Propagation time (t_{corr})				
1	25.65	44.83	4.65	75	81	69	2
2	19.38	34.37	4.81	59	60	41	3
3	22.50	39.46	5.06	67	68	46	3
4	25.65	44.83	4.65	75	80	70	2
5	40.08	70.04	5.48	116	123	83	1
6	25.65	44.83	4.65	75	81	53	2
7	26.95	47.1	4.73	79	83	69	2
8	25.65	44.83	4.65	75	80	67	2
9	23.15	40.46	4.48	68	72	61	2
10	24.38	42.62	4.56	72	75	60	2
11	25.65	44.83	4.65	75	81	81	1
12	28.28	49.42	4.81	83	86	79	1
13	15.86	28.14	5.69	50	51	47	3
14	20.31	36.03	4.90	61	65	57	2
15	21.38	37.36	4.65	63	68	56	2
16	25.65	44.83	4.65	75	81	78	1
17	28.28	49.42	4.81	83	86	75	2
18	31.04	54.24	4.98	90	96	75	2
19	25.65	44.83	4.65	75	81	73	2
20	25.65	44.83	4.65	75	81	77	1
21	25.65	44.83	4.65	75	81	67	2
22	22.25	39.46	5.06	67	69	66	2
23	13.52	23.98	4.65	42	46	56	2
24	25.65	44.83	4.65	75	81	58	2
25	22.25	39.46	5.06	67	70	60	2
26	32.46	56.74	5.06	94	98	60	2
27	22.25	39.46	5.06	67	68	59	2
28	32.46	56.74	5.06	94	97	60	2
29	22.25	39.46	5.06	67	70	60	2
30	32.47	56.74	5.06	94	98	61	2

Table 14: Sample calculation of service life for a water tank (structure No. 13)

Corrosion process	Equation	Parameters & calculations	Calculated time period (Years)
Initiation time (t_c)	$C(x, t) = C_0 \operatorname{erfc} \frac{x}{\sqrt{4D_c t_c}}$	$C(x, t) = 8 \text{ kg/m}^3$ $C_0 = 34.84 \text{ kg/m}^3$ $x = 38 \text{ mm}$ $D_c = 1 \times 10^{-12} \text{ m}^2/\text{s}$ $D_c = 31.54 \text{ mm}^2/\text{y}$ $\operatorname{erfc} \frac{x}{\sqrt{4D_c t_c}} = 0.2296$ Hence, $\frac{x}{\sqrt{4D_c t_c}} = 0.8495$	15.86
De-passivation time (t_p)	$t_p = \frac{1}{12D_c} \left[\frac{L}{1 - \sqrt{\frac{c^*}{c_0}}} \right]^2$ $t_{p'} = \frac{1}{4D_c} \left[\frac{L}{1 - \sqrt{\frac{c^*}{c_0}}} \right]^2$	$L = 38 \text{ mm}$ $c^* = 8 \text{ kg/m}^3$ $t_p = 14.07 \text{ years}$ $t_{p'} = 42.20 \text{ years}$	28.14
Propagation time (t_{corr})	$t_{\text{corr}} = \rho_{\text{cor}} \frac{D \Delta D^*}{s j_r}$ $\Delta D^* = f_t' \left[2 \left(\frac{L}{D} + 1 \right) \right] \delta_{pp}$ $\delta_{pp} = \frac{D}{E_{ef}} (1 + \vartheta) + \frac{2D^3}{s^2 E_{ef}}$	$D = 16 \text{ mm}$ $E_{ef} = 9,908 \text{ N/mm}^2$ $\vartheta = 0.18$ $S = 100 \text{ mm}$ $f_c' = 40 \text{ N/mm}^2$ $f_t' = 3.48 \text{ N/mm}^2$ $L = 38 \text{ mm}$ $j_r = 1.5 \times 10^{-7} \text{ g/m}^2\text{s}$ $j_c = 1.5 \times 10^{-13} \text{ g/mm}^2\text{s}$ $\rho_{\text{cor}} = 3,600 \text{ kg/m}^3$ $\delta_{pp} = 0.00199 \text{ mm}^3/\text{N}$ $\Delta D^* = 0.0467 \text{ mm}$ $E_c = 29,725 \text{ N/mm}^2$	5.69
Estimated Total service life ($t = t_c + t_p + t_{\text{corr}}$)			50
Age of the structure			36
The estimated remaining service life of the structure			14

Results and prediction of service life of water tanks

Evaluating service life of the water tanks

According to the proposed condition assessment procedure, structure no. 02 (a groundwater tank at Matara in Sri Lanka) shows the minimum TSS value of 41%, and it has spent 56% of the expected service life. The tank is located close to the coastal belt with an approximate distance of 420 m. In addition to that, the quality of the construction techniques adopted seems to be very poor. Furthermore, with the sea breeze, the tank has been exposed to direct winds with high salt concentrations. The prevailing physical condition of this tank is the worst compared to other structures used for the study.

Structure no. 05, a ground reinforced concrete tank in the Southern Province of Sri Lanka, has the maximum TSS value (i.e., 83%), and it has completed 11% of its expected physical service life (Refer to Table 13). The tank is located at a considerable distance from the coastal belt (approximately 4,175 m). According to the visual inspection, there are no structural failures, minor cracks, vegetation cover, or any other visual defects.

Hence it can be understood that the prevailing physical state of the structure is in good condition. Therefore, it can be identified that the deviation of the actual from the predicted structural condition is not significant.

For this type of analysis, many parameters should be known to use the mathematical models mentioned in section 4 to estimate the service lives of a reinforced concrete tank. The steel diameter D , the space of the steel bar, s (100 mm), and cover thickness, L (38 mm), were

obtained from field observation. Other parameters were extracted from literature published by the researchers, such as the diffusion coefficient of chloride ions, $D_c = 1 \times 10^{-12} \text{ m}^2/\text{s}$ (Clifton, 1993; Angst & Vennesland, 2007), the threshold value of the chloride concentration, $C^* = 8 \text{ kg/m}^3$ (Hope & Ip, 1987; Angst & Vennesland, 2007), the concentration of chloride ions in pores of concrete at the surface, $C_0 = 34.84 \text{ kg/m}^3$ (Pushpakumara, 2014), creep coefficient of concrete, $\phi_{cr} = 2.0$ (ACI 365.1R-08, 2000), Poisson's ratio, $\nu = 0.18$ (Angst & Vennesland, 2007), the rate of rust production per unit area of the plane, $j_r = 1.5 \times 10^{-15} \text{ g/m}^2\text{s}$ (Bazant, 1979a; 1979b), the density of the corrosion product, $\rho_{cor} = 0.0036 \text{ g/mm}^3$ (Bazant, 1979a; 1979b) and the average compressive strength of concrete, $f'_c = 40 \text{ N/mm}^2$ (ACI 365.1R-08, 2000).

By inserting these parameters into previously discussed formulas, values for t_e , t_p , and t_{cor} for a reinforced concrete tank can be calculated. A sample calculation of the service life for a water tank (structure no. 13) in Hambantota, Sri Lanka, is tabulated in Table 14.

The predicted service life values from both the empirical formula and Life-365 software, as well as TSS values for 30 reinforced concrete tanks are tabulated in Table 13. The selected sample of tanks (30 numbers) is located in the southern province of Sri Lanka. Lower TSS values reflect the tanks with the worst condition.

Assessing the degree, severity, and importance of each case of damage identified during the assessment process provides a detailed picture of the tank. When compared to that information, the calculated TSS values match the actual status of most tanks well. That indicates that the proposed assessment procedure can be used to assess the structural health condition of the tank more efficiently and accurately.

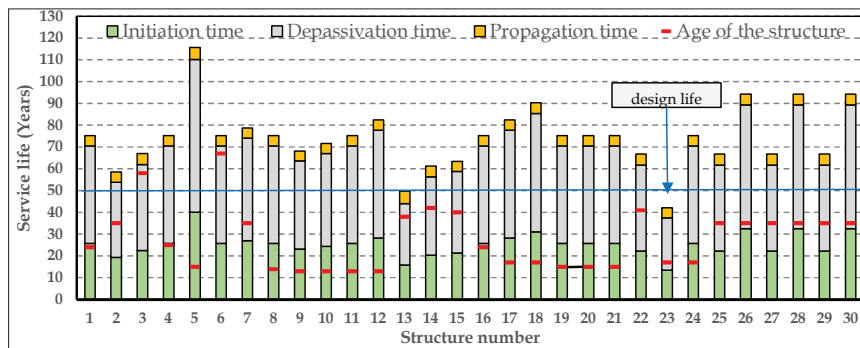


Figure 5: Variation of age with predicted service life and design life of the structures

Variation of tank age and service life

The design life of a reinforced concrete water tank should be in the range of 40–60 years, according to the BS 8007. Generally, the service life of the reinforced concrete water tank is assumed to be 50 years for the structural design as an average value. Structure numbers 13 and 23 indicate less service life than the expected design value. However, the expected service life of both of the tanks exceeds 40 years. These two structures are located very close to the sea and exposed to direct wind with high salt concentration. Therefore, such a relatively low service life is indicated due to the aggressive environmental conditions.

Further, Figure 5 indicates that some structures are within the De-passivation period. Among them, Tank nos. 3, 6, and 13 are very close to the propagation period. Hence, immediate repair or retrofitting works are needed for those tanks.

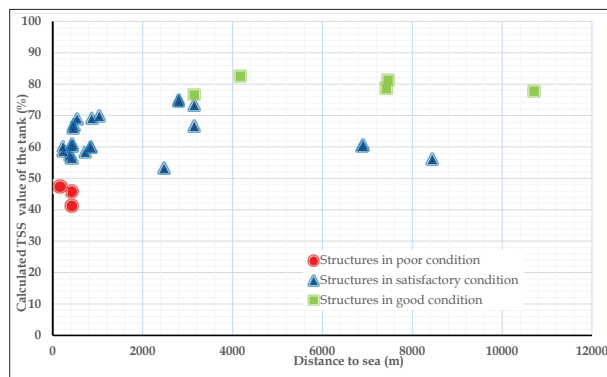


Figure 6: Variation of Tank sound score and overall tank safety condition with distance to the coastal belt

Salt spray can be carried by wind and settle on the surface of the reinforced concrete tank. The surface chloride concentration of a reinforced concrete water tank is increased over time due to constant exposure to the sea breeze. Hence the structures can deteriorate within a shorter time than expected at the design stage. Therefore, the distance from a coastal belt is an important factor that should be taken into account for the durable structural design of such structures. According to Figure 6, most of the structures which have comparatively low safety conditions (i.e., with low TSS) can be seen within 2 km of the coastal belt. The structural condition of a reinforced concrete water tank also depends on ageing, material quality, excessive loads, carbonation effects, and

poor workmanship at the construction stage. Therefore, few structures that are not in good condition but are in satisfactory condition can be seen at a considerable distance from the coastal belt (within the distance of 7.0–8.5 km), as shown in Figure 6.

CONCLUSIONS

Every water supply system has some form of a water storage tank most often constructed from reinforced concrete. These tanks are an integral part of the potable water distribution network but are often taken for granted from a maintenance and condition assessment point of view. To ensure durability and sustainability, they should be adequately inspected and maintained. To effectively achieve these objectives, a suitable assessment system should be implemented.

The objective of the paper was to introduce a suitable condition assessment system for reinforced concrete water tanks.

Both visual inspection and non-destructive data are used to calculate a Tank Soundness Score. It provides a more objective evaluation of the structural condition because it reduces reliance on the inspector's judgment for rating the tank condition. An element-level inspection enables inspectors to capture both the severity and extent of any problems that may influence the integrity of the structure. Such information is valuable for planning maintenance, repair, and rehabilitation programmes.

The service-life prediction method used here is mainly focused on the effect of one degradation process. However, more degradation processes usually occur simultaneously on structures. Hence, assessment becomes more complicated.

Both the predicted service life and the tank soundness score can be used to develop a tank remediation plan more effectively. Therefore, the repair/retrofitting methods proposed based on such assessment will be cost-effective as well as more reliable in enhancing the service life of the water retaining structures. Further, it can be shown that the deviation of the actual from the predicted structural condition of the thirty selected sample structures did not significantly change.

Hence, the proposed combined use of non-destructive tests, visual inspection, and service life prediction to ensure the reliability of the reinforced concrete water tank is more effective. In addition to that, it is a valuable tool for assessing its structural and functional health.

The graphical analysis indicates the durability of a reinforced concrete water tank constructed on standard practices depends on both exposure conditions and the distance from the coastal belt. Also, this study revealed that the quality of concrete materials, workmanship, and routine maintenance strategies, directly and indirectly, affected the service life of the reinforced concrete water tanks. Therefore, the use of impermeable denser concrete mixers and the application of a suitable protective sealer or coating to the surfaces of the water tank just after completing the construction activity are some of the major recommendations to ensure good structural and functional health for the reinforced concrete water tanks.

REFERENCES

- ACI (2000). *Service-Life Prediction—State-of-the-Art Report-ACI 365.1R-00*. American Concrete Institute (ACI), Farmington Hills, Michigan, USA.
- ACI (2008). *Guide for Conducting a Visual Inspection of Concrete in Service -ACI 201.1R-08*. American Concrete Institute (ACI), Farmington Hills, Michigan, USA.
- Angst U. & Vennesland Ø. (2007). *SINTEF Report (SP 4.2)-Critical Chloride Content*. Concrete Innovation Centre (COIN), Trondheim, Norway.
- Bazant Z.R. (1979a). Physical model for steel corrosion in concrete sea structures - theory. *Journal of Structural Division* **105**(6): 1137–1153.
DOI: <https://doi.org/10.1061/JSDEAG.0005168>
- Bazant Z.R. (1979b). Physical model for steel corrosion in concrete sea structures - application. *Journal of Structural Division* **105**(6): 1155–1166.
DOI: <https://doi.org/10.1061/JSDEAG.0005169>
- BSI (1987). *British Standard Code of Practice for Design of Concrete Structures for Retaining Aqueous Liquids -BS 8007:1987*. British Standards Institution, London, UK.
- Hope B.B. & Ip A.K.C. (1987). Chloride corrosion threshold in concrete. *ACI Materials Journal* **84**(4): 306–314.
DOI: <https://doi.org/10.14359/1617>
- Ming-Te L., Ran H., Shen-An F. & Chi-Jang Y. (2009). Service life prediction of the pier for the existing reinforced concrete bridges in the chloride-laden environment. *Journal of Marine Science and Technology* **17**(4): 312–319.
DOI: <https://doi.org/10.51400/2709-6998.1988>
- NDT James Instrument Inc. (2021). *OhmCorr™ Test System - Resistivity Meter For Concrete (manual)*. Available at https://www.ndtjames.com/Ohmcorr_Test_System_Resistivity_Meter_p/c-rm-8000.htm, Accessed 27 August 2021.
- Pillai R.G. (2011). *Corrosion and Service Life Prediction of Reinforced Concrete Structure*. Building Technology & Construction Materials Division, Dept. of Civil Engineering, IIT Madras, Chennai, India.
- Pushpakumara B.H.J. (2014). Condition Assessment, Repair and Retrofitting of Existing Bridges in Sri Lanka due to Chloride Effect. *M.Phil. Thesis*, University of Ruhuna, Sri Lanka.
- Pushpakumara B.H.J., De Silva S. & De Silva S. (2017). Visual inspection and non-destructive tests-based rating method for concrete bridges. *International Journal of Structural Engineering* **8**(1): 74–91.
DOI: <https://doi.org/10.1504/IJSTRUCTE.2017.081672>
- Rashidi M. & Gibson P. (2011). Proposal of a Methodology for Bridge Condition Assessment. *Proceedings of The 34th Australasian Transport Research Forum (ATRF)*, 28–30 September. Adelaide, Australia, pp. 1–13.
- Saaty T.L. (1980). *How to Make a Decision: The Analytic Hierarchy Process*. McGraw-Hill International, New York, USA.
DOI: <https://doi.org/10.13033/isahp.y1988.042>
- Saaty T.L. (1988). *Multicriteria Decision Making: The Analytic Hierarchy Process*. RWS Publications, Pittsburgh, USA.
- Saaty T.L. (1994). *Fundamentals of Decision Making and Priority Theory with the Analytic Hierarchy Process*. RWS Publications, Pittsburgh, USA.
- Tuutti K. (1982). *Corrosion of steel in concrete- Report No. 4.82*. Swedish Cement and Concrete Research Institute, Stockholm, Sweden, pp.1-469.
- UNDP Disaster Risk Management Programme (2007). *Condition Assessment of Building for Repair and Upgrading*. National Disaster Management Division, Ministry of Home Affairs, New Delhi, India.
- US Federal Highway Administration (FHWA) (2016). *FHWA-HRT-15-081 - Synthesis of National and International Methodologies Used for Bridge Health Indices*. U.S. Department of Transportation, Washington D.C., USA.

RESEARCH ARTICLE

Agricultural statistics

Application of Benford's law in agricultural production statistics

F Hanci

Faculty of Agriculture, Erciyes University, 38280, Melikgazi, Kayseri, Turkey.

Submitted: 24 February 2021; Revised: 17 December 2021; Accepted: 24 December 2021


Abstract: The importance of food supply throughout the world has once again shown its significance in the COVID-19 pandemic period. A continuous food supply is possible with correct agricultural programming. An effective agricultural product programming can only be possible by obtaining precise agricultural data. However, it is very difficult to gather accurate agricultural production statistics from all over the world and confirm their accuracy. In this study, the compatibility of the production statistics of six important agricultural products (wheat, rice, potato, onion, banana, apple) which had been collected from local sources, and had published as open-source by the Food and Agriculture Organization of the United Nations, with Benford's law was examined for the first time. Data for the last two decades are used to ignore the impact of annual fluctuations. The compatibility of theoretically expected and observed data was tested by Chi-square (χ^2) and Mean Absolute Deviation (MAD) tests. Although inconsistencies were found in some data by examining the numbers in the first, second, and first two digits, in general, the MAD test results gave a mostly concordant result.

Keywords: Agriculture, food, nutrition, production, statistics.

INTRODUCTION

In the globalizing world, it has become impossible to consider the agricultural production of any country independently from other countries. In particular, the

Covid-19 pandemic has demonstrated the importance of agricultural production and the food supply chain globally. Accordingly, the reliability of statistical data on world agricultural production has started to be on the agenda again. The largest agricultural production statistics data available worldwide is published by FAOSTAT (FAO, 2021). These data form the basis for many scientific studies as well as for future planning. The reliability of these data is primarily the responsibility of each country. A large number of models and methods can be used to prevent the risk of fraud and to detect fraud occurring in published large datasets. One of these methods is Benford's Law (Benford, 1938). Benford's Law, which is a proactive method, determines the numerical frequencies in the digits of the dataset. The direction and magnitude of deviations between the observed value and the rates of Benford's Law can give an idea about the reliability of the dataset. Although the data with deviations are not definitive evidence of fraud, the researcher can create the audit plan by considering the deviations in the dataset. The Benford's Law hypothesis is based on an article by Simon Newcomb published in the American Journal of Mathematics, about the incidence of numbers in digits (Newcomb, 1881). There were no calculators at the time, and many complex mathematical calculations could be made using logarithm tables printed on paper. Newcomb noticed that the first pages of logarithm tables are more obsolete than the last pages. Also, it has been found that the numbers starting with "1" are used more by the researchers than the numbers starting with "2", and those starting with "2" are used more than starting with

* Corresponding author (fatihhanci@erciyes.edu.tr;  <https://orcid.org/0000-0002-2015-0351>)



This article is published under the Creative Commons CC-BY-ND License (<http://creativecommons.org/licenses/by-nd/4.0/>). This license permits use, distribution and reproduction, commercial and non-commercial, provided that the original work is properly cited and is not changed in anyway.

“3”. Newcomb transformed this research into a formula (Lemis *et al.*, 2000):

$$P(\text{first digit number}) = \log_{10}(1+1/d), (d = 1,2,3,4,5,6,7,8,9)$$

According to Newcomb’s research, the probability of “1” in the first digit is 0.3010 while the probability of being in the second digit is 0.1139 (Miller, 2015).

Frank Benford, a physicist in General Electric’s laboratory in New York, published the results of his study in 1938, in which 20 different groups were examined with a dataset totaling 20,229 (Benford, 1938). 30.6% of this data started with number “1”; 12.4% with “3”; 8% with “5”; and 4.7% with “9” in the Benford observation. Benford’s analysis shows a logarithmic distribution rather than a homogeneous distribution (Akkaş, 2015). The logarithm functions of Benford’s Law are as follows (Ertikin, 2017):

For the first digit of the numbers;

$$P(D_1 = d_1) = \log(1 + (1/d_1)); d_1 \in \{1,2,3, \dots, 9\} \dots(1)$$

For the second digit of the numbers;

$$P(D_2 = d_2) = \sum \log(1 + (d_1/d_2)); d_2 \in \{0,1,2,3, \dots,9\} \dots(2)$$

For the first two digits of the numbers;

$$P(D_1 D_2 = d_1 d_2) = \log(1 + (1/(d_1 d_2))); d_1 d_2 \in \{10, \dots, 99\} \dots(3)$$

For example; The probability that the number in the first digit of a number is “2” and the number in the second digit is “8” can be calculated by the following formula:

$$P(28) = \log_{10}(1 + 1/28) = \log_{10}(29/28) = 0.01524. \dots(4)$$

Benford’s Law has been used by researchers from many different disciplines since its inception. While these researchers initially focused on the mathematical explanation of the law, in the following periods, research studies on different fields such as COVID-19, social welfare programs, and academic fraud were emphasized (Horton *et al.*, 2020; Lee *et al.*, 2020; Azevedo *et al.*, 2021). Various prerequisites must be met for a dataset to yield results following Benford’s Law (Nigrini, 2000). The dataset should describe the magnitude of similar

phenomena. For example, the population of cities, lengths of rivers, stock values, or daily sales amounts. Also, the values in the dataset should not have an upper or lower limit. For example, daily working hours do not follow Benford’s Law, as they have to take a limited value between “0” and “24”. The values in the dataset should not be specified numbers. Therefore, data consisting of determining numbers such as citizenship identification number, tax number, credit card number, or telephone number are not data by Benford’s Law. The Benford’s Law analysis technique consists of two stages: general analysis and special analysis tests. A general analysis test gives an idea about the data. These tests are the first digit and second digit tests. Special tests are the first two digits, the first three digits, the last two digits, and duplicate recording tests (Yanık & Samancı, 2013). First and second digit tests cannot be used for sampling in control. However, the second digit test can easily detect fundamental abnormalities in the data (Goh, 2020).

In this study, the compliance with Benford’s Law of the data published by FAOSTAT, showing the production quantities for six agricultural products, has been investigated.

MATERIALS AND METHODS

The sample data consists of six agricultural products (wheat, rice, potatoes, onion, banana, apple) published during 2000-2019. In addition to these six species, to provide an overview of all agricultural production statistics and to reach a cumulative result, the values created by bringing together all the data were also examined. Production amounts (tons) in the last two decades were collected on a country basis. In the selection of products, both the strategic importance and the production potentials in different geographies of the world are taken into consideration. For this purpose, a total of 14907 data elements including 2461 wheat, 2308 rice, 3095 potatoes, 2769 onions, 2392 bananas, and 1882 apples were examined. The frequency of the first, second, and first two digits in these data was determined using the Microsoft Excel Office program.

After calculating the frequencies of the numbers in the analysed dataset, it is necessary to determine the “conformity” limits of the deviations according to Benford’s Law. At this stage, conformity tests are used to determine how much deviation there is between the observed rates and Benford’s Law rates, and whether this deviation is significant. Conformity tests used in Benford’s Law include the Z-Statistics Test, Chi-square (χ^2) Test, Kolmogorov-Smirnov Test, and Mean Absolute

Deviation Method (MAD). Although the Z-Statistics Test, χ^2 test, and Kolmogorov-Smirnov Test are based on statistical foundations, they can often be affected by the number of data. In this study, two methods were used to confirm the theoretical expectation of Benford's Law: MAD and χ^2 test. The MAD method often gives results open to interpretation, but they are independent of the number of data. Besides, this test method has a very practical application area (Druica *et al.*, 2018). The MAD score is defined as the mean of the absolute value of the difference between the frequency of each first digit within the sample, and the frequency as determined by the formula:

$$MAD = \sum i \frac{|Af-Ef|}{K} \dots(5)$$

where *Af* is the actual frequency of the leading digit observed, *Ef* is the expected frequency as determined by Benford, and *K* is the number of leading digit bins (equal to 9 for the first, 10 for the second, and 90 for the first two leading digits).

The second measure of conformity is the χ^2 test statistic which compares expected frequencies and observed frequencies in one or more categories of a contingency table for leading digits 1–9. χ^2 is calculated as follows:

$$\chi^2 = \sum i \frac{(Av-Ev)^2}{Ev} \dots(6)$$

Av is the actual value of the leading digit observed, *Ev* is the expected value as determined by Benford.

The Microsoft Excel Office program was also used in these analyses. To evaluate the results obtained from the χ^2 test, a table of critical values of distribution with *d* degrees of freedom was used.

RESULTS AND DISCUSSION

The results of the first digit analysis of selected crops are shown in Table 1. To apply the χ^2 test, null hypotheses (H_0 : the differences between the expected and observed values are small enough to be considered insignificant) were set and the significance level approved at 5%. To interpret the results, Chi squared critical values tables were used. Results below the threshold value specified in this table prove “compatibility,” and χ^2 test results above this threshold value emphasize the inconsistency. According to the Chi-square critical values table, the critical value found at 8 and 9 degrees of freedom and 5% significance level is 15.507 and 16.919 respectively. The hypothesis in which the number set of six agricultural products conforms to Benford's Law has been rejected according to the χ^2 test. However, it should not be forgotten that the χ^2 test can be directly affected by the number of samples in the dataset, and tends to reject the null hypothesis even for small departures from the expected distribution.

Table 1: Results of the first digit analysis

Number	Wheat		Rice		Potato		Onion		Banana		Apple		Complete	
	Exp.	Obs.	Exp.	Obs.	Exp.	Obs.	Exp.	Obs.	Exp.	Obs.	Exp.	Obs.	Exp.	Obs.
1	741	823	772	802	1075	912	816	857	740	686	540	495	3921	4575
2	433	455	427	426	571	532	476	417	360	433	341	380	3010	2643
3	307	230	216	279	374	386	345	401	346	346	272	221	1751	1863
4	238	200	188	192	257	318	285	220	190	160	126	224	1774	1314
5	195	165	155	141	189	265	237	239	206	170	134	153	1212	1133
6	165	151	142	144	193	229	205	187	162	193	152	153	1212	1057
7	143	153	143	96	129	158	141	179	155	155	122	108	855	849
8	126	160	150	132	177	161	144	157	136	149	117	74	586	833
9	113	124	116	96	129	134	120	112	97	100	79	74	586	640
Σ	2461		2308		3095		2769		2392		1882		14907	
χ^2_8	52.796		42.550		87.627		46.250		37.434		114.950		414.403	
MAD	0.014		0.014		0.004		0.011		0.013		0.014		0.004	

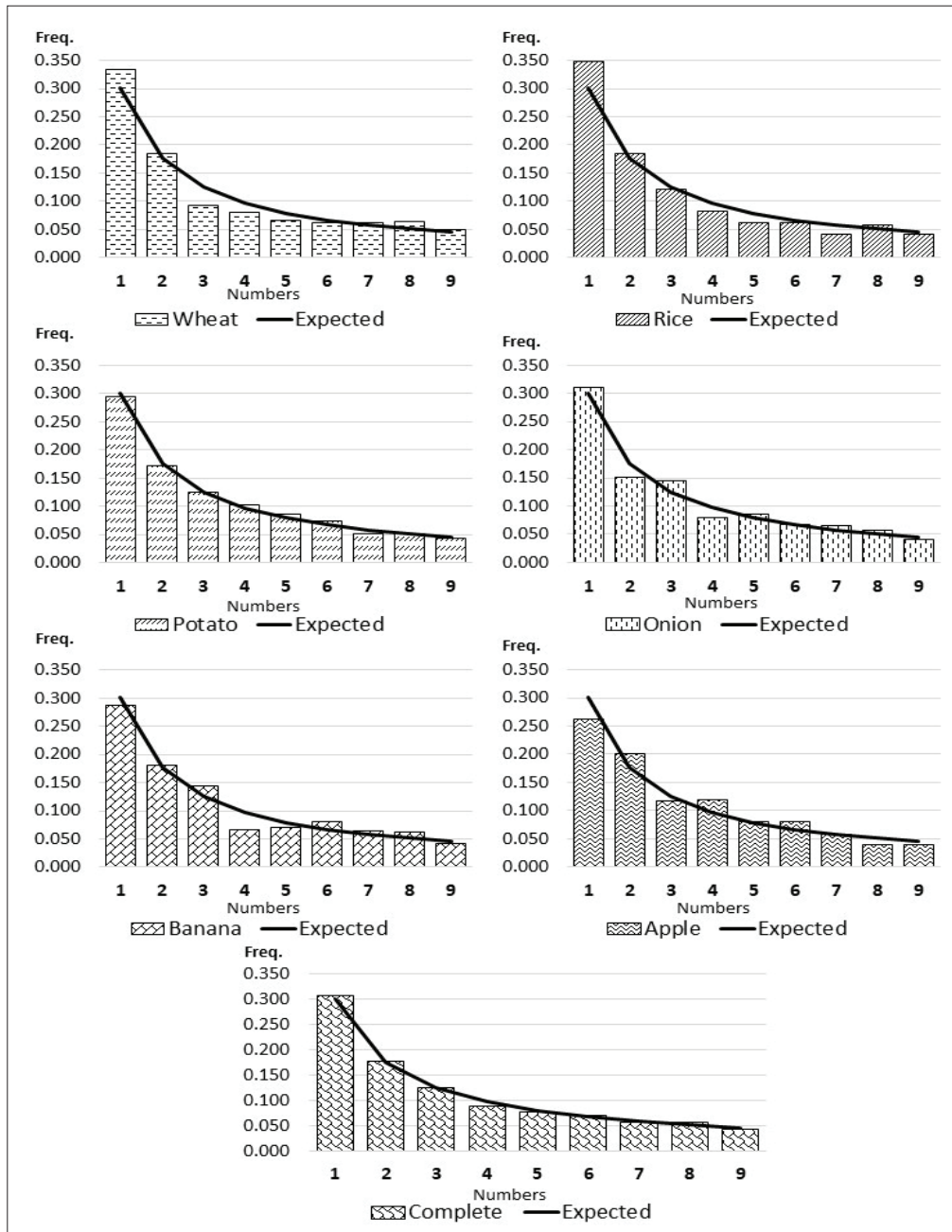


Figure 1: Relative frequencies of the first digits

The MAD test is more robust since it ignores the number of records. The lower the MAD, the smaller the average difference between the observed and theoretical distributions. MAD values under 0.015 suggest conformity (Silva and Filho, 2020). In considering this criterion, it may be concluded that the investigated

agricultural data are accordant with the Benford distribution for all crops. When Table 1 and Figure 1 are examined, it is seen that the most accordant distribution in the first digit is observed with potato, according to Benford’s law. It was followed by a dataset in which all products were displayed on a single list.

According to the MAD values, the closest values to the expected frequencies were observed in the dataset of the potato. The MAD value in the list where all products are listed together is also similar to potatoes. In onion, the data corresponding to a first digit value of “2”, “3”, and “4” showed more deviation than expected. A similar situation is found in the data starting with “1”, “5”, and “7” in rice.

The distribution of the numbers in the second digits is shown in Table 2 and Figure 2. When the compatibility of these distributions with Benford’s Law is checked with χ^2 , it is seen that the potato, onion, and apple results are compatible at different probability levels ($p = 0.1348$, $p = 0.0236$, $p = 0.0167$ respectively). In the MAD analysis results, the data of all products were found to be consistent.

Table 2: Results of the second digit analysis

Number	Wheat		Rice		Potato		Onion		Banana		Apple		Complete	
	Exp.	Obs.	Exp.	Obs.	Exp.	Obs.	Exp.	Obs.	Exp.	Obs.	Exp.	Obs.	Exp.	Obs.
0	294	387	276	343	370	403	331	391	285	386	225	272	1781	2182
1	279	265	262	268	352	339	315	316	272	286	214	231	1695	1705
2	267	251	251	261	336	342	301	312	260	245	205	200	1620	1611
3	256	257	240	225	322	308	289	262	249	201	196	181	1553	1434
4	246	248	231	233	310	291	278	247	239	198	189	179	1493	1396
5	237	237	223	201	299	286	268	279	231	247	182	204	1439	1454
6	229	236	215	182	289	313	258	257	223	207	176	160	1390	1355
7	222	174	208	207	279	266	250	229	215	216	170	159	1345	1251
8	215	200	202	200	271	250	242	232	209	213	165	152	1303	1247
9	209	199	196	184	263	293	235	243	203	186	160	144	1265	1249
Σ	2454		2304		3091		2768		2385		1882		14884	
χ^2_{99}	43.325		25.907		13.665		19.996		57.043		20.207		115.840	
MAD	0.006		0.007		0.006		0.007		0.011		0.009		0.006	

Table 3: Summarized results of the first two-digit analysis

	Wheat	Rice	Potato	Onion	Banana	Apple	Complete
Σ	2454	2304	3091	2768	2385	1882	14884
MAD	0.002	0.002	0.001	0.002	0.002	0.003	0.001
χ^2_{89}	221.387	222.031	110.174	180.380	216.021	208.868	222.789

When all six products are listed together, it can be said that the data with “0” in the second digit are doubtful in terms of compliance with Benford’s law. When the graphs of the expected and observed frequencies in Figure 2 are examined, it is understood that the largest deviation is in the values ending with “0” and “5”. But graphs of the relative frequencies of the first digit do not exhibit such behavior. The most obvious difference between these two measurement systems is that it is not possible to display a value starting with the number “0” in the first digit analysis. The discrepancy between “0” and “5” in the second digit analysis may be due to local authorities’ preference to round data associated with “1”, “4” and “6” to “0” or “5”.

In evaluations using Benford’s law, interrogation of the first two digits is generally used in complex data. In this study, all six agricultural products were examined separately and as a single list according to their numbers in the first two digits. Since there are a total of 90 (values between 10 and 99) categories, the relevant results are shared in the summary table.

The results obtained according to the numbers in the first two digits are parallel to the results in the second digit. According to MAD results, potatoes and the total list were found to be the most compatible with Benford’s law. In the χ^2 test, only the value obtained from potatoes was found to be compatible with Benford’s law (p value: 0.9364).

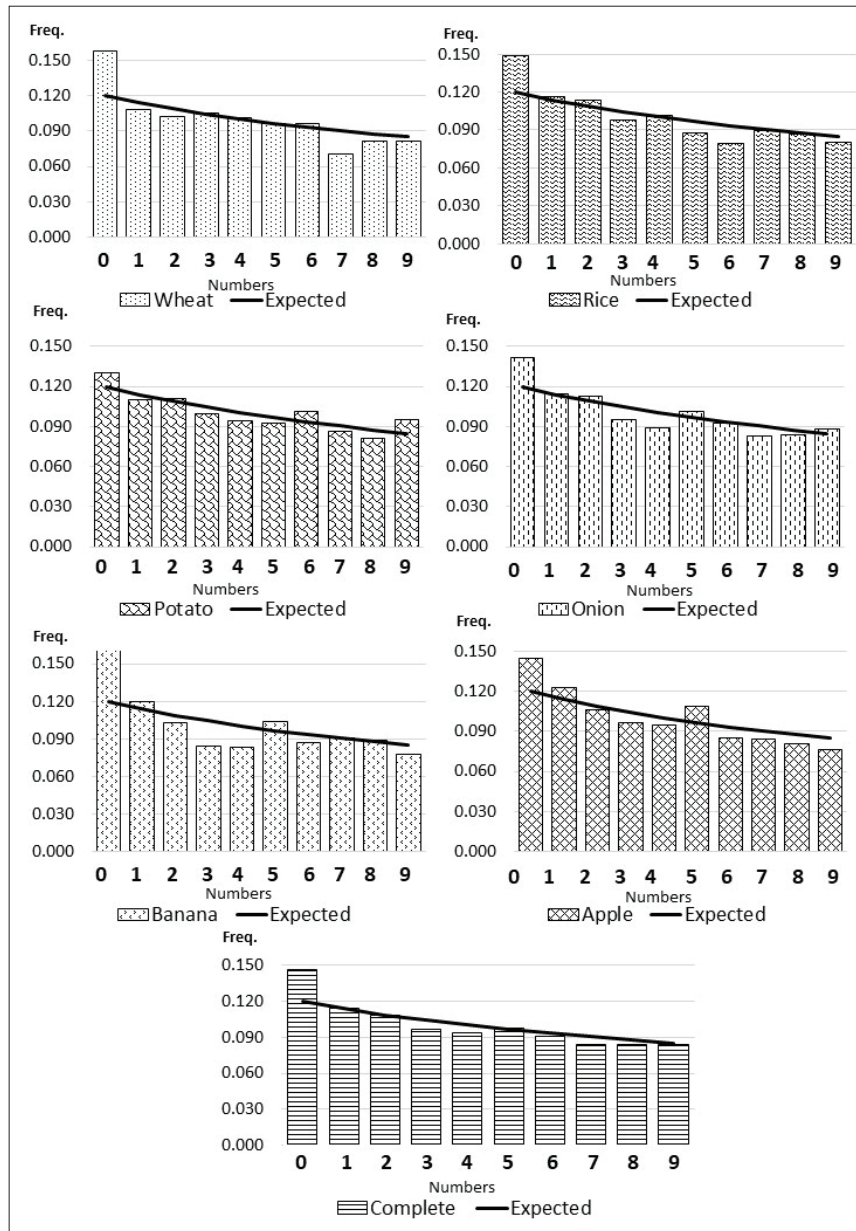


Figure 2: Relative frequencies of the second digits

CONCLUSION

As mentioned above, collecting precise data on agricultural production is a very difficult process. Governments take various measures to increase the reliability of this data. Mostly, local organizations of the central government are trying to create this data set by conducting on-site investigations. However, it is often impossible to achieve exactly this. In some cases, the statements of the farmers

are taken as a basis, and correct notifications are tried to be made with various incentives or penalties. The control of the combined data by the central authorities is generally attempted by comparison with the previous year's data, comparison with commercial records, or on-site inspections by assigned inspectors. However, these measures are often insufficient. Benford's Law is a practical statistical instrument for specifying doubtful activities in data. The agricultural production of a particular region depends on very uncertain factors such

as low temperature, drought, and excessive precipitation. Benford's Law is not a system that takes these factors into account directly. Even under uncertain conditions, it is a control system created according to normal distributions in data sets that are formed without human intervention. Therefore, regardless of the conditions, the reliability of the obtained data sets can be verified with Benford's Law. The arguments presented here do not constitute proof of illegality, but some suspected data were identified as consistent departures of agricultural statistics' reports from NBL. Benford's Law has been tested for the first time in agricultural statistics reported by all countries of the world. Therefore, the findings obtained in this study should be evaluated at the "giving an idea" stage. Also, it should not be forgotten that collecting such agricultural data on-site is a very difficult task. However, no major deviations were found in the compatibility analysis with MAD tests. This situation proves the reliability of the data obtained from FAOSTAT despite all difficulties. In this study, "doubtful" numbers in different digits can give local data collectors a quick control chance. In future studies, in addition to the six products discussed in this study, the evaluation of different agricultural products may offer new opportunities to the commentators. Also, agricultural statistics monitoring on a country basis may yield useful results.

Conflict of interest

The author declares that there is no conflict of interest.

REFERENCES

- Akkaş M.E. (2015). Testing distribution of gold returns by Newcomb-Benford law. *The Journal of International Social Research* **8**(40): 577–584.
DOI: <https://doi.org/10.17719/jisr.20154013940>
- Azevedo C.S., Goncalves R.F., Gava L.V., & Spinola M.M. (2021). A Benford's Law based methodology for fraud detection in social welfare programs: Bolsa Familia analysis. *Physica A: Statistical Mechanics and its Applications* **567**: 1–15.
DOI: <https://doi.org/10.1016/j.physa.2020.125626>
- Benford F. (1938). The law of anomalous numbers. *Proceedings of the American Philosophical Society* **78**(4): 551–572.
- Druica E., Oancea B., & Valsan C. (2018). Benford's law and the limits of digit analysis. *International Journal of Accounting Information Systems* **31**(1): 75–82.
DOI: <https://doi.org/10.1016/j.accinf.2018.09.004>
- Ertikin K. (2017). Fraud auditing: a services business example for computer-aided Use of Benford's law. *The World of Accounting Science* **19**(3): 696–726.
DOI: <https://doi.org/10.31460/mbdd.609957>
- FAO (2021). Food and Agriculture Organization of the United Nations, Statistics Division. Available at <http://www.fao.org/faostat/en/#home>, accessed 28 January 2021.
- Goh C. (2020). Applying visual analytics to fraud detection using Benford's law. *Journal of Corporate Accounting Finance* **31**: 202–208.
DOI: <https://doi.org/10.1002/jcaf.22440>
- Horton J., Kumar D.K., & Wood A. (2020). Detecting academic fraud using Benford law: The case of Professor James Hunton. *Research Policy* **49**(8): 1–19.
DOI: <https://doi.org/10.1016/j.respol.2020.104084>
- Lee K., Han S., & Jeong Y. (2020). COVID-19, flattening the curve, and Benford's law. *Physica A: Statistical Mechanics and its Applications* **559**: 1–12
DOI: <https://doi.org/10.1016/j.physa.2020.125090>
- Lemis L.M., Schmeiser B.W., & Evans D.L. (2000) Survival Distribution Satisfying Benford's Law. *American Statistician* **54**(4): 236–24.
DOI: <https://doi.org/10.2307/2685773>
- Miller S.J. (2015). A quick introduction to Benford's law. In: *Benford's Law: Theory and Applications*. Princeton University Press, USA.
- Newcomb S. (1881). Note on the frequency of use of the different digits in natural numbers. *American Journal of Mathematics* **4**(1): 39–40.
- Nigrini M. (2000). Digital analysis using Benford's law: tests and statistics for auditors. *EDPACS* **28**(9): 1–2.
DOI: <https://doi.org/10.1201/1079/43266.28.9.20010301/30389.4>
- Silva L. & Filho D.F. (2020). Using Benford's law to assess the quality of COVID-19 register data in Brazil. *Journal of Public Health* **43**(1):107–110.
DOI: <https://doi.org/10.1093/pubmed/fdaa193>
- Yanık R. & Samancı T.H. (2013). Benford's law and a practical implementation in public sector about its application to accounting data. *Journal of Graduate School of Social Sciences* **17**(1): 335–348.

RESEARCH ARTICLE

Regression analysis

Implementation of adaptive lasso regression based on multiple Theil-Sen Estimators using differential evolution algorithm with heavy tailed errors[†]

E Dünder^{1*}, T Zaman², MA Cengiz¹ and K Alakuş¹

¹ Department of Statistics, Faculty of Science, Ondokuz Mayıs University, Turkey.

² Department of Statistics, Faculty of Science, Çankırı Karatekin University, Turkey.

Submitted: 18 November 2020; Revised: 29 November 2021; Accepted: 24 December 2021

Abstract: The last decade has witnessed that penalized regression methods have become an alternative to classical methods. Adaptive lasso is one type of method in penalized regression and is commonly used in statistical modelling to perform variable selection. Apart from the classical lasso setting, the adaptive lasso requires the coefficient weights inside the target function. The main issue in adaptive lasso is to select the optimal weights in the model since the selected weights have serious impacts on the estimation results. However, there is no compromise for choosing the weights as a universal approach, and they should be chosen properly with the statistical assumptions. When the error terms are heavy-tailed, classical estimation (such as least squares) gives poor results in adaptive lasso because of the lacking robustness. This article deals with the selection of optimal weights in the presence of heavy-tailed errors for the adaptive lasso. To solve the distributional problem, we integrated the Theil-Sen estimation (TSE) approach into the adaptive lasso for heavy-tailed erroneous cases while choosing the weights. During the selection of the optimal tuning parameters, we employed a differential evolution algorithm (DEA) between a range of lambda values. The simulation studies and real data examples confirm the power of our combination of Theil-Sen estimators and differential evolution algorithm in the presence of heavy-tailed errors in the adaptive lasso.

Keywords: Adaptive lasso, heavy-tailed errors, Theil-Sen estimators, weight vector selection.

INTRODUCTION

The classical lasso solution does not consider the marginal effects of the regression coefficients during the penalization. Ignorance of the nature of each coefficient can cause poor results. To overcome this problem, adaptive lasso is proposed by Zou (2006). The researchers published many articles to improve the adaptive lasso. Lu *et al.* (2012) studied the robustness of adaptive lasso under misspecification. Huang *et al.* (2008) investigated the initial estimators for adaptive lasso and made a comparison with classical lasso. Chen and Chan (2011) performed subset selection in subset autoregressive moving-average using adaptive lasso for time series analysis. Ren and Zhang (2013) employed model selection in vector autoregressive models via adaptive lasso. Yoon *et al.* (2017) presented a new algorithm based on adaptive lasso with ARMA-GARCH errors in linear regression analysis. Foster *et al.* (2013) used adaptive lasso for monotone single-index models to estimate the index parameter. Hui *et al.* (2015) proposed a new criterion for the selection of the optimal tuning parameter in adaptive lasso and presented the efficiency of this alternative criterion. Zhang and Xiang (2015) studied the oracle properties of adaptive group lasso in high dimensional cases.

* Corresponding author (emre.dunder@omu.edu.tr;  <https://orcid.org/0000-0002-6640-5284>)

[†] This paper is an extended version of the study presented in 'International Conference on Information Complexity and Statistical Modelling in High Dimensions with Applications IC-SMHD-2016', 18–21 May, 2016



This article is published under the Creative Commons CC-BY-ND License (<http://creativecommons.org/licenses/by-nd/4.0/>). This license permits use, distribution and reproduction, commercial and non-commercial, provided that the original work is properly cited and is not changed in anyway.

The main issue in adaptive lasso is the choosing optimal weights. Generally ordinary least squares (OLS) and ridge estimators are used for the weights. Alternatively, Qian and Yang (2013) proposed a weight selection method based on standard errors of regression coefficients. Fan *et al.* (2014) suggested using a robust two-step method for the estimation of the weight vector.

In previous studies, the adaptive lasso estimators are adopted using different loss functions such as Huber-M (Lacroix & Zwald, 2011), least absolute deviation (Wang *et al.*, 2007) etc. Machkour *et al.* (2020) developed a robust estimator for adaptive lasso for contaminated data. Li and Wang (2020) implemented a least absolute deviation (LAD) based adaptive lasso approach for robust estimation of change point models.

These types of studies only focused on changing the loss function, but also the adaptive beta coefficients can be changed to improve the performance of the models when the dataset contains some problems like heavy-tailed error terms. The classical regression solutions fail to produce useful results when the error terms are heavy-tailed and robust estimators can be used as an alternative solution for adaptive lasso. Instead of changing the loss function, we indicate that the usage of robust estimators in adaptive lasso for weight selection enables to fix the results in the presence of heavy-tailed errors.

It is troublesome to decide which weights should be used in adaptive lasso when heavy-tailed errors emerge. Heavy-tailed errors occur frequently in statistical models and cause problematic cases (Barros *et al.*, 2008; Zhou & Wu, 2011; Honda, 2013). Robust techniques are widely used to eliminate the drawbacks of heavy-tailed errors.

This study proposes to use TSE as the weights in adaptive lasso when heavy-tailed errors exist. The robustness property of the TSE brings promise for successful accomplishment. This study also utilizes the DEA to select tuning parameters in adaptive lasso models, which is one of the most used heuristic optimization techniques.

MATERIALS AND METHODS

Adaptive lasso

Adaptive lasso is a type of regularization method which selects and estimates the regression coefficients simultaneously by considering a weight vector (Zou, 2006). Instead of classical lasso solutions, adaptive

lasso assigns weights to each regression coefficient, so it considers the marginal effects of predictors. Adaptive lasso estimators β^* are obtained such that

$$\beta^* = \arg \min \|y - X\beta\|^2 + \lambda \sum_{j=1}^p w_j | \dots (1)$$

where 'w' represent the weight vector for each regression coefficient, and λ shows the tuning parameter. Equation (1) can be solved efficiently as a convex optimization problem. The solution highly depends on the selected weight vector.

As an alternative to existing w estimates for the weights, we will use $\beta^{\text{TSE}} = (\beta_1^{\text{TSE}}, \beta_2^{\text{TSE}}, \dots, \beta_p^{\text{TSE}})$ which represents the regression coefficients obtained with TSE. In the first phase, we obtain the β^{TSE} estimates and put it into the weight vector. Because TSE handles the robustness issue, the adaptation of TSE improves the results of adaptive lasso models in the presence of outliers or heavy tailed errors. Also, the properties of TSE satisfy the main assumptions of the adaptive lasso weights, so TSE becomes an attractive approach.

Theil Sen estimators

The method, put forward by Theil in 1950, is one of the most commonly used slope finding methods (Theil, 1950). Theil's method, which is used to find the slope of a vector, is based on the calculation of the median of slope values calculated from an observation pair, (x_i, y_i) and (x_j, y_j) (Hussain & Sprent, 1983). The $(x_1, y_1), \dots, (x_n, y_n)$ we have, consist of n observation pairs. The x_i values are known, different, independent of each other, and sorted as $x_1 < x_2 < \dots < x_n$. In the regression model, the variances of ε_i 's consist of σ_ε^2 , and random errors resulted from a symmetric continuous distribution, whose median is zero and originates from the same distribution (Rao & Gore, 1982). In Theil's method in simple linear regression, β_0 and β_1 should be estimated in such a way that median of the error term must be zero (Maritz, 1979). Estimation of $\beta_1, \hat{\beta}_1$ while $i < j$ and $(x_i \neq x_j)$, is a weight median of all $N = \binom{n}{2}$ curve estimations of $S_{ij} = \frac{y_j - y_i}{x_j - x_i}$ (Wang & Yu, 2005).

In the literature, Theil (1950) suggested the median of common paired slopes as an estimator of the slope parameter in a simple linear regression model. Later, Sen (1968) expanded on this estimation to find the ties. Theil-Sen estimation is, with a 29.3% breakdown point, robust and has a limited effect function and high asymptotic efficiency. For this reason, it is competing well with other slope estimators (Sen, 1968; Dietz, 1989;

Wilcox, 1998). Wang (2005) explored the behaviour of TSE when the covariate is random. Also, Sen (1968) obtained consistence and asymptotic distribution of TSE. Also, when error distribution is discontinuous at a certain point, TSE is found to be super-efficient. Even though most of its good characteristics are interpreted clearly, many statisticians tried to expand on it (Oja & Niinima, 1984; Zhou & Serfing, 2008). Since TSE is formulated only for a simple linear model, it is underdeveloped and rarely used. While for TSE to be expanded to a multiple linear model is obvious and attractive, this is technically hard and slows down the generalization and exploration processes. Dang *et al.* (2008) suggested several different methods of using the multivariate median in expanding the TSE of a parameter in a simple linear model to a multivariate linear model. Multivariate medians generalize univariate medians of the variables. For the essential concept, see Small (1990). According to the study of Dang *et al.* (2008), it is applicable for any multivariate median identified through depth functions.

Multivariate Theil-Sen estimation

Let us discuss a multivariate linear regression model where $\xi \geq 1$. Through following the above mentioned procedure, first, the estimation of $\zeta = (\alpha, \beta^T)^T$ can be found as the solution of equation (1)

$$Y_j - \alpha - X_j^T \beta = 0, i \in z_{\xi+1} = \{j_1, \dots, j_{p+1}\} \dots(2)$$

Here, $z_{\xi+1}$ is the $(\xi + 1)$ subset of $\{1, \dots, n\}$. If matrix $(\xi + 1) \times (\xi + 1)$ is $(X_z : z \in z_{\xi+1})$, it can be invertible. This estimation is represented with $\hat{\zeta}_{z_{\xi+1}}$ to accentuate dependency to $\xi + 1$ observations. Then, the natural expansion of TSE from a simple linear regression model to a multivariate regression model becomes a multivariate median as below:

$$\hat{\zeta}_n = Mmed\{\hat{\zeta}_{z_{\xi+1}} : \forall z_{\xi+1}\} \dots(3)$$

Here, $\hat{\zeta}_{z_{\xi+1}}$ is at the same time the estimate of least squares of ζ depending on observations $\{(X_j, Y_j) : j \in z_{\xi+1}\} \xi + 1$. At this angle, r different arbitrary combinations of $\{(X_j, Y_j) : j \in z_r\}$ may be chosen which means, here, $\xi + 1 \leq r \leq n$ and it constitutes the least squares estimation of $\hat{\zeta}_{z_r}$. Then, the multivariate TSE of parameter ζ will naturally be the multivariate median of all possible least squares estimates, and is explained as follows:

$$\hat{\zeta}_n = Mmed\{\hat{\zeta}_{z_r} : \forall z_r\} \dots(4)$$

The least squares estimate is as below:

$$\hat{\zeta}_z = (X_z^T X_z)^{-1} X_z^T Y_z \dots(5)$$

There are as many cases as r combinations of total n for estimating the regression parameters with the multivariate Theil-Sen estimator (MTSE) method (Dang *et al.*, 2008). The regression coefficients are estimated by the least square method, considering these r combination values. For each calculated value of r combinations, in total, there will be as many regression coefficient values as the number of r combinations of n . Next, the spatial median of the estimated regression coefficients will be calculated simultaneously. This spatial median value obtained depending on the regression coefficients will be the multiple linear regression estimation values of the MTSE method. Here, the combination count may differ depending on independent variable count and sample size. So, a certain percentage of obtained combination counts can be taken. In the literature, in the study of Dang *et al.*, (2008), the process is done by taking one percent of this combination count, and it is used as an estimator.

Let us mention some asymptotic characteristics of TSE. Firstly, Sen (1968) showed that if $x_i, i = 1, 2, \dots, n$ are known non-identical constants and F is an accumulated distribution function, TSE estimation is asymptotically normal. Wang (2005) explored asymptotic characteristics of TSE estimation on the assumption of random variable x_i and researched the strong consistency of TSE estimation and asymptotic distribution under the assumption that ε and X are independent of each other and F is arbitrary (continuous or discontinuous).

TSE satisfies two main assumptions for adaptive lasso weights: consistency and asymptotic normality. The consistency and asymptotic normality properties of TSE can be found in Peng *et al.* (2008), so the proofs are omitted.

Selection of the tuning parameters with differential evolution algorithm

In this part, we present the working scheme of the DEA and describe the tuning parameter selection process. DEA and employing steps are described in the following parts.

Differential evolution algorithm

Differential evolution algorithm (DEA) is a heuristic optimization method that can give efficient results in continuous-valued problems (Mayer *et al.*, 2005; Storn & Price, 1997). DEA is especially useful where the parameters are defined in a completely arranged space (Karaboga, 2004). Another significant superiority of DEA to other intuitional methods is that it can be encoded easily (Mayer *et al.*, 2005). There have been several studies about this from the day it was developed. Some of these studies are about improvement of the algorithm (Hrstka & Kuverova, 2004; Bergey & Ragsdale, 2005; Sun *et al.*, 2005; Becerra & Coello, 2006). Fundamentally, the working scheme of DEA is based on genetic algorithm. Crossover, mutation, and selection operators are used in DEA similar to genetic algorithm. In the optimization problem, the solution sets improve with the help of operators through iterations.

Instead of applying each operator differently to all populations respectively, chromosomes are handled one by one, and a new individual in three other randomly chosen chromosomes is obtained. During this process, mutation and crossover operators are used. The fitting of the new chromosome and the existing chromosome are compared and the better one is carried over to the next population as a new individual. In DEA, after objective function, variables and constraints are determined with the following steps.

Encoding and initial population

The number of variables belonging to the problem determines the size of chromosomes and this is expressed with D . NP represents the chromosome number determined by the user. NP should be selected as more than three because at least three are required to produce new chromosomes, other than the existing ones. In the starting phase, the initial population is produced, which consists of the number NP of D sized chromosome (Karaboga, 2004).

Mutation

In DEA, except for the chromosome used in mutation, three chromosomes are selected which are different from each other. The difference value of first two selected chromosomes is calculated. Then, this difference chromosome is multiplied by the F parameter. The F parameter is selected usually between 0 and 2. As a result, the weighted difference chromosome is added to the third

selected chromosome. At the end of the mutation phase, the current chromosomes are constructed, which will be used in the crossover phase.

Crossover

In the crossover phase, the trial chromosome, $(u_{i,G+1})$, is produced as a candidate for the new generation by using the difference chromosome obtained through mutation and the previous chromosome, $x_{i,G}$. Each gene belonging to the trial chromosome is chosen with probability CR from the difference chromosome and with probability $1-CR$ from the current chromosome. If the random number, which is generated between 0 and 1, is less than CR , the gene is selected from $n_{j,i,G+1}$ or from the current chromosome. The aim is taking the gene from the new difference chromosome with a pre-determined rate.

Fitness function

A new trial chromosome is obtained by using three different chromosomes with mutation and crossover operators. The criterion for determining the chromosome, which will pass to the new generation ($G = G + 1$), is the fitness values. In this stage, the one which is going to be calculated is the fitness value of $(u_{i,G+1})$. The value of the chromosome is calculated by entering u_j values belonging to the target chromosome $(u_{i,G+1})$.

Selection

The new generation is created by evaluating the existing generation and newly produced chromosomes, with the selection operator. The existence probability of the new chromosomes is related to the fitness values. In DEA, due to the comparisons being made one-to-one, complicated selection processes are not necessary. The chromosome with better fitting relative to compared chromosomes is presented as an individual of new generation.

Ending of algorithm

The main aim in DEA is to obtain chromosomes which have always better fitness values, so the solutions approximate to optimum. This cycle needs to be kept up until equation $G = G_{max}$ is met. As an ending criterion of the algorithm, the difference between the best and the worst fitting value in the population can be determined, as it will be a very small number such as 10^{-6} (Ali & Törn, 2004). For more detail, see Keskinürk (2006).

In our study, the purpose is to find the optimal λ , the tuning parameter value in adaptive lasso. With the scheme mentioned above, DEA is employed to obtain the optimal tuning parameter. The fitness function is the Bayesian information (BIC)

$$BIC = -2LL(M_{adlaso}) + m \log(n) \quad \dots(6)$$

where $LL(M_{adlaso})$ indicates the log-likelihood of the adaptive lasso model, 'n' shows sample size, and 'm' shows the number of included predictor variables (Schwarz, 1978). The usage of DEA for selecting the optimal tuning parameter for adaptive lasso is given in Figure 1.

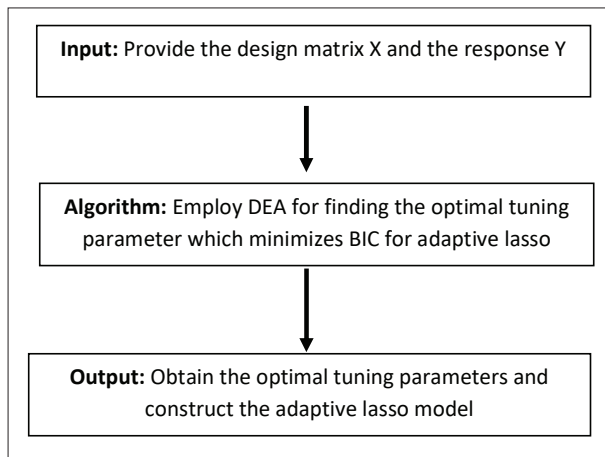


Figure 1: The working scheme of DEA for tuning parameter selection in adaptive lasso

NUMERICAL STUDIES

We conducted some numerical studies with Monte Carlo simulations and two real dataset examples. We measured the correct and incorrect identifications of zero and non-zero coefficients in simulations. In the real dataset examples, we checked the prediction accuracies of the models and sparseness of the regression coefficients. The datasets are compatible for our aims which consist of heavy-tailed errors. All implementations were performed in R software (R Core Team, 2017). Adaptive lasso models were estimated with 'glmnet' and 'sealasso' packages (Friedman *et al.*, 2010; Qian, 2013).

Monte Carlo simulations

We performed a Monte Carlo simulation study to evaluate the efficiency of the Theil-Sen approach (THEIL). To compare the performance of TSE, we employed three techniques: ordinary least squares (OLS), standard error adjusted lasso (SEA-lasso), and NSEA-lasso (Qian & Yang, 2013). The SEA-lasso and NSEA-lasso methods estimate the adaptive lasso model using the standard errors of the regression coefficients. The detailed description of these two algorithms can be found in Qian and Yang (2013).

The simulation design was constructed similar to McDonald and Galarneau (1975). We generated the datasets by taking account of heavy-tailed errors. Simulation settings include three models, and these models consist of $p = 5, 10, 15$ predictors. Predictor variables were generated such that $X_k \sim N(0, 1)$, $k = 1, 2, \dots, p$. The correlation structure was selected similar to McDonald and Galarneau (1975), as the following:

$$X_{ij} = \sqrt{1 - \alpha^2} z_{ij} + \alpha z_{ip}, \quad i = 1, 2, \dots, n, \quad j = 1, 2, \dots, p \quad \dots(7)$$

where $z \sim N(0, 1)$ and α is a control parameter for the degree of multicollinearity. In all cases, we fix $\alpha = 0.50$ so as not to account high correlation. Four models are considered with different numbers of variables and beta coefficients. The following model structures are given:

- (i) $\beta = (10, 0, 0, 0)$ (ii) $\beta = (20, 20, 0, 0)$
- (iii) $\beta = (30, 0, 0, 0, 0, 0)$ (iv) $\beta = (40, 40, 40, 0, 0, 0)$

Simulation designs include heavy-tailed errors. The error term is settled in the models with t-distributions as follows:

$$Y = X\beta + \varepsilon \quad \dots(8)$$

where $\varepsilon \sim t(u)$ with two different degrees of freedoms (df) $u = 1, 3$. These values are appropriate for illustrating the heavy-tailed errors in regression models. The prediction accuracies are evaluated with mean average errors (MAE) as the following:

$$MAE. ERR = \sum_{i=1}^n \left| \frac{Y - \hat{Y}}{Y} \right| \quad \dots(9)$$

where \hat{Y} indicates the predicted values. The difference between the true and estimated beta coefficients are measured using

$$MAE.BETA = \sum_{i=1}^n \left| \frac{\beta^{true} - \beta^{est}}{\beta^{true}} \right| \dots(10)$$

where β^{true} shows the true beta coefficients and β^{est} shows the estimated values. In simulation results, ‘C’ represents the percentage of correctly excluded redundant variables and ‘I’ represents the percentage of incorrectly excluded necessary variables. Based on this representation, a simulation result is considered as successful for higher ‘C’ and lower ‘I’ values for the relevant estimator. The sample size is $n = 50, 100, 500$ and the number of runs is fixed as 100.

We reported the simulation results in Tables 1, 2, 3, and 4 for each coefficient vector. It is seen that TSE produces lower error values when comparing with OLS, SEA and NSEA. TSE is clearly superior to each estimator in adaptive lasso. Especially, TSE provides distinctive results while keeping the relevant variables in the adaptive lasso model so ‘I’ values are lower for TSE. Almost in all cases, TSE can identify the true zeros more successfully. TSE does not fall into trap of identifying non-zero coefficients wrongly as much as OLS, SEA and NSEA. Clearly, the distinction becomes visible when heavy tailed errors are dominant with $df = 1$. All the methods can perform well for $df = 3$ but the error of

Table 1: Simulation results for the first simulation design

n	Method	df = 1				df = 3			
		C	I	MAE.PRED	MAE.BETA	C	I	MAE.PRED	MAE.BETA
50	OLS	96.66667	24	2.88193	1.38816	100	0	0.80793	0.06559
	TSE	98.33333	1	2.77776	0.90512	100	0	0.80580	0.06535
	SEA	97	24	2.87251	1.37146	100	0	0.80823	0.06578
	NSEA	97	24	2.87374	1.37714	100	0	0.80790	0.06579
100	OLS	97	26	7.94813	2.86781	100	0	0.82572	0.04784
	TSE	98.66667	2	7.58659	2.33777	100	0	0.82496	0.04753
	SEA	96.33333	26	7.96082	2.81579	100	0	0.82571	0.04787
	NSEA	96.66667	26	7.93016	2.84215	100	0	0.82573	0.04784
500	OLS	96.66667	21	4.18052	1.02275	100	0	0.89192	0.02366
	TSE	97.33333	0	3.70729	0.84695	100	0	0.89171	0.02393
	SEA	96.66667	21	4.18416	1.02505	100	0	0.89192	0.02366
	NSEA	96.33333	21	4.18663	1.02250	100	0	0.89192	0.02366

Table 2: Simulation results for the second simulation design

n	Method	df = 1				df = 3			
		C	I	MAE.PRED	MAE.BETA	C	I	MAE.PRED	MAE.BETA
50	OLS	98.50000	6.50000	4.76758	9.59747	100	0	0.33313	0.13234
	TSE	98.50000	0.50000	4.87711	10.01887	100	0	0.33290	0.12936
	SEA	98.50000	7	4.80389	9.61851	100	0	0.33302	0.13279
	NSEA	98.50000	7	4.81359	9.61466	100	0	0.33298	0.13218
100	OLS	97.50000	13.50000	2.10379	2.19424	100	0	0.37776	0.08206
	TSE	98.50000	1	2.38788	1.45866	100	0	0.37740	0.08410
	SEA	97.00000	13.50000	2.13894	2.17986	100	0	0.37609	0.08234
	NSEA	97.00000	13.50000	2.13756	2.18251	100	0	0.37611	0.08230
500	OLS	96.00000	12	5.29656	10.49660	100	0	0.43585	0.04034
	TSE	99.00000	0.50000	5.22106	9.44882	100	0	0.43586	0.04047
	SEA	96.00000	12.00000	5.29905	10.49529	100	0	0.43580	0.04034
	NSEA	96.00000	11.50000	5.30284	10.46473	100	0	0.43581	0.04034

Table 3: Simulation results for the third simulation design

N	Method	df = 1				df = 3			
		C	I	MAE.PRED	MAE.BETA	C	I	MAE.PRED	MAE.BETA
50	OLS	97.60000	2	8.78802	5.25607	100	0	0.19078	0.03952
	TSE	98.20000	0	8.36007	4.80112	100	0	0.19077	0.04004
	SEA	97.60000	2	8.81944	5.24011	100	0	0.19076	0.03952
	NSEA	97.60000	2	8.81940	5.24408	100	0	0.19075	0.03942
100	OLS	97.60000	5	1.33447	1.19090	99.80000	0	0.38087	0.02943
	TSE	98.20000	0	1.22619	0.71966	100	0	0.38231	0.02869
	SEA	97.40000	6	1.33815	1.22553	99.80000	0	0.38087	0.02943
	NSEA	97.60000	5	1.33151	1.18611	99.80000	0	0.38087	0.02937
500	OLS	97.60000	3	1.42711	1.89066	100	0	0.30288	0.01275
	TSE	98.20000	0	1.42585	1.28176	100	0	0.30287	0.01318
	SEA	97.60000	3	1.42659	1.88826	100	0	0.30288	0.01273
	NSEA	97.60000	3	1.42674	1.88867	100	0	0.30288	0.01273

Table 4: Simulation results for the fourth simulation design

n	Method	df = 1				df = 3			
		C	I	MAE.PRED	MAE.BETA	C	I	MAE.PRED	MAE.BETA
50	OLS	98.66667	0.01667	1.23140	1.18738	100	0	0.10927	0.12188
	TSE	99.66667	0	1.16676	1.03551	100	0	0.10945	0.11721
	SEA	98.66667	0.01667	1.24083	1.21144	100	0	0.10862	0.12225
	NSEA	98.66667	0.01667	1.23637	1.20414	100	0	0.10859	0.12201
100	OLS	99.33333	0.02333	1.84601	1.24895	100	0	0.12763	0.07688
	TSE	100	0.00333	1.79133	0.75646	100	0	0.12778	0.07566
	SEA	99.33333	0.02333	2.09537	1.24958	100	0	0.12756	0.07686
	NSEA	99.33333	0.02333	2.04209	1.24971	100	0	0.12756	0.07674
500	OLS	99.66667	0.03000	0.60514	1.52497	100	0	0.16789	0.03883
	TSE	100	0	0.58041	0.61665	100	0	0.16787	0.03859
	SEA	99.66667	0.03000	0.60765	1.52754	100	0	0.16797	0.03890
	NSEA	99.66667	0.03000	0.60741	1.52692	100	0	0.16796	0.03889

the coefficients was estimated better with TSE. From the above results, the chosen weights with TSE obviously improve the correctness of the estimated adaptive lasso model.

Real dataset examples

In this part, we have analysed some real datasets to evaluate the predictive performances of estimators. Meanwhile we presented the sparsity of the regression coefficients. For the application we used Alcohol and

Boston datasets which are available in R software, ‘MASS’ and ‘robustbase’ packages (Venables & Ripley, 2002; Maechler *et al.*, 2016). These datasets contain heavy-tailed errors, so the real datasets are conformable for the computations. The Alcohol dataset contains 44 observations and 6 independent variables. This dataset represents the physicochemical characteristics of 44 aliphatic alcohols. The purpose is to predict the solubility of the alcohols. The Boston dataset consists of 506 observations and 13 explanatory variables. This dataset is related to the housing values in the suburbs of Boston.

The aim of Boston dataset is to predict the crime rates by town.

Predictive performance is measured by cross validation technique. The datasets are divided into two parts as ‘test-train.’ Train sets contain 80% and test sets contain 20% of the data, respectively.

Table 5: Regression coefficients for Alcohol dataset

Regressor	OLS	TSE	SEA	NSEA
SAG	0	0	0	0
V	0	-0.01365	0	0
logPC	-1.07144	-1.42559	-1.23636	0
P	0	0	0	-0.67092
RM	-0.17295	0	-0.15721	0
Mass	0	0	0	0

Table 6: Regression coefficients for Boston dataset

Regressor	OLS	TSE	SEA	NSEA
Ht	0	0	0	0.00948
Wt	1.09996	1.08407	0.79137	1.10635
LBM	-1.24933	-1.22963	-0.92578	-1.26896
RCC	0	0	0	0
WCC	0	0	0	0
Hc	0	0	0	0
Hg	-0.13658	-0.24795	0	0
Ferr	0	0	0	0
BMI	0	0.01639	0	0
SSF	0	0	0.05241	0

Table 7: Predictive performance results

Method	AIS-Error	Alcohol-Error
OLS	0.06430	0.25919
TSE	0.06337	0.15656
SEA	0.06922	0.26448
NSEA	0.06861	0.23996

The regression coefficients are shown for each weighting method in Tables 5 and 6. It is seen that there is not much difference among the methods in terms of sparseness. The predictive performance of each approach is given in Table 7. In experimental results, TSE performs better

than OLS, SEA, and NSEA in terms of prediction for new observations. It should be pointed out that TSE accomplishes well for each dataset when used in adaptive lasso.

CONCLUSION

Adaptive lasso has become a useful alternative solution in terms of penalized regression modelling. The weights that are used in adaptive lasso have a significant effect on the regression coefficient estimates. Classical OLS and ridge estimators fail to obtain accurate parameter estimates when the regression model includes heavy-tail errors. To improve the achievement of adaptive lasso, we propose to use TSE as the weight vector. Also, we benefited from the power of heuristic optimization while finding the optimal tuning parameter. DEA is used for this task.

According to simulations studies, TSE provides more accurate parameter estimates when used as the weight in adaptive lasso. Moreover, the prediction accuracy is better than the other three weight selection approaches. One of the advantages of TSE emerged in the identification of zero and non-zero coefficients. OLS, SEA, and NSEA weight selection methods choose non-zero values as zero much more than TSE. Also, TSE is more capable of determining the zero coefficients correctly. These findings exhibit the superiority of TSE within adaptive lasso in terms of variable selection. In real dataset examples, TSE weights demonstrate preferable performance for out of sample prediction. The sparsity of regression coefficients do not differ much among weight selection approaches.

Emergence of heavy tailed errors leads to trouble, and it is hard to overcome this serious problem in regression analysis. Although robust methods provide a good way to solve this problem, there is not much research for lasso type regression methods. Within the use of lasso methods in cases with heavy tailed errors, it is possible to eliminate the redundant variables. Our proposed robust weight selection scheme gives completely successful results when using TSE and DEA within adaptive lasso. Also, our approach shows that the use of robust estimators in adaptive lasso weights significantly enhances the model selection accuracy. This result can encourage researchers to adopt different estimators for adaptive weights instead of completely changing the loss functions. Our study uncovers that the changing of the loss function is not the only way of improving the robustness of the adaptive lasso model. Even though the target function includes squared loss term, the results ameliorate heavy-tailed

errors with TSE. In our view, researchers should pay attention to this result in further studies.

Moreover, theoretical aspects of TSE satisfy the conditions of weight usage in adaptive lasso regression analysis because TSE supplies the oracle properties of consistency and asymptotic normality. Consequently, we only demonstrated the applicability of TSE with adaptive lasso and concluded the success with several numerical examples. We suggest using TSE when there are many predictors for further practical studies to accomplish model selection in the presence of heavy-tailed errors.

Conflict of Interest

All authors declared that there is no conflict of interest involved in this study.

REFERENCES

- Ali M.M. & Törn A. (2004). Population set-based global optimization algorithms: some modifications and numerical studies. *Computer and Operations Research* **31**: 1703–1725.
DOI: [https://doi.org/10.1016/S0305-0548\(03\)00116-3](https://doi.org/10.1016/S0305-0548(03)00116-3)
- Barros M., Paula G.A. & Leiva V. (2008). A new class of survival regression models with heavy-tailed errors: robustness and diagnostics. *Lifetime Data Analysis* **14**(3): 316–332.
DOI: <https://doi.org/10.1007/s10985-008-9085-1>
- Becerra R.L. & Coello C.A.C. (2006). Cultured differential evolution for constrained optimization. *Computer Methods in Applied Mechanics and Engineering* **195**(33–36): 4303–4322.
DOI: <https://doi.org/10.1016/j.cma.2005.09.006>
- Bergey P.K. & Ragsdale C. (2005). Modified differential evolution: a greedy random strategy for genetic recombination. *Omega* **33**: 255–265.
DOI: <https://doi.org/10.1016/j.omega.2004.04.009>
- Chen K. & Chan K.S. (2011). Subset ARMA selection via the adaptive Lasso. *Statistics and its Interface* **4**: 197–205.
DOI: <https://doi.org/10.4310/SII.2011.v4.n2.a14>
- Dang X., Peng H., Wang X. & Zhang H. (2008). Theil-Sen estimators in a multiple linear regression model. Available at <https://citeseerx.ist.psu.edu/viewdoc/summary?doi=10.1.1.508.3461>
- Dietz E.J. (1989). Teaching regression in a nonparametric statistics course. *The American Statistician* **43**: 35–40
DOI: <https://doi.org/10.1080/00031305.1989.10475606>
- Fan J., Fan Y. & Barut E. (2014). Adaptive robust variable selection. *Annals of Statistics* **42**(1): 324.
DOI: <https://doi.org/10.1214/13-AOS1191>
- Foster J.C., Taylor J.M. & Nan B. (2013). Variable selection in monotone single-index models via the adaptive LASSO. *Statistics in Medicine* **32**(22): 3944–3954.
DOI: <https://doi.org/10.1002/sim.5834>
- Friedman J., Hastie T. & Tibshirani R. (2010). Regularization paths for generalized linear models via coordinate descent. *Journal of Statistical Software* **33**(1): 1–22.
DOI: <https://doi.org/10.18637/jss.v033.i01>
- Honda T. (2013). Nonparametric quantile regression with heavy-tailed and strongly dependent errors. *Annals of the Institute of Statistical Mathematics* **65**(1): 23–47.
DOI: <https://doi.org/10.1007/s10463-012-0359-8>
- Hrstka O. & Kucerova A. (2004). Improvements of real coded genetic algorithms based on differential operators preventing premature convergence. *Advances in Engineering Software* **35**: 237–246.
DOI: [https://doi.org/10.1016/S0965-9978\(03\)00113-3](https://doi.org/10.1016/S0965-9978(03)00113-3)
- Huang J., Ma S. & Zhang C.H. (2008). Adaptive Lasso for sparse high-dimensional regression models. *Statistica Sinica* **18**(4): 1603–1618.
- Hui F.K., Warton D.I. & Foster S.D. (2015). Tuning parameter selection for the adaptive lasso using ERIC. *Journal of the American Statistical Association* **110**(509): 262–269.
DOI: <https://doi.org/10.1080/01621459.2014.951444>
- Hussain S.S. & Sprent P. (1983). Non-parametric regression. *Journal of the Royal Statistical Society: Series A (General)* **146**(2): 182–191.
DOI: <https://doi.org/10.2307/2982016>
- Karaboga D. (2004). *Artificial Intelligence Optimization Algorithms*. Atlas Release Publication, İstanbul, Turkey.
- Keskintürk T. (2006). Differential development algorithm. *Istanbul Commerce University Journal of Science* **5**(9): 85–99.
- Lacroix L.S. & Zwald L. (2011). Robust regression through the Huber’s criterion and adaptive lasso penalty. *Electronic Journal of Statistics* **5**: 1015–1053.
DOI: <https://doi.org/10.1214/11-EJS635>
- Li Q. & Wang L. (2020). Robust change point detection method via adaptive LAD-LASSO. *Statistical Papers* **61**(1): 109–121.
DOI: <https://doi.org/10.1007/s00362-017-0927-3>
- Lu W., Goldberg Y. & Fine J.P. (2012). On the robustness of the adaptive lasso to model misspecification. *Biometrika* **99**(3): 717–731.
DOI: <https://doi.org/10.1093/biomet/ass027>
- Machkour J., Muma M., Alt B. & Zoubir A.M. (2020). A robust adaptive Lasso estimator for the independent contamination model. *Signal Processing* **174**: 107608.
DOI: <https://doi.org/10.1016/j.sigpro.2020.107608>
- Maechler M., Rousseeuw P., Croux C., Todorov V., Ruckstuhl A., Salibian-Barrera M., Verbeke T., Koller M., Conceicao E.L.T. & Palma M.A. (2016). robustbase: Basic robust statistics r package version 0.92-7. Available at <http://CRAN.R-project.org/package=robustbase>
- Maritz J.S. (1979). On Theil’s method in distribution-free regression. *Australian Journal of Statistics* **21**(1): 30–35.
DOI: <https://doi.org/10.1111/j.1467-842X.1979.tb01116.x>
- Mayer D.G., Kinghorn B.P. & Archer A.A. (2005). Differential

- evolution – an easy and efficient evolutionary algorithm for model optimization. *Agricultural Systems* **83**: 315–328.
DOI: <https://doi.org/10.1016/j.agry.2004.05.002>
- McDonald G.C. & Galarneau D.I. (1975). A Monte Carlo evaluation of some ridge-type estimators. *Journal of the American Statistical Association* **70**(350): 407–416.
DOI: <https://doi.org/10.1080/01621459.1975.10479882>
- Oja H. & Niinimaa A. (1984). *On Robust Estimation of Regression Coefficients, Research Report*. Department of Applied Mathematics and Statistics, University of Oulu, Finland.
- Peng H., Wang S. & Wang X. (2008). Consistency and asymptotic distribution of the Theil-Sen estimator. *Journal of Statistical Planning and Inference* **138**: 1836–1850.
DOI: <https://doi.org/10.1016/j.jspi.2007.06.036>
- Qian W. (2013). sealasso: Standard error adjusted adaptive lasso. R package version 0.1-2. Available at <https://CRAN.R-project.org/package=sealasso>
- Qian W. & Yang Y. (2013). Model selection via standard error adjusted adaptive lasso. *Annals of the Institute of Statistical Mathematics* **65**(2): 295–318.
DOI: <https://doi.org/10.1007/s10463-012-0370-0>
- R Core Team (2017). R: a language and environment for statistical computing. R foundation for statistical computing, Vienna, Austria. Available at <https://www.R-project.org/>
- Rao K.S.M. & Gore A.P. (1982). Nonparametric tests for intercept in linear regression problems. *Australian Journal of Statistics* **24**(1): 42–50.
DOI: <https://doi.org/10.1111/j.1467-842X.1982.tb00806.x>
- Ren Y. & Zhang X. (2013). Model selection for vector autoregressive processes via adaptive lasso. *Communications in Statistics-Theory and Methods* **42**(13): 2423–2436.
DOI: <https://doi.org/10.1080/03610926.2011.611317>
- Schwarz G. (1978). Estimating the dimension of a model. *The Annals of Statistics* **6**(2): 461–464.
DOI: <https://doi.org/10.1214/aos/1176344136>
- Sen P.K. (1968). Estimates of the regression coefficient based on Kendall's tau. *Journal of the American Statistical Association* **63**(324): 1379–1389.
DOI: <https://doi.org/10.1080/01621459.1968.10480934>
- Small C. (1990). A survey of multidimensional medians. *International Statistical Review/Revue Internationale de Statistique* **58**: 263–277.
DOI: <https://doi.org/10.2307/1403809>
- Storn R. & Price K. (1997). Differential evolution—a simple and efficient heuristic for global optimization over continuous spaces. *Journal of Global Optimization* **11**(4): 341–359.
DOI: <https://doi.org/10.1023/A:1008202821328>
- Sun J., Zhang Q. & Tsang E.P.K. (2005). DE/EDA: A new evolutionary algorithm for global optimization. *Information Sciences* **169**: 249–262.
DOI: <https://doi.org/10.1016/j.ins.2004.06.009>
- Theil H. (1950). A rank-invariant method of linear and polynomial regression analysis. *Indagationes Mathematicae* **12**(85): 173.
- Venables W.N. & Ripley B.D. (2002). *Modern Applied Statistics with S*. 4th Edition. Springer, New York, USA.
DOI: <https://doi.org/10.1007/978-0-387-21706-2>
- Wang X. (2005). Asymptotic of the Theil-Sen estimator in a simple linear regression model with a random covariate. *Journal of Nonparametric Statistics* **17**: 107–120.
DOI: <https://doi.org/10.1080/1048525042000267743>
- Wang X. & Yu Q. (2005). Unbiasedness of the Theil-Sen estimator. *Nonparametric Statistics* **17**(6): 685–695.
DOI: <https://doi.org/10.1080/10485250500039452>
- Wang H., Li G. & Jiang G. (2007). Robust regression shrinkage and consistent variable selection through the LAD-Lasso. *Journal of Business and Economic Statistics* **25**(3): 347–355.
DOI: <https://doi.org/10.1198/073500106000000251>
- Wilcox R. (1998). Simulations on the Theil-Sen regression estimator with right censored data. *Statistics and Probability Letters* **39**(1): 43–47.
DOI: [https://doi.org/10.1016/S0167-7152\(98\)00022-4](https://doi.org/10.1016/S0167-7152(98)00022-4)
- Yoon Y.J., Lee S. & Lee T. (2017). Adaptive lasso for linear regression models with ARMA-GARCH errors. *Communications in Statistics-Simulation and Computation* **46**(5): 3479–3490.
- Zhang C. & Xiang Y. (2015). On the oracle property of adaptive group Lasso in high-dimensional linear models. *Statistical Papers* **57**(1): 249–265.
DOI: <https://doi.org/10.1007/s00362-015-0684-0>
- Zhou W. & Serfling R. (2008). Multivariate spatial U-quantiles: A Bahadur-Kiefer representation, a Theil-Sen estimator for multiple regression, and a robust dispersion estimator. *Journal of Statistical Planning and Inference* **138**(6): 1660–1678.
DOI: <https://doi.org/10.1016/j.jspi.2007.05.043>
- Zhou Z. & Wu W.B. (2011). On linear models with long memory and heavy-tailed errors. *Journal of Multivariate Analysis* **102**(2): 349–362.
DOI: <https://doi.org/10.1016/j.jmva.2010.09.009>
- Zou H. (2006). The adaptive lasso and its oracle properties. *Journal of the American Statistical Association* **101**(476): 1418–1429.
DOI: <https://doi.org/10.1198/016214506000000735>

RESEARCH ARTICLE

Geotechnical engineering

Stability analysis of a partially saturated layered soil formation associated with shallow landslides

SC Walpita^{1*}, P Ratnaweera² and G WAR Fernando³

¹ Department of Civil Engineering, Faculty of Engineering and Technology, CINEC Campus, Malabe, Sri Lanka.

² Department of Civil Engineering, Faculty of Engineering Technology, The Open University of Sri Lanka, Nawala, Nugegoda, Sri Lanka.

³ Department of Physics, Faculty of Natural Sciences, The Open University of Sri Lanka, Nawala, Nugegoda, Sri Lanka.

Submitted: 17 November 2020; Revised: 04 November 2021; Accepted: 24 December 2021

Abstract: In the event of a rainfall, the contrast in hydraulic conductivity and shear strength properties of a layered soil can be significant in determining the stability of a slope. The main objectives of this study were to model 1-D infiltration into a two-layered soil formation and to understand the effect of contrast in the permeability characteristics of the two layers on failure depth, time, and mechanism, in the event of a shallow landslide. Two hypothetical soils—relatively coarse and fine soils—were assumed for the layered soil model. 1-D infiltration into a partially saturated soil was modelled through the development of a finite difference numerical scheme by solving the mixed form of Richard's equation. The stability analysis has been conducted for varying rainfall intensities and permeabilities using a pre-defined stability envelope based on the pressure head. For the case where fine soil overlies the coarse soil in a two-layered model, results showed that the failure depth is significantly reduced when the saturated permeability of coarse soil decreases relative to the fine soil. The only possible failure mechanism was identified as 'loss of suction'. When the coarse soil overlain by a fine soil, no significant effect on failure depth has been observed. Both 'loss of suction' and the development of a 'perched water table' were identified as possible mechanisms. In both cases, it was noticed that the failure time decreases as the saturated permeability of coarse soil increases. The results suggest that contrast in permeability characteristics in layered soil formations plays a vital role in influencing failure time, depth, and mechanism.

Keywords: 1-D infiltration, layered soil, numerical solutions, partially saturated soil, pressure head, shallow landslides.

INTRODUCTION

In tropical countries such as Sri Lanka, landslides are predominantly activated by persistent, high-intensity rainfall. The customary type of landslides found in the central hill country of Sri Lanka are the flow slides, which are initiated by shallow rotational or translational slides (Cooray, 1994). The soil slopes in the hill areas, which are most susceptible to slides, mainly consist of residual soil and/or colluvium deposits. In general, tropical residual soils exhibit distinct soil layering due to the effect of weathering and tend to form more or less parallel to the ground surface (Huat *et al.*, 2004). Layered soils may exhibit vertical contrast in hydraulic and shear strength properties as a result of the natural formation. In residual soils, the weathering process results in soil horizons from a particular parent source, which shows gradual or continuous vertical variations in hydraulic and mechanical properties (Rahardjo *et al.*, 2004).

In the event of a rainfall, the contrast in hydraulic conductivity and shear strength properties of layered soils can play a significant role in determining the stability of a slope. For instance, the presence of a highly conductive layer over a less conductive layer can cause a non-uniform pore water pressure profile, especially near the layer interface. Once the wetting front advances to the top of the less conductive layer, a rapid increase

* Corresponding author (walpita88@gmail.com;  <https://orcid.org/0000-0003-1387-4156>)



in pore water pressure can be expected at the interface (Srivastava & Yeh, 1991). This may lead to a sudden decrease in shear resistance which results in failure. According to Blight (1997), if the residual soil mantle is relatively shallow in comparison to the length of the slope, a planar or a transitional slide may occur, and the stability of the soil mass with a planar failure surface should be analysed as an infinite slope.

The most common method to evaluate the stability of an infinite slope with a planar failure surface is based on the principle that the slope is stable if the magnitude of the shear strength (τ_f) exceeds its shear stress (τ). The shear strength, which is the maximum shear stress the slope could withstand without undergoing failure, can be determined based on the Mohr-Coulomb criterion:

$$\tau_f = c' + \sigma' \tan \phi' \quad \dots(1)$$

Here, ϕ' , c' and σ' are the effective angle of internal friction, effective cohesion, and the effective normal stress acting on the failure surface, respectively. Shear stress (τ) depends on several factors such as the unit weight of soil, pore water pressure and the slope angle. In general, the factor of safety, F can be defined as:

$$F = \frac{c' + \sigma' \tan \phi'}{\tau} \quad \dots(2)$$

Skempton & Delory (1957) presented a simple method to determine the factor of safety, F , for an infinite planer sliding stratum with a depth L and slope angle β based on the Mohr-Coulomb failure criterion. This analysis considered the equilibrium of a soil strip element subjected to a constant water head of H . The factor of safety, F can be expressed as:

$$F = \frac{c' + (\gamma - \gamma_w H) L \cos^2 \beta \tan \phi'}{\gamma L \sin \beta \cos \beta} \quad \dots(3)$$

Here, γ and γ_w represent the unit weight of soil and unit weight of water, respectively. Equation (3) can be used to determine F for a non-cohesive soil (*i.e.*, $c' = 0$) when the water table is at ground level (*i.e.*, $H = 1$) and when the soil is completely dry (*i.e.*, $H = 0$).

Stability analysis performed based on a completely dry or a completely saturated condition can be misleading since a partially saturated soil phase exists prior to saturation. Evaporation and evapo-transpiration cause a negative potential within the partially saturated soil matrix. This phenomenon leads to a negative pore water pressure or a matric suction. The theory of unsaturated

soil mechanics explains that matric suction enhances soil shear strength. Matric suction, which is defined as the difference between pore-air and pore-water pressure (*i.e.*, $u_a - u_w$), increases the effective stress and can be expressed according to Bishop (1959), as:

$$\sigma' = \sigma - u_a + \chi(u_a - u_w) \quad \dots(4)$$

Here, χ is an effective stress parameter.

Fredlund *et al.* (1978) have expressed the Mohr-Coulomb failure envelope for partially saturated soils using two independent stress-state variables, σ' and $(u_a - u_w)$ as:

$$\tau_f = c_t + \sigma' \tan \phi' \quad \dots(5)$$

where, total cohesion, c_t is defined as $c_t = c' + (u_a - u_w) \tan \phi^b$

The term ϕ^b represents the frictional resistance due to matric suction. Fredlund *et al.* (1996) proposed the shear strength equation of unsaturated soil shown in equation (6), where Θ is normalized volumetric water content, and R is an unknown fitting parameter used to determine the best-fit failure envelope with the experimental data.

$$\tau = c' + (\sigma_n - u_a) \tan \phi' + (u_a - u_w) \Theta^R \tan \phi' \quad \dots(6)$$

Equation (6) is a modification of equation (5), where the term ϕ^b is expressed as a function of Θ and ϕ . Fredlund *et al.* (1996) suggested that $R = 1.0$ is a satisfactory prediction for a sandy soil, but R tends to increase with the plasticity of soils. To evaluate ϕ^b , the shear strength contributions due to effective cohesion [$c' + (u_a - u_w) \Theta^R \tan \phi'$] can be plotted against matric suction. Plots between matric suction and shear strength at failure can be fitted based on three different approaches such as the linear envelope, second order polynomial, and that of Vanapalli *et al.* (1996). Kankanamge *et al.*, (2018) conducted suction-monitored direct shear tests on compacted samples of residual soils in Sri Lanka (shear parameters $c' = 8.3$ kPa & $\phi' = 32^\circ$), and determined a constant angle of $\phi^b = 11.8^\circ$. It was also shown that the linear envelope model could be used for the matric suctions ranging from 0 to 100 kPa.

When water infiltrates, the matric suction is gradually reduced, causing a reduction in the effective stress and hence the shear strength. Such a loss in shear strength may be sufficient to trigger certain shallow landslides (Fourie *et al.*, 1999; Godt *et al.*, 2009). The modified factor of safety, F , can be expressed as:

$$F = \frac{c' + (u_a - u_w) \tan \phi^b + (\gamma - \gamma_w H) L \cos^2 \beta \tan \phi'}{\gamma L \sin \beta \cos \beta} \quad \dots(7)$$

Even with these developments, the hydrological mechanisms causing failure in shallow slides are not yet completely understood (Meisina *et al.*, 2019). All failures cannot be attributed to one particular mechanism. Brönnimann (2011) postulates that failure mechanisms are predominantly due to an increase in the positive pore water pressure or due to loss of suction. The phenomenon of positive pore water pressure can be further classified into two types: a) due to the development of a perched water table when saturation occurs from the top of the stratum, and b) due to the upsurge of the groundwater table. Therefore, it is evident that the pressure head profile during the critical period of an infiltration event is paramount in determining the failure mechanism.

Collins and Znidarcic (2004) proposed a coupled formulation for an infinite slope analysis considering the effect of negative and positive pressure heads. This method pre-emptly the time and critical depth of failure in relationship to the soil shear strength and rainfall parameters. Even though a soil slice can be treated as a one-dimensional soil column under rainwater infiltration, the effect of lateral seepage is also considered in this analysis to account for the slope angle. The formulation uses an approach which expresses the total forces acting on the part of the slice behind the wetting front as the sum of the effect of buoyant unit weight and seepage force. According to Collins and Znidarcic (2004), the stability equation can be given in the form of a critical depth of failure (d_{cr}), as shown in equation (8). Here h_c represent the negative pressure head which can be encountered in the unsaturated phase, while h_p stands for the positive pressure head, which develops after saturation. This equation indicates that for any pressure head value ranging from negative to positive, there exists a critical depth at which a failure could occur. If these conditions (pressure head value and respective depth) are satisfied for a particular slope during rainwater infiltration, failure can be expected. The application of this equation is further elaborated in the explanation associated with Figure 4.

$$d_{cr} = \frac{c' + (\gamma_w h_c \tan \phi^b - \gamma_w h_p \tan \phi')}{\gamma \cos^2 \beta (\tan \beta - \tan \phi')} \quad \dots(8)$$

As indicated in equations (7) and (8), rainwater infiltration in an unsaturated soil plays a vital role in determining the factor of safety of a particular slope. Therefore, it is imperative to gain an understanding of saturated and unsaturated flow through soil for an

accurate assessment. Richards' equation (1931) is widely used to represent fluid flow through a partially saturated soil. This equation can be expressed in three different forms.

$$\frac{d\theta}{dh} \frac{\partial h}{\partial t} = \frac{\partial k}{\partial z} \frac{\partial h}{\partial z} + k \frac{\partial^2 h}{\partial z^2} - \frac{\partial k}{\partial z} \quad \dots(9)$$

This is the pressure head based form, explained as above

$$\frac{\partial \theta}{\partial t} = \frac{\partial D}{\partial z} \frac{\partial \theta}{\partial z} + D \frac{\partial^2 \theta}{\partial z^2} - \frac{\partial k}{\partial z} \quad \dots(10)$$

This form expresses in terms of the volumetric water content based, as explained above.

$$\frac{\partial \theta}{\partial t} = \frac{\partial k}{\partial z} \frac{\partial h}{\partial z} + k \frac{\partial^2 h}{\partial z^2} - \frac{\partial k}{\partial z} \quad \dots(11)$$

This is the mixed form, also explained as above. In equations 9, 10 and 11, t represents time, z is the spatial dimension, k is the unsaturated coefficient of permeability, θ is the volumetric water content, D is the unsaturated diffusivity, and h is the pressure head.

Due to the nonlinear nature of these equations, obtaining analytical solutions is not possible except for a few specific cases. In general, numerical techniques such as the Finite Difference Method and/or the Finite Element Method can be used to obtain a solution. Out of the three different forms of Richards' equation, the mixed form equation can be considered the most suitable for numerical modelling due to stability in numerical convergence and conservation of mass. Considering conservation of mass does not guarantee an accurate outcome since within an element of the FEM formulation, oscillatory solutions may be generated. This, however, does not occur in the finite difference formulation due to the diagonalization of the time matrix (Celia *et al.*, 1990).

The soil-water characteristic curve (SWCC) is a graphical illustration of the relationship that exists between the amount of water held within the soil pores and the applied matric suction (Fredlund, 2006). The accuracy of the SWCC enables accurate prediction of change in parameters θ and k with h , when used with Richards' equation. Figure 1 represents a typical SWCC with its significant parameters. The matric suction value at which air begins to displace the water in the largest pores of the soil mass is the air entry value. The residual volumetric water content θ_r represents the volumetric water content of a soil at which no further increase in suction causes a significant change in water content.

The saturated volumetric water content θ_s is indicative of the maximum water storage capacity of the soil. A relationship similar to Figure 1 can be observed for a plot between matric suction and the coefficient of permeability. Soil obtains its maximum value of the coefficient of permeability at saturation, and this tends to decrease as the matric suction increases.

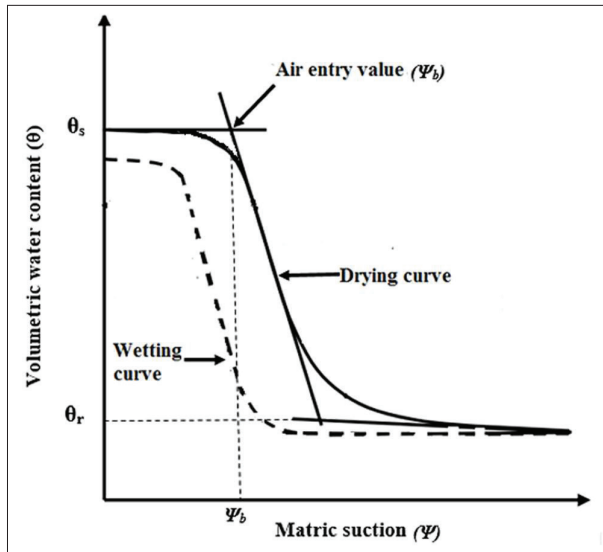


Figure 1: Typical soil water characteristic curve

Typical lab testing for the SWCC provides only a drying curve. The SWCC commonly reported in the literature is the drying curve rather than the wetting curve. This change in behaviour of the drying path and the wetting path is known as hysteresis. However, as the soil undergoes several wetting and drying cycles, this hysteresis effect becomes more and more insignificant. Natural soils have undergone numerous wetting and drying cycles, and therefore SWCC should be expected to fall within the two boundary curves.

According to Hillel (1998), the volumetric water content of a sandy soil decreases more sharply with the increasing matric suction compared to a clayey soil. Much greater steepness of the quasi-linear portion of the curve can be observed for a sandy soil when compared to a clayey soil. This is attributed to the difference in pore sizes and pore size distribution in the two soils. As defined by Fredlund *et al.* (1994), the air entry value is the matric suction value that must be exceeded before air recedes into the soil pores. The larger the air entry value, the higher the water retention ability at a given matric

suction of a soil. In general, clayey soils exhibit greater air entry values compared to sandy soils.

According to the model proposed by Brooks and Corey (1964), the effective degree of saturation of a soil can be expressed as

$$S = \left(\frac{\psi_b}{\psi}\right)^\lambda \quad \dots(12)$$

where λ is a shape parameter which expresses the steepness of the quasi-linear portion of the soil water characteristics curve. When the λ value gets smaller, the steepness of the curve tends to decrease. In principle, fine-grained soil possesses a smaller λ value compared to coarse-grained soil. With the inclusion of saturated permeability (k_s), the coefficient of permeability (k) of a given soil can be expressed, according to Brooks and Corey (1964), as

$$k = k_s S^{(3+\frac{2}{\lambda})} \quad \dots(13)$$

Numerical solutions of modelled rainwater infiltration in unsaturated soils have been presented by researchers considering boundary conditions, the effect of multiple soil layers, different geometries, and varying rainfall conditions. For infinite slope analysis, the numerical solutions can be obtained using one-dimensional (1-D) infiltration. The 1-D model uses a soil column with vertical infiltration, which ignores the slope inclination and lateral seepage flow while taking the effect of ponding into account. When 1-D infiltration is to be adopted for an infinite slope analysis, the effect of ponding should be ignored due to the action of runoff. In a slope stability analysis, the 2-D model is capable of handling both slope inclination and lateral seepage flow, which is advantageous when special variability and soil inhomogeneity exist in the lateral direction. However, in the infinite slope theory, the soil is assumed to be homogeneous and isotropic, and therefore the 1-D model is adequate in analysing infinite slopes.

Many researchers have investigated slope instabilities using 1-D infiltration incorporated into an infinite slope model. Godt *et al.* (2012) conducted an infinite slope analysis for partially saturated soils using 1-D transient infiltration model and found that the depth and time of the potential slope failure depend on the soil water characteristics of the slope material. Zhan *et al.* (2013) analysed shallow slope failures in response to layered soil formations and concluded that slope angle, depth of least permeable layer, and rainfall intensity are significantly contribute to slope instability. According

to the study conducted by Santoso *et al.* (2011) on a spatially variable slope in the depth direction, it was concluded that the failure probability values indicated by 1-D infiltration are much higher than those of 2-D analysis of the same slope. Also, it was observed that slope inclination and lateral flow have no significant impact on failure. By the equation (8) (as proposed by Collins and Znidarcic, 2004), the effect of lateral seepage force was also incorporated in the infinite slope analysis, which can be coupled with the 1-D infiltration analysis to obtain a critical failure depth of the slope.

In this particular study, the behaviour of 1-D infiltration into the simplest form of two-layered soil formation is being modelled, and attempts to understand the effect of contrast in the permeability characteristics of the two layers on failure depth, time, and mechanism.

MATERIALS AND METHODS

Stability model

In residual soil formations, different weathering grades and colluvium deposits may cause a layered soil profile with varying permeability characteristics. In order to understand the influence of varying permeability characteristics on failure mechanism, a hypothetical two-layered soil model was considered with the thickness of each layer set to 2m. The groundwater table was set at a depth of 4m from the ground surface. The saturated coefficient of permeabilities of the top layer and bottom layer were denoted as k_{s1} and k_{s2} , respectively. The following arrangements of two layers were considered using the two hypothetical soils, which exhibit coarse and fine characteristics.

- i. Case A: fine soil overlain by the coarse soil ($k_{s1} < k_{s2}$)
- ii. Case B: coarse soil overlain by the fine soil ($k_{s1} > k_{s2}$)

The above model was introduced with a varying rainfall intensity (I) at the top. Since the topsoil layer always controls the infiltration, the scenario of $I > k_{s1}$ was omitted, as the excess water will result in a runoff (no ponding). All the other possible scenarios, namely, $I = k_{s1} < k_{s2}$, $I < k_{s1} < k_{s2}$, $I < k_{s2} < k_{s1}$, and $k_{s2} < I < k_{s1}$, were analysed in this study.

Infiltration analysis

In a partially saturated soil, matric suction may cause permeability to be less than its saturated permeability. Richards' mixed form equation (11) for one-dimensional

unsaturated flow (Richards, 1931) was used in this analysis to model the behaviour of infiltration. Therefore, a finite difference numerical scheme was developed by solving Richards' equation and programmed using MATLAB software.

By Euler's backward finite difference approximation, the discretized version of Richards' mixed form equation can be written as

$$\frac{\theta_j^{t+\Delta t} - \theta_j^t}{\Delta t} - \frac{k_{j+\frac{1}{2}}^{t+\Delta t} - k_{j-\frac{1}{2}}^{t+\Delta t}}{\Delta z} + \left[k_{j+\frac{1}{2}}^{t+\Delta t} * \frac{h_{j+1}^{t+\Delta t} - h_j^{t+\Delta t}}{\Delta z} - k_{j-\frac{1}{2}}^{t+\Delta t} * \frac{h_{j+1}^{t+\Delta t} - h_j^{t+\Delta t}}{\Delta z} \right] = 0 \quad \dots(14)$$

Where, j is the spatial node at time stage t , Δz is the spatial discretization, Δt is the time step.

By introducing an iteration level 'm' such as

$$h_j^{t+\Delta t, m+1} = h_j^{t+\Delta t, m} + \Delta h_j^{t+\Delta t, m+1} \quad \dots(15)$$

The equation (14) can be rewritten as a tridiagonal system of linear equations

$$A * \Delta h_{j-1}^{t+\Delta t, m+1} + B * \Delta h_j^{t+\Delta t, m+1} + C * \Delta h_{j+1}^{t+\Delta t, m+1} = E \quad \dots(16)$$

Here, A , B , C , and E are the respective coefficients of the linearized form after rearrangement. By solving the system of linear equations for $\Delta h_j^{t+\Delta t, m+1}$, the Picard iteration is set to continue until convergence is obtained for a pre-defined error (ϵ).

$$\text{maximum } |\Delta h_j^{t+\Delta t, m+1}| < \epsilon \quad \dots(17)$$

Once the convergence criterion has been satisfied, the pressure head value is updated as shown in equation (15), before moving to the next time step.

Table 1 shows the Brooks and Corey parameters selected for the hypothetical soils (relatively coarse soil and fine soil). In terms of classification, the two soils can be approximated as a silty sand and a sandy silt, respectively. Figures 2 and 3 represent the permeability characteristics of the two soils.

Table 1: Assumed Brooks and Corey parameters for hypothetical soils

Fine soil	Coarse soil
$\theta_s = 0.45 \text{ (m}^3/\text{m}^3\text{)}$	$\theta_s = 0.35 \text{ (m}^3/\text{m}^3\text{)}$
$\theta_r = 0.20 \text{ (m}^3/\text{m}^3\text{)}$	$\theta_r = 0.05 \text{ (m}^3/\text{m}^3\text{)}$
$\lambda = 0.2$	$\lambda = 0.5$
$\Psi_b = 1 \text{ kPa}$	$\Psi_b = 10 \text{ kPa}$

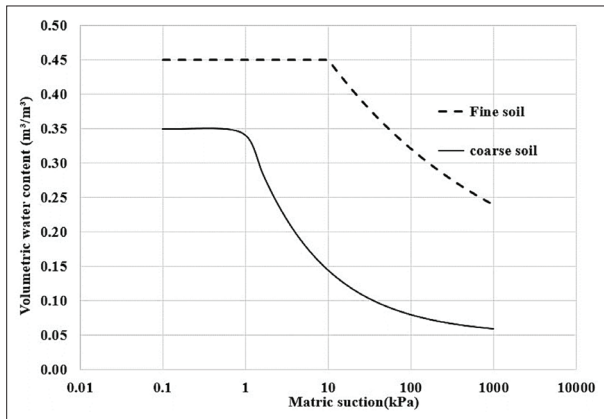


Figure 2: Soil water characteristic curves for hypothetical soils

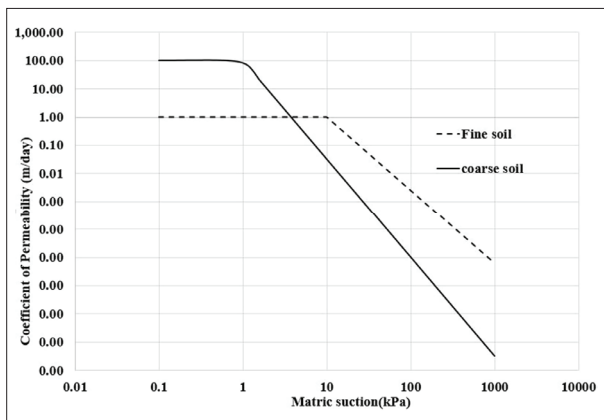


Figure 3: Coefficient of permeability curves for hypothetical soils when saturated permeability of fine soil is 1 m/day, and saturated permeability of coarse soil is 100 m/day

Stability analysis

The effective shear strength parameters for the two hypothetical soils were assumed as $c' = 10 \text{ kPa}$ and $\phi' = 20^\circ$ for fine soil and $c' = 3 \text{ kPa}$ and $\phi' = 35^\circ$ for coarse soil. The angle of frictional resistance due to matric suction (ϕ^b) has been determined using the linear envelope model, with the R value equal to one. For fine soil and coarse soil, it was calculated as 13.5° and 5° , respectively.

Throughout the analysis, the saturated permeability of fine soil was maintained at a constant value of 1 m/d, while different saturated permeability values were adopted for coarse soil. This analysis uses different permeability characteristics to represent the two layered formations and intends to study its effect on failure mechanism, failure depth and time.

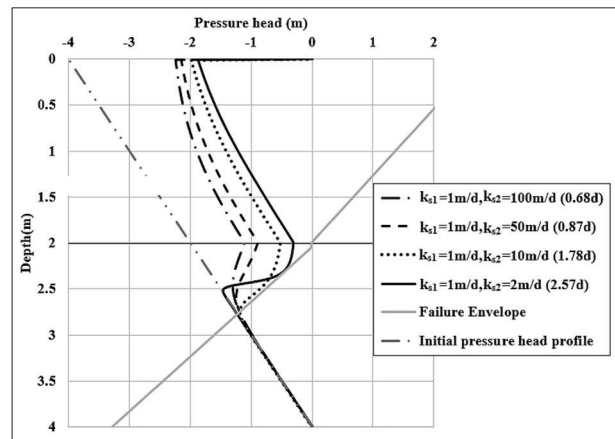


Figure 4: Stability analysis for case 1 ($I = 0.1 \text{ m/day}$)

The failure envelope was generated based on Equation 8, with relevant shear strength parameters. Figure 4 shows the failure envelope generated for the case where the coarse soil is overlain by the fine soil. In principle, any given point on the failure envelope indicates the failure depth corresponding to its pressure head. It is seen that the failure envelope moves from a positive pressure head to a negative value, with increasing depth. This shows that slope failure could occur even under a negative pressure head condition, at higher depths and this is due to an increase in the effective weight of the

sliding mass. Negative pressures at shallow depths do not trigger failure. Failure at shallow depths are associated with positive pressure conditions.

The initial pressure head profile shown in Figure 4 is based on the 'no infiltration' condition. This line represents zero hydraulic gradient and becomes a no-flow boundary condition. An infiltration-led pressure head profile can only be realized once the pressure head value at a given depth deviates from its initial boundary value. This interpretation indicates that the failure envelope plots towards the right-hand side of this no-flow boundary, which is within the zone of infiltration. The intersection between the failure envelope and the initial pressure head profile do not idealize a failure. Once infiltration takes place, the pressure head profile deviates from the initial boundary profile and intersects with the failure envelope, indicating a slope failure.

RESULTS AND DISCUSSION

Case A: $k_{s1} < k_{s2}$ (fine soil overlain by coarse soil)

When $I < k_{s1} < k_{s2}$, (Figure 4), the development of positive pore water pressure of either of the soil layer cannot be expected since the rainfall intensity is not adequate to saturate either of the two soils. As a result, the pressure head profile always lie in the negative pressure head regime. To understand the infiltration process and its effect on the variation of the pressure head, it is important to refer to Figure 3, which illustrates the behaviour of the coefficient of permeability with negative pressure. As indicated in Figure 3, the coefficient of permeability of coarse soil remains quite low compared to fine soil for almost all the negative pressure values. For fine soil, the coefficient of permeability changes more gradually compared to coarse soil. Therefore, gradual reduction of matric suction or negative pressure can be observed throughout the infiltration process. However, when the wetting front reaches coarse soil, the water tends to percolate due to a smaller coefficient of permeability. Hence, the wetting front tends to move more slowly, and significant destruction of negative pressure takes place at lower wetting depth compared to fine soil. When the saturated permeability of coarse soil (k_{s2}) is reduced, this effect tends to be enhanced, and hence the pressure head profile moves abruptly rather than gradually towards the positive pressure regime. Therefore the failure point where the stability envelope meets the pressure head profile, becomes shallower and moves closer to the boundary between the two layers as the saturated

permeability of coarse soil (k_{s2}) is reduced. The time taken for failure also tends to increase as k_{s2} reduces, and this phenomenon can be observed across all combinations belonging to case A (Table 3).

For the combination, $I = k_{s1} < k_{s2}$ (Figure 5), if the infiltration is continued, the development of positive pressure in the fine layer can be expected. However, due to the location of the stability envelope, which resides in a negative pressure regime, failure occurs before the saturation of the fine soil layer. Then again, the failure depth tends to decrease with decreased k_{s2} , similar to Figure 4 but becomes more distinguishable due to the high rainfall intensity.

From the above observations, the loss of suction or negative pressure can be identified as the only possible failure mechanism pertinent to case A. It is also important to notice that the failure depth and failure

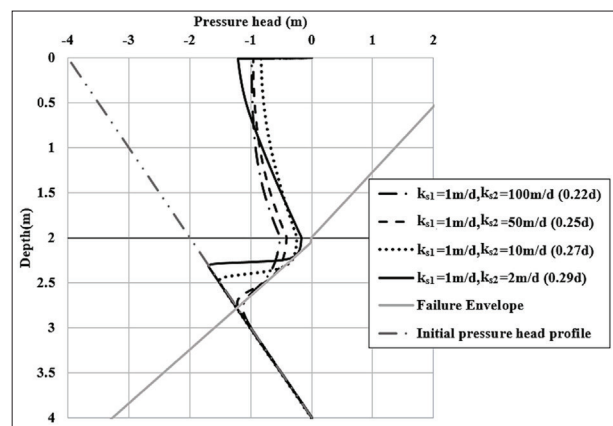


Figure 5: Stability analysis for case A ($I = 1$ m/day)

Table 2: Variation of failure depth with respect to different k_{s2} and I values

Saturated permeability of coarse soil (m/day)	Failure depth (m)		
	$I = 0.1$ m/day	$I = 0.5$ m/day	$I = 1$ m/day
100	2.75	2.75	2.73
50	2.75	2.74	2.46
10	2.74	2.31	2.27
2	2.31	2.28	2.15

time also tend to decrease when the k_{s1} approaches k_{s2} value. For instance, we can observe that the location at which the infiltration profile meets the failure envelope moves towards the boundary of the two layers as the k_{s2} value approaches k_{s1} (Figure 5). It is evident that the amount of water retained around the boundary and the active depth of infiltration depend upon the value of k_{s2} . When k_{s2} is less, more water will be retained around the boundary, which leads to steep destruction of negative pressure close to the boundary. Also, the active depth of infiltration in the bottom layer tends to be shallower due to the above fact. Therefore, the failure depth tends to decrease or move towards the boundary as the k_{s1} and k_{s2} values get closer. This particular trend has been consistently observed over different rainfall intensities, as shown in Table 2. These results indicate that if the difference in permeability values of the two layers is greater, an event of slope failure may move greater soil mass during a landslide and cause more damage.

As the k_{s2} value decreases, the time taken to destroy the negative pressure will increase and therefore, the time taken for failure also increases. Therefore, the further the k_{s2} value is away from k_{s1} , the shorter the time span after which failure may occur. In the event of a relatively shorter rainfall interval, it can be understood that the failure susceptibility increases with the difference in permeability values of the two layers. Similar to the failure depth, this observation has been consistently made over different rainfall intensities, as indicated in Table 3. Overall, it is fair to conclude that the larger the k_{s2} value, the more likely a slope is to fail quickly under any particular rainfall event.

As the rainfall intensity increases, it is observed that the aforementioned trends tend to continue with decreased failure depth and time (Tables 2 and 3). With increased intensity, destruction of negative pressure tends to take place closer to the boundary at a rapid pace due to the increased availability of water. It is important

to notice that high-intensity rainfalls could cause failure in a shorter time period, while a persistent and relatively low-intensity rainfall may move a larger soil mass, which increases the magnitude of the damage.

Even though rainfall intensity such as 1 m/day is impractical to sustain throughout a day, it is important to notice that the failure occurs at a maximum of 0.29 days. The total rainfall received by the slope during this event until failure is around 290 mm. This is rare but definitely a possible high-intensity rainfall event that can be expected in the tropics.

Case B: $k_{s1} > k_{s2}$ (coarse soil overlain by fine soil)

Figure 6 elaborates the scenario pertaining to the combination $I < k_{s2} < k_{s1}$. Since the rainfall intensity is less than that of the saturated permeability of the coarse layer, saturation or development of positive pore water pressure cannot be expected. However, destruction of negative pressure takes place slowly at first and soon becomes a steady pressure head profile as the wetting front

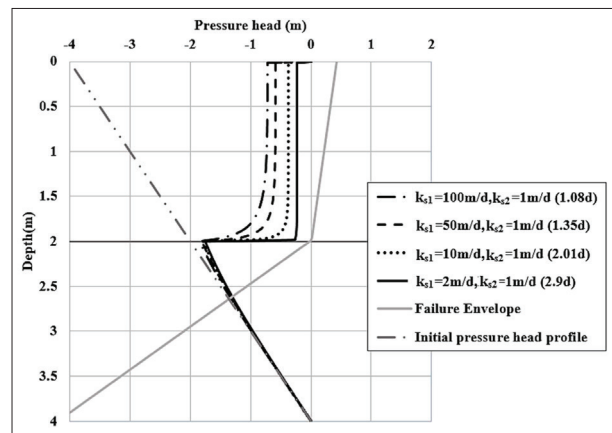


Figure 6: Stability analysis for case B (I = 0.1 m/day)

Table 3: Variation of failure time with respect to different k_{s2} and I values

Saturated permeability of coarse soil (m/day)	Failure time (days)		
	I = 0.1 m/day	I = 0.5 m/day	I = 1 m/day
100	0.68	0.31	0.22
50	0.87	0.4	0.25
10	1.78	0.52	0.27
2	2.57	0.58	0.29

Table 4: Variation of failure depth with respect to different k_{s2} and I values (case B)

Saturated permeability of coarse soil (m/day)	Failure depth (m)		
	I = 0.1 m/day	I = 0.5 m/day	I = 2 m/day
100	2.66	2.66	2.66
50	2.66	2.66	2.66
10	2.65	2.65	2.66
2	2.65	2.65	0.36

advances towards the boundary. Once the water reaches the fine layer, the wetting front tends to move quickly, with less resistance due to the higher permeability in the unsaturated phase. As a result, the wetting front advances relatively quickly and reduces the negative pressure so that the pressure head profile eventually meets the failure envelope. It is also observed that the failure depth tends to be almost the same for different values of k_{s1} (Table 4). Similar to case A, failure time tends to decrease as the saturated permeability of coarse soil (k_{s1}) is reduced, as shown in Table 5.

Table 5: Variation of failure time with respect to different k_{s2} and I values (case B)

Saturated permeability of coarse soil (m/day)	Failure time (days)		
	$I = 0.1$ m/day	$I = 0.5$ m/day	$I = 2$ m/day
100	1.08	0.32	0.12
50	1.35	0.39	0.13
10	2.01	0.55	0.18
2	2.9	0.8	0.19

The scenario $k_{s2} < I < k_{s1}$ is indicated by all the infiltration profiles (dashed curves), except the one shown as a solid curve in Figure 7. Similar to the previous scenario ($I < k_{s2} < k_{s1}$), failure depth tends to be almost constant. Since the saturated permeability of the top (coarse) layer is larger than that of rainfall intensity, no saturation will occur at the top layer. Positive pore water pressure is expected to build up at the boundary after a certain time since the saturated permeability of the bottom (fine) layer is lower than that of the rainfall intensity. If this occurs, failure at the boundary is a possibility. However, it can be seen (Figure 7) that failure occurs at the bottom layer before the occurrence of positive pore water pressure due to the small amount of water already seeping into the bottom layer.

The curve shown as a solid line in Figure 7 represents the scenario of $k_{s2} < I = k_{s1}$. The rainfall intensity is now equal to the saturated permeability value of coarse soil (top layer). Therefore, the amount of water seeping through the top layer will cause it to eventually become saturated. This results in a buildup of positive pore water or a perched water table at the top of the coarse soil layer. As the positive pressure increases, the pressure head profile eventually meets the failure envelope at a shallow depth and results in failure.

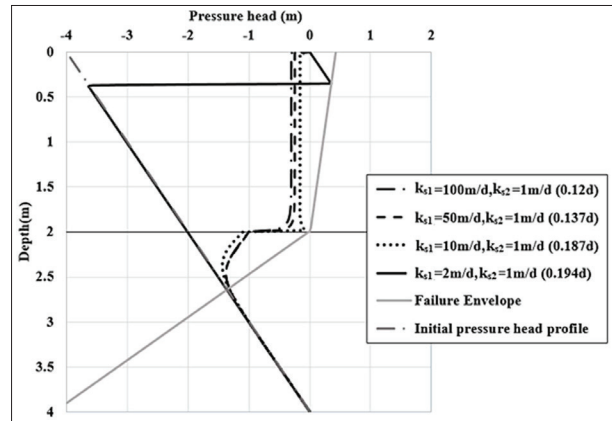


Figure 7: Stability analysis for case 2 ($I = 2$ m/day)

CONCLUSIONS

This study provides an insight to understand the planer failure occurring in shallow landslides, idealized considering a two-layered soil formation with varying permeability characteristics. It delivers several important observations on failure time, failure depth and the mechanism, under partially saturated conditions. Even though the saturated permeability of coarse soil is larger than the saturated hydraulic conductivity of fine soil, it is evident that the opposite behaviour takes place in the unsaturated phase and contributes significantly to the nature of the failure time and depth.

In the case where fine soil overlain by the coarse soil, a significant reduction of failure time and depth was observed as the saturated permeability of coarse soil increases relative to the fine soil. This has been consistently observed irrespective of the rainfall intensity. This phenomenon increases its susceptibility to failure under short rainfall events and, on the other hand, decreases the susceptibility to mobilize larger soil mass during failure. The only possible failure mechanism relevant to this particular case was identified as the ‘loss of suction.’

In the case where coarse soil overlain by the fine soil, no significant trends or implications on failure depth have been observed in relation to the difference in saturated permeability between the two soils. Reduction of failure time has been observed as the saturated permeability of coarse soil increases relative to the fine soil. The failure mechanism is deemed more sensitive to the change in rainfall intensity. When the rainfall intensity is less than

the saturated permeability of both soils, the failure occurs in the negative pore water pressure regime. Failure due to positive pore water pressure is only realized when the rainfall intensity exceeds the saturated permeability of the fine soil. Once the rainfall intensity exceeds the saturated permeability of the coarse soil, failure occurs due to the development of a perched water table.

This study concludes that contrasting permeability characteristics, the layer arrangement and the rainfall intensities of a two layer unsaturated soil formation tend to influence the failure time, depth, and the mechanism.

The model used in this study considers the layers to be homogeneous and the results are based on this idealization. The applicability of this study can be further enhanced by considering the influence of varying layer thickness on failure depth, failure time and the associated failure mechanism.

Acknowledgements

The authors gratefully acknowledge the support given by Mr. Ryan Haagenson and Professor Harihar Rajaram of University of Colorado. The MATLAB formulation used in this study is based on the initial work carried out by the said two researchers.

REFERENCES

- Bishop A.W. (1959). The principle of effective stress. *Technisk Ukeblad* **106**(39): 859–863.
- Blight G.E. (1997). Case histories of volume change and shear strength of residual soils. In: *Mechanics of Residual Soils* (eds. G.E. Blight & E.C. Leong), pp. 285–345. A.A. Balkema, Rotterdam, Netherlands.
- Brönnimann C.S. (2011). Effect of groundwater on landslide triggering, *PhD Thesis*, Swiss Federal Institute of Technology, Lausanne, Switzerland.
DOI: <https://doi.org/10.5075/epfl-thesis-5236>
- Brooks R. & Corey T. (1964). Hydraulic properties of porous media. *Hydrology Paper no 3*, Colorado State University, Colorado, USA. Available at https://mountainscholar.org/bitstream/handle/10217/61288/HydrologyPapers_n3.pdf?se, Accessed 12 February 2019.
- Celia M.A., Bouloutas E.T. & Zarba R.L. (1990). A general mass-conservative numerical solution for the unsaturated flow equation. *Water Resources Research* **26**(7): 1483–1496.
DOI: <https://doi.org/10.1029/WR026i007p01483>
- Collins B.D. & Znidarcic D. (2004). Stability analyses of rainfall induced landslides. *Journal of Geotechnical and Geoenvironmental Engineering* **130**(4): 362–372.
DOI: [https://doi.org/10.1061/\(ASCE\)1090-0241\(2004\)130:4\(362\)](https://doi.org/10.1061/(ASCE)1090-0241(2004)130:4(362))
- Cooray P.G. (1994). Geological factors affecting landslides in Sri Lanka. *Proceedings of National Symposium of Landslides in Sri Lanka*, Colombo, Sri Lanka, pp. 15–22.
- Fourie A.B., Rowe D. & Blight G.E. (1999). The effect of infiltration on the stability of the slopes of a dry ash dump. *Geotechnique* **49**(1): 1–13.
DOI: <https://doi.org/10.1680/geot.1999.49.1.1>
- Fredlund D.G. (2006). Unsaturated soil mechanics in engineering practice. *Journal of Geotechnical and Geoenvironmental Engineering* **132**(3): 286–321.
DOI: [https://doi.org/10.1061/\(ASCE\)1090-0241\(2006\)132:3\(286\)](https://doi.org/10.1061/(ASCE)1090-0241(2006)132:3(286))
- Fredlund D.G., Morgenstern N.R. & Widger R.A. (1978). The shear strength of unsaturated soils. *Canadian Geotechnical Journal* **15**(3): 313–321.
DOI: <https://doi.org/10.1139/t78-029>
- Fredlund D.G., Xing A. & Huang S. (1994). Predicting the permeability function for unsaturated soils using the soil-water characteristic curve. *Canadian Geotechnical Journal* **31**(4): 533–546.
DOI: <https://doi.org/10.1139/t94-062>
- Fredlund D.G., Xing A., Fredlund M.D. & Barbour S.L. (1996). The relationship of the unsaturated soil shear strength to the soil-water characteristic curve. *Canadian Geotechnical Journal* **33**(3): 440–448.
DOI: <https://doi.org/10.1139/t96-065>
- Godt J.W., Baum R.L. & Lu N. (2009). Landsliding in partially saturated materials. *Geophysical Research Letters* **36**(2): 1–5.
DOI: <https://doi.org/10.1029/2008GL035996>
- Godt J.W., Şener-Kaya B., Lu N. & Baum R.L. (2012). Stability of infinite slopes under transient partially saturated seepage conditions. *Water Resources Research* **48**(5): 5505.
- Hillel D. (1998). *Environmental Soil Physics: Fundamentals, Applications, and Environmental Considerations*. 1st edition, pp. 157–161. Academic Press, San Diego, USA.
- Huat B.B., Gue S.S. & Ali F.H. (2004). *Tropical Residual Soils Engineering*, 1st edition, pp. 28–32. CRC Press, London, UK.
- Kankanamge L., Jotisankasa A., Hunsachainan N. & Kulathilaka A. (2018). Unsaturated shear strength of a Sri Lankan residual soil from a landslide-prone slope and its relationship with soil–water retention curve. *International Journal of Geosynthetics and Ground Engineering* **4**(3): 20–29.
DOI: <https://doi.org/10.1007/s40891-018-0137-7>
- Meisina C., Bittelli M., Valentino R., Bordini M. & Tomás-Jover R. (2019). Advances in shallow landslide hydrology and triggering mechanisms: a multidisciplinary approach. *Geofluids (Online)* 2019.
DOI: <https://doi.org/10.1155/2019/1607684>
- Rahardjo H., Aung K.K., Leong E.C. & Rezaur R.B. (2004). Characteristics of residual soils in Singapore as formed by weathering. *Engineering Geology* **73**(1-2): 157–169.
DOI: <https://doi.org/10.1016/j.enggeo.2004.01.002>
- Richards L.A. (1931). Capillary conduction of liquids through porous mediums. *Physics* **1**(5): 318–333.
- Santoso A.M., Phoon K.K. & Quek S.T. (2011). Effects of soil

- spatial variability on rainfall-induced landslides. *Computers and Structures* **89**(11–12): 893–900.
DOI: <https://doi.org/10.1016/j.compstruc.2011.02.016>
- Skempton A.W. & DeLory F.A. (1957). Stability of natural slopes in London clay. *Proceedings of the Conference in Soil Mechanics*, London, UK, pp. 70–73.
- Srivastava R. & Yeh T.C.J. (1991). Analytical solutions for one-dimensional, transient infiltration toward the water table in homogeneous and layered soils. *Water Resources Research* **27**(5): 753–762.
DOI: <https://doi.org/10.1029/90WR02772>
- Vanapalli S.K., Fredlund D.G., Pufahl D.E. & Clifton A.W. (1996). Model for the prediction of shear strength with respect to soil suction. *Canadian Geotechnical Journal* **33**(3): 379–392
DOI: <https://doi.org/10.1139/t96-060>
- Zhan T.L., Jia G.W., Chen Y.M., Fredlund D.G. & Li H. (2013). An analytical solution for rainfall infiltration into an unsaturated infinite slope and its application to slope stability analysis. *International Journal for Numerical and Analytical Methods in Geomechanics* **37**(12): 1737–1760.
DOI: <https://doi.org/10.1002/nag.2106>

RESEARCH ARTICLE

Nuclear medicine

Comparison of radioactive iodine therapy outcome and the duration of pretreatment discontinuation of carbimazole among hyperthyroid patients: a prospective study

S Raheem^{1*} and DKK Nanayakkara²

¹ Department of Clinical Sciences, Faculty of Health-Care Sciences, Eastern University, Batticaloa, Sri Lanka.

² Nuclear Medicine Unit, Faculty of Medicine, University of Peradeniya, Peradeniya, Sri Lanka.

Submitted: 25 March 2021; Revised: 29 October 2021; Accepted: 24 December 2021

Abstract: The outcome of radioactive iodine (¹³¹I) treatment among hyperthyroid patients can be affected by pretreatment with antithyroid drugs (ATD) and they should be discontinued before ¹³¹I treatment. This study aims to compare the outcome of ¹³¹I treatment among hyperthyroid patients who were off carbimazole for 3–7 days and 8–30 days before the ¹³¹I treatment. This prospective cohort study was carried out among 89 hyperthyroid patients referred for ¹³¹I treatment at the Nuclear Medicine Unit, Peradeniya (NMU) during August 2018 to February 2020. All these patients received a fixed activity of 10 mCi ¹³¹I. Each patient was followed up at a three-month interval for 06 months. The data were collected by directly interviewing the patients, from the clinical records and from the NMU database. Six months after ¹³¹I treatment among Graves' disease (GD) patients, 17.9 % had euthyroidism, 59.7 % had hypothyroidism and 22.4 % had hyperthyroidism. The therapeutic success was 77.6 % among them. Of the Toxic Multi Nodular Goitre (TMNG) patients, 36.4 % had euthyroidism, 31.8 % had hypothyroidism and 31.8 % had hyperthyroidism. The overall therapeutic success was 68.2 % among them. Carbimazole discontinuation for 3–7 days and 8–30 days did not show a statistical difference with the ¹³¹I treatment outcomes in both GD (Chi-square value = 0.264, p value = 0.876) and TMNG (Chi-square value = 1.743, p value = 0.418). The minimum carbimazole off days among GD was 5 days and 3 days for the TMNG patients. Withholding carbimazole for more than 7 days (8–30 days) before ¹³¹I treatment did not influence the therapeutic outcome and discontinuation of carbimazole can be decided on individual basis depending on the comorbid conditions.

Keywords: Carbimazole, hyperthyroidism, radioactive iodine.

INTRODUCTION

Radioactive iodine (¹³¹I) is considered as one of the first line treatment in the management of hyperthyroidism (Clarke, 1991). The safety and the effectiveness of ¹³¹I have been proven by several long-term follow up studies (Bonnema & Hegedüs, 2012).

Antithyroid drugs (ATD) control the severity and the symptoms of disease in the management of hyperthyroidism. Hyperthyroid patients are brought to euthyroidism or near euthyroidism before ¹³¹I treatment to prevent thyroid storm and exacerbation of toxic symptoms after ¹³¹I therapy. However, several prospective and retrospective studies have shown that pretreatment with ATD has a negative effect on the final outcome of ¹³¹I therapy (Cooper, 2003). This has made the management of primary hyperthyroidism a challenge. Several retrospective studies have assessed the effect of ATD on the outcome of ¹³¹I therapy, while only a smaller number of prospective studies have evaluated the effect of ATD on ¹³¹I. Studies have shown that ATD reduce the efficacy of ¹³¹I therapy (Marcocci *et al.*, 1990; Andrade *et al.*, 2001.; Braga *et al.*, 2002) and this is high among patients pretreated with propylthiouracil compared to methimazole or carbimazole (Hancock *et al.*, 1997; Imseis *et al.*, 1998; Braga *et al.*, 2002).

* Corresponding author (sanoozarm@yahoo.com;  <https://orcid.org/0000-0002-5042-6363>)



This article is published under the Creative Commons CC-BY-ND License (<http://creativecommons.org/licenses/by-nd/4.0/>). This license permits use, distribution and reproduction, commercial and non-commercial, provided that the original work is properly cited and is not changed in anyway.

To minimize the effect of ATD on the ^{131}I treatment, it is suggested to withdraw ATD prior to the ^{131}I administration. Current recommendations and guidelines on this are solely based on single trials and narrative reviews (Walter *et al.*, 2007). The newer recommendation is to withdraw the ATD 3-7 days before the ^{131}I administration to increase the efficacy of ^{131}I therapy (Andrade *et al.*, 2001; Bonnema *et al.*, 2002; Eschmann *et al.*, 2006; Walter *et al.*, 2006). Challenging these recommendations, certain studies have suggested to stop the antithyroid drugs more than 7 days before radioactive iodine administration (Lewis *et al.*, 2013; Prasanna Kumar and Shivaprasad, 2015). But discontinuing the antithyroid drugs for seven days or less has shown a benefit with large dose ^{131}I therapy. But with low dose ^{131}I treatment, the discontinuation required more than seven days (Walter *et al.*, 2009).

The aim of this study was to compare the outcome of radioactive iodine treatment among hyperthyroid patients who were off carbimazole for 3–7 days and 8–30 days before the 10 mCi radioactive iodine treatment.

MATERIALS AND METHODS

Study subjects

This prospective cohort study was carried out among 89 hyperthyroid patients who received radioactive iodine treatment at the Nuclear Medicine Unit (NMU), Faculty of Medicine, University of Peradeniya from August 2018 to February 2020.

Hyperthyroid patients attending the thyroid clinic at the NMU during the study period and who received 10 mCi ^{131}I therapy were accommodated in the study. Initial diagnosis of hyperthyroidism was made by the referring clinicians based on clinical examination and biochemical assessment. All these patients had been pre-treated with carbimazole and were receiving the first dose of ^{131}I . The common indications for requesting ^{131}I treatment were poor response to ATD or reactions to ATD, and unfitness for or refusal of surgery. Routinely, GD and TMNG patients are treated with ^{131}I on an outpatient basis at the NMU. Solitary toxic nodules (STN) patients are not treated with ^{131}I at the NMU, as they require a larger dose of ^{131}I which needs to be treated inward.

Patient preparation and administration of ^{131}I therapy

Once the NMU accepted the patients for radioactive iodine therapy, thyroid function tests were repeated and thyroid uptake studies were done to confirm the diagnosis

and the aetiology of thyrotoxicosis. Patients who were on ATD were advised to discontinue antithyroid drugs for at least 1 wk prior to the isotope scan and uptake measurement. Those who were on beta-blockers for symptomatic relief was advised to continue the drug, as beta-blockers do not affect the ^{131}I treatment. If needed, they were asked to continue before and after ^{131}I treatment until they get rid of toxic symptoms.

All hyperthyroid patients underwent $^{99\text{m}}\text{Tc}$ -pertechnetate thyroid scan and uptake studies before ^{131}I therapy. Thyroid images were obtained using the MEDISO dual-head SPECT Gamma Camera fitted with a low energy high-resolution parallel hole collimator. Thyroid uptake was calculated by computer software using the image-based pre-injection and post-injection counts and the thyroid image. If the thyroid gland exhibited adequate tracer uptake, the decision to give radioactive iodine therapy was taken by the Nuclear Medicine Physician.

A fixed activity of 10 mCi (370 MBq) of ^{131}I was given under the supervision of a Nuclear Medicine Physician and these patients were referred back to the referring physician. The referring clinicians were requested not to restart ATD for at least 6 wks after the radioactive iodine therapy, and to perform the initial TSH and FT4 tests after 6 wks. All ^{131}I administered patients were followed up jointly at their respective referring centers and NMU thyroid clinic. The referring physician or NMU physician decided on the outcome of the radioactive iodine therapy after clinical and biochemical assessments. Each patient after ^{131}I treatment was followed up at 3 month intervals for 6 months.

Biochemical investigations

At the diagnosis of hyperthyroidism and during follow-up, FT4 and TSH levels were assessed at the referring hospitals or at NMU. The Radio Immuno-Assay (RIA) method is widely used to measure the FT4 and TSH levels. The normal reference range used for serum FT4 was 9.9–24.3 pmol/L (0.8–1.9 ng/dl), and 0.25–4.2 mU/L for serum TSH.

The outcome of radioactive iodine therapy

Patients who received ^{131}I were categorized according to the thyroid status at 6 months, *i.e.*, euthyroidism, hypothyroidism, or hyperthyroidism, based on the clinical and biochemical findings. Therapeutic success was considered at 6 months after ^{131}I therapy if a patient was euthyroid or permanently hypothyroid.

Persistent hyperthyroidism at 6 months was considered as therapeutic failure. Permanent hypothyroidism was considered after 3 months from ¹³¹I therapy, if FT4 was low and TSH elevated, with or without hypothyroid symptoms requiring indefinite thyroxine replacement. This can avoid confusion with transient hypothyroidism which may occur during the first 3 months after ¹³¹I therapy.

Discontinuation of antithyroid drugs

It is a routine practice to discontinue ATD at least 7 days before ¹³¹I administration. Depending on the number of days patients were off carbimazole, they were classified into two groups; 3–7 days and 8–30 days of carbimazole discontinuation prior to ¹³¹I administration.

Ethical clearance

Ethical clearance for this study was granted by the Ethical Clearance Committee, Faculty of Medicine, University of Peradeniya. Informed written consent was obtained before recruiting the patients for the study. An interviewer-administered questionnaire was used for the data collection. A code number was used to identify the patients and no personal identification detail was used in the questionnaire.

Data analysis

Data was entered in SPSS and statistical analysis was done using the SPSS version 25. The results were considered statistically significant at p value ≤ 0.05. The Chi-Square test was used to compare the difference in the outcome between carbimazole discontinuation for 3–7 days vs 8–30 days.

RESULTS AND DISCUSSION

Of the total of 89 patients, the majority were females, including 53 females (59.6 %) and 36 males (40.4 %). The underlying cause for hyperthyroidism in most was Graves’ disease (N = 67, 75.3 %); in the rest it was TMNG (N = 22, 24.7 %). The mean age of the male and female patients in the whole study group was 55.00 years (SD = 12.89) and 49.19 years (SD = 13.98), respectively. The mean age of GD patients was 50.28 years (SD = 14.76) and TMNG patients was 55.36 years (SD = 9.55).

By the end of 6 months after ¹³¹I administration, the total study population had 22.5 % (N = 20) of euthyroid patients, 52.8 % (N = 47) of hypothyroid and 24.7 % (N = 22) of hyperthyroid patients. Among the GD patients,

17.9 % remained euthyroid, 59.7 % were hypothyroid and 22.4 % were hyperthyroid. Among TMNG patients, 31.8 % were hypothyroid, 36.4 % remained euthyroid and 31.8 % were hyperthyroid at 6 months.

Depending on the thyroid status at 6 months after ¹³¹I treatment, the therapeutic outcomes of ¹³¹I were considered as therapeutic success (either euthyroid or hypothyroid) and therapeutic failure (persistent hyperthyroidism) (DeGroot *et al.*, 1990; Leslie *et al.*, 2003; Jaiswal *et al.*, 2014). In this study, 75.3 % (N = 67) of the total study population had shown therapeutic success while 24.7 % (N = 22) had a therapeutic failure. When considering different aetiologies of hyperthyroidism, 77.6 % of GD patients showed therapeutic success and 22.4 % had a therapeutic failure, while 68.2 % of the TMNG patients showed therapeutic success and 31.8 % showed therapeutic failure.

Pretreatment carbimazole discontinuation before ¹³¹I therapy

The analysis revealed that carbimazole was withheld from all patients in this study group before ¹³¹I treatment. Carbimazole had been withheld for a minimum of 3 days and a maximum of 30 days, with a mean of 14.15 days (SD = 7.18) in the total study population. The GD patients had 5 days as the minimum, and a maximum of 30 days, with a mean of 13.70 days (SD = 6.91). TMNG patients had 3 days as the minimum drug free days, and a maximum of 30 days, with a mean of 15.50 days (SD = 7.96).

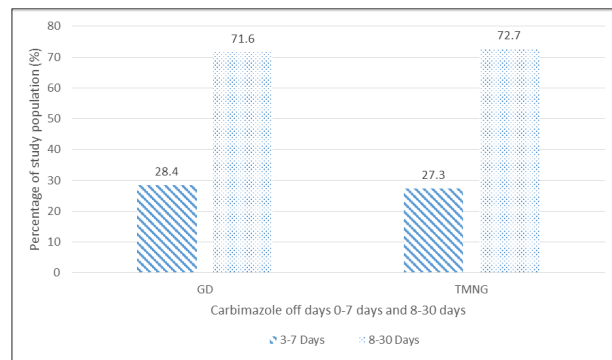


Figure 1: Carbimazole off for 3–7 days and 8–30 days in GD and TMNG patients

The number of drug free days was classified as 3–7 days and 8–30 days for purposes of analysis. Results showed that 71.9 % of the total population had been off carbimazole for 8–30 days (mean no. of days = 17.03,

SD = 6.45) and 28.1 % for 3–7 days (mean no. of days = 6.76, SD = 0.88). When the different aetiologies were considered, 71.6 % of GD patients (mean no. of days = 16.40, SD = 6.39) and 72.7 % of TMNG patients (mean no. of days = 18.94, SD = 6.45) were carbimazole free for 8–30 days. However, the remaining one third received ^{131}I while they were off carbimazole for less than a week (3–7 days); for GD patients, mean no. of days = 6.89, SD = 0.46, and for TMNG patients, mean no. of days = 6.33, SD = 1.63 (Figure 1).

Carbimazole discontinued for 3–7 days and 8–30 days vs thyroid status at 6 months after ^{131}I therapy

The difference in thyroid status at 6 months was compared between the groups, *i.e.*, carbimazole discontinued for 3–7 days and 8–30 days, and the results showed no statistically significant difference in thyroid status between them for the whole study population (Chi-square value = 0.866, p value = 0.648). This analysis also showed that there was no significant difference in thyroid status within the GD patients (Chi-square value = 0.264, p value = 0.876) and the TMNG patients (Chi-square value = 1.743, p value = 0.418) (Table 1).

Table 1: Comparison of thyroid status at 6 months among 8–30 and 3–7 ATD free days

	Total sample		GD		TMNG	
	8-30	3-7	8-30	3-7	8-30	3-7
Euthyroid %	17.9	4.5	13.4	4.5	31.8	4.6
Hypothyroid %	37.1	15.7	43.3	16.4	18.2	13.6
Hyperthyroid %	16.9	7.9	14.9	7.5	22.7	9.1
P value	0.648		0.876		0.418	

Therapeutic success, failure of ^{131}I therapy vs Carbimazole free for 3-7 days and 8–30 days

The total study population had 55.1 % therapeutic success and 16.9 % therapeutic failure among patients carbimazole free for 8–30 days, and a further 20.2 % of therapeutic success and 7.8 % of therapeutic failure among patients who were carbimazole free for 3–7 days. Even though good therapeutic success was noticed among those who had discontinued carbimazole for 8–30 days, there was no statistical difference between the patients who had done so for 8–30 days and for 3–7 days in the ^{131}I therapy outcome, within the total study sample (Chi-square = 0.201, p value=0.654), GD and TMNG patients (Table 2).

Table 2: ^{131}I therapy outcome vs carbimazole off 8–30 days or 3–7 days

	GD		TMNG	
	8-30	3-7	8-30	3-7
Therapeutic success	56.7 %	20.9 %	50%	18.2 %
Therapeutic failure	14.9 %	7.5 %	22.7 %	9.1 %
Chi square value	0.235		0.009	
P value	0.628		0.926	

ATD can decrease the radiosensitivity of thyrocytes by altering the biokinetics of ^{131}I and the free radical scavenger properties, reducing the absorption of ^{131}I , inhibiting thyroid peroxidase enzyme, and reducing the effective half-life of ^{131}I (Walter *et al.*, 2005). These effects are mostly seen among patients treated with propylthiouracil compared to methimazole or carbimazole. To overcome these inhibitory effects as a general rule, all the patients are advised to stop the antithyroid drugs at least 7 days before ^{131}I therapy (Wilson *et al.*, 1990; Sabri *et al.*, 1999; Urbanek *et al.*, 2001; Walter *et al.*, 2007; Oszukowska *et al.*, 2010).

This study found a therapeutic success in 75.3% of hyperthyroid patients after 10 mCi (370 MBq) ^{131}I therapy. This is compatible with several other previous studies where the patients were pretreated with carbimazole and given 10 mCi ^{131}I activity (Bogazzi *et al.*, 1999; Andrade *et al.*, 2001; Leslie *et al.*, 2003; Walter *et al.*, 2005; El Refaei and Shawkat, 2008; Prasanna Kumar & Shivaprasad, 2015).

Effect of the number of pretreatment carbimazole free days on the ^{131}I therapy outcome

Antithyroid drugs are given before the ^{131}I therapy to prevent exacerbation of thyroid crisis and to prevent the aggravation of cardiac related morbidity and mortality (Bonnema *et al.*, 2011). There are various suggestions about the number of days in which antithyroid drugs should be withdrawn before ^{131}I therapy, to achieve satisfactory radioactive iodine uptake by the thyroid (Oszukowska *et al.*, 2010). The common recommendations are to stop the antithyroid drugs for 7 days before ^{131}I administration, while some centres recommend stopping at least 2–3 days before ^{131}I administration (Lewis *et al.*, 2013; Prasanna Kumar & Shivaprasad, 2015). Discontinuing the antithyroid drugs for 7 days or less has shown a benefit with a large activity of ^{131}I . However, for a low dose of ^{131}I treatment, the discontinuation of ATD required more than 7 days (Walter *et al.*, 2009).

Carbimazole had been withdrawn from all the study subjects in this study group before ¹³¹I treatment. Both GD and TMNG patients did not show a significant difference in the therapeutic outcome after 6 months from ¹³¹I therapy, between patients who were off carbimazole for less than seven days or more than seven days. The minimum number of carbimazole free days were 3 for the TMNG patients and 5 for the GD patients. A similar therapeutic success rate has been noted with a previous study where carbimazole has been used as the pretreatment antithyroid drug and discontinued prior to the ¹³¹I therapy (Bogazzi *et al.*, 1999).

The main reason to withdraw antithyroid drugs before ¹³¹I therapy is to increase the effectiveness of ¹³¹I therapy. Studies have shown that withdrawing carbimazole 2–7 days before ¹³¹I therapy leads to prolongation of biological half-time of ¹³¹I, increases the uptake of radioactive iodine in thyrocytes, activates the thyroid peroxidase enzyme, and increases iodine organification. These mechanisms increase the therapeutic effect of ¹³¹I by more than 50 % (Urbanek *et al.*, 2001; Dunkelmann *et al.*, 2007). Many studies have recommended to withdraw antithyroid drugs 3–7 days before the ¹³¹I therapy (Andrade *et al.*, 2001; Bonnema *et al.*, 2002; Eschmann *et al.*, 2006; Kubota *et al.*, 2006; Walter *et al.*, 2006). However, administering ¹³¹I while continuing antithyroid drugs gives worse therapeutic outcomes to a greater extent (Bonnema *et al.*, 2006).

Patients with GD have a shorter biological half-time for ¹³¹I compared to the TMNG patients. This biological half-time is further reduced in hyperthyroid patients if they are given concurrent antithyroid drugs with ¹³¹I. However, both GD and TMNG are affected similarly by the antithyroid agents (Körber *et al.*, 2001). The findings in this study also showed similar results with the number of carbimazole free days in both GD and TMNG compared to the ¹³¹I therapy outcome, because both aetiologies did not have significant differences in the therapeutic outcome as a result of the number of carbimazole free days.

There are a few recommendations to withdraw antithyroid drugs for more than 7 days prior to ¹³¹I therapy. These studies have observed that the therapeutic effects improve with lengthening the intervals between the antithyroid drugs and the ¹³¹I treatment (Einhorn & Säterborg, 1962). But this benefit has been linked to smaller activities of ¹³¹I treatment (Dunkelmann *et al.*, 2007). The findings of the present study are in contrast

to this recommendation. There was no difference in the ¹³¹I therapy outcome with 10 mCi activity among patients who were off carbimazole for 3–7 days or 8–30 days.

The discontinuation of antithyroid drugs prior to the ¹³¹I therapy can be individualized depending on the severity of the disease, type of antithyroid drug, and the associated comorbidities of the patients. Studies have provided evidence that carbimazole has a smaller effect on ¹³¹I therapy outcome compared to propylthiouracil, and that the latter requires a longer duration of discontinuation. Patients with arrhythmia, myocardial insufficiency, and arterial hypertension may experience exacerbation as a result of worsening thyrotoxicosis due to prolonged withdrawal of the antithyroid drug. Taking these factors into consideration, the duration of discontinuing ATD should be decided on a case by case basis before the ¹³¹I therapy (Dunkelmann *et al.*, 2007). This study showed that withdrawing carbimazole 3–7 days prior to ¹³¹I administration had an adequate level of outcome for radioactive iodine treatment, which was similar to previous studies, while showing no extra benefits for discontinuing ATD for more than 7 days. This may be due to fixed larger activities of ¹³¹I (10 mCi) used among this study population (Dunkelmann *et al.*, 2007). But the intracellular findings have shown that, one day after withdrawal of carbimazole, the intrathyroidal kinetics of ¹³¹I are still altered but they are normalized 2 days after discontinuation. As a consequence, carbimazole or methimazole medication should be discontinued at least 2 days before ¹³¹I therapy (Dunkelmann *et al.*, 2007). This principle is further strengthened by our findings.

CONCLUSIONS

There was no difference in 10 mCi radioactive iodine therapy outcome at 6 months between patients who were off carbimazole for 3–7 days and 8–30 days. There is no extra benefit in the outcome of withdrawing carbimazole more than 7 days. However, this pretreatment discontinuation can be decided on individual basis depending on the comorbidities associated.

Conflict of interests

None.

Acknowledgements

We acknowledge the study participants and the technical staff at Nuclear Medicine Unit, Univ. of Peradeniya.

REFERENCES

- Andrade V.N.A., Gross J.L. & Maia A.L. (2001). The effect of methimazole pretreatment on the efficacy of radioactive iodine therapy in graves' hyperthyroidism: one-year follow-up of a prospective, randomized study. *The Journal of Clinical Endocrinology and Metabolism* **86**(8): 3488–3493.
DOI: <https://doi.org/10.1210/jc.86.8.3488>
- Bogazzi F., Bartalena L., Brogioni S., Scarcello G., Burelli A., Campomori A., Manetti L., Rossi G., Pinchera A. & Martino E. (1999). Comparison of radioiodine with radioiodine plus lithium in the treatment of graves' hyperthyroidism. *Journal of Clinical Endocrinology and Metabolism* **84**(2): 499–503.
DOI: <https://doi.org/10.1210/jcem.84.2.5446>
- Bonnema S., Bartalena L., Toft A. & Hegedus L. (2002). Controversies in radioiodine therapy: relation to ophthalmopathy, the possible radioprotective effect of antithyroid drugs, and use in large goitres. *European Journal of Endocrinology* **147**(1): 1–11.
DOI: <https://doi.org/10.1530/eje.0.1470001>
- Bonnema S.J., Bennedbaek F.N., Vejse A., Marving J. & Hegedus L. (2006). Continuous methimazole therapy and its effect on the cure rate of hyperthyroidism using radioactive iodine: an evaluation by a randomized trial. *The Journal of Clinical Endocrinology and Metabolism* **91**: 2946–2951.
DOI: <https://doi.org/10.1210/jc.2006-0226>
- Bonnema S.J., Grupe P., Boel-Jorgensen H., Brix T.H. & Hegedus L. (2011). A randomized trial evaluating a block-replacement regimen during radioiodine therapy: block-replacement regimen during radioiodine therapy. *European Journal of Clinical Investigation* **41**: 693–702.
DOI: <https://doi.org/10.1111/j.1365-2362.2010.02452.x>
- Bonnema S.J. & Hegedus L. (2012). Radioiodine therapy in benign thyroid diseases: effects, side effects, and factors affecting therapeutic outcome. *Endocrine Reviews* **33**: 920–980.
DOI: <https://doi.org/10.1210/er.2012-1030>
- Braga M., Walpert N., Burch H.B., Solomon B.L. & Cooper D.S. (2002). The effect of methimazole on cure rates after radioiodine treatment for graves' hyperthyroidism: a randomized clinical trial. *Thyroid* **12**: 135–139.
DOI: <https://doi.org/10.1089/105072502753522365>
- Clarke S.E.M. (1991). Radionuclide therapy of the thyroid. *European Journal of Nuclear Medicine* **18**: 984–991.
DOI: <https://doi.org/10.1007/BF00180421>
- Cooper D.S. (2003). Antithyroid drugs in the management of patients with graves' disease: an evidence-based approach to therapeutic controversies. *The Journal of Clinical Endocrinology and Metabolism* **88**: 3474–3481.
DOI: <https://doi.org/10.1210/jc.2003-030185>
- DeGroot L.J., Manglabruks A. & McCormick M. (1990). Comparison of RA1311treatment protocols for Graves' disease. *Journal of Endocrinological Investigation* **13**: 111–118.
DOI: <https://doi.org/10.1007/BF03349519>
- Dunkelmann S., Kuenstner H., Nabavi E., Rohde B., Groth P. & Schuemichen C. (2007). Change in the intrathyroidal kinetics of radioiodine under continued and discontinued antithyroid medication in Graves' disease. *European Journal of Nuclear Medicine and Molecular Imaging* **34**: 228–236.
DOI: <https://doi.org/10.1007/s00259-006-0234-z>
- Einhorn J. & Säterborg N.-E. (1962). Antithyroid drugs in iodine 131 therapy of hyperthyroidism. *Acta Radiologica* **58**(3): 161–167.
DOI: <https://doi.org/10.3109/00016926209169557>
- El Refaei S.M. & Shawkat W. (2008). Long-term carbimazole intake does not affect success rate of radioactive ¹³¹Iodine in treatment of Graves' hyperthyroidism: *Nuclear Medicine Communications* **29**: 642–648.
DOI: <https://doi.org/10.1097/MNM.0b013e3282fda205>
- Eschmann S., Thelen M., Dittmann H. & Bares R. (2006). Influence of short-term interruption of antithyroid drugs on the outcome of radioiodine therapy of graves' disease: results of a prospective study. *Experimental and Clinical Endocrinology and Diabetes Reports* **114**: 222–226.
DOI: <https://doi.org/10.1055/s-2006-924238>
- Hancock L.D., Tuttle R.M., LeMar H., Bauman J. & Patience T. (1997). The effect of propylthiouracil on subsequent radioactive iodine therapy in Graves' disease. *Clinical Endocrinology* **47**: 425–430.
DOI: <https://doi.org/10.1046/j.1365-2265.1997.2741075.x>
- Imseis R.E., Vanmiddlesworth L., Massie J.D., Bush A.J. & Vanmiddlesworth N.R. (1998). Pretreatment with propylthiouracil but not methimazole reduces the therapeutic efficacy of Iodine-131 in hyperthyroidism. *Journal of Clinical Endocrinology and Metabolism* **83**(2): 685–687.
DOI: <https://doi.org/10.1210/jcem.83.2.4538>
- Jaiswal A.K., Bal C., Damle N.A., Ballal S., Goswami R., Hari S. & Kumar P. (2014). Comparison of clinical outcome after a fixed dose versus dosimetry-based radioiodine treatment of Graves' disease: Results of a randomized controlled trial in Indian population. *Indian Journal of Endocrinology and Metabolism* **18**(5): 648–654.
DOI: <https://doi.org/10.4103/2230-8210.139222>
- Körber C., Schneider P., Körber-Hafner N., Hänscheid H. & Reiners C. (2001). Antithyroid drugs as a factor influencing the outcome of radioiodine therapy in Graves' disease and toxic nodular goitre? *European Journal of Nuclear Medicine and Molecular Imaging* **28** 1360–1364.
DOI: <https://doi.org/10.1007/s002590100565>
- Kubota S., Ohye H., Yano G., Nishihara E., Kudo T., Ito M., Fukata S., Amino N., Kuma K. & Miyauchi A. (2006). Two-day thionamide withdrawal prior to radioiodine uptake sufficiently increases uptake and does not exacerbate hyperthyroidism compared to 7-day withdrawal in graves' disease. *Endocrine Journal* **53**: 603–607.
DOI: <https://doi.org/10.1507/endocrj.K06-057>
- Leslie W.D., Ward L., Salamon E.A., Ludwig S., Rowe R.C. & Cowden E.A. (2003). A randomized comparison of radioiodine doses in graves' hyperthyroidism. *The Journal of Clinical Endocrinology and Metabolism* **88**: 978–983.

- DOI: <https://doi.org/10.1210/jc.2002-020805>
- Lewis A., Rea T., Atkinson B., Bell P., Courtney H., McCance D. & Hunter S. (2013). Outcome of ¹³¹I therapy in hyperthyroidism using a 550MBq fixed dose regimen. *Ulster Medical Journal* **82**(2): 85–88.
- Marcocci C., Giancchetti D., Masini I., Golia F., Ceccarelli C., Bracci E., Fenzi G.F. & Pinchera A. (1990). A reappraisal of the role of methimazole and other factors on the efficacy and outcome of radioiodine therapy of Graves' hyperthyroidism. *Journal of Endocrinological Investigation* **13**: 513–520.
DOI: <https://doi.org/10.1007/BF03348615>
- Oszukowska L., Knapska-Kucharska M. & Lewiński A. (2010). Effects of drugs on the efficacy of radioiodine (¹³¹I) therapy in hyperthyroid patients. *Archives of Medical Science* **1**: 4–10.
DOI: <https://doi.org/10.5114/aoms.2010.13499>
- Prasanna Kumar K. & Shivaprasad C. (2015). Long-term carbimazole pretreatment reduces the efficacy of radioiodine therapy. *Indian Journal of Endocrinology and Metabolism* **19**(1): 84–88
DOI: <https://doi.org/10.4103/2230-8210.146865>
- Sabri O., Zimny M., Schulz G., Schreckenberger M., Reinartz P., Willmes K. & Buell U. (1999). Success rate of radioiodine therapy in Graves' disease: the influence of thyrostatic medication. *Journal of Clinical Endocrinology and Metabolism* **84**(4): 1229–1233.
DOI: <https://doi.org/10.1210/jcem.84.4.5588>
- Urbanek V., Voth E., Moka D. & Schicha H. (2001). [Radioiodine therapy of Graves' disease--a dosimetric comparison of various therapy regimens of antithyroid agents]. *Nuklearmedizin* **40**: 111–115.
DOI: <https://doi.org/10.1055/s-0038-1625922>
- Walter M.A., Briel M., Christ-Crain M., Bonnema S.J., Connell J., Cooper D.S., Bucher H.C., Müller-Brand J. & Müller B. (2007). Effects of antithyroid drugs on radioiodine treatment: systematic review and meta-analysis of randomised controlled trials. *BMJ* **10**(334): 514.
DOI: <https://doi.org/10.1136/bmj.39114.670150.B>
- Walter M.A., Christ-Crain M., Müller B. & Müller-Brand J. (2005). Radioiodine uptake and thyroid hormone levels on or off simultaneous carbimazole medication. *Nuklearmedizin* **44**(1): 33–36.
- Walter M.A., Christ-Crain M., Schindler C., Müller-Brand J. & Müller B. (2006). Outcome of radioiodine therapy without, on or 3 days off carbimazole: a prospective interventional three-group comparison. *European Journal of Nuclear Medicine and Molecular Imaging* **33**: 730–737.
DOI: <https://doi.org/10.1007/s00259-006-0092-8>
- Walter M.A., Schindler C., Christ-Crain M., Müller-Brand J. & Müller B. (2009). Different strategies to overcome the effect of carbimazole on high- and low-dose radioiodine therapy: results from continuous dose-effect models. *European Journal of Clinical Investigation* **39**: 51–57.
DOI: <https://doi.org/10.1111/j.1365-2362.2008.02061.x>
- Wilson R., McKillop J.H., Buchanan L.M., Bradley H., Smith W.E. & Thomson J.A. (1990). The effect of carbimazole therapy on interleukin 2, interleukin 2 receptors and free radicals. *Autoimmunity* **8**: 3–7.
DOI: <https://doi.org/10.3109/08916939008998426>

RESEARCH ARTICLE

Mathematical statistics

The odd modified Burr-III exponential distribution: properties, estimation and application

H Rasheed¹, IS Dar¹, M Saqib¹, N Abbas², and M Suhail^{3*}

¹ College of Statistical and Actuarial Sciences, University of the Punjab, Lahore, Pakistan.

² Department of Statistics, Government Postgraduate College, Jhang, Pakistan.

³ Department of Statistics, The University of Agriculture Peshawar, Amir Muhammad Khan Campus Mardan, Pakistan.

Submitted: 18 January 2021; Revised: 09 December 2021; Accepted: 24 December 2021

Abstract: Modelling waiting times have always been the earnest need of experts. In this paper, we proposed a new lifetime model entitled Odd Modified Burr-III Exponential Distribution which has four parameters. The proposed model has the heterogeneity in shapes of the density and hazard curves. The density curves of the model are unimodal and reversed J-shaped. The study of the various statistical properties such as moments (raw moments, mean moments, negative moments, incomplete moments, and conditional moments), mode, harmonic mean, geometric mean, hazard, survival, quantile and characteristics function, coefficient of skewness, and kurtosis of the proposed model are presented. In the reliability study, we derive the expressions of mean residual life, mean waiting time, and entropies (Renyi and Shannon). Furthermore, order statistics and L- moments are also presented in this study. The maximum likelihood technique is used to estimate the parameters of the model. Monte Carlo simulation is used to evaluate the performance of the maximum likelihood estimates in terms of absolute average biases and mean square errors. The impact of sample size on parametric properties is also studied. The importance of the proposed model has been illustrated through real-life application from the field of engineering and manufacturing material.

Keywords: Exponential distribution, maximum likelihood estimation, modified Burr-III distribution, order statistics.

INTRODUCTION

Burr (1942) defined a framework centred on twelve different types of cumulative distribution functions,

which are based on the Pearson differential equations that have several types of density functions. This framework is true for a broad variety of applications. The Burr-XII and Burr-III models are the most widely used in the Burr system. The Burr-III distribution, also called Dagum distribution, is useful in the studies of wages, wealth, and income (Dagum, 1977), and kappa distribution in the meteorological field (Mielke Jr, 1973). The Burr-III is the inverse form of the Burr-XII distribution and is used in several fields for modelling statistical data such as forestry, fracture roughness, options market price, life testing, operational risks, etc. (Wingo, 1983; Lindsay *et al.*, 1996; Sherrick *et al.*, 1996; Nadarajah & Kotz, 2004; 2006; Chernobai *et al.*, 2007; Gove *et al.*, 2008; Abbas *et al.*, 2019). It was later used (Mielke Jr, 1973) in meteorology (Abdel-Ghaly *et al.*, 1997), in reliability analysis, and in low-flow frequency analysis (Shao *et al.*, 2008).

A lot of attempts have been made over the last few decades to enhance the chances of modelling datasets of different types. Such efforts led to the development of various methods for the generation of new probability distribution families. Further, various extensions and modifications of distributions have been developed by researchers. For instance, the exponentiated Weibull distribution was suggested by Mudholkar and Srivastava (1993), the Marshall-Olkin generated family by Marshall and Olkin (1997), the Kumaraswamy-G family by

* Corresponding author (msuhail88@aup.edu.pk ;  <https://orcid.org/0000-0003-1784-5272>)



This article is published under the Creative Commons CC-BY-ND License (<http://creativecommons.org/licenses/by-nd/4.0/>). This license permits use, distribution and reproduction, commercial and non-commercial, provided that the original work is properly cited and is not changed in anyway.

Cordeiro and de Castro (2011), the modified Burr III G family of distributions by Arifa et al. (2017) and the Pseudo-gamma Distribution by Abbas and Mohsin (2020). The most recent developments on the Burr III are presented in Modi and Gill (2020), Afify et al. (2021), El Shekh Ahmed (2021), Mahmoud et al. (2021), and ul Haq et al. (2021).

We rarely come across a practical situation in the real world that has a constant hazard function during the lifetime. Hence, assuming hazard rate as a function of time seems practical, and this has led to the development of an alternative model for lifetime data analysis. Hence, this study provides distribution of mixtures using existing baseline distributions, which is useful for modelling real-life datasets whose failure rate is not constant. Many compound distributions work better on versatility than their baseline distributions, when applied to real-life datasets. Many authors have discovered that the analytical properties of the baseline distributions can be improved by increasing the number of parameters, as the new distribution can exhibit stronger structure in terms of better results than the baseline distribution. Recently, several statistical models are used to explain the phenomena of real-world situations, but their use is limited to improper exploration in various fields such as engineering, finance, reliability, and the other similar areas. This paper aims at introducing a new flexible and tractable distribution, which among the other competitive models, offers the best fit for various real-life datasets.

MATERIALS AND METHODS

In this section, the proposed model and the mathematical and statistical properties, such as cumulative distribution function (cdf), probability density function (pdf), hazard function (hf), survival function (sf), reverse hazard function (rhf), and cumulative hazard function (chf) of the proposed distribution are derived, along with their graphical representation. Alzaatreh et al. (2013) defined the following generator to propose a new family of distributions, called the T-X family. Let $g_2(x)$ be the probability density function (pdf) of a random variable (r. v) $X \in [u, v]$, for $-\infty \leq u < v \leq \infty$ and let $G(F(x)) = \frac{G_1(x)}{1-G_1(x)}$ be a function of the cdf $F(x)$ of any r.v X so that $G(F(x))$ satisfies the following conditions:

$$G(F(x)) \in [u, v].$$

$G(F(x))$ is differentiable and monotonically non-decreasing.

$$G(F(x)) \rightarrow u \text{ as } x \rightarrow -\infty \text{ and } G(F(x)) \rightarrow b \text{ as } x \rightarrow \infty.$$

Then, the cdf of the T-X family of distributions for r.v X is given by:

$$F(x) = \int_0^{\frac{G_1(x)}{1-G_1(x)}} g_2(x) dx \tag{1}$$

Here, the odd $\frac{G_1(x)}{1-G_1(x)}$ is obtained from an exponential distribution (ED), $g_2(x)$ is the pdf of the Modified

Burr-III (MB-III) distribution and the resultant distribution is named as the Odd Modified Burr-III Exponential distribution (OMBED-III). This generator would provide the flexible shapes of the pdf and hazard function (hf). The modified Burr III-G family of distributions was proposed by Arifa et al (2017). Ali et al (2015) defined the cdf and pdf of MB-III respectively as:

$$G_2(x) = (1 + \lambda x^{-\beta})^{-\frac{\alpha}{\lambda}}, x \geq 0,$$

and

$$g_2(x) = \alpha \beta x^{-\beta-1} (1 + \lambda x^{-\beta})^{-\frac{\alpha}{\lambda}-1}, x \geq 0 \tag{2}$$

where $a > 0$, $\beta > 0$, and $\lambda > 0$ are shape parameters of MB-III. There are various special cases of MB-III. For example, when $\theta \rightarrow 0$, it reduces to generalized inverse Weibull distribution (De Gusmao et al., 2011); for $\theta = 1$, it transforms to Burr-III distribution (Burr, 1942); and it becomes the log-logistic distribution having the scale parameter $a = \theta = 1$ (Shoukri et al., 1988).

A random variable X is said to have an exponential distribution with cdf defined as:

$$G_1(x) = 1 - e^{-\theta x}, x \geq 0, \theta > 0 \tag{3}$$

Then, the cdf of OMBED-III is obtained by putting equation (2) and equation (3) in equation (1) as:

$$F(x; \varphi) = \left[1 + \lambda \left(\frac{e^{-\theta x}}{1 - e^{-\theta x}} \right)^\beta \right]^{-\frac{\alpha}{\lambda}}, x \geq 0, \tag{4}$$

with the pdf

$$f(x; \varphi) = \alpha\beta\theta \left[1 + \lambda \left(\frac{e^{-\theta x}}{1 - e^{-\theta x}} \right)^\beta \right]^{-\frac{\alpha}{\lambda} - 1} \frac{(e^{-\theta x})^\beta}{(1 - e^{-\theta x})^{\beta+1}}, x \geq 0, \dots(5)$$

where $\varphi = (\alpha, \beta, \theta, \lambda) > 0$ is a parameter vector, and $\alpha, \beta, \lambda, \theta$ are shape parameters. The corresponding sf, hf, rhf, and chf are respectively given by:

$$S(x) = 1 - \left[1 + \lambda \left(\frac{e^{-\theta x}}{1 - e^{-\theta x}} \right)^\beta \right]^{-\frac{\alpha}{\lambda}},$$

$$h(x) = \left[\alpha\beta\theta \left\{ 1 + \lambda \left(\frac{e^{-\theta x}}{1 - e^{-\theta x}} \right)^\beta \right\}^{-\frac{\alpha}{\lambda} - 1} \frac{(e^{-\theta x})^\beta}{(1 - e^{-\theta x})^{\beta+1}} \right] \left[1 - \left\{ 1 + \lambda \left(\frac{e^{-\theta x}}{1 - e^{-\theta x}} \right)^\beta \right\}^{-\frac{\alpha}{\lambda}} \right]^{-1},$$

$$\tau(x) = \left[\alpha\beta\theta \left\{ 1 + \lambda \left(\frac{e^{-\theta x}}{1 - e^{-\theta x}} \right)^\beta \right\}^{-\frac{\alpha}{\lambda} - 1} \frac{(e^{-\theta x})^\beta}{(1 - e^{-\theta x})^{\beta+1}} \right]$$

$$\left[1 + \lambda \left(\frac{e^{-\theta x}}{1 - e^{-\theta x}} \right)^\beta \right]^{-\frac{\alpha}{\lambda}},$$

and

$$H(x) = -\log \left[1 - \left\{ 1 + \lambda \left(\frac{e^{-\theta x}}{1 - e^{-\theta x}} \right)^\beta \right\}^{-\frac{\alpha}{\lambda}} \right].$$

The above graphs show some possible shapes of pdf and hf of OMBED-III for different values of parameters. Figure 1 (a) shows that the density of distribution exhibits a reverse J-shaped and unimodal behaviour. Figure 1 (b) provides a bathtub trend of hf of the proposed distribution.

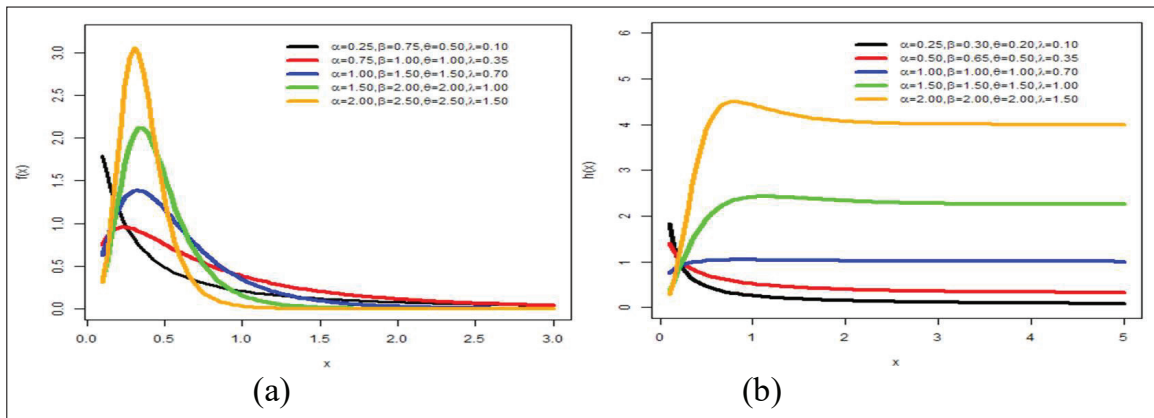


Figure 1: The (a) pdf and (b) hf of OMBED-III at various combinations of parameter values

Expansion of pdf: This section offers a useful linear representation of the density function shown in equation (5).

Using expansion $(a + b)^n = \sum_{i=0}^{\infty} \binom{n}{i} a^{n-i} b^i$, we get

$$f(x) = \alpha\beta\theta \sum_{i=0}^{\infty} \binom{-\frac{\alpha}{\lambda} - 1}{i} \lambda^i (e^{-\theta x})^{\beta(i+1)} (1 - e^{-\theta x})^{-(\beta(i+1)+1)}$$

Using $(1-z)^{-k} = \sum_{j=0}^{\infty} \binom{-k}{j} (-1)^j z^j$ now we can write

$$(1 - e^{-\theta x})^{-\beta(i+1)+1} = \sum_{j=0}^{\infty} \binom{-\beta(i+1)+1}{j} (-1)^j e^{-\theta x j} .$$

Then, we get

$$f(x) = \alpha\beta\theta \sum_{i,j=0}^{\infty} \binom{-\frac{\alpha}{\lambda}-1}{i} \binom{-\beta(i+1)+1}{j} \lambda^i (-1)^j (e^{-\theta x})^{\beta(i+1)+j}$$

Thus,

$$f(x; \varphi) = \alpha\beta\theta \sum_{i,j=0}^{\infty} \delta_{ij} (e^{-\theta x})^{\beta(i+1)+j} \dots(6)$$

where $\delta_{ij} = \binom{-\frac{\alpha}{\lambda}-1}{i} \binom{-\beta(i+1)+1}{j} \lambda^i (-1)^j .$

Properties

In this section, we derived measures of central tendency (i.e., mean, median, mode, geometric mean, and harmonic mean), the measures of dispersion such as variance, moments (raw moments, mean moments, negative moments, incomplete moments, and conditional moments), coefficients of skewness and kurtosis, coefficient of variation, and moment generating function (mgf), characteristic function (cf), mean residual life (MRL), mean waiting time (MWT), order statistics, L-moments, and entropies of OMBED-III.

By using the inverse transformation technique, the simplified form of the quantile function of OMBED-III is given by:

$$x = \frac{1}{\theta} \log \left[\left\{ \lambda \left(u^{-\frac{\lambda}{\alpha}} - 1 \right)^{-1} \right\}^{\frac{1}{\beta}} + 1 \right] . \dots(7)$$

Hence, the median of the underlying distribution is obtained by substituting $u = 0.50$ in equation (7). Similarly, we get the first quartile (Q_1) and third quartile (Q_3) by substituting $u = 0.25, 0.75$, respectively in equation (7).

Mode

The mode of the proposed distribution can be obtained by taking the logarithm of the pdf given in equation (5) and by taking the derivative with respect to \mathcal{X} . Then, we have

$$\frac{d[\log f(x)]}{dx} = - \frac{\theta [(e^{\theta x} - 1)^\beta + e^{\theta x} \{ (e^{\theta x} - 1)^\beta - \alpha \} \beta + \lambda]}{(e^{\theta x} - 1) [(e^{\theta x} - 1)^\beta + \lambda]} .$$

In order to obtain the mode we write $\frac{d(\log f(x))}{dx} = 0$ and after simplification, we get

$$(e^{\theta x} - 1)^\beta (\beta e^{\theta x} + 1) = \alpha \beta e^{\theta x} - \lambda$$

The modal equation of OMBED-III is a non-linear one, that can be solved numerically for various parameter values of α, β, θ and λ .

Harmonic mean

The simplified form of the harmonic mean of OMBED-III is

$$H = \frac{1}{\alpha\beta\theta \sum_{i,j=0}^{\infty} \delta_{ij}} .$$

Geometric mean

The simplified form of the geometric mean of OMBED-III is

$$G = \text{antilog} \left[\sum_{i,j=0}^{\infty} \delta_{ij} \frac{\alpha\beta [-\gamma - \log(\theta(\beta(i+1)+j))]}{\beta(i+1)+j} \right]$$

Moments

The r^{th} moment of OMBED-III is obtained as

$$E(X^r) = \int_0^{+\infty} x^r f(x) dx.$$

To solve μ_r' , substitute $f(x)$ as given in equation (5) into the above equation as given below:

$$\mu_r' = \int_0^{+\infty} x^r \alpha \beta \theta \sum_{i,j=0}^{\infty} \delta_{ij} (e^{-\theta x})^{\beta(i+1)+j} dx$$

Let $y = \theta x(\beta(i+1)+j)$; $x = \frac{y}{\theta(\beta(i+1)+j)}$;

$$dx = \frac{dy}{\theta(\beta(i+1)+j)}, \text{ and}$$

$$\text{limits} = \begin{cases} x = 0, & y = 0 \\ x = \infty, & y = \infty \end{cases}$$

we get,

$$\begin{aligned} \mu_r' &= \alpha \beta \theta \sum_{i,j=0}^{\infty} \delta_{ij} \int_0^{\infty} \left(\frac{y}{\theta(\beta(i+1)+j)} \right)^r e^{-y} \frac{dy}{\theta(\beta(i+1)+j)} \\ \mu_r' &= \alpha \beta \sum_{i,j=0}^{\infty} \delta_{ij} \frac{1}{\theta^r (\beta(i+1)+j)^{r+1}} \int_0^{\infty} e^{-y} y^r dy \end{aligned}$$

Since $\int_0^{\infty} e^{-y} y^{n-1} dy = \Gamma(n)$, the r^{th} ordinary moment of OMBED-III is

$$\mu_r' = \sum_{i,j=0}^{\infty} \delta_{ij} \frac{\alpha \beta r!}{\theta^r (\beta(i+1)+j)^{r+1}} \quad \dots(8)$$

Now, we will find the central moments of the proposed distribution, using the following relationship:

$$\mu_r = \sum_{i=0}^r \binom{r}{i} (-1)^i (\mu_1')^i \mu_{r-i}' \quad \dots(9)$$

where, μ_r' is given in equation (8).

Remarks:

- i. We can obtain the mean of OMBED-III by inserting $r=1$ in equation (8).

- ii. By inserting $r=2$ in equation (9), we can obtain the variance of OMBED-III.

The coefficient of skewness and kurtosis of OMBED-III can be obtained from equation (9) by putting $r=3$ and $r=2$ as $\beta_1 = \frac{\mu_3^2}{\mu_2^3}$, respectively.

We get the coefficient of variation

$$C.V = \frac{S.D}{Mean} \times 100.$$

by substituting $r=1$ in equation (8), and $r=2$ in equation (9) and taking its square root.

The negative moment of OMBED-III can be obtained by substituting negative r in equation (8) as

$$E(X^{-r}) = \sum_{i,j=0}^{\infty} \delta_{ij} \frac{\alpha \beta (-r)!}{\theta^{-r} (\beta(i+1)+j)^{(-r)+1}}; \quad r=1,2,3,4,\dots$$

The lower and upper incomplete moments of OMBED-III are respectively obtained by using the following formulae:

$$m_{r(t)} = \int_{-\infty}^x x^r f(x) dx$$

and

$$M_{r(t)} = \int_x^{\infty} x^r f(x) dx$$

After solving the above equations, we get the following simplified results:

$$m_{r(t)} = \sum_{i,j=0}^{\infty} \delta_{ij} \frac{\alpha \beta \theta \gamma [r+1, \theta x(\beta(i+1)+j)]}{[\theta(\beta(i+1)+j)]^{r+1}}$$

and

$$M_{r(t)} = \sum_{i,j=0}^{\infty} \delta_{ij} \frac{\alpha \beta \theta \Gamma[r+1, \theta x(\beta(i+1)+j)]}{[\theta(\beta(i+1)+j)]^{r+1}}.$$

The conditional moment of OMBED-III is obtained as

$$E(x^d | X > x) = \frac{1}{S(x)} \int_x^{+\infty} x^d f(x) dx.$$

Then, we get the simplified form as

$$E(x^d | X > x) = \left[1 - \left\{ 1 + \lambda \left(\frac{e^{-\theta x}}{1 - e^{-\theta x}} \right)^\beta \right\}^{-\frac{\alpha}{\lambda}} \right]^{-1} \sum_{i,j=0}^{\infty} \delta_{ij} \frac{\alpha \beta \theta \Gamma [d+1, \theta x (\beta(i+1) + j)]}{[\theta [\beta(i+1) + j]]^{d+1}}$$

The moment generating function (mgf) of OMBED-III is given by

$$M_x(t) = E(e^{tx}) = \int_0^{+\infty} e^{tx} f(x) dx = \sum_{m=0}^{\infty} \frac{(t)^m x^m}{m!} f(x) dx = \sum_{m=0}^{\infty} \frac{(t)^m}{m!} E(x^m)$$

By substituting equation (8) to the above equation, we get mgf as

$$M_x(t) = \sum_{m=0}^{\infty} \frac{(t)^m}{m!} \left[\sum_{i,j=0}^{\infty} \delta_{ij} \frac{\alpha \beta m!}{\theta^m [\beta(i+1) + j]^{m+1}} \right]$$

Similarly, we derive the characteristic function (cf) of OMBED-III using its well-known definition given by

$$\varphi(x) = \int_0^{+\infty} e^{itx} f(x) dx = \sum_{p=0}^{\infty} \frac{(it)^p}{p!} \int_0^{\infty} x^p f(x) dx = \sum_{p=0}^{\infty} \frac{(it)^p}{p!} E(x^p)$$

After substituting equation (8), now we have

$$\varphi(x) = \sum_{p=0}^{\infty} \frac{(it)^p}{p!} \left[\sum_{i,j=0}^{\infty} \delta_{ij} \frac{\alpha \beta p!}{\theta^p [\beta(i+1) + j]^{p+1}} \right]$$

Mean residual life and mean waiting time

The mean residual life of the random variable X following OMBED-III has the form

$$m(t) = E[X - t | X > t] = [S(x)]^{-1} \int_t^{+\infty} (x - t) f(x) dx$$

By solving the above equation, we obtained

$$m(t) = \left[1 - \left\{ 1 + \lambda \left(\frac{e^{-\theta t}}{1 - e^{-\theta t}} \right)^\beta \right\}^{-\frac{\alpha}{\lambda}} \right]^{-1} \sum_{i,j=0}^{\infty} \delta_{ij} \frac{\alpha \beta \theta \Gamma [2, \theta t (\beta(i+1) + j)]}{\theta [\beta(i+1) + j]^2} - t$$

and the mean waiting time is given by

$$r(t) = E(t - X | X \leq t) = \frac{1}{F(t)} \int_0^t (t - x) f(x) dx$$

Now, we obtained the following simplified result.

$$r(t) = t - \left[1 + \lambda \left(\frac{e^{-\theta t}}{1 - e^{-\theta t}} \right)^\beta \right]^{\frac{\alpha}{\lambda}} \sum_{i,j=0}^{\infty} \delta_{ij} \frac{\alpha \beta \theta \Gamma [2, \theta t (\beta(i+1) + j)]}{\theta [\beta(i+1) + j]^2}$$

Order statistics

The k^{th} order statistics of OMBED-III can be obtained from the following equation:

$$f_{k:n}(x) = \frac{n!}{(k-1)!(n-k)!} f(x) [F(x)]^{k-1} [1 - F(x)]^{n-k} \dots(10)$$

Substituting pdf and cdf to the above equation, we have

$$f_{k:n}(x) = \frac{n!}{(k-1)!(n-k)!} \left\{ 1 + \lambda \left(\frac{e^{-\theta x}}{1 - e^{-\theta x}} \right)^\beta \right\}^{-\frac{k\alpha}{\lambda}-1} \frac{\alpha \beta \theta (e^{-\theta x})^\beta}{(1 - e^{-\theta x})^{\beta+1}} \left[1 - \left\{ 1 + \lambda \left(\frac{e^{-\theta x}}{1 - e^{-\theta x}} \right)^\beta \right\}^{-\frac{\alpha}{\lambda}} \right]^{n-k}$$

The minimum and maximum order statistics can be obtained by substituting $k = 1$ and $k = n$ in equation (10), respectively as

$$f_{1:n}(x) = n \left[\left\{ 1 + \lambda \left(\frac{e^{-\theta x}}{1 - e^{-\theta x}} \right)^\beta \right\}^{-\frac{\alpha}{\lambda}-1} \frac{\alpha \beta \theta (e^{-\theta x})^\beta}{(1 - e^{-\theta x})^{\beta+1}} \right]$$

$$\left[1 - \left\{ 1 + \lambda \left(\frac{e^{-\theta x}}{1 - e^{-\theta x}} \right)^\beta \right\}^{-\frac{\alpha}{\lambda}} \right]^{n-1}$$

and

$$f_{n:n}(x) = n \left[\left\{ 1 + \lambda \left(\frac{e^{-\theta x}}{1 - e^{-\theta x}} \right)^\beta \right\}^{-\frac{n\alpha}{\lambda}-1} \frac{\alpha\beta\theta (e^{-\theta x})^\beta}{(1 - e^{-\theta x})^{\beta+1}} \right]$$

L-Moments

The L-moments can be computed by using the following expression:

$$\lambda_r = \sum_{i=0}^{r-1} (-1)^{r-1-i} \binom{r-1}{i} \binom{r-1+i}{i} \beta_i, \quad r=1,2,3,4,\dots$$

...(11)

where

$$\begin{aligned} \beta_i &= E\left(x[F(x)]^i\right) = \int_0^\infty x[F(x)]^i f(x) dx \\ &= \alpha\beta\theta \int_0^\infty x \left[1 + \lambda \left(\frac{e^{-\theta x}}{1 - e^{-\theta x}} \right)^\beta \right]^{-\frac{i\alpha}{\lambda}} \\ &\quad \left[1 + \lambda \left(\frac{e^{-\theta x}}{1 - e^{-\theta x}} \right)^\beta \right]^{-\frac{\alpha}{\lambda}-1} \frac{(e^{-\theta x})^\beta}{(1 - e^{-\theta x})^{\beta+1}} dx \\ &= \alpha\beta\theta \int_0^\infty x \left[1 + \lambda \left(\frac{e^{-\theta x}}{1 - e^{-\theta x}} \right)^\beta \right]^{-\frac{\alpha}{\lambda}(i+1)-1} \\ &\quad \frac{(e^{-\theta x})^\beta}{(1 - e^{-\theta x})^{\beta+1}} dx \end{aligned}$$

Using

$$(a + b)^n = \sum_{k=0}^n \binom{n}{k} a^{n-k} b^k$$

we get

$$\begin{aligned} &\left[1 + \lambda \left(\frac{e^{-\theta x}}{1 - e^{-\theta x}} \right)^\beta \right]^{-\frac{\alpha}{\lambda}(i+1)-1} \\ &= \sum_{k=0}^\infty \binom{-\frac{\alpha}{\lambda}(i+1)-1}{k} \left(\lambda \left(\frac{e^{-\theta x}}{1 - e^{-\theta x}} \right)^\beta \right)^k \\ &= \alpha\beta\theta \sum_{k=0}^\infty \binom{-\frac{\alpha}{\lambda}(i+1)-1}{k} \lambda^k \int_0^\infty \frac{(e^{-\theta x})^{\beta(k+1)}}{(1 - e^{-\theta x})^{\beta(k+1)+1}} dx \\ &= \alpha\beta\theta \sum_{k=0}^\infty \binom{-\frac{\alpha}{\lambda}(i+1)-1}{k} \lambda^k \int_0^\infty (e^{-\theta x})^{\beta(k+1)} \\ &\quad (1 - e^{-\theta x})^{-[\beta(k+1)+1]} dx \end{aligned}$$

Using binomial theorem we get

$$\begin{aligned} &(1 - e^{-\theta x})^{-[\beta(k+1)+1]} \\ &= \sum_{j=0}^\infty \binom{-(\beta(k+1)+1)}{j} (-1)^j e^{-\theta x j}, \end{aligned}$$

and the above equation becomes

$$\begin{aligned} &= \alpha\beta\theta \sum_{k=0}^\infty \binom{-\frac{\alpha}{\lambda}(i+1)-1}{k} \sum_{j=0}^\infty \binom{-(\beta(k+1)+1)}{j} \\ &\quad \lambda^k (-1)^j \int_0^\infty x (e^{-\theta x})^{(\beta(k+1)+j)} dx \end{aligned}$$

Substitute

$$\begin{aligned} y &= \theta x (\beta(k+1) + j); \\ x &= \frac{y}{\theta(\beta(k+1) + j)}; \\ dx &= \frac{dy}{\theta(\beta(k+1) + j)}, \end{aligned}$$

and

$$limits = \begin{cases} x = 0, y = 0 \\ x = \infty, y = \infty \end{cases}$$

into the above equation, and we get

$$= \sum_{k,j=0}^{\infty} \binom{-\frac{\alpha}{\lambda}(i+1)-1}{k} \binom{-(\beta(k+1)+1)}{j} \frac{\alpha\beta\lambda^k (-1)^j}{\theta(\beta(k+1)+j)^2} \int_0^{\infty} e^{-y} y dy$$

Now, we have

$$\beta_i = \sum_{k,j=0}^{\infty} \binom{-\frac{\alpha}{\lambda}(i+1)-1}{k} \binom{-(\beta(k+1)+1)}{j} \frac{\alpha\beta\lambda^k (-1)^j}{\theta(\beta(k+1)+j)^2}, i = 0, 1, 2, 3, \dots$$

Substituting the above summation in place of β_i in equation (11) allows us to obtain L-moments. Then, by taking $r = 2, 3$ and 4, we can obtain the L-skewness (τ_3) and L-kurtosis (τ_4) by using the following formulae:

$$\tau_3 = \frac{\lambda_3}{\lambda_2} \text{ and } \tau_4 = \frac{\lambda_4}{\lambda_2}$$

Entropies

The entropy is defined as a measure of uncertainty; the larger the value of entropy, the more uncertain the data. Given a random variable X with a density function $f(x)$, the Renyi entropy is defined as

$$I_{R(a)} = \frac{1}{1-a} \log \left(\int_0^{\infty} f^a(x) dx \right), a > 0, a \neq 1,$$

By solving the above integral, we get the following simplifying result:

$$I_{R(a)} = \frac{1}{1-a} \log \left[\left(\alpha\beta\theta \sum_{i,j=0}^{\infty} \delta_{ij} \right)^a \frac{1}{\theta a [\beta(i+1)+j]} \right]$$

The Shannon entropy can be obtained from the following expression.

$$E(-\log[f(x)]) = -\int_0^{\infty} f(x) \log[f(x)] dx.$$

Solving the above integral, the Shannon entropy takes the simplest form

$$E(\log[f(x)]) = \left[\alpha\beta\theta \sum_{i,j=0}^{\infty} \delta_{ij} \right] \times \log \left[\alpha\beta\theta \sum_{i,j=0}^{\infty} \delta_{ij} \right] \times \frac{1}{\theta [\beta(i+1)+j]}.$$

Maximum likelihood estimation

Although several approaches exist for parameter estimation; in the present study, we considered the maximum likelihood (ML) method to estimate parameters of OMBED-III. Let X_1, X_2, \dots, X_n be a random sample from OMBED-III. The log-likelihood function of equation (5) is given as:

$$\log(f(x)) = n \log(\alpha) + n \log(\beta) + n \log(\theta) -$$

$$\left(\frac{\alpha}{\lambda} + 1 \right) \sum_{i=1}^n \log \left[1 + \lambda \left(\frac{e^{-\theta x_i}}{1 - e^{-\theta x_i}} \right)^\beta \right] - \beta\theta \sum_{i=1}^n x_i - (\beta + 1) \sum_{i=1}^n \log(1 - e^{-\theta x_i}) \dots(12)$$

The ML estimates can be achieved by solving the equations obtained by differentiating the log-likelihood function given in equation (12) with respect to the parameters α, β, θ , and λ and equating them to zero, i.e.,

$$\frac{\partial \log(f(x))}{\partial \alpha} = \frac{n}{\alpha} - \left(\frac{1}{\lambda} \right) \sum_{i=1}^n \left[\log \left(1 + \lambda \left(\frac{e^{-\theta x_i}}{1 - e^{-\theta x_i}} \right)^\beta \right) \right] = 0$$

$$\frac{\partial \log(f(x))}{d\beta} = \frac{n}{\beta} - \theta \sum_{i=1}^n x_i - \sum_{i=1}^n \left[\log(1 - e^{-\theta x_i}) \right]$$

$$-(\alpha + \lambda) \sum_{i=1}^n \left[\frac{\log \left(\frac{e^{-\theta x_i}}{1 - e^{-\theta x_i}} \right)}{\left(\frac{e^{-\theta x_i}}{1 - e^{-\theta x_i}} \right)^{-\beta} + \lambda} \right] = 0$$

$$\frac{\partial \log(f(x))}{\partial \theta} = \frac{n}{\theta} - \left(\frac{\alpha}{\lambda} + 1\right) \sum_{i=1}^n \left[\frac{\beta \lambda \left(\frac{-x(e^{-\theta x_i})^\beta}{(1-e^{-\theta x_i})^{\beta+1}} \right)}{1 + \lambda \left(\frac{e^{-\theta x_i}}{1-e^{-\theta x_i}} \right)^\beta} \right]$$

$$-\beta \sum_{i=1}^n x_i - (\beta + 1) \sum_{i=1}^n \left(\frac{x_i e^{-\theta x_i}}{1 - e^{-\theta x_i}} \right) = 0$$

$$\frac{\partial \log(f(x))}{\partial \lambda} = \frac{\alpha}{\lambda^2} \sum_{i=1}^n \left[\log \left\{ 1 + \lambda \left(\frac{e^{-\theta x_i}}{1 - e^{-\theta x_i}} \right)^\beta \right\} \right]$$

$$- \left(\frac{\alpha}{\lambda} + 1 \right) \sum_{i=1}^n \left[\frac{\left(\frac{e^{-\theta x_i}}{1 - e^{-\theta x_i}} \right)^\beta}{1 + \lambda \left(\frac{e^{-\theta x_i}}{1 - e^{-\theta x_i}} \right)^\beta} \right] = 0.$$

The above system of nonlinear equations cannot be solved analytically. However, they can be solved using numerical iterative techniques. The function (optim) is used for solving non-linear equations in R programming language. The R-code is provided in Appendix A-3.

RESULTS AND DISCUSSION

In this section, the results from Monte Carlo simulation and a real-life application are discussed in detail.

Simulation study

A simulation study was conducted to examine the performance of ML estimators, the impact of parameters, and sample size on the fit of the model. For this purpose, 1000 samples of different sizes $n = 25, 50, 150, 250$ and 350 were generated from OMBED-III with different combinations of parameters values $\varphi = \alpha, \beta, \theta, \lambda$. In the simulation, all programmes were written in the R version 3.6.1 using the following procedure.

Step 1: A random number U was generated from a uniform distribution on unit interval $(0, 1)$, i.e., Generate $U \sim \text{Uniform}(0, 1)$.

Step 2: The cdf was calculated, and used to generate random numbers from a particular distribution by using the inverse transformation technique, as:

$$F(x; \varphi) = \left[1 + \lambda \left(\frac{e^{-\theta x}}{1 - e^{-\theta x}} \right)^\beta \right]^{-\frac{\alpha}{\lambda}},$$

Step 3: x was obtained from the following expression

$$x = \frac{1}{\theta} \log \left[\left\{ \lambda \left(U^{-\frac{\lambda}{\alpha}} - 1 \right)^{-1} \right\}^{\frac{1}{\beta}} + 1 \right].$$

Step 4: We considered four different cases for parameter estimation as follows: Set I ($\alpha = 1.0, 1.5, 2.0, 2.5$) at fixed values of $(\beta, \theta, \lambda) = (0.75, 1.6, 1.5)$; Set II ($\beta = 0.75, 1.0, 1.5, 2.0$) at fixed values of $(\alpha, \theta, \lambda) = (0.75, 2.0, 1.5)$; Set III ($\theta = 1.0, 1.5, 2.0, 2.5$) at fixed values of $(\alpha, \beta, \lambda) = (0.75, 1.0, 1.5)$; and Set IV ($\lambda = 0.75, 1.0, 1.5, 2.0$) at fixed values of $(\alpha, \beta, \theta) = (1.0, 1.5, 0.75)$.

Step 5: We repeated steps 1, 2, 3, and 4 for each of the combinations of parameters and sample sizes; 1000 samples were generated using the R software version 3.6.1.

Let $\hat{\theta}$ be the estimator of θ . An average absolute bias (AAB) and mean squared error (MSE) of $\hat{\theta}$ is obtained as:

$$AAB(\hat{\theta}) = |\hat{\theta} - \theta|$$

$$MSE(\hat{\theta}) = \text{variance}(\hat{\theta}) + (\text{bias}(\hat{\theta}))^2$$

For each of the 1000 samples and combinations of parameters, AAB and MSE of estimates is obtained.

Step 6: We plotted the absolute bias and MSE versus sample size n for four sets of parameters in Figures A-1 and A-2 given in the appendix. We observed from figures that MSE and absolute bias decreases for all parameters by increasing the sample size. Moreover, MSE and absolute bias increase by increasing the particular parameter while keeping the effect of other parameters constant.

Real-life application

This section provides application of the proposed distribution using a real-life dataset to show its importance in the real world. Furthermore, model parameters are estimated using the ML method and different information criteria, such as Akaike information

criteria (AIC), Bayesian information criteria (BIC), consistent Akaike information criteria (CAIC), and Hannon-Quinn information criteria (HQIC), and the Kolmogorov-Smirnov (K-S) statistic is given to suggest the best-fit model. Lower values of these criteria provide a well-fitted model. The fitted pdf and cdf plot, total time test (TTT) plot and Q-Q plot of the proposed distribution are also provided for better understanding. All the required results are estimated using R software.

Illustrative example

The dataset comprises 64 observations for the breaking strength of single carbon fibres of length 10 mm. This dataset was studied by (AL-Hussaini & Hussein, 2011) and given in Table 1. For comparison purpose, we choose

the following models:

1. Modified Burr-III Distribution (MB_III)

$$G(x) = (1 + \lambda x^{-\beta})^{-\frac{\alpha}{\lambda}}$$

2. Exponential Distribution (ED)

$$G(x) = (1 - x^{-\theta x})$$

3. Exponential Pareto Distribution (EPD)

$$G(x) = \left(1 - x^{-\lambda \left(\frac{x}{\beta}\right)^\beta} \right)$$

Table 1: Strengths of single carbon fibres of length 10 mm

1. 901	2. 132	2. 203	2. 228	2. 257	2. 350	2. 361	2. 396	2. 397	2. 445	2. 614	2. 616	2. 618
2. 624	2. 659	2. 675	2. 532	2. 575	2. 454	2. 454	2. 474	2. 518	2. 522	2. 525	2. 738	2. 400
2. 856	2. 917	2. 928	2. 937	2. 937	2. 977	2. 996	3. 030	3. 125	3. 139	3. 145	3. 220	3. 223
3. 235	3. 243	3. 264	3. 272	3. 294	3. 332	3. 346	3. 377	3. 408	3. 435	3. 493	3. 501	3. 537
3. 554	3. 562	3. 628	3. 852	3. 871	3. 886	3. 971	4. 024	4. 027	4. 225	4. 395	5. 020	

Table 2 shows the results of ML estimates and $-2 \log L$.

Table 2: Estimates of parameters and the corresponding log-likelihood

Model	$\hat{\alpha}$	$\hat{\beta}$	$\hat{\theta}$	$\hat{\lambda}$	$-2 \log L$
OMBED-III	41. 0719	2. 9348	0. 5477	3. 4815	115. 30
MBIIID	150. 831	5. 0435	--	2. 5834	119. 78
ED	--	--	0. 3285	--	270. 51
EPD	--	4. 9944	3. 3907	1. 1430	126. 62

In Table 3 goodness of fit statistics such as AIC, BIC, CAIC, HQIC, K-S statistic and p value are reported. It is observed from the results in Tables 5 that the smaller values of different goodness of fit criteria confirm that OMBED-III is the best-fitted model among other competitive models.

According to Table 3, for the dataset of strengths of single carbon fibres of length 10, Odd Modified Burr-III exponential distribution exhibits a better fit comparative to the other defined distributions, based on different goodness of fit criteria.

Table 3: Goodness of fit measures

Model	AIC	BIC	CAIC	HQIC	KS	p value
OMBED-III	123. 30	131. 94	123. 98	126. 70	0. 0945	0. 6169
MBIIID	125. 78	132. 25	126. 18	128. 33	0. 0876	0. 7079
ED	272. 51	274. 67	272. 57	273. 36	0. 4879	0
EPD	132. 62	139. 09	133. 02	135. 17	0. 0954	0. 6043

Figure 2 displays the TTT plot, Q-Q plot, estimated density plot, and empirical cumulative density plot (ECDF) on the strengths of single carbon fibres of length 10 for OMBED-III. The fitted pdf and cdf plot reveal that the proposed distribution gives a good fit to this dataset;

the scaled TTT plot indicates empirical hazard function is an increasing function, and based on the Q-Q plot, we conclude that the proposed distribution provides a good fit for the given dataset.

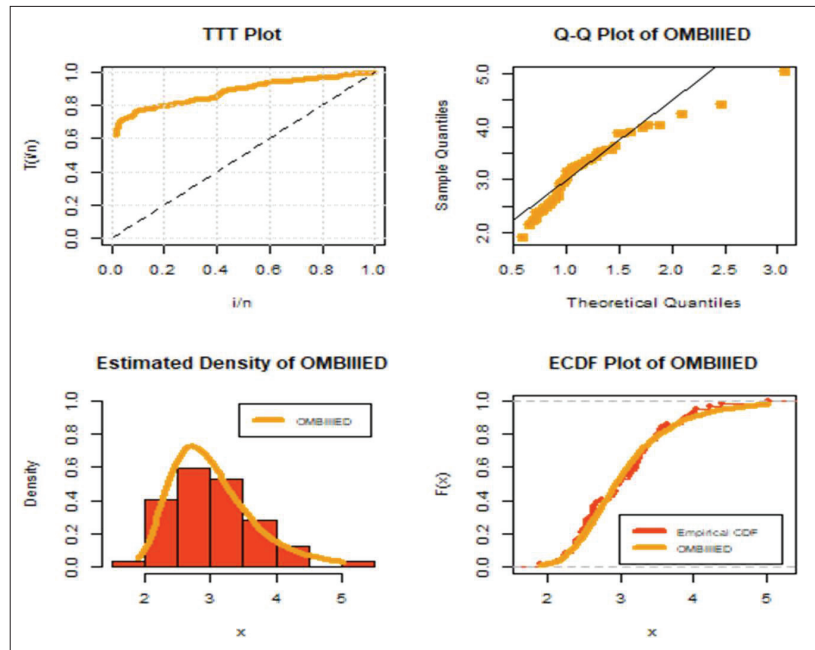


Figure 2: TTT Plot, Q-Q Plot, Estimated Density (EPDF) and ECDF plot of OMBED-III.

CONCLUSIONS

In this article, we proposed a new lifetime distribution named odd modified Burr-III exponential distribution. Statistical properties of the distribution are derived, such as moments, measure of central tendency, and measure of dispersions. The tools of reliability including hazard function, mean residual life, and Shannon and Renyi entropies are derived. Order statistics and L-moments are also included in this study. The ML method is used to estimate the parameters of the distribution. It is found that bias and MSE decrease as sample size increases for all parameters of the distribution. We empirically demonstrate the significance and versatility of the proposed model by using a real-life dataset. The OMBED-III distribution may be considered as the best fitted model on the basis of information criteria. Therefore, we recommend the use of the proposed model which can be preferred to its existing competitors. It is hoped that the proposed model will attract the practitioners.

REFERENCES

- Abbas S., Hameed M., Cakmakyapan S. & Malik S. (2019). On gamma inverse Weibull distribution. *Journal of the National Science Foundation of Sri Lanka* 47(4): 445–453. DOI: <https://doi.org/10.4038/jnsfsr.v47i4.8520>
- Abbas S. & Mohsin M. (2020). On the characteristics of the pseudo-gamma distribution with application in reliability and medical sciences. *Iranian Journal of Science and Technology, Transactions A: Science* 44(5): 1447–1460. DOI: <https://doi.org/10.1007/s40995-020-00950-z>
- Abdel-Ghaly A.A., Al-Dayian G.R. & Al-Kashkari F.H. (1997). The use of burr type XII distribution on software reliability growth modelling. *Microelectronics Reliability* 37(2): 305–313. DOI: [https://doi.org/10.1016/0026-2714\(95\)00124-7](https://doi.org/10.1016/0026-2714(95)00124-7)
- AL-Hussaini E.K. & Hussein M. (2011). Estimation using censored data from exponentiated Burr type XII population. *American Open Journal of Statistics* 1: 33–45. DOI: <https://doi.org/10.4236/ojs.2011.12005>
- Ali A., Hasnain S.A. & Ahmad M. (2015). Modified Burr-III

- distribution, properties and applications. *Pakistan Journal of Statistics* **31**(6): 697–708.
- Alzaatreh A., Lee C. & Famoye F. (2013). A new method for generating families of continuous distributions. *Metron* **71**(1): 63–79.
- Arifa S., Yab M.Z. & Ali A. (2017). The modified Burr III G family of distributions. *Journal of Data Science* **15**(1): 41–60.
DOI: [https://doi.org/10.6339/JDS.201701_15\(1\).0003](https://doi.org/10.6339/JDS.201701_15(1).0003)
- Burr I.W. (1942). Cumulative frequency functions. *The Annals of Mathematical Statistics* **13**(2): 215–232.
DOI: <https://doi.org/10.1214/aoms/1177731607>
- Chernobai G.B., Chesalov Y.A., Burgina E.B., Drebushchak T.N. & Boldyreva E.V. (2007). Temperature effects on the IR spectra of crystalline amino acids, dipeptides, and polyamino acids. I. Glycine. *Journal of Structural Chemistry* **48**(2): 332–339.
DOI: <https://doi.org/10.1007/s10947-007-0050-8>
- Cordeiro G.M. & de Castro M. (2011). A new family of generalized distributions. *Journal of Statistical Computation and Simulation* **81**(7): 883–898.
DOI: <https://doi.org/10.1080/00949650903530745>
- Dagum C. (1977). A new model of personal income distribution: specification and estimation. *Economie Appliquée* **30**: 413–437.
- De Gusmao F.R.S., Ortega E.M.M. & Cordeiro G.M. (2011). The generalized inverse Weibull distribution. *Statistical Papers* **52**(3): 591–619.
DOI: <https://doi.org/10.1007/s00362-009-0271-3>
- El Shekh Ahmed H.I. (2021). Explicit forms of generalized order statistics of Burr III distribution. *Pakistan Journal of Statistics* **37**(3): 179–187.
- Gove J.H., Ducey M.J., Leak W.B. & Zhang L. (2008). Rotated sigmoid structures in managed uneven-aged northern hardwood stands: a look at the Burr Type III distribution. *Forestry* **81**(2): 161–176.
DOI: <https://doi.org/10.1093/forestry/cpm025>
- Lindsay S.R., Wood G.R. & Woollons R.C. (1996). Modelling the diameter distribution of forest stands using the Burr distribution. *Journal of Applied Statistics* **23**(6): 609–620.
DOI: <https://doi.org/10.1080/02664769623973>
- Marshall A.W. & Olkin I. (1997). A new method for adding a parameter to a family of distributions with application to the exponential and Weibull families. *Biometrika* **84**(3): 641–652.
DOI: <https://doi.org/10.1093/biomet/84.3.641>
- Mielke Jr. P.W. (1973). Another family of distributions for describing and analyzing precipitation data. *Journal of Applied Meteorology* **12**(2): 275–280.
DOI: [https://doi.org/10.1175/1520-0450\(1973\)012<0275:AFODFD>2.0.CO;2](https://doi.org/10.1175/1520-0450(1973)012<0275:AFODFD>2.0.CO;2)
- Mahmoud A., Refaey R., AL-Dayian G. & EL-Helbawy A. (2021). Bivariate Burr type III distribution: estimation and prediction. *Journal of Advances in Mathematics and Computer Science* **36**(1): 16–36.
DOI: <https://doi.org/10.9734/jamcs/2021/v36i130327>
- Modi K. & Gill V. (2020). Unit Burr-III distribution with application. *Journal of Statistics and Management Systems* **23**(3): 579–592.
DOI: <https://doi.org/10.1080/09720510.2019.1646503>
- Mudholkar G.S. & Srivastava D.K. (1993). Exponentiated Weibull family for analyzing bathtub failure-rate data. *IEEE Transactions on Reliability* **42**(2): 299–302.
DOI: <https://doi.org/10.1109/24.229504>
- Nadarajah S. & Kotz S. (2004). The beta Gumbel distribution. *Mathematical Problems in Engineering* **2004**: Article ID 529485.
DOI: <https://doi.org/10.1155/S1024123X04403068>
- Nadarajah S. & Kotz S. (2006). The beta exponential distribution. *Reliability Engineering and System Safety* **91**(6): 689–697.
DOI: <https://doi.org/10.1016/j.res.2005.05.008>
- Shao Q., Chen Y.D. & Zhang L. (2008). An extension of three-parameter Burr III distribution for low-flow frequency analysis. *Computational Statistics and Data Analysis* **52**(3): 1304–1314.
DOI: <https://doi.org/10.1016/j.csda.2007.06.014>
- Sherrick B.J., Garcia P. & Tirupattur V. (1996). Recovering probabilistic information from option markets: Tests of distributional assumptions. *Journal of Futures Markets* **16**(5): 545–560.
DOI: [https://doi.org/10.1002/\(SICI\)1096-9934\(199608\)16:5<545::AID-FUT3>3.0.CO;2-G](https://doi.org/10.1002/(SICI)1096-9934(199608)16:5<545::AID-FUT3>3.0.CO;2-G)
- Shoukri M.M., Mian I.U.H. & Tracy D.S. (1988). Sampling properties of estimators of the log logistic distribution with application to Canadian precipitation data. *Canadian Journal of Statistics* **16**(3): 223–236.
DOI: <https://doi.org/10.2307/3314729>
- ul Haq M.A., Afify A.Z., Al-Mofleh H., Usman R.M., Alqawba M. & Sarg A.M. (2021). The extended Marshall-Olkin Burr III distribution: properties and applications. *Pakistan Journal of Statistics and Operation Research* **17**(1): 1–14.
DOI: <https://doi.org/10.18187/pjsor.v17i1.3649>
- Wingo D.R. (1983). Estimating the location of the Cauchy distribution by numerical global optimization. *Communications in Statistics-Simulation and Computation* **12**(2): 201–212.
DOI: <https://doi.org/10.1080/03610918308812311>

Appendix

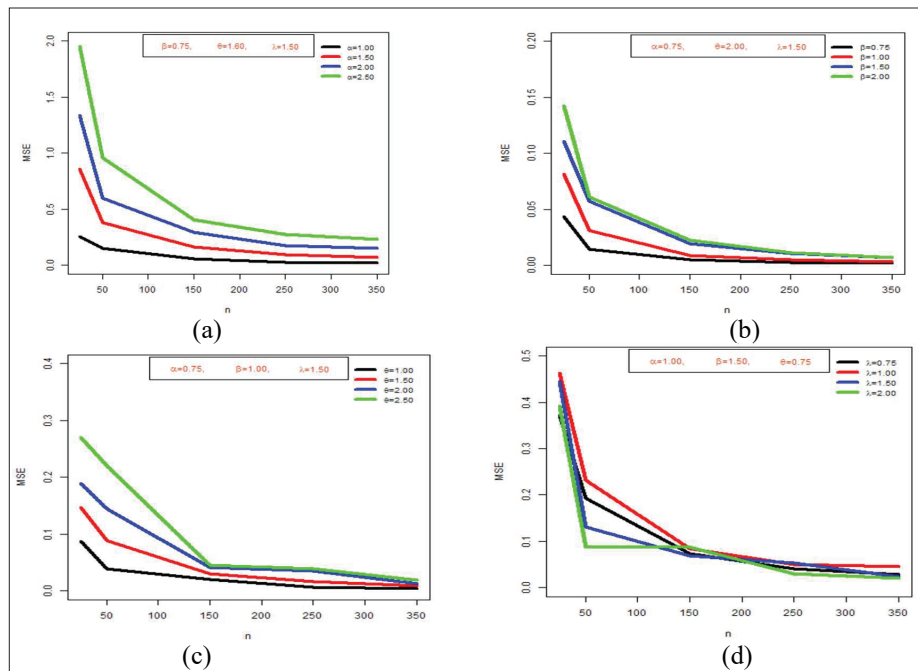


Figure A-1: MSE plot for different values of $\alpha, \beta, \theta, \lambda$ in (a), (b), (c), (d) respectively against sample size.

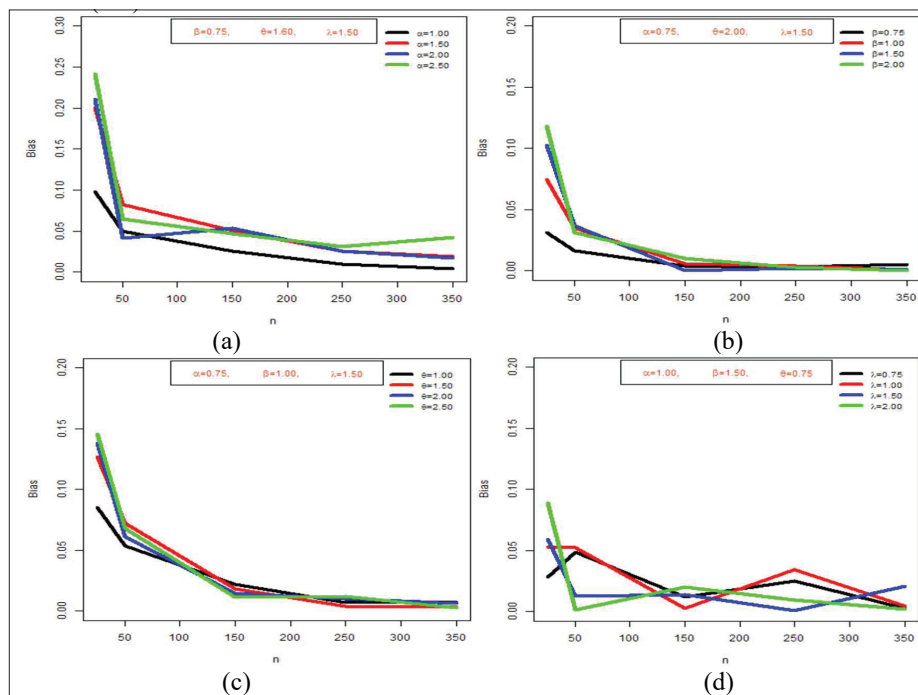


Figure A-2: Absolute bias plot for different values of $\alpha, \beta, \theta, \lambda$ in (a), (b), (c), (d) respectively against sample size

A-3: R-code

Maximum Likelihood Estimation (MLE) of Parameters of OMBED-III distribution

```

rm(list=ls())
library(lars)
library(lamW)
library(data.table)
m = 1000 #Monte Carlo Runs
n = 350 #sample size 25, 50, 150, 250, 350
true.values = c(2.50,0.75,1.60,1.50)
initial = c(2.49,0.74,1.59,1.49)
m11 = rep(0,m)
m12 = rep(0,m)
m13 = rep(0,m)
m14 = rep(0,m)
set.seed(10)
for(i in 1:m){
  y = rep(0,n)
  a = true.values[1]
  b = true.values[2]
  C = true.values[3]
  d = true.values[4]
  u = runif(n)
  for(j in 1:n){ #Quantile Function
    y[j] = (1/C)*( log(( d/ (((u[j])^(-d/a)-1))^(1/b))+1)
  }
  f2 = function(x){ #Log Likelihood Function
    x1 = x[1]
    x2 = x[2]
    x3 = x[3]
    x4 = x[4]
    return( n*(log(x1)) + n*(log(x2)) + n*(log(x3)) + ((-x1/x4)-1)*(sum(log(1+x4*(((exp(-x3*y))/(1-(exp(-x3*y))))^x2))))
    - (x2*x3*(sum(y)))-((x2+1)*(sum(log(1-(exp(-x3*y)))))))
  }
  g2 = function(x){ #Differential Equations of Parameter
    x1 = x[1] #a
    x2 = x[2] #b
    x3 = x[3] #C
    x4 = x[4] #d
    da = (n/x1) - ((1/x4)*(sum(log(1+x4*(((exp(-x3*y))/(1-(exp(-x3*y))))^x2)))) # eq(1) for alpha.

    db = (n/x2) - (C*(sum(y))) - (sum(log(1-(exp(-x3*y)))) +
      ((-x1/x4)-1)*(sum( ((x4*(((exp(-x3*y))/(1-(exp(-x3*y))))^x2))*log((exp(-x3*y)/
      (1-(exp(-x3*y)))))) / (1+x4*(((exp(-x3*y))/(1-(exp(-x3*y))))^x2)))) # eq(2) for beta.
    dC = (n/x3) - ( (x2*x4*(x1/x4)+1) * (sum( (((exp(-x3*y))/(1-(exp(-x3*y))))^x2-1))*((-y*(exp(-x3*y)))/
      ((1-(exp(-x3*y))))^2) / (1+x4*(exp(-x3*y) / (1-(exp(-x3*y))))^x2))) -(x2*(sum(y)))-
      ((b+1)*(sum((y*(exp(-y*x3)))/(1-(exp(-y*x3)))))) #eq(3) for theta.
    dd = ((x1*(sum(log(1+x4*(((exp(-x3*y))/(1-(exp(-x3*y))))^x2))))/(x4^2))+((-x1/x4)-1)*
      (sum(((exp(-x3*y))/(1-(exp(-x3*y))))^x2)/(1+x4*(((exp(-x3*y))/(1-(exp(-x3*y))))^x2)))) #eq(4) for
    lemnda.

```

```

    return(c(da,db,dC,dd))
  }
result = optim(initial,f2,g2,method="BFGS",control=list(trace=2,fnscale=-1)) #optim command
estimates = result$par
m11[i] = estimates[1]
m12[i] = estimates[2]
m13[i] = estimates[3]
m14[i] = estimates[4]
}
length(m11)
length(m12)
length(m13)
length(m14)
##### Average MLE #####
  round(mean(m11),4)
  round(mean(m12),4)
  round(mean(m13),4)
  round(mean(m14),4)
##### Average Bias #####
  m1 = m11- true.values[1]
  AB1 = (1/m)*sum(m1); round(AB1,4)
  m2 = m12- true.values[2]
  AB2 = (1/m)*sum(m2); round(AB2,4)
  m3 = m13- true.values[3]
  AB3 = (1/m)*sum(m3); round(AB3,4)
  m4 = m14- true.values[4]
  AB4 = (1/m)*sum(m4); round(AB4,4)
##### Average MSE #####
  MSE1 = (1/m)*sum(m1^2); round(MSE1,4)
  MSE2 = (1/m)*sum(m2^2); round(MSE2,4)
  MSE3 = (1/m)*sum(m3^2); round(MSE3,4)
  MSE4 = (1/m)*sum(m4^2); round(MSE4,4)

```


RESEARCH ARTICLE

Plant taxonomy

First record of *Thottea duchartrei* Sivar., A. Babu & Balach. (Aristolochiaceae) in Sri Lanka

TMSG Tennakoon^{1*}, R Borosova², C Suraweera¹, S Herath¹, T De Silva¹, C Padumadasa³, J Weerasena⁴, N Gunaratna⁴, N Gunasekera¹, S Edwards², and S Wijesundara⁵

¹ Research and Development Centre, Link Natural Products (Pvt) Ltd, Malinda, Kapugoda, Sri Lanka.

² Herbarium, Royal Botanic Gardens, Kew, Richmond, Surrey, TW9 3AE, UK, Sri Lanka.

³ Department of Chemistry, Faculty of Applied Sciences, University of Sri Jayewardenepura, Nugegoda, Sri Lanka.

⁴ Institute of Biochemistry, Molecular Biology and Biotechnology, University of Colombo, 90, Cumaratunga Munidasa Mawatha, Colombo 03, Sri Lanka.

⁵ National Institute of Fundamental Studies, Hantana Road, Kandy, Sri Lanka.

Submitted: 02 June 2021; Revised: 13 December 2021; Accepted: 24 December 2021

Abstract: The occurrence of *Thottea duchartrei* Sivar., A. Babu & Balach. (Aristolochiaceae), a shrub species previously recorded as endemic to India, has been reported in Sri Lanka for the first time. Previously, only one species of *Thottea* (*T. siliquosa* (Lam.) Ding Hou) has been recorded in the Revised Handbook to the Flora of Ceylon. Two new populations of *T. duchartrei* were discovered in two isolated sites of disturbed, mid country secondary forest at Polthenna and Ihalagama in Hatharaliyadda, Sri Lanka. The taxonomic treatment includes a species description of *T. duchartrei*, its distribution, and phenology. A comparative account of the morphological differences between *T. duchartrei* and *T. siliquosa* is provided for easy identification of the two species of *Thottea*. Further, floral characteristics which are unique to the original collection of *T. duchartrei* from Sri Lanka are also reported. The gene sequences, *rbcl*, *tRNA-Lys (trnK)* and *psba-transH* were submitted to the GenBank database as the first record of this species. Iconography of floral variations, habitats, and local and global distribution maps are also included. Identification using morphological characters, DNA barcoding to confirm the species, and its conservation status are discussed. Biogeographical influences such as habitat fragmentation, soil erosion, invasive species, the low density of natural pollinators and human settlement are also discussed. Based on morphological characters and DNA analysis, we confirmed the first known collections of *T. duchartrei* from Sri Lanka.

Keywords: Biodiversity, DNA barcodes, Flora of Sri Lanka, GenBank, *Thottea*.

INTRODUCTION

Thottea Rottb. (Aristolochiaceae) is a genus of about 43 species distributed in the Andaman Islands, Bangladesh, Borneo, Hainan, India, Jawa, Laos, Malaya, Myanmar, The Nicobar Islands, The Philippines, Sri Lanka, Sulawesi, Sumatera, Thailand, and Vietnam (POWO, 2021). The genus occurs rarely in tropical lowland forests, up to an altitude of ca. 1000 m (Hou, 1981). Diversification of *Thottea* species have been reported in two biogeographic regions: the Western Ghats in India and the Malesian region. High degrees of species endemism were found in both regions and only one species is shared in both regions.

In 1783 Rottboll named the genus *Thottea*. Since then, seven further genera have been published and used by various authors, *Apama* Lam (1783), *Bragantia* Lour (1790), *Ceramium* Blume (1826-27), *Trimeriza* Lindl (1832), *Asiphonia* Griff (1845), *Lobbia* Planch (1847) and *Strakaea* C. Presl (1851). These genera have been

* Corresponding author (tennakoon@linknaturalproducts.com;  <https://orcid.org/0000-0002-5497-6573>)



This article is published under the Creative Commons CC-BY-ND License (<http://creativecommons.org/licenses/by-nd/4.0/>). This license permits use, distribution and reproduction, commercial and non-commercial, provided that the original work is properly cited and is not changed in anyway.

classified under different tribes and sections by Klotzch (1859), Duchartre (1864), Hooker (1890), Solereder (1894), Hou (1981) and Huber (1985). Duchartre (1864) recognized only two genera, *Thottea* and *Bragantia* and synonymised the others. Hooker (1890) accepted this but also noted these genera displayed morphological similarities and could be united. Solereder (1894) renamed *Bragantia* as *Apama* and later Hou (1981) also concluded that *Thottea* and *Apama*, cannot be separated and should be merged into a single genus *Thottea*. In 1985 Huber excluded one genus *Asiphonia* Griff. from *Thottea* due to differences in seed anatomy. Recent phylogenetic studies did not support this exclusion and authors decided to follow Hou (1981) with *Asiphonia piperiformis* being included in the genus *Thottea*. These studies have strongly supported the genus *Thottea* sensu lato as a monophyletic taxon with *Thottea piperiformis* a sister to the other *Thottea* species. The most widely distributed species, *Thottea tomentosa* was identified as a subsequent sister to the rest of the *Thottea* species (Oelschlägel et al., 2011; Madhumita, 2013).

Thottea species are used for the treatment of coughs, malaria, healing wounds, toothache, gum diseases, mouth ulcers and poisonous snake bites in rural and tribal communities in Malaysia, Indonesia, India and Sri Lanka (Perry & Judith, 1980; Udayan et al., 2005; Anilkumar et al., 2014; Sabran et al., 2016; *Unpublished data*, T.M.S.G. Tennakoon). In Sri Lanka, *T. siliquosa* leaves are chewed with betel leaves to experience mild stimulant effect by rural people (*Unpublished data*, T.M.S.G. Tennakoon). Tribal communities in India used to apply crushed roots of *T. duchartrei* externally to treat abscesses, inflammation, and poisonous snake bites (Anilkumar et al., 2014). There have not been any reported uses of *T. duchartrei* in Sri Lanka.

Thottea species have been reported to possess several biological activities such as antibacterial, antioxidant, anticancer, and anti-inflammatory properties (John et al., 2008; Merrine & Ramesh, 2012; Nusaiba & Murugan, 2013; Moorthy et al., 2015; Fatimah et al., 2018; Koottasseril et al., 2020). Biologically active endophytic *Streptomyces* bacteria have been isolated and described from *Thottea grandiflora* (Zin et al., 2007). Aristolochic acid sequestration by *Pachliopta neptunus* and *Troides amphrysus* larvae that feed on *T. tricorns* and *T. dependens* leaves have also been reported (Nishida et al., 1993).

Ten species of *Thottea* Rottb. have been recorded in India (Sunil & Kumar, 2014). In Sri Lanka, *Thottea*

has been represented by only one species, *T. siliquosa* (Heart et al., 1999) with the vernacular name *thapasara bulath* (Sinhala) (Wijesundara et al., 2021). It is distributed in wet lowland evergreen forests. Here we report the first recorded occurrence of *T. duchartrei* in Hatharaliyadda, Kandy, Sri Lanka. Originally described from Western Ghats, India (Nazarudeen & Sabu, 2002; Shaiju & Omanakumari, 2009; 2010; Madhumita 2013) *T. duchartrei* was not found in any other known locality of *T. siliquosa*, during a survey of the wet lowland evergreen forests of the Galle, Kalutara, Kandy, Kegalle and Ratnapura districts in Sri Lanka.

MATERIALS AND METHODS

Field sampling and morphological investigation

During a field visit to the disturbed secondary midland forest in Hatharaliyadda, Kandy, the first author found populations of a *Thottea* species on a small rocky and steeply sloped hill at Polthenna with approximately 70 plants and a slightly sloped hill at Ihalagama with 5 plants. Herbarium specimens, including flowers and fruits preserved in alcohol, were prepared, and sent to the Herbarium of the Royal Botanic Gardens, Kew (K) for taxonomic verification as those were not matched with the specimens of *T. siliquosa* nor its related species deposited at the National Herbarium, Peradeniya (PDA) and Research and development Centre, Link Natural Products (Pvt) Ltd, Sri Lanka (LNP). The *Index Herbariorum* was followed for herbarium acronyms (it is updated continuously). In addition, 1,118 flowers, 50 fruits and 50 leaves were preserved in alcohol for further investigation and photographs were taken. The morphological and anatomical characters were observed using stereo microscope BMS7045 Biobase and Axio Lab A1 series and digital Carl Zeiss Microscopy GmbH. Plant photographs were taken by digital phone camera (iPhone Xs, Apple Inc., USA). Beentje (2016) and World Checklist of Vascular Plants (WCVP, 2021) were followed for morphological terms and taxonomy, respectively. Characters listed in the protologues, and descriptions were compared to those present in herbarium and spirit material. Turland et al. (2018) was followed for nomenclatural practices. The geographical measurements were recorded using a GARMIN eTrex 30 x device. The phenological details, associated species, and soil characteristics were noted in the field. The herbarium specimens were deposited at LNP, K and PDA.

Table 1: Oligonucleotide primers used to amplify barcoding sequences

Primer name	Direction	Sequence 5'-3'	Reference
<i>rbcL</i>	Forward	ATGTCAACCACAAACAGAGACTAAAGC	Lee <i>et al.</i> , 2016
<i>rbcL</i>	Reverse	CTTCTGCTACAATAAGAATCGATCTC	Lee <i>et al.</i> , 2016
<i>psbA3'f</i>	Forward	GTTATGCATGAACGTAATGCTC	Lee <i>et al.</i> , 2016
<i>trnHf_05</i>	Reverse	CGCGCATGGTGGATTCAATCC	Lee <i>et al.</i> , 2016
<i>matk390F</i>	Forward	CGATCTATTCAATCAATATTC	Cuénoud <i>et al.</i> , 2002
<i>matk1326R</i>	Reverse	TCTAGCACACGAAAGTCGAAGT	Cuénoud <i>et al.</i> , 2002

DNA barcoding

Total genomic DNA was extracted from fresh leaf tissues using a Phytospin D™ plant genomic extraction kit (CEYGEN Biotech). Barcoding regions of chloroplast genome were amplified by PCR using primers given in Table 1.

Amplified PCR products were purified by Wizard PCR cleanup kit (Promega) and bidirectionally sequenced with BigDye Terminator Cycle Sequencing Kits, version 3.1 (Applied Biosystems) and ABI 3500Dx automated DNA sequencer.

Analysis of sequences

Bidirectional DNA sequences of each amplicon were assembled using BioEdit version 4 software and the contiguous sequences were searched over the GenBank database at the National Center for Biotechnology Information, USA and BOLD system version 3 using Basic Local Alignment Search Tool (BLAST). The sequences were deposited in GenBank database.

RESULTS AND DISCUSSION

Taxonomic treatment

Thottea duchartrei Sivar., A. Babu & Balach. Indian J. Forest. 8(4): 267. (1986). Type: India, Kerala, Malappuram District, Herbal Garden, Arya Vaidya Sala, Kottakkal, *Indu* 1191 (holotype MH; isotypes CALI & CMPR).

Specimens examined

Sri Lanka: Hatharaliyadda, Polthenna, Kandy, N 7° 19' 39" E 80° 29' 7", 200 – 213 m, 2 July 2018, *Tennakoon* 11-001-21 (K! [K0003423376]) (Figure 3); 29 May 2020, *Tennakoon* 11-001-23 (PDA! [PDA 11-001-23])

Hatharaliyadda, Ihalagama, Kandy, N 7° 19' 44" 80° 30' 38", 265 m, 29 May 2020, *Tennakoon* 11-001-46 (LNP! [LNP 11-001-46]).

Description of *T. duchartrei*

Shrub 0.5–1.5 m tall. Mature stem woody, greyish brown, 6.5–14 mm in diameter; vegetative shoots light to deep green, often flexuous, branching profusely, with 17–43 swollen nodes. Leaves alternate; petiole 8–12 mm long; blade lanceolate, 16–28 × 4–7 cm, base cuneate, apex acuminate, margin entire; strongly 3-veined from base, lateral veins exceeding ¾ of the lamina; young leaves greenish yellow, mature leaves shiny green and pubescent beneath, minutely pubescent above; crushed leaves emit strong aromatic smell. Inflorescence cymose, 1–3 partial inflorescences arising from the foliar axis or from the lower leaf nodes, 1–6 flowered; flowers emit mild rotten fish smell, peduncle 4–12 mm long, pubescent; basal bracts (prophylls) entire, 1.5–3.0 mm long, pubescent; floral bracts 2–12 mm long, entire, pubescent; flowers reddish purple, deep purple or yellow; perianth trimerous, fused up to the middle, pubescent, bell-shaped; tepal lobes 3, orbicular–obovate, apex acute, broader than long, stamens 8–12, fused, commonly arranged in three groups of 3+3+3, 4+3+3, and 4+4+3 around the stylar column opposite to perianth lobes, anthers slightly curved, dithecous, four lobed, extrorse and fully adnate to the filaments, connectives slightly extended at the apex, 1.2–2 mm long; gynostemium with 0–3 tooth like floral appendages alternate to filaments; ovary 6–12 mm long, inferior, densely pubescent, syncarpous, 4 carpels, 4 locules; stylodia 6–12, sometimes bifid. Fruit a dehiscent capsule, 34–80 × 3.06–3.67 mm, subterete, cylindrical to squared, yellowish green at maturity, straight or slightly curved, narrowed at base and apex, reflexed, fruit dehiscence acropetal, fruit valves persistent after dehiscing, twisted spirally. Seeds numerous, light yellow, 2–2.64 mm long, trigonous, rugose, attached to furrows of placenta longitudinally (Figure 1 and Figure 2).

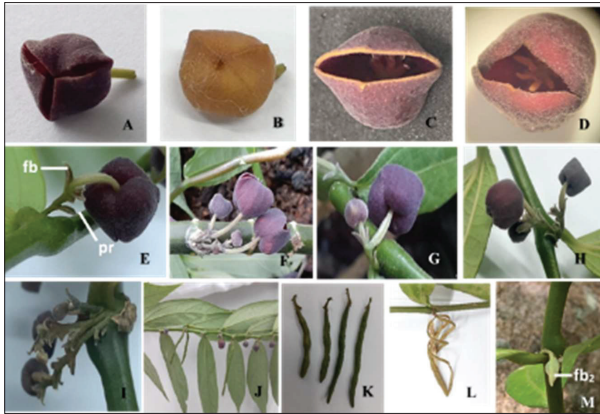


Figure 1: Floral, inflorescence and fruit morphology of *T. duchartrei*. A: purple flower; B: yellow flower; C – D: perianth with two lobes; E: cymose partial inflorescence (fb: floral bract, pr: prophyll); F: inflorescence arising from lower leaf node; G: single partial inflorescence from foliar axis with two flowers; H: two partial inflorescences from the same foliar axis; I: three partial inflorescences from the same foliar axis; J: abaxial view of partial inflorescence and capsules of a branch; K: capsule; L: capsule after dehiscent; M: abaxial view of leaf like floral bracts (fb₂).

Key to species

Young shoots light to deep green, leaf blade 16 – 28 cm long. Peduncle 4 – 12 mm long, floral bract 2 – 12 mm long, stamen arrangement variable (3+3+3, 4+3+3 or 4+4+3), perianth fused up to the middle *T. duchartrei*
 Young shoots light to deep purple, leaf blade 7 – 25 cm long. Peduncle 3 – 6 mm long, floral bract 0.5 – 1 mm long, stamen arrangement usually 3+3+3, perianth free to the base *T. siliquosa*

Notes: Differences in the morphological characters of *T. duchartrei* and *T. siliquosa* are given in Table 2.

Morphological variations

The morphological variations that are observed in the inflorescences and flowers of *T. duchartrei* growing in Sri Lanka and India may be due to geographical and environmental factors (Caruso, 2006). In this study, we examined 1,118 individual flowers and revealed several modifications of previously reported characters in *T. duchartrei* from Sri Lanka. These are described for the first time in this article.



Figure 2: A mature *T. duchartrei* plant observed in Hatharaliyadda, Polthenna, Kandy

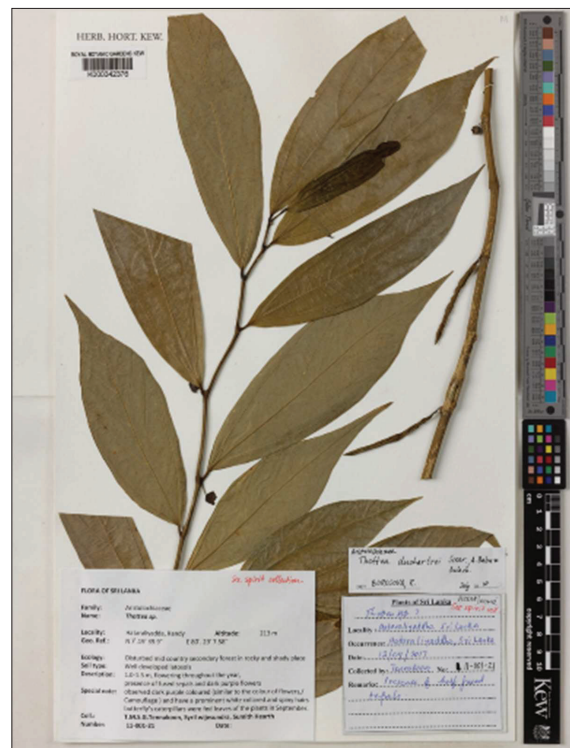


Figure 3: Specimen of *T. duchartrei* collected from Sri Lanka at the Herbarium, Royal Botanic Gardens, Kew

Table 2: Comparison of the morphological characters of *T. duchartrei* and *T. siliquosa*

Character	<i>T. duchartrei</i>	<i>T. siliquosa</i>
Habit	Shrub, 0.5 – 1.5 m	Shrub, 1 – 3 m
Young shoot	Light to deep green	Light to deep purple
Leaf blade length	16 – 28 cm	7 – 25 cm
Flowers	Perianth fused up to the middle, bell shaped	Perianth free to the base, cup shaped
Arrangement of stamens	Variable (3+3+3, 4+3+3 or 4+4+3)	Usually, 3+3+3
Stylodia	6 – 12	6 – 10
Floral appendages	0 – 3	0 – 10
Peduncle length	4 – 12 mm	3 – 6 mm
Capsule length	3.4 – 8 cm	Up to 19 cm
Floral bract length	2 – 12 mm	0.5 – 1 mm
Prophyll length	1.5 – 3 mm	1 – 2 mm

Inflorescence morphology: The occurrence of two partial inflorescences arising from the same foliar axis and a peduncle of less than 5 mm were reported as common morphological characters in the *T. duchartrei* growing in India (Shaiju & Omanakumari, 2009).

However, a single partial inflorescence is very common in this species growing in Sri Lanka and only a few plants (n = 5) had 2 or 3 partial inflorescences arising from the same foliar axis, prominent leaf like floral bracts (10 – 12 mm long) and longer peduncles (10 – 12 mm long).

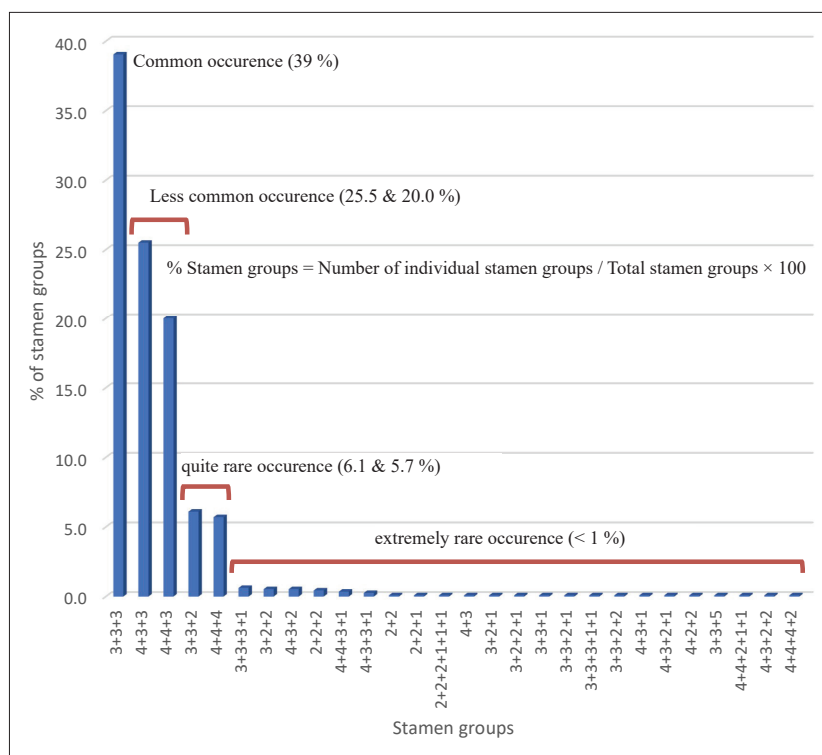


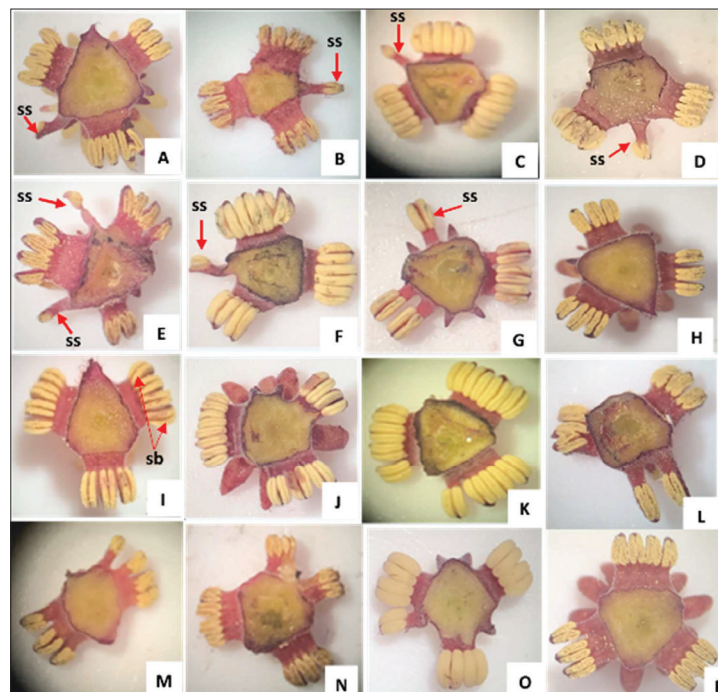
Figure 4: Frequency of occurrence of the 28 different stamen arrangements in the flowers of *T. duchartrei* collected in Sri Lanka.

Perianth morphology: Large bell shaped perianths with three completely fused tepal lobes and small cup shaped perianths with two tepal lobes fused to halfway from the base are reported here for the first time in *T. duchartrei* (Figure 1: C, D).

Stamen morphology: Our study highlights variations in the morphology, arrangement, and the number of stamens of the Indian and Sri Lankan plants. Although flowers with single stamens were rare in the Indian specimens (Renuka & Swarupanandan, 1986) they were found occasionally in our specimens (Figure 5: A – G). In some specimens we found appendiculate stamens with or without sterile remnants of anthers (Figure 6: 1 – 8), stamen-stylodium fusion (Figure 6: 9 – 13) and a fertile stylodium which carried an abaxial, monothealous anther extrorsely (Figure 6: 14 – 18). Stamen-perianth fusion (Figure 6: 19), fusion of anthers with adjacent stamens (Figure 6: 20 – 22), undeveloped anthers (Figure 6: 23 – 26), free stamens with monothealous anthers and dithealous anthers (Figure 6: 30 – 31) were observed. Anther connectives of free stamens (Figure 6: 32 – 33) and fused stamens (Figure 6 : 34 – 35) in the main bundles were occasionally separated half-way to the

apex and the free stamens in the main bundles (Figure 6: 37).

The arrangement of stamen bundles in the Indian plants varied according to the records of different authors. Renuka & Swarupanandan (1986) reported the presence of 4+3+3 and 3+2+2 stamen bundles as common and the occurrence of a single stamen or pairs of stamens as very rare. According to Shaiju and Omanakumari (2010), 3+3+3 was more common but 4+3+3 and 3+2+2 were very rare. The percentage variation of stamen bundles in Indian plant has been reported as 40% for 3+3+3, 37% for 4+4+3, 12% for 4+3+3, and 7% for 4+4+4 (Nazarudeen & Sabu, 2002). Our study has revealed that the arrangement of stamens is different from what has been previously reported (Figure 5). The most common stamen arrangement in Sri Lankan species is 3+3+3, occurring in 39 % of specimens. Less common arrangements are 4+3+3 (25.5 %) and 4+4+3 (20 %) and quite rare arrangements are 4+4+4 (5.7 %) and 3+3+2 (6.1 %). In addition, this is the first time that 28 different combinations of stamen groups from the flowers of *T. duchartrei* were reported (Figure 4). Variation and high plasticity of androecial patterns of the genus *Thottea*



ss – single stamen, sb – stamen bundle

Figure 5: Stamen arrangements of *T. duchartrei* flower (View of transections at the base of androecium). A: 4+4+3+1, B: 4+3+3+1, C: 4+3+3+1, D: 3+3+3+1, E: 4+4+2+1+1, F: 4+3+2+1, G: 3+2+1, H: 3+3+3, I: 4+4+3, J: 4+3+2, K: 4+4+4, L: 3+3+2, M: 4+3, N: 4+3+2+2, O: 3+2+2, P: 4+3+3.

has been previously reported and emphasized. However those androecium characters were not appropriated for the delimitation of *Thottea* species (Leins *et al.*, 1988; Nazarudeen & Sabu, 2002).

Floral appendages are present in two whorls, as an outer series, and an inner series. Renuka & Swarupanandan (1986) describe the outer series as having 3 and the inner series as having 6 – 12 appendages. In the Sri Lankan specimens, the authors describe the outer series as having 0 – 4 and, the inner 0 – 5 appendages (Figure 6: 36). In

addition, stamens were found with vestigial anther sacs (Figure 6: 27 – 29). The morphology of vestigial anther sacs was shown to completely deviate from the original arrangement of anthers in size, bearing monotheous anthers, and anthers containing fewer pollen grains (Figure 6:28). This observation is supported by the gradual evolutionary transition of stamens to sterile floral appendages or stamonoïdes and the reduction of stamen appendages in the family Aristolochiaceae (Leins *et al.*, 1988; Kelly, 2001; Shaiju and Omanakumari, 2010).

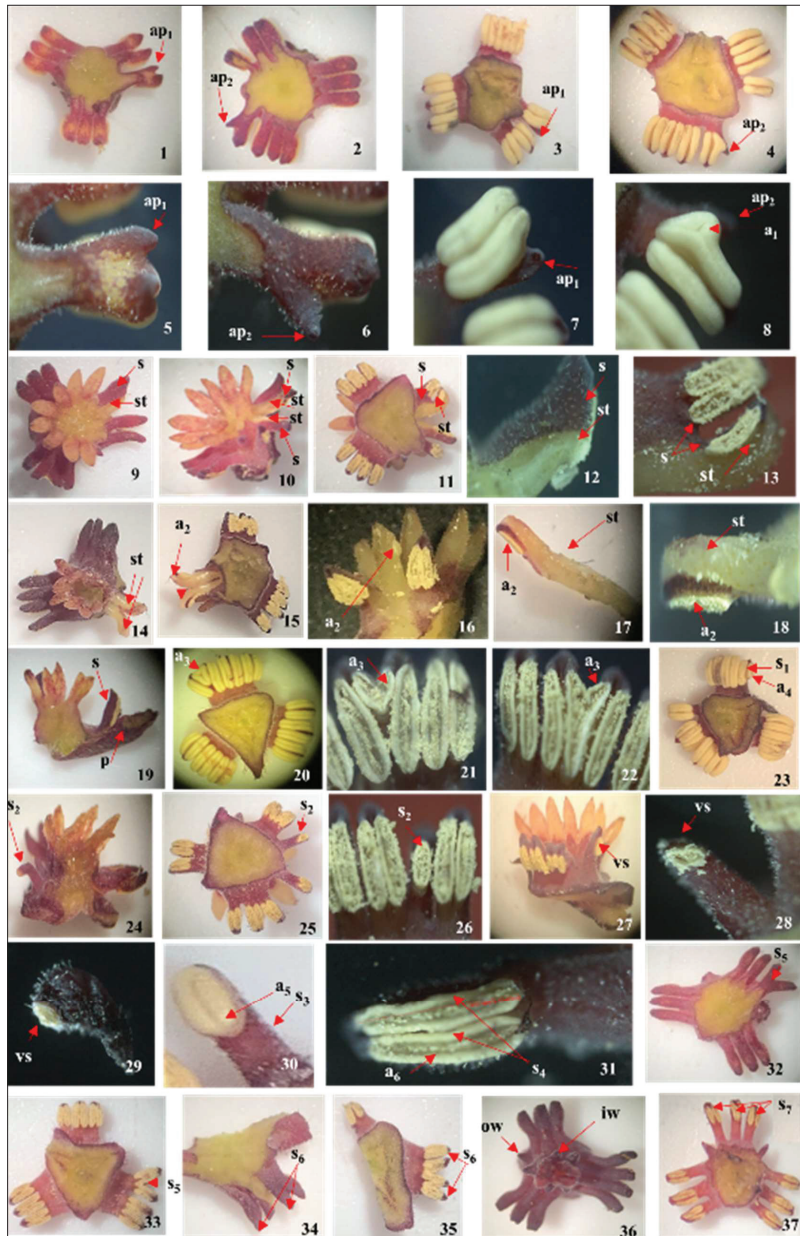


Figure 6: Stamen morphology

Connective appendage: 1. Appendage (ap_1) is positioned inside of the stamen bundle - view of transection at the base of the gynostemium, 2. Appendage (ap_2) is positioned outside of the stamen bundle - view of transection at the base of the gynostemium, 3. Appendage (ap_1) is positioned inside of the stamen bundle - view of transection at the base of the androecium, 4. Appendage (ap_2) is positioned outside of the stamen bundle - view of transection at the base of the androecium, 5. Top view of enlarged connective appendage (ap_1) positioned inside of the stamen bundle, 6. Top view of enlarged connective appendage (ap_2) positioned outside of the stamen bundle, 7. Bottom side view of enlarged connective appendage (ap_1) positioned inside of the stamen bundle, 8. Bottom side view of enlarged connective appendage (ap_2) positioned outside of the stamen bundle with a sterile remnant of an anther (a_1); **Stamen (s) and stylodium (st) fusions (arrows point to fusion):** 9. Inner top view of the androecium and pistil, 10. Lateral view of the androecium and pistil, 11. Transection view at base of the androecium, 12. Upper position - lateral view of enlarged s & st fusion, 13. Lateral view - lower position of s & st fusion; **Anther (a_2) bearing stylodium (st):** 14. Inner top view of the androecium, 15. Bottom view of transection at the base of the androecium, 16. Lateral view of the androecium and stylodium, 17. Lateral view of enlarged anther (a_2) bearing stylodia (st), 18. Lateral view of anther (a_2) bearing enlarged tip of stylodia (st); **Stamen(s)-perianth (p) fusion:** 19. Longitudinal section of flower; **Anther lobes (a_3) of adjacent stamens partially fused by theca:** 20. Bottom view of transection at the base of the androecium, 21 & 22. Bottom view of enlarged stamens bundles. **Undeveloped fused anther (a_4), stamen bundle (s_1):** 23. Bottom view of transection at base of the androecium; **Undeveloped anther on free stamen (s_2):** 24. Lateral view of the androecium and pistil, 25. Bottom view of transection at the base of the androecium, 26. Bottom view of enlarged undeveloped anther (s_2) in a free stamen; **Vestigial anther (vs):** 27. Lateral view of androecium and pistil, 28 & 29. Bottom view of enlarged vestigial stamens; **Free stamen (s_3) with monotheous anther (a_5):** 30. Bottom view of enlarged monotheous anther (a_5); **Free stamen (s_4) with ditheous anther (a_6):** 31. Lower view of enlarged ditheous stamen. **Free stamen divided half-way (s_5):** 32. Top view of transection at base of the gynostemium, 33. Bottom view of transection at base of the androecium; **Fused stamens divided half-way (s_6):** 34. Top view of transection at base of the gynostemium, 35. Bottom view of transection at base of the androecium; **Inner (iw) and outer (ow) whorls of floral appendage:** 36. Inner top view of the androecium; **Free stamens bundle (s_7):** 37. Bottom view of transection at the base of the androecium.

Phenology: Flowering and fruiting were observed throughout the year.

Molecular Analysis: The barcode sequences were deposited in the GenBank database, as partial sequences *matK* (Acc. No. MK074729), *rbcL* (Acc. No. MK524718), and *psba-tranH* (Acc. No. MK074730). The *matK* sequence was aligned with 100 % identity with *T. duchartrei* (Acc. No. JN415678) which is the first sequence of *T. duchartrei* in the GenBank database. This further confirmed the identification of the species in this study based on morphological characters.

Phytogeography

Sri Lanka is a tropical island country located between 5° 55' - 9° 51' N and 79° 41' - 81° 54' E, in the Indian Ocean, off the southern tip of the Indian subcontinent. The total area of the country is 65,610 km² and consists of three peneplains, namely, lowland (up to 300 m altitude), upland (300 - 900 m altitude) and highland (more than 900 m altitude). The three major climatic zones are defined based on the rainfall, namely, dry zone (annual rainfall less than 1900 mm), intermediate zone (annual rainfall between 1900 - 2500 mm) and wet zone (annual rainfall more than 2500 mm). There are three unique mountain ranges in the Island, which have been described as the Central hill massif, the Rakwana range in the south-west, and the Knuckles range to the north of the Central massif (Ashton *et al.*, 1997).

The flora of Sri Lanka consists of 3087 angiosperm species belonging to 186 families, with 28 % of them (863) recorded as endemic, belonging to 98 of the families. A total of 1496 of the species (48.4 %) are threatened. Most of the endemic species are found in the central and southwest regions of Sri Lanka (Wijesundara, 2020).

The flora of Sri Lanka is a relic of Deccan flora which evolved during the Tertiary period and the late Cretaceous epoch. The Indian plate broke away from Gondwana and migrated north of the equator. With the aridification of the Deccan flora during the Miocene epoch, most of the rainforest taxa gradually disappeared from the Deccan plate and only remained restricted in isolated areas of Asia. The Western Ghats and the Southwest of Sri Lanka have similar geology, climate, and evolutionary history, and the present-day rainforest taxa persisted as "relicts and vicariants or endemics" in these biodiversity hotspots. Moreover, approximately 433 plant species and 3 genera are confined to Sri Lanka and Western Ghats in India (Ashton & Gunatilleke 1987; Bossuyt *et al.*, 2004; Mittermeier *et al.*, 2004; Gunawardene *et al.*, 2007; Gunatilleke *et al.*, 2017).

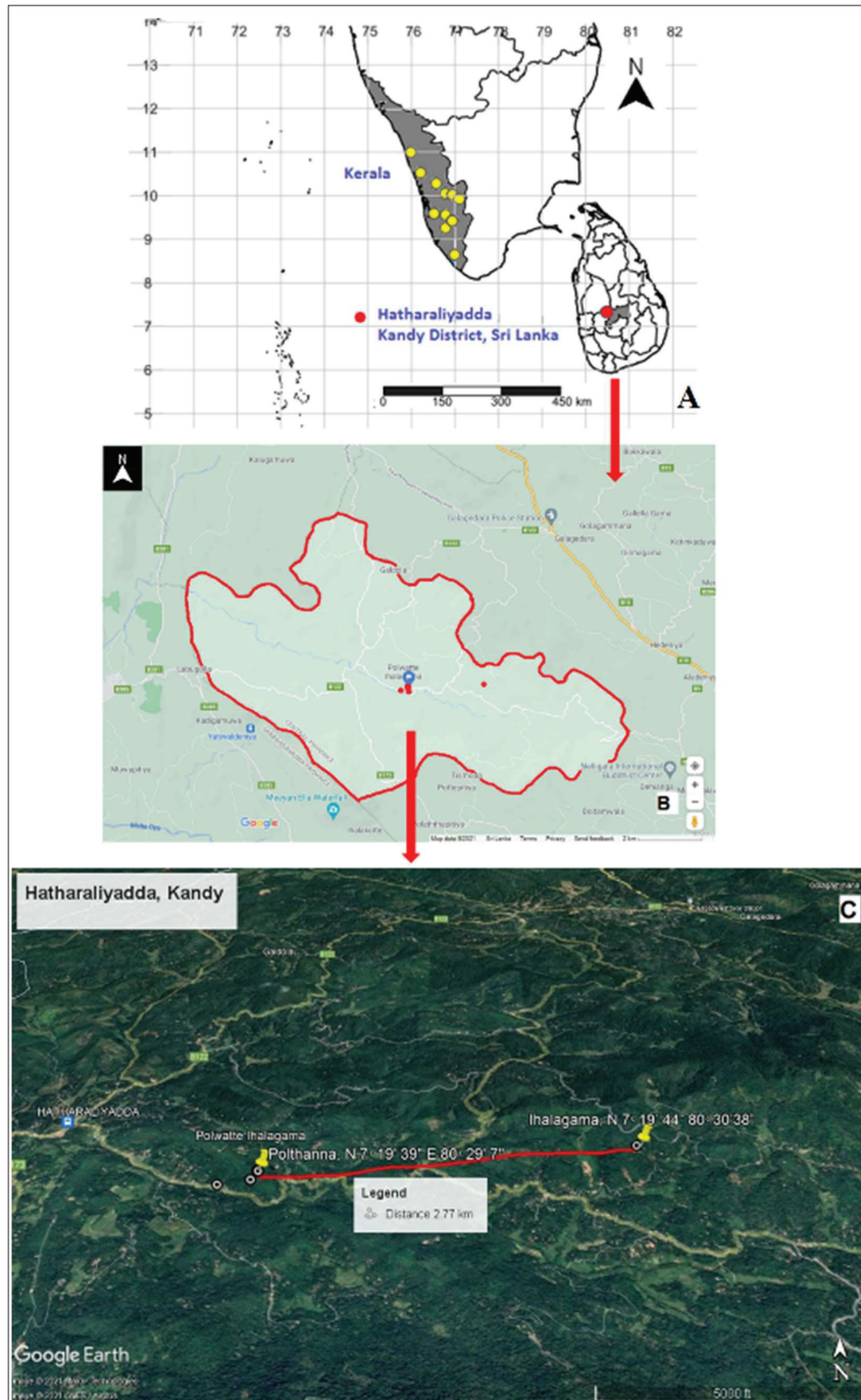


Figure 7: Geographical locations of *T. duchartrei* in India and Sri Lanka. **A:** Previous locations in Kerala state, India, and new records at Hatharaliyadda, Kandy, Sri Lanka; **B:** Satellite image of the two new locations at Polthenna and Ihalagama villages in Hatharaliyadda, Kandy; **C:** Expanded satellite image representing the topography of the two new locations, Polthenna and Ihalagama villages in Hatharaliyadda, Kandy.

The global distribution of the genus *Thottea* is mainly confined to the Western Ghats in India, and Malaysia. A single species *T. celebica* occurs across the whole distribution area of *Thottea*, from India to the Philippines via the Greater Sunda Islands. The Western Ghats and Sri Lanka shared one species, *Thottea siliquosa* (Oelschläge *et al.*, 2011) until the discovery of *T. duchartrei* in Sri Lanka. Fewer species crossed the ocean from mainland India and Malaysia to the more remote islands. Most of the time single species crossed from the mainland of Asia to the islands of southeast Asia. The presence of *T. duchartrei* in Sri Lanka could be an indication of the existence of similar flora in the two land masses before the last disruption happened via Palk Isthmus 10,000 years before present (ybp).

The discovery of *T. duchartrei* in both locations, Polthenna and Ihalagama in the Kandy district is a novel addition to the known flora of Sri Lanka. Previously *T. duchartrei* has been reported in the Western Ghats of India and was considered an endemic species to the region. (Nazarudeen & Sabu, 2002; Shaiju & Omanakumari, 2009; 2010) (Figure 7: A). Since our discovery of *T. duchartrei* in Sri Lanka the species can no longer be considered as an endemic taxon to India. The topography and anthropogenic activities are the most important factors affecting the distribution of vegetation (Wang *et al.*, 2015). It was globally recognized that progressive habitat fragmentation caused by human activities has resulted in a reduction of biodiversity (Mullu, 2016; Rogan & Lachen, 2018). The dominant soil type of the Kandy district is reddish brown laterite which is more prone to erosion (Moormann & Panabokke, 1961). The new locations of *T. duchartrei* were rocky, steep hills with the same soil type and high soil erosion. In addition, the existence of exotic invasive species, anthropogenic habitat modifications, and fragmentation of the landscape may also have affected the dispersal of *T. duchartrei* over large areas.

The influence on the distribution of vegetation by reduction in propagation, availability of pollinators, dispersal vectors, and survival capacity of seedlings has been well documented in fragmented areas (Benitez-Malvido & Martinez-Ramos, 2003). Similar low abundance of animal pollinators and a high rate of seedling mortality were observed in our study areas. These natural geological and biological factors, including human activities could be a hindrance to species richness and survival in both locations.

Ecology: Polthenna is a rocky and steeply sloped hill area at an altitude 200 – 213 m. Seventy plants were observed growing with *Cinnamomum* species, *Panicum*

maximum Jacq., *Atrocarpus nobilis* Thw., *Atrocarpus heterophyllus* Lam., *Piper nigrum* L., *Hevea brasiliensis* (A. Juss) Muell. Arg., *Coffea arabica* L., *Macaranga peltata* (Roxb.) Muell. Arg., *Clidemia hirta* (L.) D. Don, *Alstonia macrophylla* Wall. ex G. Don and *Adiantum* species. Ihalagama is a slightly sloped hill area at an altitude 265 m. *Adiantum* species, *C. arabica*, *Costus speciosus* (J. Koenig) Sm. and naturalized ornamental plants were the common species in the area (Figure 7: B & C).

Conservation status

T. duchartrei could be considered as a critically endangered species based on the IUCN Red list categories and criteria, version 3.1, and present records. It is not currently protected by legislation despite the high conservation value to the flora of Sri Lanka. Therefore, for the future conservation of this species, it is suggested that an official Red List assessment and further studies using *in situ* and *ex situ* conservation need to be undertaken. The related species, *T. siliquosa* is found in low country and mid country wetland secondary forest and it is currently in the least concern category of the National red list of Sri Lanka (Wijesundara *et al.*, 2020). We observed isolated patches of *T. siliquosa* in human settlement areas adjacent to the forest reserves, in agricultural fields, and beside streams and foot trails. However, gradual but not immediate elimination of the common species *T. siliquosa* from natural ecosystems was noted. *Ex situ* conservation measures are in place at Link Natural nursery in Sri Lanka.

CONCLUSION

The discovery of *T. duchartrei* marks a new addition to the known flora of Sri Lanka. Modifications of the flower characters and androecium plasticity in the Sri Lankan specimens were highly significant and reconfirmed the high variability of morphological characters of the genus *Thottea*. This is the first report of *T. duchartrei* occurring outside of India and it increases the total number of Aristolochiaceae species from 4 to 5 and *Thottea* species from 1 to 2 in the flora of Sri Lanka.

Acknowledgements

The authors thank Dr. P. N. Shaiju Fatima Mata from the National College Kerala for his insightful comments and advice with the identification of *T. duchartrei* and Dr. Irina V. Belyaeva-Chamberlain for useful nomenclatural guidance and support. We also thank Mr. Samarajeewa for his assistance during field work in Sri Lanka. The authors

gratefully acknowledge Link Natural Products (Pvt) Ltd for technical and financial support and are grateful for the comments of two anonymous reviewers which have helped to improve the manuscript.

REFERENCES

- Anilkumar E.S., Mathew D., Nishanth K.S., Dileep K.B.S. & Latha P.G. (2014). A Comparative study on the in-vitro antimicrobial activity of the roots of four *Thottea* species. *International Journal of Pharmacy and Pharmaceutical Sciences* **6**(10): 444–447.
- Ashton P.S. & Gunatilleke C.V.S. (1987). New light on the plant geography of Ceylon. I. Historical plant geography. *Journal of Biogeography* **14**: 249–285. DOI: <https://doi.org/10.2307/2844895>
- Ashton P.M., Gunatilleke C.V.S., Zoyza N., Dassanayake M.D., Gunatilleke I.A.U.N. & Wijesundara S. (1997). Introduction to the flora. In: *A Field Guide to the Common Trees and Shrubs of Sri Lanka*, pp.1–3. WHT Publications (Pvt) Ltd., Sri Lanka.
- Beentje H. (2010). *The Kew Plant Glossary: An Illustrated Dictionary of Plant Identification Terms*, 1st edition, pp.1–160. Royal Botanic Gardens, Kew, Richmond, Surrey, TW9 3AB, UK.
- Benitez-Malvid J. & Martinez-Ramos M. (2003). Impact of forest fragmentation on seedling abundance in a tropical rain forest. *Conservation Biology* **12**: 380–389. DOI: <https://doi.org/10.1111/j.1523-1739.1998.96.295.x>
- Bossuyt F. et al. (13 authors) (2004). Local endemism within the Western Ghats - Sri Lanka Biodiversity Hotspot. *Science* **306**: 479–481.
- Caruso C.M. (2006). Plasticity of inflorescence traits in *Lobelia siphilitica* (Lobeliaceae) in response to soil water availability. *American Journal of Botany* **93**(4): 531–538. DOI: <https://doi.org/10.3732/ajb.93.4.531>
- Cuénoud P., Savolainen V., Chatrou L.W., Powell M., Grayer R.J. & Chase M.W. (2002). Molecular phylogenetics of Caryophyllales based on nuclear 18S rDNA and plastid *rbcl*, *atpB*, and *matK* DNA sequences. *American Journal of Botany* **89**(1): 132–144.
- Duchartre P.E.S. (1864). Aristolochiaceae. In: *Prodromus Systematis Naturalis Regni Vegetabilis* 15 (ed. A.P. de Candolle), pp. 421–498. Sumptibus Sociorum Treuttel & Würtz, Paris, France.
- Fatimah S.S., Maryati M., Mohd Fadzelly A. & Cuevas A.L. (2018). Phytochemical profiling and antimycobacterial activity of ethnomedically selected *Thottea* species (Aristolochiaceae) from Peninsular Malaysia. *Journal of Engineering and Applied Sciences* **13** (Spec.Iss.3): 1–9. DOI: <http://doi.org/10.36478/jeasci.2018.3110.3118>
- Gunatilleke N., Gunatilleke S. & Ashton P.S. (2017). South-west Sri Lanka: a floristic refugium in South Asia. *Ceylon Journal of Science* **46**(5): 65–78. DOI: <http://doi.org/10.4038/cjs.v46i5.7454>
- Gunawardene N.R. et al. (11 authors) (2007). A brief overview of the Western Ghats-Sri Lanka biodiversity hotspot. *Current Science* **93**: 1567–1572.
- Heart T.R., Somaratne S. & Wickremasinghe K.L. (1999). Aristolochiaceae. In: *A Revised Handbook to the Flora of Ceylon*, volume 13 (eds. M.D. Dassanayake & W.D. Clayton), pp. 11–22. Oxford and IBH Publishing Co. Pvt. Ltd, New Dehli, India.
- Hooker J.D. (1890). *The Flora of British India* 5, pp. 72–74. L. Reeve & Co., London, UK.
- Hou D. (1981). Florae Malesianae Praecursores LXII On the genus *Thottea* (Aristolochiaceae). *Blumea* **27**: 301–332.
- Huber H. (1985). Samenmerkmale und Gliederung der Aristolochiaceen. *Botanische Jahrbücher für Systematik, Pflanzengeschichte und Pflanzengeographie* **107**: 277–320.
- IUCN (2001). *IUCN Red List Categories and Criteria: Version 3.1*, IUCN Species Survival Commission, IUCN, Gland, Switzerland and Cambridge, UK.
- John J.A., Jose J.O., George V., Pradeep N.S. & Sethuraman M.G. (2008). Volatile constituents and antibacterial activity of leaf oil of *thottea ponmudiana* Sivar. *Journal of Essential Oil Research* **20**(5): 460–463.
- Kelly L.M. (2001). Taxonomy of *Asarum* section *Asarum* (Aristolochiaceae). *Systematic Botany* **26**: 17–53. DOI: <https://doi.org/10.1043/0363-6445-26.1.17>
- Klotzsch F. (1859). Die Aristolochiaceae des Berliner Herbariums. *t.1. Monatsberichte der Königlich Preussischen Akademie der Wissenschaften zu, Berlin*, pp. 571–626.
- Koottasseri A., Babu A., Augustin A., Job J.T. & Narayanankutty A. (2020). Antioxidant, anti-inflammatory and Anticancer activities of methanolic Extract of *Thottea siliquosa*: an in vitro study. *bioRxiv*.
- Lee S.Y., Ng W.L., Mahat M.N., Nazre M. & Mohamed R. (2016). DNA barcoding of the endangered *Aquilaria* (Thymelaeaceae) and its application in species authentication of agarwood products traded in the market. *PloS one* **11**(4): e0154631. DOI: <https://doi.org/10.1371/journal.pone.0154631>
- Leins P., Erbar C. & Heel W.A. (1988). Note on the floral development of *Thottea* (Aristolochiaceae). *Blumea* **33**: 357–370.
- Madhumita M. (2013). Taxonomic revision of the family Aristolochiaceae Juss. in India. *PhD thesis*, Kalyan University, West Bengal, India.
- Merrine R. & Ramesh B. (2012). Phytochemical investigation and pharmacological activity in the root extracts of *Thottea siliquosa* Lam. *Asian Journal of Biological and Life Sciences* **1**(1): 72–75.
- Mittermeier R.A., Gil P.R., Hoffman M., Pilgrim J., Brooks T., Mittermeier C.G., Lamoreux J. & da Fonseca G.A.B. (2004). *Hotspots Revisited: Earth's Biologically Richest and Most Threatened Terrestrial Ecoregions*. CEMEX, Mexico City, Mexico.
- Moormann F.R. & Panabokke C.R. (1961). *Soils of Ceylon, A New Approach to the Identification and Classification of the Most Important Soil Groups of Ceylon*. The Government Press, Ceylon.
- Moorthy K., Punitha, T., Vinodhini, R., Mickymaray S., Shonga A., Tomass Z. & Thajuddin N. (2015). Efficacy of different

- solvent extracts of *Aristolochia krisagathra* and *Thottea ponmudiana* for potential antimicrobial activity. *Journal of Pharmacy Research* **9**(1): 35–40.
- Mullu D. (2016). A Review on the effect of habitat fragmentation on ecosystem. *Journal of Natural Sciences Research* **6**: 1–16.
- Nazarudeen A. & Sabu T. (2002). Staminal instability in *Thottea duchartrei*. *Indian Journal of Forestry* **25**(2): 194–195.
- Nishida R., Weintraub J.D., Feeny P. & Fukami H. (1993). Aristolochic acids from *Thottea* spp. (Aristolochiaceae) and the osmeterial secretions of *Thottea*-feeding troidine swallowtail larvae (Papilionidae). *Journal of Chemical Ecology* **19**: 1587–1594.
DOI: <https://doi.org/10.1007/BF00984899>
- Nusaiba S.A.W. & Murugan K. (2013). In vitro analysis on bactericidal screening and antioxidant potentiality of leaf and root extracts of *Thottea siliquosa* (Lam.) Ding Hou. An ethnobotanical plant. *Asian Pacific Journal of Tropical Biomedicine* **3**(11): 859–865.
- Oelschlägel B., Wagner S., Salomo K., Pradeep N.S., Yao T.L., Isnard S., Rowe N., Neinhuis C. & Wanke S. (2011). Implications from molecular phylogenetic data for systematics, biogeography and growth form evolution of *Thottea* (Aristolochiaceae). *Gardens' Bulletin Singapore* **63**(1&2): 259–275.
- Perry L.M. & Metzger J. (1980). *Medicinal Plants of East and Southeast Asia: Attributed Properties and Uses*, pp. 620. MIT Press, USA.
- POWO (2021). Plants of the World Online. Facilitated by the Royal Botanic Gardens, Kew. Available at <http://www.plantsoftheworldonline.org/>, Accessed 23 August 2021
- Renuka C. & Swarupnandan K. (1986). Morphology of the flower in *Thottea siliquosa* and the existence of staminodes in Aristolochiaceae. *BLUMEA* **31**: 313–318.
- Rogan J.E. & Lacher T.E. (2018). Impacts of habitat loss and fragmentation on terrestrial. In: *Reference Module in Earth Systems and Environmental Sciences* (ed. S.A. Elias), pp. 1–18. Elsevier, Oxford, UK.
DOI: <http://dx.doi.org/10.1016/B978-0-12-409548-9.10913-3>
- Sabran S.F., Mohamed M. & Abu Bakar M.F. (2016). Ethnomedical knowledge of plants used for the treatment of tuberculosis in Johor, Malaysia. *Evidence-Based Complementary and Alternative Medicine* **2016**: 2850845.
DOI: <https://doi.org/10.1155/2016/2850845>
- Shaiju P.N. & Omanakumari N. (2009). Inflorescence morphology and systematics of the genus *Thottea* Rottb. (Aristolochiaceae) from the Western Ghats, India. *Systematics and Biodiversity* **7**(4): 445–451.
DOI: <https://doi.org/10.1017/S1477200009990181>
- Shaiju P.N. & Omanakumari N. (2010). Floral morphology and systematics of the genus *Thottea* Rottb. (Aristolochiaceae) from the Western Ghats, India. *Plant Systematics and Evolution* **288**: 213–225.
DOI: <https://doi.org/10.1007/s00606-010-0326-x>
- Sivarajan V.V., Balachandran I. & Babu A. (1986). A new species of *Thottea* Rottb. (Aristolochiaceae) with notes on the identity of *Thottea siliquosa* (Lam.) Ding Hou. *Indian Journal of Forestry* **8**(4): 265–268.
- Solereder H. (1894). Aristolochiaceae. In: *Die natürlichen Pflanzenfamilien* 3 (eds. A. Engler & K. Prantl), pp. 264–273.
- Sunil C.N. & Kumar V.V.N. (2014). *Thottea adichilthottiana* (Aristolochiaceae), a new species from Ernakulam, Western Ghats, India. *Webbia* **69**(2): 239–242.
DOI: <https://doi.org/10.1080/00837792.2014.951205>
- The World Checklist of Vascular Plants (WCVP). Checklist Data set. Royal Botanic Gardens, Kew, Available at <https://doi.org/10.15468/6h8ucr>, Accessed 10 December 2020.
- Thiers B. (continuously updated). *Index Herbariorum*: A global directory of public herbaria and associated staff. New York Botanical Garden's Virtual Herbarium. Available at <http://sweetgum.nybg.org/science/ih/>, Accessed February 2020.
- Turland N.J. et al. (15 authors) (2018). International Code of Nomenclature for algae, fungi, and plants (Shenzhen Code) adopted by the Nineteenth International Botanical Congress Shenzhen, China, July 2017. Koeltz Botanical Books, Germany.
- Udayan P.S., George S., Tushar K.V. & Balachandran I. (2005). Medicinal plants used by the Kaadar tribes of Sholayar forest Thrissur district, Kerala. *Indian Journal of Traditional Knowledge* **4**(2): 159–163.
- Wang B.W., Zhang G.H. & Duan J. (2015). Relationship between topography and the distribution of understory vegetation in a *Pinus massoniana* forest in Southern China. *International Soil and Water Conservation Research* **3** (4): 291–304.
DOI: <https://doi.org/10.1016/j.iswcr.2015.10.002>
- Wijesundara S., Ranasinghe S., Jayasinghe H., Gunawardena N., Fonseka G. & Wijesooriya S. (2020). Angiosperms in Sri Lanka, In: *The National Red List 2020 of Sri Lanka*. Biodiversity Secretariat of the Ministry of Environment and National Herbarium, Department of National Botanic Gardens, Peradeniya, Sri Lanka.
- Zin N.M., Sarmin N.I., Ghadin N., Basri D.F., Sidik N.M., Hess W.M. & Strobel G.A. (2007). Bioactive endophytic streptomycetes from the Malay Peninsula. *FEMS Microbiology Letters* **274**(1): 83–88.
DOI: <https://doi.org/10.1111/j.1574-6968.2007.00819.x>

RESEARCH ARTICLE

Earthquake engineering

Seismic performance of stiffened steel box column with different corner stiffener arrangements: a numerical approach

T Thevega*, JASC Jayasinghe and KAS Susantha

Department of Civil Engineering, Faculty of Engineering, University of Peradeniya, Peradeniya, Sri Lanka.

Submitted: 02 June 2021; Revised: 20 January 2022; Accepted: 28 January 2022

Abstract: The purpose of this study is to investigate a stiffening method with numerical analysis to improve the performance of hollow steel box columns, which are commonly and widely used in highway bridges. The major issue with the hollow steel column is local and global buckling at the base under different loadings. There are several methods to prevent local buckling and also to enhance the strength and ductility of the hollow column. Here, the performance of the steel column is improved by adding longitudinal (vertical and corner) and transverse stiffeners inside the column. In this research, the stiffened steel columns are numerically analysed by finite element method incorporating material and geometric non-linearities under constant axial and lateral cyclic loadings. From three different hardening models, the combined hardening material model is used for the steel material for the numerical analysis based on performance. The analytical results clearly show that the strength is improved by stiffening the column in the middle of the plates using vertical stiffeners, and the ductility is improved by stiffening the column at the corners using corner plates. The corner stiffeners avoid faster degradation of strength and also increase the lateral load-carrying capacity at maximum displacement level. It is clear from the numerical results that the overall performance of the hollow steel column is improved with vertical and corner stiffeners.

Keywords: Cyclic analysis, ductility, non-linear finite element analysis, steel column, stiffener arrangements, strength.

INTRODUCTION

Steel columns are commonly used in elevated highway systems because of their high strength and torsional rigidity. Also, the contribution of the steel column

becomes important in the construction, as they are cost-effective, sustainable, durable, ductile, and safe. The steel columns are susceptible to damage when subjected to severe lateral deformations that occur due to earthquake loadings. This damage is mainly due to the local buckling of plates and global buckling of the column. In past decades, investigations on the strength and ductility of steel columns under cyclic and dynamic loading have been widely carried out analytically and experimentally by many researchers (Kumar & Usami, 1996; Usami & Ge, 1998; Zheng *et al.*, 2000; Mamaghani, 2004; Aoki & Susantha, 2005).

There are several retrofitting methods introduced by researchers to enhance the strength and ductility capacity of steel columns based on past analytical and experimental studies. One of the commonly used methods is the concrete infilling of steel tubes. In the case of steel bridge piers usually, concrete infilling is done partially, and the height of the concrete-filled in the steel piers can be adjusted to prevent the local buckling (Goto *et al.*, 1998; 2009; Tao *et al.*, 2008; 2015). Linearly tapered thin-walled steel columns can also be used to improve the performance by eliminating severe local buckling near the base of the column (Al-Kaseasbah & Mamaghani, 2019a; 2019b). The steel plates are constructed by different types of welding methods to investigate the sensitivity of ultimate strength and the failure mechanism (Khedmati *et al.*, 2007). To improve the ductility capacity, Low Yield Strength (LYS) steel has been investigated with steel bridge piers (Aoki &

* Corresponding author (thevegat@eng.pdn.ac.lk;  <https://orcid.org/0000-0001-7939-2876>)



This article is published under the Creative Commons CC-BY-ND License (<http://creativecommons.org/licenses/by-nd/4.0/>). This license permits use, distribution and reproduction, commercial and non-commercial, provided that the original work is properly cited and is not changed in anyway.

Susantha, 2015; He *et al.*, 2015; Li *et al.*, 2020a; 2020b). The effects of different types of stiffener arrangements are studied to prevent local buckling prior to overall buckling and to increase the overall buckling strength (Nishikawa *et al.*, 1998; Zhu *et al.*, 2006; Aizhu *et al.*, 2016; Qian & Astaneh-Asl, 2016).

In the first stage of recent work by Rajavijayan *et al.* (2019), a finite element model has been developed in ABAQUS for a previously tested steel box column (Susantha *et al.*, 2007). The analysis was carried out by simulating the same loading patterns of the experimental data from past literature (Tao *et al.*, 2008) with three different material models, namely, isotropic, kinematic, and combined hardening models. Comparisons were made between the test and predicted results. Then the analyses were repeated for different loading conditions using the combined hardening model, which was found to be the best material model (Rajavijayan *et al.*, 2019). As the second stage of improving the hollow steel columns, different cross-sectional configurations were proposed with constant cross-sectional area by changing the stiffener arrangement inside the column to select the optimum stiffener arrangement. The box column with vertical stiffeners and corner stiffeners are analysed separately. And also, the effects of different lateral cyclic loading patterns were studied with different cross-sections. It was found that the strength of the hollow steel box column could be improved by using the vertical stiffener arrangement, but the ductility was not significantly improved (Thevega *et al.*, 2021). Then corner stiffeners were found to enhance the ductility of the column.

In the present study, steel columns with vertical and corner stiffeners are proposed and numerically analysed to examine their effectiveness in strength and ductility improvement. Here, two cases with corner stiffeners only and a combination of corner stiffeners and vertical stiffeners are considered. The analyses are conducted under constant axial and lateral cyclic loadings.

MATERIALS AND METHODS

The methodology consists of a series of numerical analyses carried out using a finite element model in ABAQUS software, considering the effects of both material and geometric non-linearities. The reliability of prediction of this type of investigation highly depends on the details of the finite element model, such as material models, element types, mesh, boundary conditions, and solution technique. The finite element model was analysed with different hardening material models.

A suitable material model was selected to do further analyses after comparing numerical results with the experimental result. After that, three sets of columns with different cross-sectional configurations, designed by changing the number of vertical stiffeners and length of corner stiffeners, were analysed under lateral cyclic loading. Finally, the strength and ductility were compared using the envelope curves of these hysteretic curves.

Cross-sectional details

The vertical stiffeners are important to improve the performance of the column (Rajavijayan *et al.*, 2019). In addition, when the number of stiffeners of the same size is increased, the performance of the column improves. Figure 1 clearly shows the performance of the column (450 mm × 450 mm) with different numbers of stiffeners (n), which are the same size (length of the stiffener = 53 mm, the thickness of the plate and the stiffener = 5.8 mm). According to that, the cross-sections with two and four vertical stiffeners, with the same size of stiffeners, were selected for further analyses with different lengths of corner stiffeners.

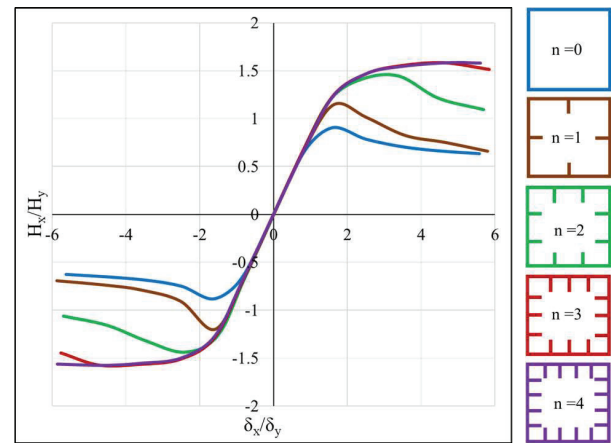


Figure 1: The variation of lateral force with lateral displacement (envelope curves)

Sixteen different cross-sectional configurations are proposed to investigate the effects of corner stiffeners and the combination of corner stiffeners with vertical stiffeners. All cross-sections are maintained as 450 mm × 450 mm in outer size. The height of the column is 2420 mm. In addition to the longitudinal stiffeners, three horizontal stiffeners (diaphragms) are provided at intervals of about 450 mm from the base of the column.

All the steel plates have welded connections (main plates, longitudinal stiffeners and transverse stiffeners). In this research, there are three different sets considered. In column Set-1, five cross-sections (C1-C5) are selected with only corner stiffeners by changing the length of the corner stiffener (cross-sectional configuration for the hollow box column is kept, as shown in Figure 2). The cross-sectional details are given in Table 1. The other two sets are defined with vertical and corner stiffeners.

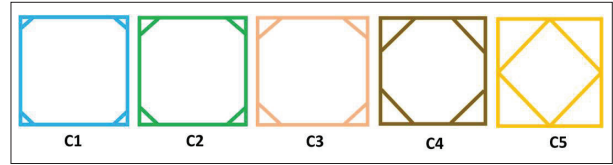


Figure 2: Different corner stiffeners arrangement in Set-1

Table 1: Cross-sectional details of the columns in Set-1

Cross-section	B,D (mm)	t (mm)	b _c (mm)	t _c (mm)
C1	450	5.8	59.5	5.8
C2	450	5.8	89.3	5.8
C3	450	5.8	119.0	5.8
C4	450	5.8	201.2	5.8
C5	450	5.8	310.0	5.8

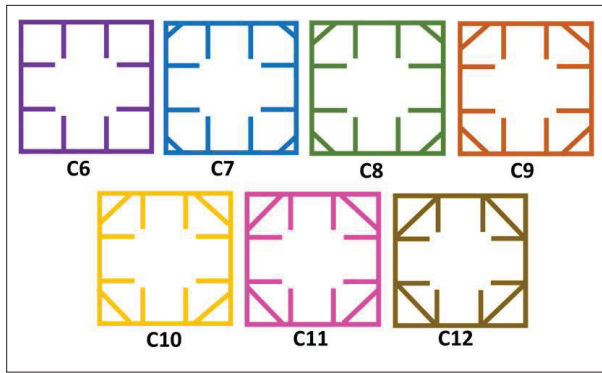


Figure 3: Different corner stiffener arrangements with vertical stiffeners in Set-2

Set-2 consists of columns (C6-C12) with two vertical stiffeners with corner stiffeners, and Set 3 includes the

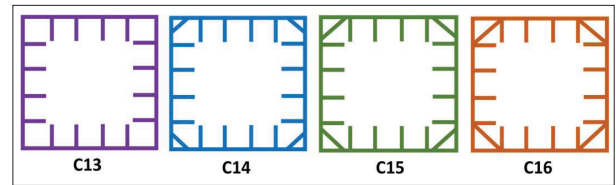


Figure 4: Different corner stiffener arrangements with vertical stiffeners in Set-3

columns (C13-C16) with four vertical stiffeners with corner stiffeners. The corner stiffeners are inserted in different lengths to study the effect of the corner stiffeners on the vertical stiffeners. The inclination of corner stiffeners with the outer plate is kept constant at 45 degrees for all the cases, as shown in Figures 3 and 4. Tables 2 and 3 show the cross-sectional details of columns Set-2 and Set-3.

Table 2: Cross-sectional details of the columns in Set-2

Cross-section	B,D (mm)	t (mm)	b _s (mm)	t _s (mm)	b _c (mm)	t _c (mm)
C6	450	5.8	53	5.8	-	-
C7	450	5.8	53	5.8	59.5	5.8
C8	450	5.8	53	5.8	89.3	5.8
C9	450	5.8	53	5.8	119.0	5.8
C10	450	5.8	53	5.8	144.0	5.8
C11	450	5.8	53	5.8	169.7	5.8
C12	450	5.8	53	5.8	201.2	5.8

Material model

For the proposed non-linear analysis procedure, both geometric and material non-linearity need to be incorporated as the columns are expected to deform beyond several times their yield displacement. Yield surface, flow rule, and stress-strain envelope of unidirectional loading curves are important in numerical simulation of material behaviour. Von Mises, Tresca, and Mohr-Coulomb are some yield criteria to define the yield surface where material undergoes yielding. The Von Mises yield criterion is commonly used in steel material models. The steel material can be differentiated with three different hardening rules (4) in the inelastic range, such as Isotropic Hardening (IH), Kinematic Hardening (KH) and Combined Hardening (CH). The IH rule states that the yield surface expands proportionally in all directions when stress exceeds its yield stress. The KH involves a translation of the yield surface without expansion of the surface. It is known as the Bauschinger effect. The CH rule states that the yield surface expands and translates in the direction of the stress rising.

Material properties

Three hardening material models were used with bilinear stress-strain material (see Figure 5). The bilinear stress-strain model was assumed from the trilinear material model, as shown in Figure 5. The steel material of grade SM490 (JIS - Japanese Industrial Standard) (Susantha et al., 2001), with material properties of yield stress (σ_y) = 412 MPa, Young modulus (E_s) = 206,000 MPa, Poisson ratio (ν) = 0.276, ϵ_{st}/ϵ_y (Elastic strain/ Yield strain) = 7, and E_{st}/E_s (Secant modulus/Tangent modulus) = 1/30 were used for the main plates, stiffeners and diaphragms.

Finite element model

The stiffened steel columns were modelled using the 4 node shell elements (S4R) in the ABAQUS program. The mesh sensitivity on the result was tested first, and the optimum element mesh was selected to maintain the accuracy of results and good computational efficiency. This is very important because the analyses involve severe

Table 3: Cross-sectional details of the columns in Set-3

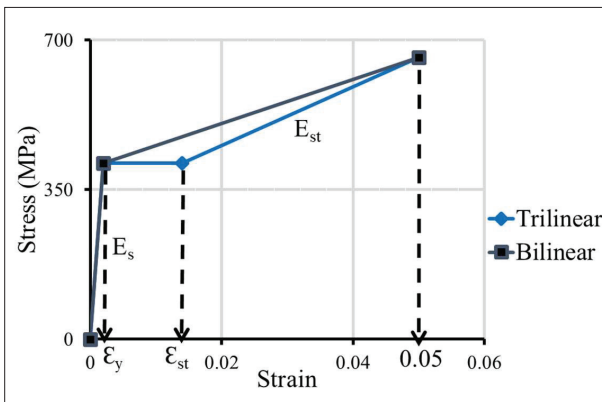
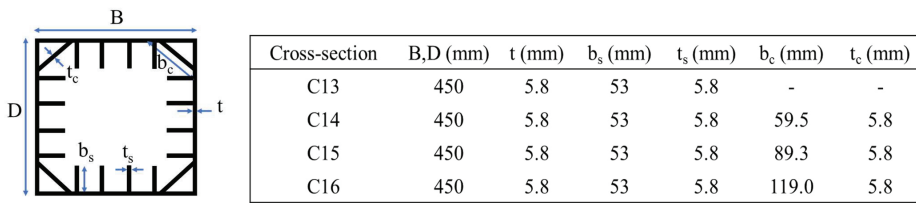


Figure 5: Stress-Strain relationship of steel

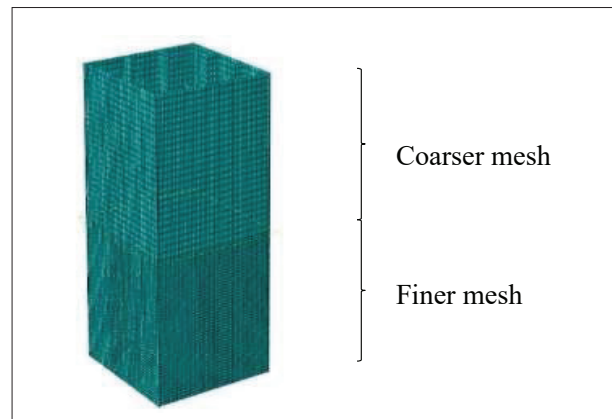


Figure 6: Finite element mesh

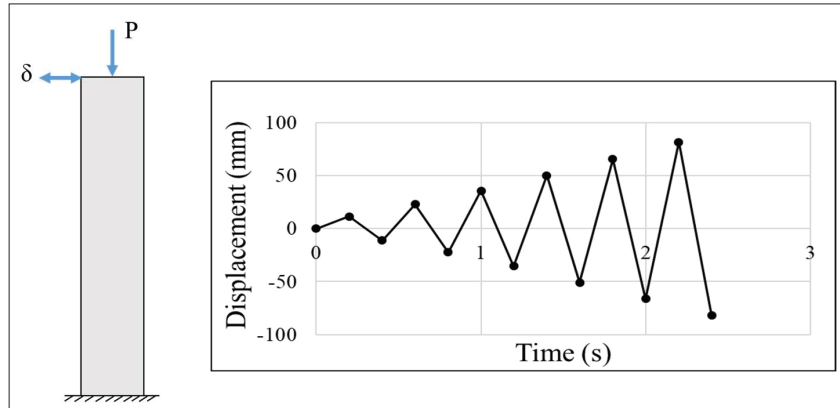


Figure 7: The loading arrangement on the column

non-linearity and are to be conducted for several cycles where each cycle needs a large number of increments. As a result, a finer mesh at the bottom where high stresses and buckling are expected and a coarser mesh at the top of the column were selected, as shown in Figure 6. All nodes at the bottom of the column are fixed.

Loading arrangement

For the numerical analysis, the loading arrangement used is the same as the experimental arrangement of the column in Susantha *et al.* (2007) (see Figure 7). First, the axial load ($P = 0.2 P_y$, $P_y = A_s \sigma_y$, where P_y is the yield axial load, A_s is the cross-sectional area and σ_y is the yield stress of steel) is applied at the top of the column, and next, lateral cyclic displacements are incrementally applied at the top for all the columns. The same loading pattern was employed for all the columns that have different cross-sectional configurations.

RESULTS AND DISCUSSION

Numerical simulation of stiffened steel box columns

The lateral load-lateral displacement hysteretic curves were normalized by corresponding yield load H_y and yield displacement δ_y (Susantha *et al.*, 2007), given in equations 1 and 2.

$$H_y = \frac{M_y}{h} \left(1 - \frac{P}{P_y} \right) \quad \dots(1)$$

$$\delta_y = \frac{H_y h^3}{3EI} \quad \dots(2)$$

Where,

H_y = Lateral yield load, δ_y = Lateral yield displacement, M_y = Bending moment at yield load, P = Axial load, P_y = Yield axial load, h = Height of column, E = Young’s modulus, and I = Second moment of inertia

The value of M_y is computed from equation 3.

$$M_y = \frac{\sigma_y I}{h} \quad \dots(3)$$

Validation and selection of the material model

Analyses were conducted using all three hardening models (IH, KH, and CH). The experimental result (Susantha *et al.*, 2007) and predicted results using IH, KH, and CH models were compared. It was found that among the three models, the CH model gave a relatively better comparison with experimental results, and a large difference in lateral load capacity was observed with the IH model (see Figure 8). Also, the combined hardening material model was performed as a combination of isotropic hardening and kinematic hardening material. Therefore, the CH model was identified as the most suitable material model to be used in the rest of the finite element analyses.

The performance of columns with only corner stiffeners

The results of the lateral load-lateral displacement curves of column Set-1 having different corner stiffener arrangements are shown in Figures 9 and 10. As shown in Figure 9, it is proved by using lateral load - lateral displacement curves without normalizing that the initial

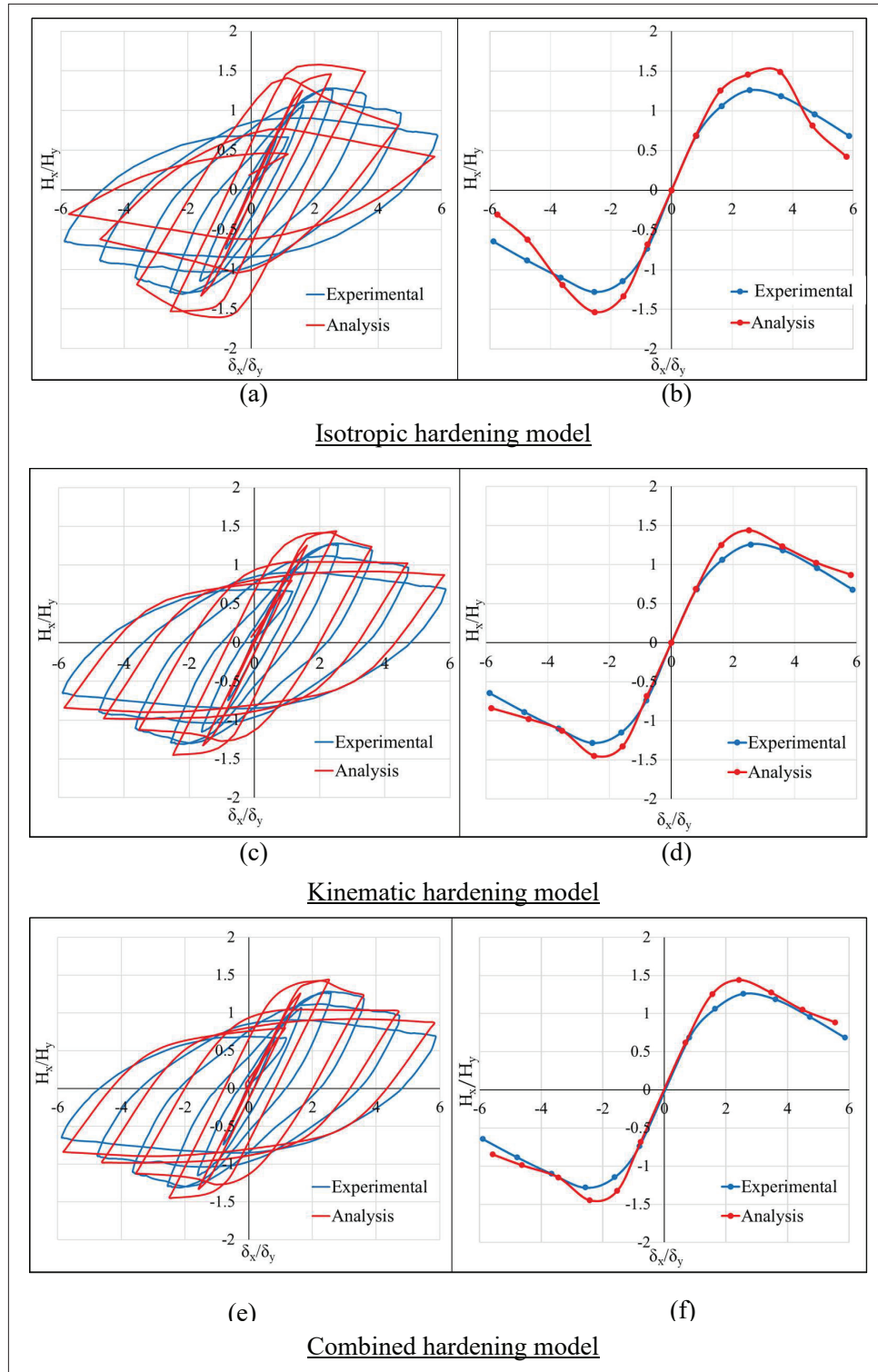


Figure 8: Normalized lateral load-lateral displacement curves (experimental versus analyses): (a) IH hysteresis, (b) IH envelope, (c) KH hysteresis, (d) KH envelope, (e) CH hysteresis and (f) CH envelope

stiffness of the columns increases with the length of the corner stiffeners. This fact should also be considered when deciding on the optimum cross-sectional shape. When the length of the corner stiffeners was increased, strength and ductility increased. However, when the length of the stiffener reaches its maximum while maintaining the same angle with outer plates, the maximum lateral load capacity is reduced.

The strength of the column is defined by index (H_m/H_y) , where H_m is the maximum lateral load (Ucak & Tsopelas, 2006). The cross-section type C4 gives the maximum strength. But the cross-section C3 performs better than C4 at the maximum lateral displacement as corner stiffeners start to buckle (see Figure 10). And also, the performance of the cross-section C4 is less than C2 between displacement levels of $4\delta_y$ and $5\delta_y$.

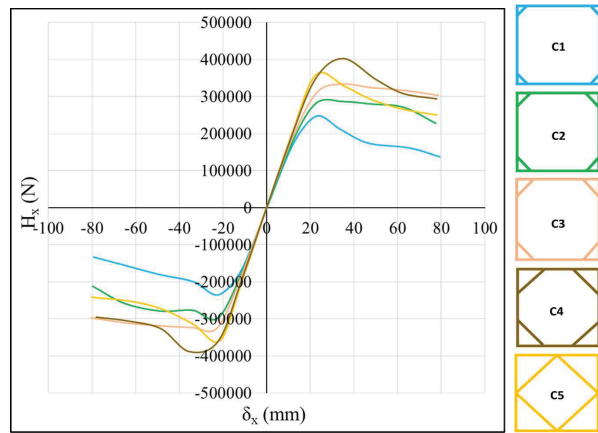


Figure 9: Lateral load versus lateral displacement curves for different corner stiffener arrangements

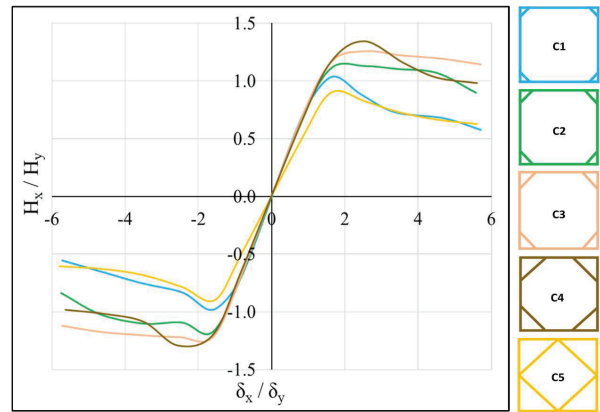


Figure 10: Normalized lateral load versus lateral displacement curves (Envelope curves) for Set-1

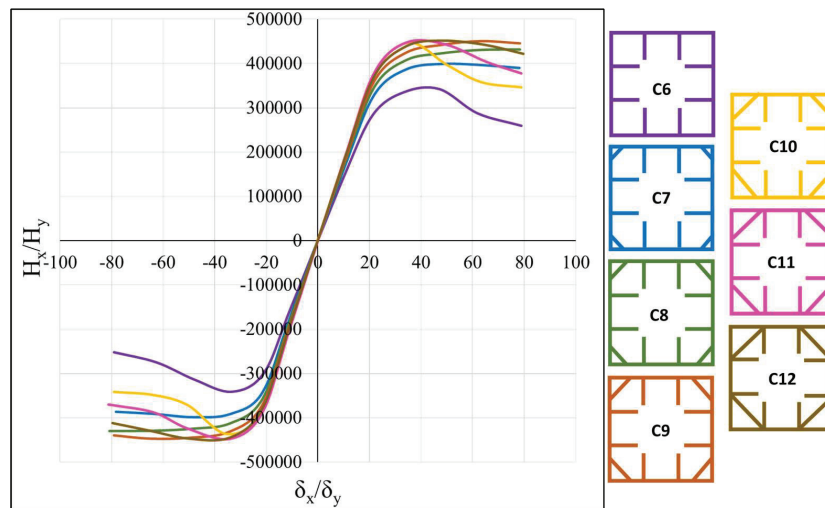


Figure 11: Lateral load versus lateral displacement curves for different corner stiffener arrangements with two vertical stiffeners

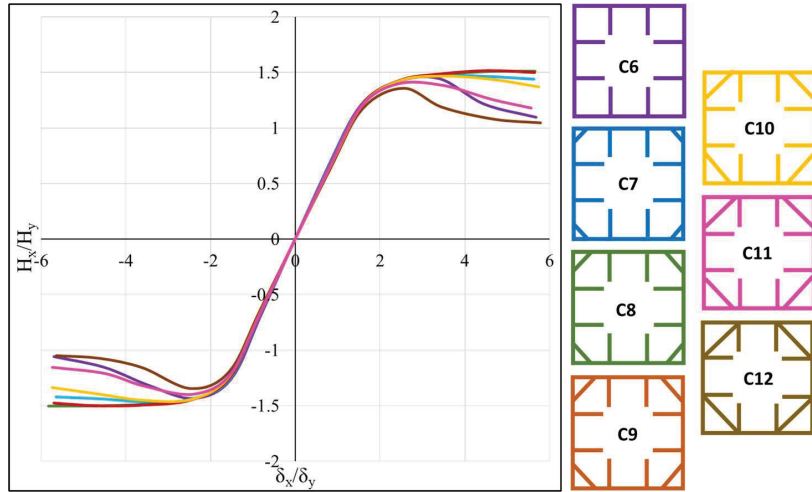


Figure 12: Normalized lateral load versus lateral displacement curves (Envelope curves) for Set-2

The performance of columns with two vertical stiffeners and corner stiffeners

Next, the effects of different corner stiffener arrangements with two vertical stiffeners were analysed. Figure 11 illustrates that the performance of the column is enhanced by increasing the second moment of area of the column in the elastic range. But the strength and ductility do not depend on the second moment of area in the plastic range.

After normalizing, the variation of lateral load with lateral displacement is shown in Figure 12. It clearly shows that the ductile behaviour is improved with corner stiffeners. However, it depends on the length of the corner stiffeners. The maximum lateral load capacity of cross-section C12 is less than that of cross-section C6. Even though the length of the corner stiffener in cross-section C9 is less than that in cross-sections C10, C11, and C12, the performance of C9 is high. The strength and ductility are improved with cross-section C9 when compared with other cross-sections.

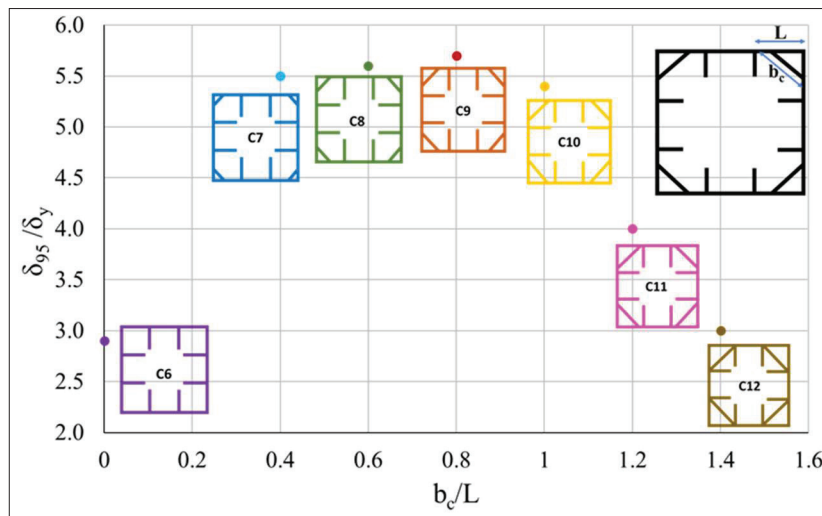


Figure 13: The variation of ductility index with different cross-sectional configurations of Set-2

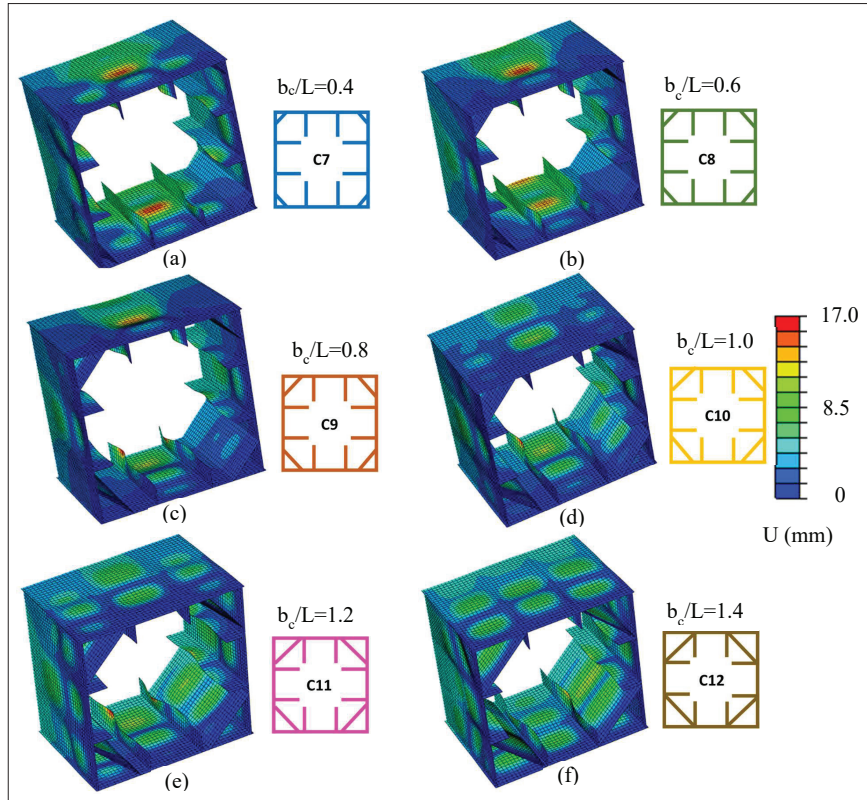


Figure 14: Deformed shapes for different cross-sectional arrangement of Set-2

After a particular length, the corner stiffener does not enhance the ductility of the column. The performance is drastically reduced, similar to the column without corner stiffeners. The strength of the cross-section C12 (with a maximum length of corner stiffener) is less than C6 (without corner stiffener). Therefore, it is important to select a length for a corner stiffener to be used effectively. There are two definitions for ductility (Gao & Ge, 2000; Aoki & Susantha, 2005) which can be defined as the ratio of lateral displacement at the maximum load to yield displacement (δ_m/δ_y) and the ratio of lateral displacement at 95% of the maximum load to yield displacement (δ_{95}/δ_y). Figure 13 shows the variation of the ductility index (δ_{95}/δ_y) with the ratio of the length of corner stiffener and space between vertical stiffeners (b_c/L) in Set-2. It is apparent that the ductility is drastically increased with different lengths of corner stiffeners, and also it is reduced by increasing the length of the corner plates. When the b_c/L ratio is equal to 0.8, the ductility is high as 5.7.

The buckling shapes are obtained at the end of the lateral displacement level for different cross-sectional configurations, as shown in Figure 14. It clearly shows that when b_c/L is less than 0.8, the outer plates start to buckle with vertical stiffeners prior to the corner plates. At $b_c/L = 0.8$, the corner stiffeners start to buckle. After that, outer plates, vertical stiffeners, and corner stiffeners perform together under cyclic loading.

The performance of columns with four vertical stiffeners and corner stiffeners

Finally, the effects of different corner stiffener arrangements with four vertical stiffeners were investigated. The lateral load - lateral displacement curves without normalizing are shown in Figure 15. It clearly shows that the maximum strength increases with the cross-sectional area of the columns.

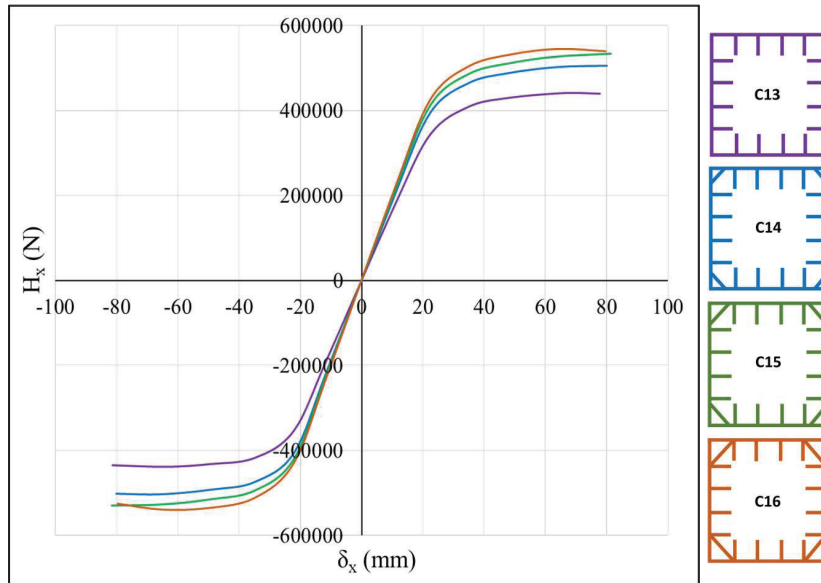


Figure 15: Lateral load versus lateral displacement curves for different corner stiffener arrangements with four vertical stiffeners

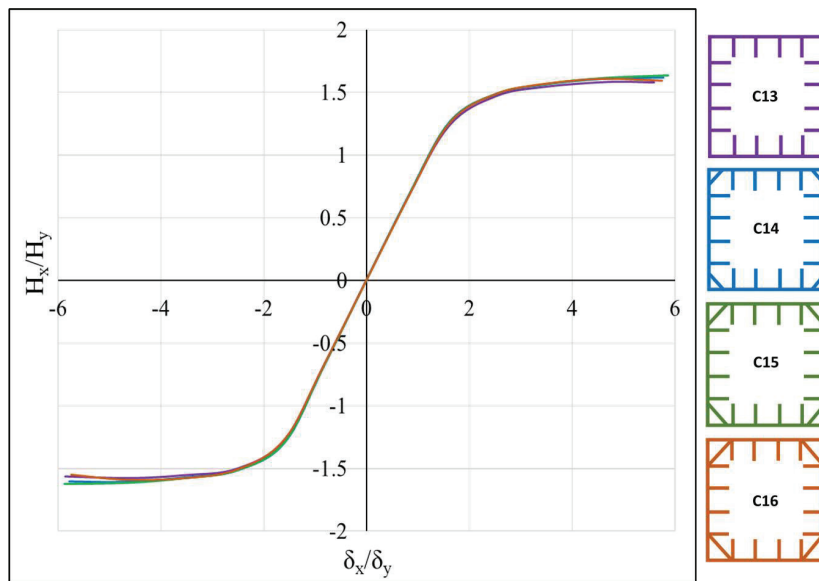


Figure 16: Normalized lateral load versus lateral displacement curves (Envelope curves) for Set-3

After normalizing by corresponding yield load H_y and yield displacement δ_y , the variation of lateral load with lateral displacement is shown in Figure 16. It clearly shows that the lateral load capacity and ductility are nearly the same for all cross-sections C13, C14, C15, and C16. Before normalizing, the lateral load capacity

increases with the second moment of area (see Figure 15). However, it is clear from Figure 16 that the performance of columns with four vertical stiffeners and corner stiffeners is approximately the same for all, even though the length of the corner stiffeners is different.

The variation of the ductility index (δ_{95}/δ_y) with (b_c/L) of Set-3 is shown in Figure 17. The ductility, which is slightly increased with the length of the corner stiffener, is high when b_c/L is 1.1. When the length of the corner stiffener increases from 59.5 to 89.3 mm with the same

size of vertical stiffeners, the ductility index increases from 5.8 to 5.9 and the length of the corner stiffener increases from 89.3 to 119.0 mm with the same size of vertical stiffeners, the ductility index decreases from 5.9 to 5.7.

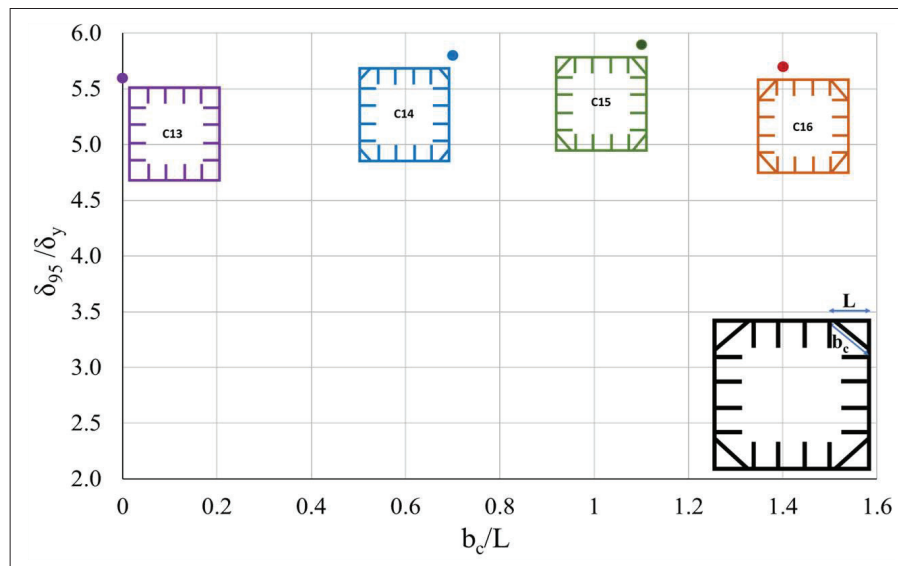


Figure 17: The variation of ductility index with different cross-sectional configurations of Set-3

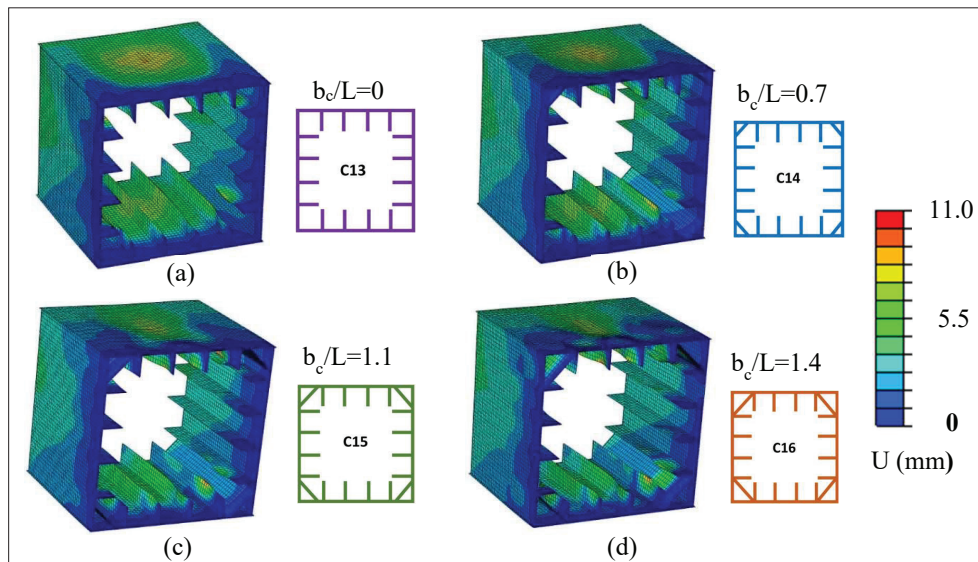


Figure 18: Deformed shapes for the different cross-sectional arrangement of Set-3

The deformed shape is obtained at the end of the lateral displacement level for different cross-sectional configurations, as shown in Figure 18. The buckling modes are comparatively the same for all cross-sections in column Set-3. Even though the length of corner stiffeners changes with cross-section, all cross-sections deform similarly. When the lateral load is applied, outer plates, vertical stiffeners, and corner stiffeners bear the load and delay the buckling.

Table 4 shows the comparison of strength and ductility of all cross-sections in columns Set-1, Set 2 and Set-3. The performance of the column depends on the number of stiffeners and the size of the stiffeners. And also, the b_c/L ratio plays a major role in the columns with corner stiffeners. The cross-sections C9 and C15 show better performance in Set-2 and Set-3, respectively. However, the performance of the cross-section C15 is higher than other cross-sections.

Table 4: The comparison of strength and ductility index of column Set-2 and Set-3

Cross-sections	b_c/L	H_m/H_y	δ_{95}/δ_y
C1	0.1	1.03	2.0
C2	0.2	1.15	3.4
C3	0.3	1.25	4.0
C4	0.5	1.34	2.9
C5	0.7	0.92	2.2
C6	0	1.45	2.9
C7	0.4	1.48	5.5
C8	0.6	1.50	5.6
C9	0.8	1.52	5.7
C10	1.0	1.47	5.4
C11	1.2	1.42	4.0
C12	1.4	1.36	3.0
C13	0	1.58	5.6
C14	0.7	1.62	5.8
C15	1.1	1.64	5.9
C16	1.4	1.60	5.7

CONCLUSIONS

In this study, numerical analyses have been conducted to examine the performance of steel hollow box columns by stiffening the outer plates with vertical and corner stiffeners arranged longitudinally. The analyses were conducted using the non-linear large deformation finite element method with the help of ABAQUS. Primarily, three sets of columns are considered as (1) Set-1: only corner stiffeners; (2) Set-2: corner stiffeners and two vertical stiffeners and (3) Set-3: corner stiffeners and four vertical stiffeners. The following are drawn as the key conclusions of this study.

The cross-sections having only corner stiffeners contribute significantly to increasing the ductility compared with those having only vertical stiffeners. However, the strength increase with corner stiffeners alone is lower than those with vertical stiffeners. Therefore, it is important to have vertical stiffeners to increase the strength (maximum lateral load).

In column Set-1, the size (length) and the arrangement of corner stiffeners play a major role in the ductility performance of columns. Increasing the length abruptly will not yield favourable results, as seen in the case of cross-section C5. There is an optimum length for the best performance.

With only corner stiffeners, after buckling, the strength gradually decreases, but with both types of stiffeners, there is no reduction in strength, and also ductility is greatly improved. Therefore, providing a combination of stiffeners (vertical and corner stiffeners) will give a more favourable performance.

The results of columns in Set-2 show the importance of the length of the corner stiffener. The strength and ductility depend on the length of the corner stiffener. When b_c/L increases from 0 to 0.8, the ductility increases by 97% and the strength increases by 5%. However, when b_c/L increases further from 0.8 to 1.4, there is a drastic drop in the performance. Even though the cross-section C12 has a larger length of corner stiffener, it was not useful for improving strength with corner plates. There is a huge difference in the lateral load capacity of C12, which is 7% less than C6 (without corner stiffener).

1. In column Set-3, the ductile behaviour of cross-section types C14, C15, and C16 is slightly better than that of cross-section C13 (without corner stiffeners).

And also, the maximum lateral load capacity, which is achieved, is nearly the same for all cross-sections. However, the cross-section C15 ($b_c/L = 1.1$) has high strength and ductility, which are increased by 4% and 6 % respectively compared to C13 ($b_c/L = 0$).

2. While comparing the performance of all cross-sections, the cross-section C15 with four vertical stiffeners and corner stiffeners ($b_c/L = 1.1$) can be selected for enhanced strength and ductility. When the column with cross-section C15 is compared with the column without stiffener (only having outer plates), there is a huge improvement in strength and ductility, by 41% and 181%, respectively.
3. When the length of the corner stiffener increases, the corner stiffeners perform together with the vertical stiffeners and outer plates. Therefore, the performance of columns with vertical and corner stiffeners depends on the b_c/L ratio. When b_c/L is equal to 0.8, the column shows high performance with two vertical stiffeners, and when b_c/L is equal to 1.1, the capacity is improved with four vertical stiffeners.

The strength and ductility of the column are enhanced with vertical and corner stiffeners. The length of the corner stiffener plays a major role with a given number of vertical stiffeners, and also different values perform optimally with different numbers of vertical stiffeners. From the numerical analyses, the number of stiffeners and the size of stiffeners can be selected to construct the column effectively.

Acknowledgement

The authors would like to express their acknowledgement for licensed applications of the ABAQUS package facilitated by the Finite Element Analysis and Simulation Centre, Rubber Research Institute of Sri Lanka, Ratmalana.

REFERENCES

- Aizhu, Z., Hongping, Z., Xiaowu, Z. & Yong L. (2016). Experimental study and analysis of inner stiffened cold-formed SHS steel stub columns. *Thin-walled Structures* **107**: 28–38.
DOI: <https://doi.org/10.1016/j.tws.2016.04.026>
- Al-Kaseasbah Q. & Mamaghani P.H.I. (2019a). Design and cyclic elastoplastic analysis of graded thin-walled steel tubular columns with enhanced strength and ductility. *International Journal of Modern Engineering* **19**.
- Al-Kaseasbeh Q. & Mamaghani P.H.I. (2019b). Buckling strength and ductility evaluation of thin-walled steel stiffened square box columns with uniform and graded thickness under cyclic loading. *Engineering Structures* **186**: 498–507.
DOI: <https://doi.org/10.1016/j.engstruct.2019.02.026>
- Aoki T. & Susantha K.A.S. (2005). Seismic performance of rectangular-shaped steel piers under cyclic loading. *Journal of Structural Engineering* **131**(02): 240–249.
DOI: [https://doi.org/10.1061/\(ASCE\)0733-9445\(2005\)131:2\(240\)](https://doi.org/10.1061/(ASCE)0733-9445(2005)131:2(240))
- Aoki T. & Susantha S. (2015). Application of low yield strength steel in steel bridge piers. *13th Conference on Earthquake Engineering*, Paper No. 339.
- Gao S. & Ge H. (2000). Eccentrically loaded steel columns under cyclic in-plane loading. *Journal of Structural Engineering* **126**(08).
DOI: [https://doi.org/10.1061/\(ASCE\)0733-9445\(2000\)126:8\(964\)](https://doi.org/10.1061/(ASCE)0733-9445(2000)126:8(964))
- Goto Y., Kumar P.G. & Kawanishi N. (2009). FEM analysis for hysteretic behavior of CFT bridge piers considering interaction between steel tube and infilled concrete. *Japan Society of Civil Engineers* **65**(02): 487–504.
DOI: <https://doi.org/10.2208/jsceja.65.487>
- Goto Y., Wang Q. & Obata M. (1998). FEM analysis for hysteretic behavior of thin-walled columns. *Journal of Structural Engineering* **124**(11): 1290–1301.
DOI: [https://doi.org/10.1061/\(ASCE\)0733-9445\(1998\)124:11\(1290\)](https://doi.org/10.1061/(ASCE)0733-9445(1998)124:11(1290))
- He H., Chen K. & Li R. (2015). Seismic performances of replaceable steel connection with low yield point metal. *Advances in Materials Science and Engineering* **2015**: Article ID 134189.
DOI: <https://doi.org/10.1155/2015/134189>
- Khedmati M.R., Ghavami K. & Rastani M. (2007). A comparative study on three different construction methods of stiffened plates strength behavior and ductility characteristics. *Revista Escola de Minas Ouro Preto* **60**(02): 365–379.
DOI: <https://doi.org/10.1590/S0370-44672007000200019>
- Kumar S. & Usami T. (1996). Damage evaluation in steel box columns by cyclic loadings. *Journal of Structural Engineering* **122**(06).
DOI: [https://doi.org/10.1061/\(ASCE\)0733-9445\(1996\)122:6\(626\)](https://doi.org/10.1061/(ASCE)0733-9445(1996)122:6(626))
- Li H., Lv K. & Cui R. (2020a). Seismic behavior of eccentrically compressed steel-box bridge-pier columns with embedded energy-dissipating shell plates. *Bulletin Earthquake Engineering* **18**(7): 3401–3432.
DOI: <https://doi.org/10.1007/s10518-020-00830-2>
- Li H., Luo W. & Luo J. (2020b). Seismic performance of steel box bridge piers with earthquake-resilient function. *Advances in Civil Engineering* **2020**: Article ID 8877785.
DOI: <https://doi.org/10.1155/2020/8877785>
- Mamaghani P.H.I. (2004). Seismic design and retrofit of thin-walled steel tubular columns. *13th World Conference on Earthquake Engineering*, Paper No. 271.
- Nishikawa K., Yamamoto S., Natori T., Terao K., Yasunami H. & Terada M. (1998). Retrofitting for seismic upgrading of steel bridge piers. *Engineering Structures* **20**: 540–551.

- DOI: [https://doi.org/10.1016/S0141-0296\(97\)00025-4](https://doi.org/10.1016/S0141-0296(97)00025-4)
- Qian X. & Astaneh-Asl A. (2016). Behavior and seismic design of stiffeners for steel bridge tower legs and piers. *Proceedings of the World Congress on Civil, Structural, and Environmental Engineering (CSEE'16)*, Paper No. ICSENM 117.
DOI: <https://doi.org/10.11159/icsenm16.117>
- Rajavijayan K., Thevega T., Jayasinghe J.A.S.C. & Susantha K.A.S. (2019). Performance of steel bridge piers using lateral cyclic load analysis. *10th International Conference on Structural Engineering and Construction Management 2*: 251–257.
DOI: <https://doi.org/10.1080/13632460109350403>
- Susantha K.A.S., Ge H. & Usami T. (2001). A capacity prediction procedure for concrete-filled steel columns. *Journal of Earthquake Engineering* **5**(04): 483–520.
DOI: [https://doi.org/10.1016/S0263-8231\(98\)00027-5](https://doi.org/10.1016/S0263-8231(98)00027-5)
- Susantha S., Aoki T. & Jayasinghe R.T.M. (2007). Finite element analysis of steel columns subjected to bi-directional cyclic loads. *Journal of the Institution of Engineers, Sri Lanka* **40**(04): 35–41.
DOI: <https://doi.org/10.4038/engineer.v40i4.7152>
- Tao Z., Han L.H. & Wang D.Y. (2008). Strength and ductility of stiffened thin-wall hollow steel structural stub columns filled with concrete. *Thin-wall Structures* **46**(10): 1113–1128.
DOI: <https://doi.org/10.1016/j.tws.2008.01.007>
- Tao Z., Han L.H. & Wang D.Y. (2015). Experimental behavior of stiffened concrete-filled thin-walled hollow structural steel (HSS) stub column. *Journal of Constructional Steel Research* **61**: 962–983.
DOI: <https://doi.org/10.1016/j.jcsr.2004.12.003>
- Thevega T., Rajavijayan K., Jayasinghe J.A.S.C. & Susantha K.A.S. (2021). Strength and ductility of stiffened steel box columns of various cross-sectional configurations under lateral cyclic loadings. *Journal of the Institution of Engineers, Sri Lanka* **LIV**(02): 25–32.
DOI: <https://doi.org/10.4038/engineer.v54i2.7440>
- Ucak A. & Tsopelas P. (2006) Cellular and corrugated cross-sectioned thin-walled steel bridge- piers/columns. *Structural Engineering and Mechanics* **24**(03): 355–374.
DOI: <https://doi.org/10.12989/sem.2006.24.3.355>
- Usami T. & Ge B.H. (1998). Cyclic behavior of thin-walled steel structures - numerical analysis. *Thin-walled Structures* **32**: 41–80.
DOI: [https://doi.org/10.1061/\(ASCE\)0733-9445\(2000\)126:11\(1304\)](https://doi.org/10.1061/(ASCE)0733-9445(2000)126:11(1304))
- Zheng Y., Usami T. & Ge H. (2000). Ductility of thin-walled steel box stub columns. *Journal of Structural Engineering* **126**(11).
DOI: <https://doi.org/10.1016/j.tws.2016.04.026>
- Zhu A., Zhu H., Zhang X. & Lu Y. (2006). Experimental study and analysis of inner-stiffened cold-formed SHS steel stub columns. *Thin-walled Structures* **106**: 28–38.
DOI: <https://doi.org/10.1016/j.tws.2016.04.026>

RESEARCH ARTICLE

Nanomedicine

Effect of PEGylated gold nanorods on the circulating vascular endothelial growth factor, platelet-derived growth factor, and miR-29a in CD-1 mice

AM Gamal-Eldeen^{1*}, BM Raafat², CA Fahmy^{3,4}, MT Abo-Elfadl^{3,4}, SM El-Daly^{4,5} and MRK Ali⁶

¹ Clinical Laboratory Sciences Department, College of Applied Medical Sciences, Taif University, Taif 21944, Saudi Arabia.

² Radiological Sciences Department, College of Applied Medical Sciences, Taif University, Taif 21944, Saudi Arabia.

³ Biochemistry Department, National Research Centre, 33 El Buhouth St. Dokki, Cairo, 12622, Egypt.

⁴ Cancer Biology and Genetics Laboratory, Centre of Excellence for Advanced Sciences, National Research Centre, 33 El Buhouth St. Dokki, Cairo, 12622, Egypt.

⁵ Medical Biochemistry Department, National Research Centre, 33 El Buhouth St. Dokki, Cairo, 12622, Egypt.

⁶ Advanced Material Sciences and Nanotechnology Laboratory, Center of Excellence for Advanced Sciences, National Research Centre, Dokki, Cairo, 12622, Egypt.

Submitted: 25 August 2021; Revised: 05 February 2022; Accepted: 25 February 2022

Abstract: Gold nanorods (GNRs) show promising biomedical therapeutic/imaging applications. This study investigated the effect of PEGylated-GNRs on the angiogenesis factors: vascular endothelial growth factor (VEGF) and platelet derived growth factor (PDGF) and their regulator (miR-29a-3p) under variable administration conditions—dosage, gender, routes of administration, and post-treatment intervals. In CD-1 mice of both genders, PEG-GNRs (94, 375, 750, and 1500 ng/kg body weight, ~40 nm, aspect ratio ~4.5) were injected via different routes: intravenous, subcutaneous, and intramuscular, and then VEGF and PDGF were estimated in sera by ELISA, after post-treatment intervals (1, 3, and 7 days). Low doses of PEG-GNRs (94 and 375 ng/kg body weight) resulted in anti-angiogenic effects, while the highest dose (1500 ng/kg body weight) provoked a pro-angiogenic effect, especially in females and with intravenous route. The expression of miR-29a was significantly diminished in intravenous (IV) and intramuscular (IM) groups at day 7, in both males and females. miR-29a may be responsible for the increased VEGF in the highest PEG-GNRs dose, but it is not responsible for the inhibited VEGF and PDGF levels in low PEG-GNRs doses. The study recommends the consideration of the critical role of dose, gender, and route of administration in PEG-GNRs pro-angiogenic activity, in medical applications as a direct cancer therapy and as a drug delivery agent.

Keywords: Angiogenesis, gender, gold nanorods, miR-29a-3p, routes of administration, VEGF and PDGF.

INTRODUCTION

Gold nanoparticles (GNPs) have emerged as a promising candidate for photothermal therapy (PTT) and imaging agents for biomedical applications (Bansal *et al.*, 2020). Depending on the GNP's size, structure, and the suspension media, a narrow range of light frequencies stimulate the resonant conduction band electron oscillation. Rod-shaped gold nanoparticles (GNRs) have two surface plasmon bands resulting from the coherent electron oscillations (Kang *et al.*, 2020). The transverse plasmon band of GNRs occurs at ~520 nm. The longitudinal plasmon and much stronger band at longer wavelengths is controlled by the GNRs ratio of length and width (aspect ratio). GNRs of variable dimensions have been prepared which absorb within ~800–1200 nm, a range covering the biological water window, where water does not absorb, a diminished background fluorescence occurs, limited chromophores absorb, and consequently

* Corresponding author (aeldeen7@yahoo.com;  <https://orcid.org/0000-0002-4423-5616>)



This article is published under the Creative Commons CC-BY-ND License (<http://creativecommons.org/licenses/by-nd/4.0/>). This license permits use, distribution and reproduction, commercial and non-commercial, provided that the original work is properly cited and is not changed in anyway.

light can penetrate deeper into biological tissues. Those characteristics provide a promising clinical application and support the recommendation of GNR as a biomedical therapeutic/imaging agent (Bansal *et al.*, 2020).

In biological systems, the aggregates of GNRs regulate their affinity to cross cell membranes and to interact with cells (Okoampah *et al.*, 2020). Additionally, plasma comprises electrolytes and proteins that can modulate the active surface charge of GNRs and their state of aggregation. GNRs can be functionalized with poly(ethylene) glycol (PEG), a surface coat that is frequently used to prevent both the adsorption of GNRs to non-specific proteins and the aggregation of GNRs (Okoampah *et al.*, 2020). PEG-GNRs possess a strong surface plasmon band that provides fluorescence, absorption, and light scattering in the near-infrared (NIR) region and NIR induced-luminescence (Zong *et al.*, 2021). Accordingly, PEG-GNRs have been proved as contrast agents for *in vivo* bioimaging and as plasmonic PTT (PPTT) agents, via their efficient conversion of the absorbed light energy into heat (Mantri & Jokerst, 2020).

Angiogenesis, the development of new blood capillaries from current vessels, is essential for the growth and progression of tumours (Lugano *et al.*, 2020). Tumours cannot expand larger than a certain size (1–2 mm), as a result of deficiencies of oxygen and critical nutrients (Akbarpour Ghazani *et al.*, 2020). Accretion of inflammatory infiltrates and fibrosis provokes tissue resistance to the blood flow and accordingly oxygen delivery. Under these conditions, angiogenesis arises, dominating the upregulation of pro-angiogenic factors that stimulate the vascular remodelling and the development of new vessels (Alkilany & Murphy, 2010). Vascular endothelial growth factor (VEGF) and platelet derived growth factor (PDGF) are essential inflammatory angiogenesis promoters (Alkilany & Murphy, 2010). They bind to cell surface receptors that enhance the release of plasminogen activators and proteases, which degrade the basement membrane. This degradation stimulates cells to migrate, multiply, and differentiate into lumen-containing capillaries (Alkilany & Murphy, 2010). Measuring the angiogenic factors and their receptors in serum provides an important tool to follow-up cancer progression.

The inhibition of angiogenesis has been reported as a potential therapeutic modality for cancers, by abolishing their oxygen and nourishment supply and by preventing further proliferation and metastasis (Alkilany & Murphy, 2010; Lugano *et al.*, 2020). Many angiogenesis inhibitors have been discovered as potential treatments in various pathological angiogenesis-mediated disorders; one of

these is GNPs. Although studies have reported the varied biomedical uses of PEG-GNRs in sensing, imaging, PTT of cancer, antibody-targeting (Pan *et al.*, 2009), and drug delivery (Huang *et al.*, 2006), in addition to investigating the cytotoxicity and genotoxicity in cells (Abo-Zeid *et al.*, 2015a, b; Gamal-Eldeen *et al.*, 2016), no studies, to our knowledge, have explored the effect of PEG-GNRs in angiogenesis. Since VEGF and PDGF are essential cytokines for angiogenesis induction, the aim of this study is to investigate the influence of different routes of administration [intravenous (IV), subcutaneous (SC), and intramuscular (IM) injections], gender (male and female), PEG-GNRs dose (94–1500 ng/kg body weight), and post-treatment intervals (1, 3, and 7 days) on the circulating pro-angiogenic growth factors (VEGF and PDGF) and on their regulator (miR-29a-3p) in CD-1 mice.

MATERIALS AND METHODS

Materials

Male and female wild type CD-1 mice (5–6 weeks old; 18–20 g; n = 520) were divided into 26 groups (20 mice/group) (Theodor Bilharz institute, Cairo, Egypt) and maintained under controlled conditions (24°C, a 12 h light/dark cycle, drinking water and feed *ad libitum*) (UCCMA feed mill factories, Cairo, Egypt). After 10 d of acclimatization, mice experiments were performed, adhering to the guidelines for animal care of the Ethical Committee, National Research Centre, Cairo, Egypt, and followed the guidelines of National Institutes of Health (USA) for the animal care and use. Chemicals were purchased from Aldrich and Fisher, USA, unless mentioned.

Preparation of PEG-GNRs

Preparation of PEG-GNRs was carried out using the seed-mediated growth method described elsewhere (Nikoobakht & El-Sayed, 2003; Abo-zeid *et al.*, 2015b). The absorption spectrum of PEG-GNRs solution was measured using a Jasco UV-vis-near-infrared spectrophotometer, V-630. A JEOL JEM-100CXII Transmission electron microscope (TEM) type JEOL-JSGM T1230 was used to examine the morphology and particle size of the prepared nanoparticles. Quantitative gold analysis was estimated by ICP mass spectrometry (Tang *et al.*, 2020), using an Agilent 7500c (Agilent, Tokyo, Japan). Dilutions and concentrations of PEG-GNRs solution were precisely measured, spectrophotometrically.

Animal experiments

In order to compare the effect of gender, dose, and route of administration of the PEG-GNRs on angiogenesis factors, 3.75, 15, 30, and 60 ng Au/100 μ L injection volume were administered to CD-1 mice in physiological saline (equivalent to 94, 375, 750, and 1500 ng/kg body weight) by IV, SC and IM routes of administration. Each experiment included its corresponding control group (saline-administrated). These doses were selected according to a preliminary clearance study, under publication, which indicated that PEG-GNRs remained in tissues after seven days from the treatment and we selected 5% of LD50 (31.2 mg/kg body weight) to be the highest dose to use, with no adverse effects. Mice of 1500 ng/kg body weight were sacrificed after 1, 3 and 7 days of injections, while mice groups of other doses were sacrificed after 7 days post-injection. One mL of the blood was collected from the caudal vein of each mouse, using a restrainer, after immersion in 0.75% Bupivacaine, as a topical anaesthetic, for 30 s. After mice scarification, sera were obtained by centrifugation of mice blood at 3000 rpm/min at 4°C for 15 min, aliquoted and stored at - 80°C until analysis.

Evaluation of angiogenesis factors

Serum levels of VEGF and PDGF-BB of the 26 groups were evaluated by quantitative Solid Phase Sandwich ELISA using Mouse Quantikine ELISA Kit (R&D Systems, Minneapolis, MN), according to the manufacturer's instructions. Colour intensity was measured at 450 nm by a microplate reader (FLUOstar OPTIMA, BMG LABTECH GmbH, Offenburg, Germany).

Expression of miR-29a-3p

Total RNA including miRNA were extracted from the sera of mice (miRNeasy Serum/Plasma Kit; #217184; Qiagen, USA). In qRT-PCR analysis, cDNA was reverse-transcribed (miScriptII RT kit; #218061; Qiagen). The hsa-miR-29a-3p miRCURY LNA miRNA PCR Assay (YP00204698, Qiagen), similar to mmu-miR-29a-3p, was applied with miScript SYBR Green PCR Kit (#218073, Qiagen). The qRT-PCR protocol included 95°C for 10 min, followed by 40 cycles of 95°C for 10 s and 60°C for 60 s. RNU6B expression, endogenous normalization control, was analysed. Changes in Ct values (Ct) between RNU6B and miRNA were submitted for the relative expression calculations, the $2^{-\Delta\Delta CT}$ method, using this formula: ($\Delta\Delta Ct = \Delta Ct$ of the tested sample - ΔCt of the control sample). The relative miRNA expression was calculated by $\Delta\Delta Ct$ protocol

(Livak & Schmittgen, 2001), after normalization to U6 expression of control.

Statistical analysis

Statistical analyses were performed using SPSS version 22 (SPSS, Inc., Chicago, IL). The normality was assessed using the Shapiro-Wilk test. Data were normally distributed and presented as (means \pm SE). Comparisons between different groups were carried by one-way analysis of variance, followed by *post hoc* Tukey test. Correlations between variables were estimated using Pearson's correlation test. The level of significance was set at $p < 0.05$.

RESULTS AND DISCUSSION

A tumour initiates as a nonvascular mass of host-derived cells which multiply atypically. Intratumoral hypoxia occurs when the tumour grows far from the maximum effusion area of nearby vessels (around 200 μ m) (Lacal & Graziani, 2018). To confront hypoxia, tumour cells create new capillaries to sustain their needs, a mechanism that is strictly similar to normal angiogenesis (Nussenbaum & Herman, 2010). However, the walls of these abnormal capillaries are regularly made of endothelial cells (ECs) and tumour cells. VEGF is an important regulator of both vasculogenesis and angiogenesis, where it is capable of exciting microvascular EC propagation, enhance EC migration, as well as inhibiting EC apoptosis, and encouraging the development of new capillaries from preexisting vessels (Nussenbaum & Herman, 2010). High levels of VEGF and its receptor VEGFR-2 have been detected in several cancers. The diminution of VEGF signalling results in a dramatic drop in the tumour vascularity (Lacal & Graziani, 2018).

Characterization of PEG-GNRs

As indicated in Figure 1a, the prepared PEG-GNRs exhibited dual-absorption bands. The first band is at 530 nm. This band corresponds to the electrons perpendicular to the long rod axis and the so-called transverse plasmon absorption. The other absorption band appears at a lower energy end at 840 nm, corresponding to PEG-GNRs with an aspect ratio of ≥ 4.5 . Figure 1b showed the TEM graph of PEG-GNRs that corresponds to the absorption spectrum shown in Figure 1a. The sizes of the prepared PEG-GNRs are relatively uniform, with an average diameter of 8–9 nm, a length of 35–42 nm, and an aspect ratio of about 4.5. The higher extinction ratio of the longitudinal surface plasmon resonance peak to the transverse one, suggests that the percentage of PEG-GNRs in the solution is enormously high.

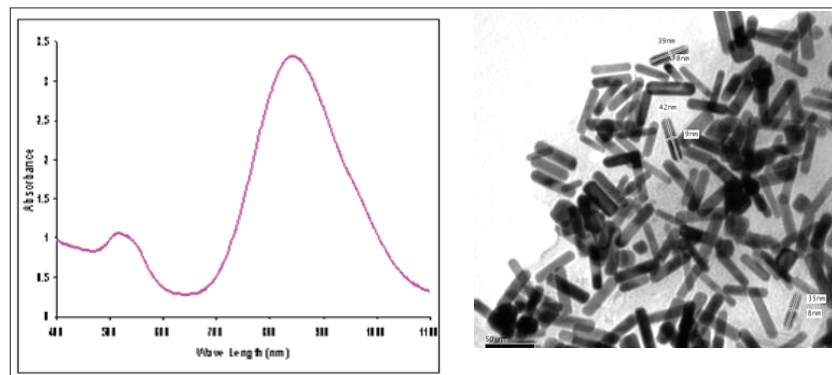


Figure 1: a. Ultraviolet-visible (UV-vis) extinction spectra of PEG-GNRs solutions. b. TEM images of PEG-GNRs

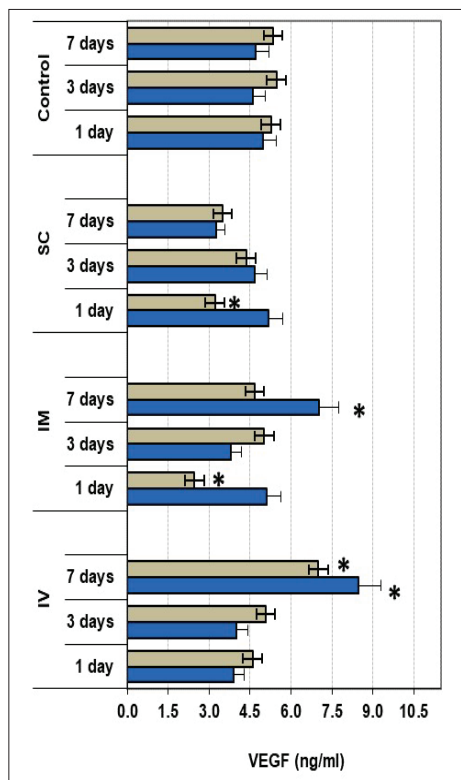


Figure 2: The effect of post-treatment intervals (1, 3, and 7 days) on serum VEGF concentration: female (blue bars) and male (grey bars) CD-1 mice were injected with PEG-GNRs (1500 ng/kg body weight) via intravenous (IV), subcutaneous (SC), and intramuscular (IM) routes. The results are expressed as mean \pm standard error. * $p < 0.05$; statistically significant from control mice.

Evaluation of vascular endothelial growth factor in sera

To investigate the influence of the administration routes, gender, and PEG-GNRs doses on the circulating pro-angiogenic growth factors in CD-1 mice, the effect of post-treatment interval on VEGF concentration was firstly investigated. Mice were treated with PEG-GNRs (1500 ng/kg body weight) using different routes of administration and then sacrificed after different intervals (1, 3, and 7 days). Among these groups, IV treatment induced serum VEGF ($p < 0.05$) in both genders only after 7 days (Figure 2). IM groups showed a significant VEGF induction ($p < 0.05$) only in females after 7 days, however a significant inhibition ($p < 0.05$) was observed in males after 1 day (Figure 2), compared to their corresponding controls. In SC groups, no change was observed in VEGF in females (Figure 2), while in males an inhibited VEGF was noticeable after one day. A high positive correlation coefficient was recorded between males and females VEGF in IV groups ($r = 0.988$), while there was no correlation between males and females in IM and SC groups.

As shown in Figure 3c, after 7 days post-injection, only the highest dose led to a highly significant elevation ($p < 0.01$) in VEGF in both genders, while low doses (94 and 375 ng/kg body weight) led to a significant reduction ($p < 0.05$) in VEGF only in IV males (Figure 3a). IM groups showed a significant VEGF reduction ($p < 0.05$) in males and females treated with low doses (94 and 375 ng/kg body weight), as shown in Figure 3b. The sharp increase in PEG-GNRs dose to 1500 ng/kg

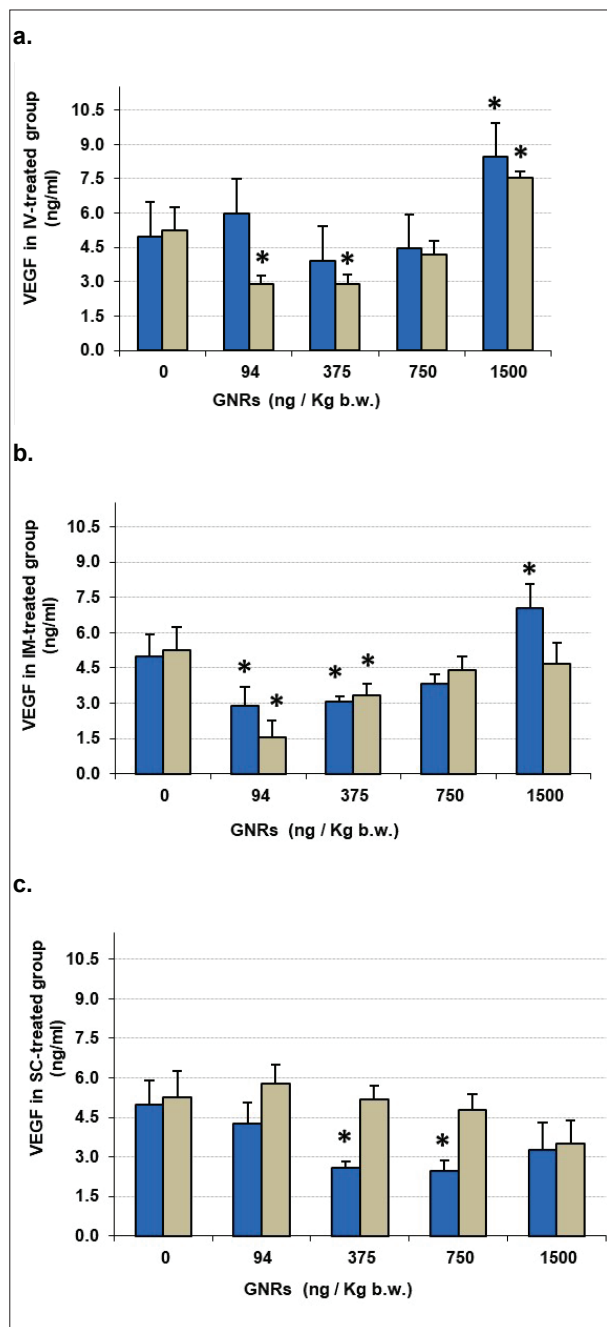


Figure 3: Effect of the administration routes, dose and gender on serum VEGF, after seven days of injection: Female (blue bars) and male (grey bars) CD-1 mice were injected with PEG-GNRs (0–1500 ng/kg body weight) via intravenous (IV) (a), intramuscular (IM) (b), and subcutaneous (SC) (c) routes. Results are expressed as mean ± standard error. *p < 0.05 and **p < 0.01; statistically significant from control mice.

body weight led to a high VEGF induction in females (p < 0.05) (Figure 3b). No change was found among all tested doses in SC male, while in females, the doses 375 and 750 ng/kg body weight suppressed VEGF levels (p < 0.05), Figure 3c.

Although there is a lack of studies of the effect of GNR on VEGF, several studies investigated the effect of other nanogold shapes as promising anti-angiogenic agents. The Mukherjee group has reported that naked GNP spheres inhibit angiogenesis through their binding to heparin-binding growth factors (including bFGF and VEGF165) and inhibit their activity (Mukherjee *et al.*, 2005; Bhattacharya & Mukherjee, 2008). The Pan group and Arvizo group have reported that GNP spheres significantly suppress the angiogenesis and growth of liver cancer cells and inhibit VEGF165-induced signalling (Pan *et al.*, 2009; Arvizo *et al.*, 2011). These data suggest that the inhibitory outcome of naked GNPs spheres results from their direct binding to VEGF165, which may be the same mechanism as GNRs, a suggestion that needs more investigation. In another study, Karthikeyan *et al.* (2010) have reported that big-size spheres (300 nm) noticeably block VEGF- and IL-1β-induced Src phosphorylation, cell growth, migration, and spreading of bovine retinal pigment epithelial cells. These reports support our findings that GNRs inhibit angiogenesis through suppressing VEGF, at low GNRs doses.

Evaluation of platelet-derived growth factor in sera

PDGF is another essential multi-role proangiogenic signalling molecule. It was initially purified from platelets; however, it has been recognized in ECs, astrocytes fibroblasts, and variable cell types. ECs express PDGF-BB receptors, and in case of receptor stimulation, an elevated DNA synthesis and angiogenic emergent can be detected. Pericytes (PCs) alleviate blood capillaries through cell-to-cell contact, and secrete PDGF (Thijssen *et al.*, 2018). Growth and migration of PCs, at the growing capillary are essentially stimulated by the interaction with PDGF (Thijssen *et al.*, 2018). Mice bred without PDGF-BB or its receptor display a dramatic elevation in the permeability of blood vessels, and they eventually died prenatally (Nussenbaum & Herman, 2010). It has been hypothesized that preventing PDGF from binding to its receptor will inhibit the growing stability of capillaries and prevent the delivery of nutrients to cancer cells (Nussenbaum & Herman, 2010).

In the current study, the effect of the post-treatment interval on PDGF concentration was investigated. Mice were treated with the highest PEG-GNRs dose. In IV males, a significant induction in serum PDGF ($p < 0.01$) was detected after all intervals, while in females PDGF was induced only after 7 days ($p < 0.01$) (Figure 4). An insignificant change in serum PDGF in IM groups observed after 1 and 3 days (Figure 4), while after 7 days, females and males had high PDGF levels ($p < 0.05$ and $p < 0.01$, respectively).

Surprisingly, in SC groups early after day 1 and day 3 of PEG-GNRs injection, PDGF showed a significant induction ($p < 0.01$) in females only, which decreased further after 7 days, whereas in males, the 7th day showed a significant elevation in PDGF ($p < 0.01$) (Figure 4). A direct correlation was found between the

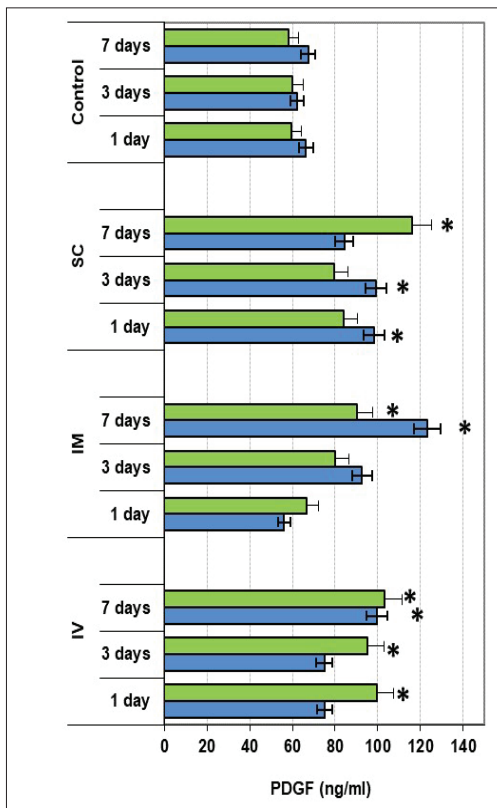


Figure 4: The effect of post-treatment intervals (1, 3, and 7 days) on serum PDGF concentration: female (blue bars) and male (green bars) CD-1 mice were injected with PEG-GNRs (1500 ng/kg body weight) via intravenous (IV), subcutaneous (SC), and intramuscular (IM) routes. The results are expressed as mean \pm standard error. * $p < 0.05$ and ** $p < 0.01$; statistically significant from control mice.

PDGF of males and females in both IV and IM groups ($r = 0.840$ and 0.999 , respectively). However, a reverse correlation was found between males and females PDGF in SC groups ($r = -0.997$).

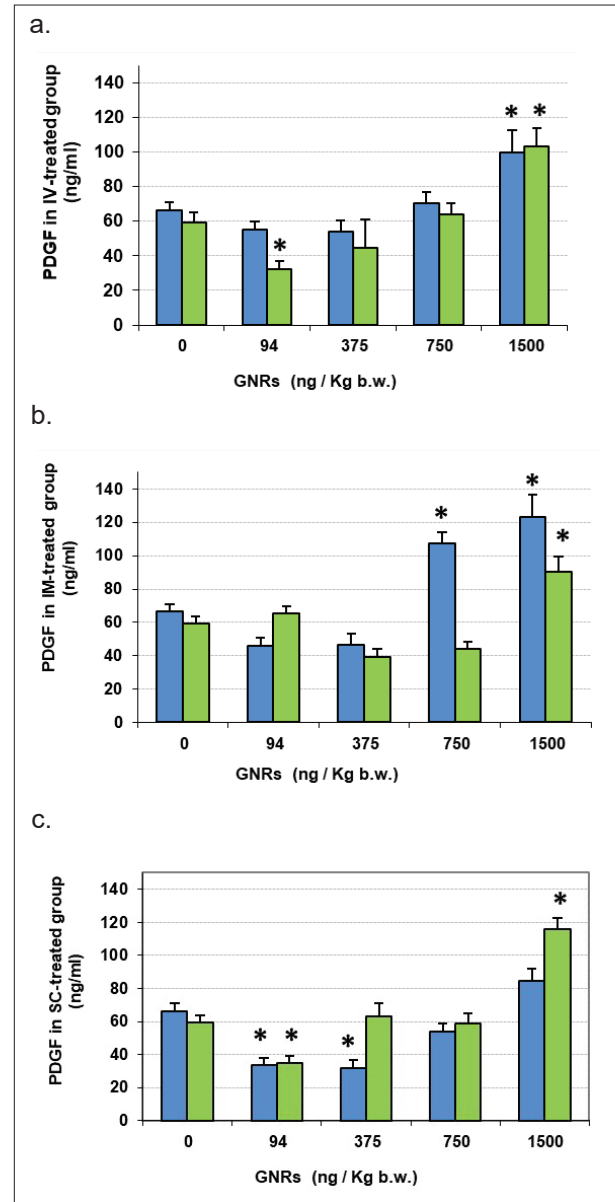


Figure 5: The effect of the administration routes, dose, and gender on serum PDGF, after seven days of injection: Female (blue bars) and male (green bars) CD-1 mice were injected with PEG-GNRs (0–1500 ng/kg body weight) via intravenous (IV) (a), intramuscular (IM) (b), and subcutaneous (SC) (c) routes. The results are expressed as mean \pm standard error. * $p < 0.05$ and ** $p < 0.01$; statistically significant from control mice.

The effect of dosage of PEG-GNRs on serum PDGF concentration was investigated using different doses and routes including IV- (Figure 5a), IM- (Figure 5b) and SC- (Figure 5c). After 7 days, IV injection of 1500 ng/kg body weight dramatically elevated PDGF ($p < 0.01$) in both genders (Figure 5a), while 94 ng/kg body weight inhibited PDGF ($p < 0.05$) in males (Figure 5a). PDGF displayed a significant elevation ($p < 0.01$ and $p < 0.05$) in females at high doses (750 and 1500 ng/kg body weight respectively), and in males only at 1500 ng/kg body weight, in the IM group (Figure 5b). In SC males treated with 94 ng/kg body weight, PDGF was reduced ($p < 0.05$), whereas 1500 ng/kg body weight of PEG-GNRs remarkably elevated PDGF ($p < 0.01$), (Figure 5c). In SC females, a noticeable inhibition ($p < 0.01$) of PDGF was observed at low doses (94 and 375 ng/kg body weight), (Figure 5c).

These findings suggest that low doses are capable of suppressing intratumoral angiogenesis and that particularly SC injection is a successful route to the desired biodistribution of PEG-GNRs and to diminish angiogenesis. There is a lack of studies in the published research that investigate the *in vitro* or *in vivo* effect of the gold nanostructures on PDGF. Most of the investigations were dealing with using gold aptamer conjugation to PDGF antibodies for detecting PDGF (Wang *et al.*, 2009). Cancer cells initiate angiogenesis via PCs spreading, which releases VEGF and stimulates the expression of PDGF by PCs though PDGF itself increases VEGF secretion. PDGF-BB over-expression is associated with elevated cell growth and tumour progression (Treiber *et al.*, 2009).

Expression of circulating miR-29a

The microRNA (miRNA) family includes single-stranded, small, non-coding RNAs, ~22 nucleotides, and is widely-expressed in cells and tissues (Lin *et al.*, 2020). They function mainly post-transcriptionally, where they regulate gene expression. VEGF-A was suggested to be a potential target gene of miR-29a (Chen *et al.*, 2014). Recently, it has been reported using luciferase assays and Western blot that the results confirmed that miR-29a can suppress the endogenous expression level of VEGF-A by binding to the 3'-untranslated region of VEGF-A (Zhao *et al.*, 2020).

The influence of PEG-GNRs on the expression of mmu-miR-29a-3p, which is one of the key regulators of VEGF and PDGF was investigated. The findings indicated that miR-29a expression was diminished in the

IV group at day 7 in both males and females ($p < 0.01$) as well as in SC males ($p < 0.05$) and females ($p < 0.01$), as demonstrated in Figure 6. These findings suggest that miR-29a may be responsible for the increased VEGF level in high doses of PEG-GNRs, but it is not responsible for the inhibited VEGF level in low doses. This conclusion was predicted from the non-significant change in miR-29a expression in day 1, which is in contrast with the VEGF level in Figure 2. Additionally, comparing PDGF results with the miR-29a expression indicated that the changes in PDGF level (Figure 4) were not regulated by miR-29a.

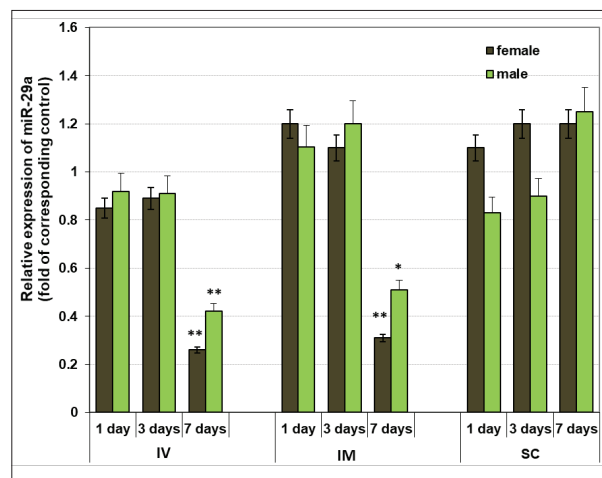


Figure 6: The effect of the administration routes, dose, and gender on the relative expression of circulating mmu-miR-29a-3p: CD-1 mice were injected with PEG-GNRs (1500 ng/kg body weight) via intravenous (IV), intramuscular (IM), and subcutaneous (SC) routes. Sera were collected from mice after 1, 3 and 7 days of injections. The results are expressed as mean \pm standard error. * $p < 0.05$ and ** $p < 0.01$ compared with the corresponding control. Control expression is 1-fold.

CONCLUSION

This study is the first *in vivo* investigation of the effect of safe doses of PEG-GNRs on the pro-angiogenesis growth factors VEGF and PDGF and their regulator miR-29a, and the influence of PEG-GNRs administration conditions: dosage, gender, routes of administration, and post-administration time intervals, on both factors. Taken together, the study's findings highlight the following conclusive remarks:

- Low doses (94 and 375 ng/kg body weight) resulted in

anti-angiogenic effects.

- The highest dose of PEG-GNRs (1500 ng/kg body weight) provoked pro-angiogenic effects.
- The intravenous route resulted in pro-angiogenic effects more than other routes.
- Females exhibited more pro-angiogenic effects than males.
- miR-29a is suggested to be responsible for VEGF increase at high dose.
- Anti-angiogenic low doses can be used in PPTT of cancer.
- Consideration should be taken with high doses, especially in the bioaccumulation and clearance studies of therapeutic doses.
- Special considerations should be taken regarding the influence of dose, gender, route of administration, and post-treatment intervals.

Acknowledgement

This work was supported by Taif University Researchers Supporting Project (Number TURSP-2020/103) and National Research Centre, Cairo, Egypt.

Conflict of interest

The authors declare no conflict of interest.

REFERENCES

- Abo-Zeid M.A.M., Liehr T., Gamal-Eldeen A.M., Zawrah M., Ali M. & Othman M.A.K. (2015a). Potential of rod, sphere and semi-cube shaped gold nanoparticles to induce cytotoxicity and genotoxicity in human blood lymphocytes in vitro. *European Journal of Nanomedicine* **7**: 63–75. DOI: <https://doi.org/10.1515/ejnm-2014-0031>
- Abo-zeid M.A.M., Liehr T., Gamal-Eldeen A.M., Zawrah M. & Ali M. (2015b). Detection of cyto- and genotoxicity of rod-shaped gold nanoparticles in human blood lymphocytes using comet-FISH. *Cytologia* **80**: 173–181. DOI: <https://doi.org/10.1508/cytologia.80.173>
- Akbarpour Ghazani M., Nouri Z., Saghafian M. & Soltani M. (2020). Mathematical modeling reveals how the density of initial tumor and its distance to parent vessels alter the growth trend of vascular tumors. *Microcirculation* **27**(1): e12584. DOI: <https://doi.org/10.1111/micc.12584>
- Alkilany A.M. & Murphy C.J. (2010). Toxicity and cellular uptake of gold nanoparticles: what we have learned so far? *Journal of Nanoparticle Research* **12**(7): 2313–2333. DOI: <https://doi.org/10.1007/s11051-010-9911-8>
- Arvizo R.R., Rana S., Miranda O.R., Bhattacharya R., Rotello V.M. & Mukherjee P. (2011). Mechanism of anti-angiogenic property of gold nanoparticles: role of nanoparticle size and surface charge. *Nanomedicine: Nanotechnology, Biology, and Medicine* **7**(5): 580–587. DOI: <https://doi.org/10.1016/j.nano.2011.01.011>
- Bansal S.A., Kumar V., Karimi J., Singh A.P. & Kumar S. (2020). Role of gold nanoparticles in advanced biomedical applications. *Nanoscale Advances* **2020**(2): 3764–3787. DOI: <https://doi.org/10.1039/D0NA00472C>
- Bhattacharya R. & Mukherjee P. (2008). Biological properties of “naked” metal nanoparticles. *Advanced Drug Delivery Reviews* **60**(11): 1289–1306. DOI: <https://doi.org/10.1016/j.addr.2008.03.013>
- Chen L., Xiao H., Wang Z.H., Huang Y., Liu Z.P., Ren H. & Song H. (2014). miR-29a suppresses growth and invasion of gastric cancer cells in vitro by targeting VEGF-A. *BMB Reports* **47**(1): 39–44. DOI: <https://doi.org/10.5483/bmbrep.2014.47.1.079>
- Gamal-Eldeen A., Abo-Zeid M., El-Daly S.M., Abo-elfadl M.T., Fahmy C.A., Ali M.R. & El-Sayed M. (2016). In vivo genotoxicity of gold nanorods in mouse bone marrow compared with cyclophosphamide. *Nano Biomedicine and Engineering* **8**: 306–314. DOI: <https://doi.org/10.5101/nbe.v8i4.p306-314>
- Huang X., El-Sayed I.H., Qian W. & El-Sayed M.A. (2006). Cancer cell imaging and photothermal therapy in the near-infrared region by using gold nanorods. *Journal of the American Chemical Society* **128**(6): 2115–2120. DOI: <https://doi.org/10.1021/ja057254a>
- Kang M.S., Lee S.Y., Kim K.S. & Han D.W. (2020). State of the art biocompatible gold nanoparticles for cancer theragnosis. *Pharmaceutics* **12**(8): 701. DOI: <https://doi.org/10.3390/pharmaceutics12080701>
- Karthikeyan B., Kalishwaralal K., Sheikpranbabu S., Deepak V., Haribalaganesh R. & Gurunathan S. (2010). Gold nanoparticles downregulate VEGF-and IL-1 β -induced cell proliferation through Src kinase in retinal pigment epithelial cells. *Experimental Eye Research* **91**(5): 769–778. DOI: <https://doi.org/10.1016/j.exer.2010.09.003>
- Lacal P.M. & Graziani G. (2018). Therapeutic implication of vascular endothelial growth factor receptor-1 (VEGFR-1) targeting in cancer cells and tumor microenvironment by competitive and non-competitive inhibitors. *Pharmacological Research* **136**: 97–107. DOI: <https://doi.org/10.1016/j.phrs.2018.08.023>
- Lin H.-Y., Yang Y.-L., Wang P.-W., Wang F.-S. & Huang Y.-H. (2020). The emerging role of microRNAs in NAFLD: Highlight of MicroRNA-29a in modulating oxidative stress, inflammation, and beyond. *Cells* **9**: 1041. DOI: <https://doi.org/10.3390/cells9041041>
- Livak K.J. & Schmittgen T.D. (2001). Analysis of relative gene expression data using real-time quantitative PCR and the 2(-Delta Delta C(T)) method. *Methods* **25**(4): 402–408. DOI: <https://doi.org/10.1006/meth.2001.1262>
- Lugano R., Ramachandran M. & Dimberg A. (2020). Tumor angiogenesis: causes, consequences, challenges and opportunities. *Cellular and Molecular Life Sciences* **77**(9): 1745–1770. DOI: <https://doi.org/10.1007/s00018-019-03351-7>

- Mantri Y. & Jokerst J.V. (2020). Engineering plasmonic nanoparticles for enhanced photoacoustic imaging. *ACS Nano* **14**(8): 9408–9422.
DOI: <https://doi.org/10.1021/acsnano.0c05215>
- Mukherjee P., Bhattacharya R., Wang P., Wang L., Basu S., Nagy J.A., Atala A., Mukhopadhyay D. & Soker S. (2005). Antiangiogenic properties of gold nanoparticles. *Clinical Cancer Research* **11**(9): 3530–3534.
DOI: <https://doi.org/10.1158/1078-0432.CCR-04-2482>
- Nikobakht B. & El-Sayed M.A. (2003). Preparation and growth mechanism of gold nanorods NRs using seed-mediated growth method. *Chemistry of Materials* **15**: 1957–1962.
DOI: <https://doi.org/10.1021/cm020732l>
- Nussenbaum F. & Herman I.M. (2010). Tumor angiogenesis: insights and innovations. *Journal of Oncology* **2010**: 132641.
DOI: <https://doi.org/10.1155/2010/132641>
- Okoampah E., Mao Y., Yang S., Sun S. & Zhou C. (2020) Gold nanoparticles–biomembrane interactions: From fundamental to simulation. *Colloids and Surfaces B: Biointerfaces* **196**: 111312.
DOI: <https://doi.org/10.1016/j.colsurfb.2020.111312>
- Pan Y.L., Qiu S.Y., Qin L., Cai J.Y. & Sun J.S. (2009). Nanogold inhibits angiogenesis and growth of liver cancer: experiment with mice. *Zhonghua Yi Xue Za Zhi* **89**(12): 800–804. (Chinese)
- Tang X., Li B., Lu J., Liu H. & Zhao Y. (2020). Gold determination in soil by ICP-MS: comparison of sample pretreatment methods. *Journal of Analytical Science and Technology* **11**: 45.
DOI: <https://doi.org/10.1186/s40543-020-00245-3>
- Thijssen V.L. *et al.* (15 authors) (2018). Targeting PDGF-mediated recruitment of pericytes blocks vascular mimicry and tumor growth. *The Journal of Pathology* **246**(4): 447–458.
DOI: <https://doi.org/10.1002/path.5152>
- Treiber G., Wex T. & Malfertheiner P. (2009). Impact of different anticancer regimens on biomarkers of angiogenesis in patients with advanced hepatocellular cancer. *Journal of Cancer Research and Clinical Oncology* **135**(2): 271–281.
DOI: <https://doi.org/10.1007/s00432-008-0443-x>
- Wang J., Meng W., Zheng X., Liu S. & Li G. (2009). Combination of aptamer with gold nanoparticles for electrochemical signal amplification: application to sensitive detection of platelet-derived growth factor. *Biosensors and Bioelectronics* **24**(6): 1598–1602.
DOI: <https://doi.org/10.1016/j.bios.2008.08.030>
- Zhao Z., Sun W., Guo Z., Zhang J., Yu H. & Liu B. (2020). Mechanisms of lncRNA/microRNA interactions in angiogenesis. *Life Sciences* **254**: 116900.
DOI: <https://doi.org/10.1016/j.lfs.2019.116900>
- Zong Q., Dong N., Yang X., Ling G. & Zhang P. (2021). Development of gold nanorods for cancer treatment. *Journal of Inorganic Biochemistry* **220**: 111458.
DOI: <https://doi.org/10.1016/j.jinorgbio.2021.111458>

RESEARCH ARTICLE

Ecotoxicology

Effects of dietary lead exposure on the call of Japanese quail (*Coturnix japonica*) hatchlings

RPTI Ranasinghe¹, TSP Fernando² and MR Wijesinghe^{1*}

¹ Department of Zoology and Environment Sciences, Faculty of Science, University of Colombo, Cumaratunga Munidasa Mawatha, Colombo 03, Sri Lanka.

² Department of Zoology, Faculty of Natural Sciences, The Open University of Sri Lanka, Nawala, Nugegoda, Sri Lanka.

Submitted: 25 October 2021; Revised: 24 January 2022; Accepted: 25 February 2022

Abstract: Effects of experimental dietary exposure to the heavy metal Lead (Pb) on the calls of Japanese quail (*Coturnix japonica*) hatchlings were investigated in the present study. Trials with the heavy metal were conducted over three weeks (5 days of exposure, 3 days of non-exposure and 13 days of exposure) with two-week old hatchlings, following recommendations for exposure trials. A control trial was also included. The Pb concentrations in the prepared feed used in the exposure trials were 238, 389 and 532 $\mu\text{g kg}^{-1}$. The daily food consumption was quantified to calculate the ingested amounts of the heavy metal. Calls of the hatchlings were recorded prior to exposure, and on days 5 and 21 of the exposure trial, and the sonograms were assessed for five endpoints –frequency of notes, duration of syllables, notes per syllable, inter-syllable duration and inter-note duration. Exposure to all three tested levels of Pb resulted in calls with shorter syllables and fewer notes. Changes were evident only at day 21. Both directional and hormetic responses were noted for the different endpoints. These findings highlight that vocalization patterns, which are relatively easily detected, could serve as an important non-invasive tool for monitoring Pb pollution in the environment.

Keywords: Birds, calls, heavy metals, pollution, toxicity.

INTRODUCTION

Communication is a vital aspect of animal behaviour, and in birds the primary means of communication are visual and vocal (Kumar, 2003). Elaborate plumage, brightly coloured bare skin, wattles, and colouration in tail, beak and feet are physical features that play a role

in communication (Torres & Velando, 2003). Acoustic signals may be produced only when required (Kumar, 2003) and can be used to transmit a high volume of information efficiently making it an ideal method for communication over long distances.

Two categories of bird sounds can be recognized, namely, songs and calls. Usually, songs are of longer duration and are more complex and contain more musical variations than calls. Songs mainly play a role in mate choice and territorial defence (Catchpole, 1987). Calls have less musical variation than songs and tend to be of shorter duration (Marler, 2004). Combinations of different calls or note types have been documented as forms of communication in birds (Kumar, 2003). Unlike songs, calls have a wider range of functions which include indicating a bird's location or the location of food sources, maintaining cohesiveness within a flock, raising an alarm in the presence of predators, and expressing hunger (Marler, 2004).

In their development, songs and calls have a learnt and/or a genetic component. Recently, evidence has come to light of the development of song and other secondary sexual signals being linked to physiological stress. For instance, food deprivation (Buchanan *et al.*, 2004), parasite infestations (Buchanan *et al.*, 1999) and challenges to the immune system (Garamszegi *et al.*, 2004) have been shown to cause changes in song characteristics in birds. A few studies have shown that

* Corresponding author (mayuri@sci.cmb.ac.lk;  <https://orcid.org/0000-0002-3402-951X>)



This article is published under the Creative Commons CC-BY-ND License (<http://creativecommons.org/licenses/by-nd/4.0/>). This license permits use, distribution and reproduction, commercial and non-commercial, provided that the original work is properly cited and is not changed in anyway.

stress imposed by environmental pollution could also adversely affect vocal characteristics of birds (Wingfield & Sapolsky, 2003). Slabbekoorn and Peet (2003) have reported that birds sing at a higher pitch in areas with noise pollution. Gorissen *et al.* (2005) document that heavy metal exposure altered song patterns of the male Great tit (*Parus major*). Fields and Mitchell (2014) report that songs of wrens and sparrows along a methyl mercury contaminated river were simpler, shorter and lower-pitched than songs of birds in unpolluted sites. De Leon *et al.* (2013), studying the effect of polychlorinated biphenyls (PCBs) on the songs of two passerines, Black-capped chickadee (*Poecile atricapillus*) and Song sparrow (*Melospiza melodia*), document that there was a link between the pollutant load and features of the songs, *viz.*, the species-specific identity signal in the Black-capped chickadee and the trill performance of the Song sparrow. These studies show that environmental pollution can have an impact on song attributes, but its effect on bird calls has not been investigated.

Lead (Pb) is a highly toxic non-essential trace metal which has been recorded in the environment at levels that exceed safety thresholds (Wijayawardhana *et al.*, 2016; Merismon *et al.*, 2017). Work on over 120 avian species has shown that Pb exposure leads to sublethal or lethal toxic responses, and that there was considerable interspecific variation in tolerance to this metal (Haig *et al.*, 2014). Pb ingestion is reported to cause direct mortality in some bird species (Hoffman *et al.*, 1981; Finkelstein *et al.*, 2012). Among other impacts are the alteration of the structure and function of the kidney, bone, the central nervous system, and the haematopoietic system, leading to adverse biochemical, histopathological, neurological, and reproductive effects, with many of these effects being evident at a very young age as shown in studies with nestlings of the Western bluebird (*Sialia mexicana*) and Japanese quail (*Coturnix japonica*) (Fair & Myers, 2002; Fair & Ricklefs, 2002). Li *et al.* (2021) have shown that air pollutants including aluminium, arsenic, cadmium, iron, manganese and lead have caused changes in immunological, antioxidative and haematological parameters, and body condition of Eurasian tree sparrows (*Passer montanus*). Adverse effects of Pb have been observed at levels above 4 mg kg⁻¹ (Burger & Gochfeld, 2000).

The objective of this study was to investigate the effects of dietary exposure of Pb on the calls of hatchlings of the Japanese quail (*Coturnix japonica*). To the best of our knowledge, this work is the first attempt to experimentally test the possible impacts of a heavy

metal on bird calls. An extensive review by Richard *et al.* (2021) has outlined the impacts of the most common anthropogenic pollutants on birds, which included heavy metals and their impact on direct mortality and sublethal effects, although the impact of vocalization has not been documented.

MATERIALS AND METHODS

Collection and housing of the experimental animals for acclimatization

The experimental facility to conduct the trials was set-up in an isolated part of a residential building located in proximity to the poultry farm in a rural area in Sri Lanka (6.890489 N, 80.086396 E). This avoided the hatchlings from being unduly stressed owing to transport and allowed the experimental conditions (with respect to silence, physical space, ventilation, and lighting) to be satisfactorily provided. Twenty four one-week old hatchlings of the Japanese quail were collected from the nearby selected poultry farm. In doing so, it was ensured that the hatchlings were from different parental stocks and hence non-related. Selection for sexes was not attempted since males and females could not be distinguished with high accuracy before hatchlings are three weeks old (Rathert *et al.*, 2017). The hatchlings were then individually picked at random to form four lots of six hatchlings – the four lots being for the control and the three levels of Pb to be tested. These were housed in four specially constructed cages for acclimatization. The cages (each 75 cm × 24 cm × 25 cm) were constructed out of wood and wire-mesh following Richard *et al.* (2010). Noting that previous studies have reported that the development of quails of this species takes about 4 weeks (Sant'Ana *et al.*, 2005), the acclimatization period was set as one week (OECD, 1984), and the hatchlings were exposed to the heavy metal when they were 14 days old. During acclimatization, the hatchlings were supplied with a basal diet of commercial starter feed (Chick starter, Prima, Sri Lanka) at the prescribed weights following Ahuja (1990). Water was provided *ad libitum*. Each cage was provided with heat from an incandescent bulb of 100 W (Rezende *et al.*, 2017). The bulb was suspended above the centre of the cage and its height was adjusted as necessary to keep the temperature within the cage at 31.5° ± 0.1 °C (IR thermometer gun ±0.1 °C, Spher Scientific, Taiwan) following Randall and Bolla (2008). The one-week old hatchlings were provided with 24 hour lighting during the acclimatization period (following Ahuja, 1990).

Selection of test concentrations

Previous work on the Japanese quail has reported zero mortality for dietary exposure to $10^6 \mu\text{g kg}^{-1}$ of Pb acetate (Edens *et al.*, 1976; Hamidipour *et al.*, 2016). Hence any impact of much lower concentrations was expected to be sub-lethal. Therefore, 250, 400 and 550 μg of Pb per kilogram of dry commercial feed were used for preparing the test feed. The mean levels of Pb recorded by Diyabalanage *et al.* (2016) in rice (*Oryza sativa*) growing in the three climatic regions of Sri Lanka, which were 257 $\mu\text{g kg}^{-1}$ (wet zone), 271 $\mu\text{g kg}^{-1}$ (intermediate zone) and 322 $\mu\text{g kg}^{-1}$ (dry zone) were also considered. The low and mid test levels of the metal selected for the study broadly covered this range and could hence be considered environmentally relevant on a local scale.

Preparation of the exposure diets

Commercial feed (Chick starter, Prima, Sri Lanka) was used as the basal diet for the hatchlings (Emadi *et al.*, 2015). For preparing each test level feed the following procedure was adopted. Initially, 500 g of starter feed was taken. The starter feed, which is in the form of pellets, was ground in a blender and approximately 100 g of this was then transferred to a plastic mixing bowl and the appropriate quantity of Pb acetate was added. The rest of the ground feed was then gradually added, and the mixture was thoroughly homogenized using a hand-held mixer for 10 to 15 min, following Chowdhury *et al.* (2004) and Zhou *et al.* (2014). Hot distilled water was then gradually added until the consistency of the mix was appropriate for pelleting. The paste was then processed through a meat grinder with a 3 mm diameter outlet and the emerging mix pelleted, and the pellets were air dried ($<50^\circ\text{C}$) to a moisture content of 8 – 10%. After drying, a small quantity of each mixture was analysed for Pb, and the pellets were crumbled, packed in sealed plastic bags, and stored in a freezer until used (Zhou *et al.*, 2014). This procedure was repeated as required for providing an adequate quantity of the feed. The measured concentrations (mean \pm SD) of Pb in the test feed were $238.0 \pm 3.7 \mu\text{g kg}^{-1}$, $389.0 \pm 5.2 \mu\text{g kg}^{-1}$ and $532.0 \pm 6.6 \mu\text{g kg}^{-1}$. The pellets for the controls were also prepared in this manner but without Pb. The measured Pb concentrations in the control (with no metal addition) were $1.2 \pm 0.4 \mu\text{g kg}^{-1}$.

Exposure procedure

For exposing the hatchlings to the heavy metal, they were kept in four cages especially constructed for this

purpose. Each cage had a wooden circular base (radius 24 cm) and six compartments separated by thin wooden partitions arranged radially. The cage was enclosed on the outside with wire mesh, with provision to access each compartment. Each compartment had a floor area of approximately 300 cm^2 (as per OECD guidelines). The six hatchlings from each acclimatization cage were weighed and ringed with different coloured bands for identification, and transferred to one of the circular experimental cages, placing one hatchling in each of the six compartments. One set of six hatchlings would serve as the control and the other three sets would be exposed to the three levels of the heavy metal. They remained in their compartments during the trial period of 21 days. During the entire exposure trial of 21 days, they were maintained under natural light, 12 L: 12 D, (Calandreau *et al.*, 2011; Simova-Curd *et al.*, 2013), and at room temperature $28.82 \pm 1.01^\circ\text{C}$ (Edens *et al.*, 1976; Gayathri *et al.*, 2004). The four cages were set well apart; this would have reduced the possibility of hatchlings in a cage hearing the calls of those in other cages. The hatchlings used were 18 to 25 g in weight, with no significant differences among the treatments and controls (one-way Anova, $F_{3,20} = 0.93$, $p > 0.05$).

The trial was conducted over 21 days, which included 5 days of exposure (short term exposure), 3 days of non-exposure and 13 days of exposure (long term exposure), following OECD (1984) for dietary exposures. During the period of non-exposure, the hatchlings were provided with the basal feed without Pb. The amount of food provided per hatchling (which was increased twice during the trial) was as prescribed by Ahuja (1990) (days 1 to 5, 12 g per hatchling per day; days 6 to 8, 15 g per hatchling per day; days 9 to 21, 18 g per hatchling per day). The food provided to each hatchling was weighed and placed within its compartment daily at around 1100 h. The food which remained after 2 h was removed and weighed. These values were used for calculating the amount of food consumed and thereby the mean weight of the heavy metal ingested per hatchling (Table 1). Water was provided *ad libitum*. The weights of the quail hatchlings were recorded prior to exposure and at days 5 and 21. Ethical clearance was obtained from the Institute of Biology Sri Lanka for conducting the exposure trials (Reference No. ERC IOBSL 190 03 2019).

Recording calls

Prior to commencing the exposure trials, the methods used for attempting to record bird calls were reviewed. Two previously used methods, *viz.*, (i) holding an individual within a cloth bag (Moore *et al.*, 2008) and (ii)

Table 1: Mean (\pm SD) amounts of Pb ingested per day per hatchling for each exposure level. Values are means for six hatchlings per treatment and control.

Exposure period	Mean \pm SD values of the amounts of metal consumed ($\mu\text{g g}^{-1}$ body wt* of the hatchling)			
	Control	Low	Mid	High
Pb exposure concentration ($\mu\text{g kg}^{-1}$ of feed)	1.20 \pm 0.40	238.00 \pm 3.70	389.00 \pm 5.20	532.00 \pm 6.60
D 1 to D 5 (5 days of exposure)	0.00 \pm 0.00	0.85 \pm 0.14	1.38 \pm 0.21	1.98 \pm 0.39
D 6 – D 8 (3 days of non-exposure)	0.00 \pm 0.00	0.61 \pm 0.11	1.02 \pm 0.15	1.44 \pm 0.30
D 9 – D 21 (13 days of exposure)	0.01 \pm 0.00	2.97 \pm 0.42	4.86 \pm 0.67	7.08 \pm 1.34
Mean food provided per day per hatchling (g)	16.14 \pm 2.59			
Mean food ingested per day per hatchling (g)	15.08 \pm 0.29	14.94 \pm 0.27	14.71 \pm 0.36	15.14 \pm 0.05
Total quantity of food ingested per hatchling over 21 days(g)	316.67 \pm 6.09	313.67 \pm 5.61	308.83 \pm 7.49	317.83 \pm 0.98
Total quantity of Pb ingested per hatchling over 21 days ($\mu\text{g g}^{-1}$ body wt*)	0.02 \pm 0.00	4.43 \pm 0.67	7.26 \pm 1.01	10.51 \pm 2.03

*Body weight is the pre-treatment weight of the hatchlings of the exposure trial.

placing the hatchling individually in a meshed cage (Shafi *et al.*, 1984) were also tested. Both methods failed as the hatchlings did not call. Hence, it was decided to record calls while the hatchlings were in their experimental cages. A sound recorder (TASCAM DR- 40 Linear PCM Recorder, USA) was placed directly above the centre of the cage with the microphone facing down. Recordings were done on three days – day 1 (prior to exposure), day 5 (after acute exposure), and day 21 (after chronic exposure). Three recordings were made, each of 2 min duration (following Simmons & Zuk, 1992), between 0800 – 1000 h for each treatment and the control. The individuals were distinguished by auditory and visual cues (the latter facilitated by the presence of coloured rings). When calls were emitted, the individual that was emitting the call was noted.

Analyses of sonograms

Syllables were used as the unit of assessment. A syllable is a group of notes separated by silent intervals (O'Reilly & Harte, 2017). The three 2-min sonograms recorded for each of the treatments/control on a given day were examined to pick six pairs of syllables for analysis. In doing so it was assured that each of the six pairs of syllables were those emitted by each of the six different hatchlings. The first syllable of a pair was used to record the mean frequency of notes (Hz), duration of the syllable (in seconds), number of notes per syllable, and

inter-note duration (in seconds), whereas both syllables of each pair was used to record the inter-syllable duration (in seconds) ($n = 6$ for each of the five endpoints). The sonograms were analysed using Raven Pro 1.5 software.

Statistical analysis

Body weights and song characteristics were tested for significant differences in means among the control and exposure concentrations using one-way analysis of variance (ANOVA) followed by Tukey's tests. The nature of the dose-responses was tested using linear and non-linear regression analyses for each of the endpoints. To approximate normal distribution, the endpoints used as variables were log-transformed prior to analyses. All statistical analyses were performed with SPSS 20.0 (IBM Corporation, 2011).

RESULTS AND DISCUSSION

The study showed that the body weights of the Japanese quail hatchlings at the end of the trial, *i.e.*, at day 21, were significantly different across the treatments and control ($F = 5.38$, $p < 0.01$, $R^2 = 44.65$). Those in the control (not exposed to heavy metals) were significantly heavier than those that were exposed, which was observed across all three concentrations (Table 2). No differences in weight were apparent between low, mid and high exposure levels.

Table 2: Mean weight (\pm SD) of quail hatchlings ($n = 6$ per treatment and control) at the end of the 21-day trial with exposure to three levels of Pb. Ingested amounts of the metal are given as $\mu\text{g g}^{-1}$ initial body wt.

	Control	Low	Mid	High	One-way Anova and posthoc Tukey		
					F _{3,20}	P	R ²
Provided ($\mu\text{g kg}^{-1}$ feed)	1.2 \pm 0.4	238.0 \pm 3.7	389.0 \pm 5.2	532.0 \pm 6.6			
Ingested ($\mu\text{g g}^{-1}$)	0.02 $\mu\text{g g}^{-1}$	4.43 $\mu\text{g g}^{-1}$	7.26 $\mu\text{g g}^{-1}$	10.51 $\mu\text{g g}^{-1}$			
Body weight (g)	84.2 \pm 10.2 ^a	62.7 \pm 10.3 ^b	60.0 \pm 12.3 ^b	60.0 \pm 10.8 ^b	5.3	0.01	44.65

Different superscripts indicate significant differences in body weights at $p < 0.05$

Table 3: Call parameters in quail hatchlings ($n = 6$ per treatment and control) prior to exposure, and at two stages of exposure (day 5 and day 21) to three Pb levels. The ingested metal levels at each exposure (low, mid and high) are given as $\mu\text{g g}^{-1}$ initial body wt.

Parameter	Control	Low	Mid	High	One-way Anova and posthoc Tukey		
					F _{3,20}	p	R ² (%)
	0.02 $\mu\text{g g}^{-1}$	4.43 $\mu\text{g g}^{-1}$	7.26 $\mu\text{g g}^{-1}$	10.51 $\mu\text{g g}^{-1}$			
Day 0 (Prior to exposure)							
Frequency of notes (Hz)	4376.6 \pm 206.3	4358.2 \pm 151.9	4575.0 \pm 257.0	4383.0 \pm 261.0	1.17	0.35	14.97
Duration of a syllable (s)	3.34 \pm 0.69	3.98 \pm 0.50	3.45 \pm 1.07	3.61 \pm 1.71	0.48	0.70	6.75
Notes per syllable	5.50 \pm 0.55	6.17 \pm 0.98	5.50 \pm 1.52	5.83 \pm 2.23	0.31	0.82	4.45
Inter-syllable duration (s)	1.77 \pm 1.44	1.97 \pm 1.07	1.28 \pm 0.53	1.16 \pm 0.92	1.51	0.24	18.46
Inter-note duration (s)	0.48 \pm 0.11	0.50 \pm 0.12	0.54 \pm 0.08	0.39 \pm 0.17	1.78	0.18	21.08
Day 5 (Short term exposure)							
Frequency of notes (Hz)	3987.0 \pm 293.0	3956.9 \pm 224.2	3863.0 \pm 128.8	4057.0 \pm 334.0	0.55	0.66	7.56
Duration of a syllable (s)	3.80 \pm 0.87	2.83 \pm 1.41	2.71 \pm 0.87	3.99 \pm 1.48	2.03	0.14	23.34
Notes per syllable	5.83 \pm 0.75	5.33 \pm 1.97	4.83 \pm 1.72	6.33 \pm 1.63	1.22	0.33	15.51
Inter-syllable duration (s)	1.31 \pm 0.57	1.74 \pm 1.26	1.42 \pm 0.70	1.47 \pm 1.23	0.06	0.98	0.96
Inter-note duration (s)	0.38 \pm 0.06	0.37 \pm 0.05	0.42 \pm 0.05	0.44 \pm 0.08	2.08	0.14	23.80
Day 21 (Long term exposure)							
Frequency of notes (Hz)	1867.0 ^a \pm 544.0	2971.0 ^b \pm 880.0	3204.6 ^b \pm 114.8	2400.0 ^{a,b} \pm 505.0	5.54	0.01*	45.38
Duration of a syllable (s)	1.24 ^a \pm 0.59	0.32 ^b \pm 0.11	0.13 ^c \pm 0.11	0.12 ^c \pm 0.08	20.29	0.001*	75.26
Notes per syllable	4.50 ^a \pm 2.07	2.83 ^a \pm 0.41	1.67 ^b \pm 0.82	1.17 ^b \pm 0.41	14.68	0.001*	68.77
Inter-syllable duration (s)	0.77 \pm 0.22	0.55 \pm 0.15	1.02 \pm 0.95	0.87 \pm 0.44	0.62	0.61	8.45
Inter-note duration (s)	0.39 ^a \pm 0.32	0.13 ^{a,b} \pm 0.03	0.04 ^b \pm 0.05	0.05 ^b \pm 0.07	5.81	0.01*	57.26

In each row, different superscript letters indicate significant differences between these values ($p < 0.05$)

The study showed that the exposure of Japanese quail hatchlings to Pb resulted in changes to the properties of their call (Tables 2 & 3). The nature and magnitude of these changes varied with the test level of the metal, and the duration of exposure. Prior to exposure, there were

no significant differences in the five measured endpoints of toxicity across the control and the three groups that would be subsequently exposed to the heavy metal. Therefore, any significant changes could be attributed to the ingestion of Pb.

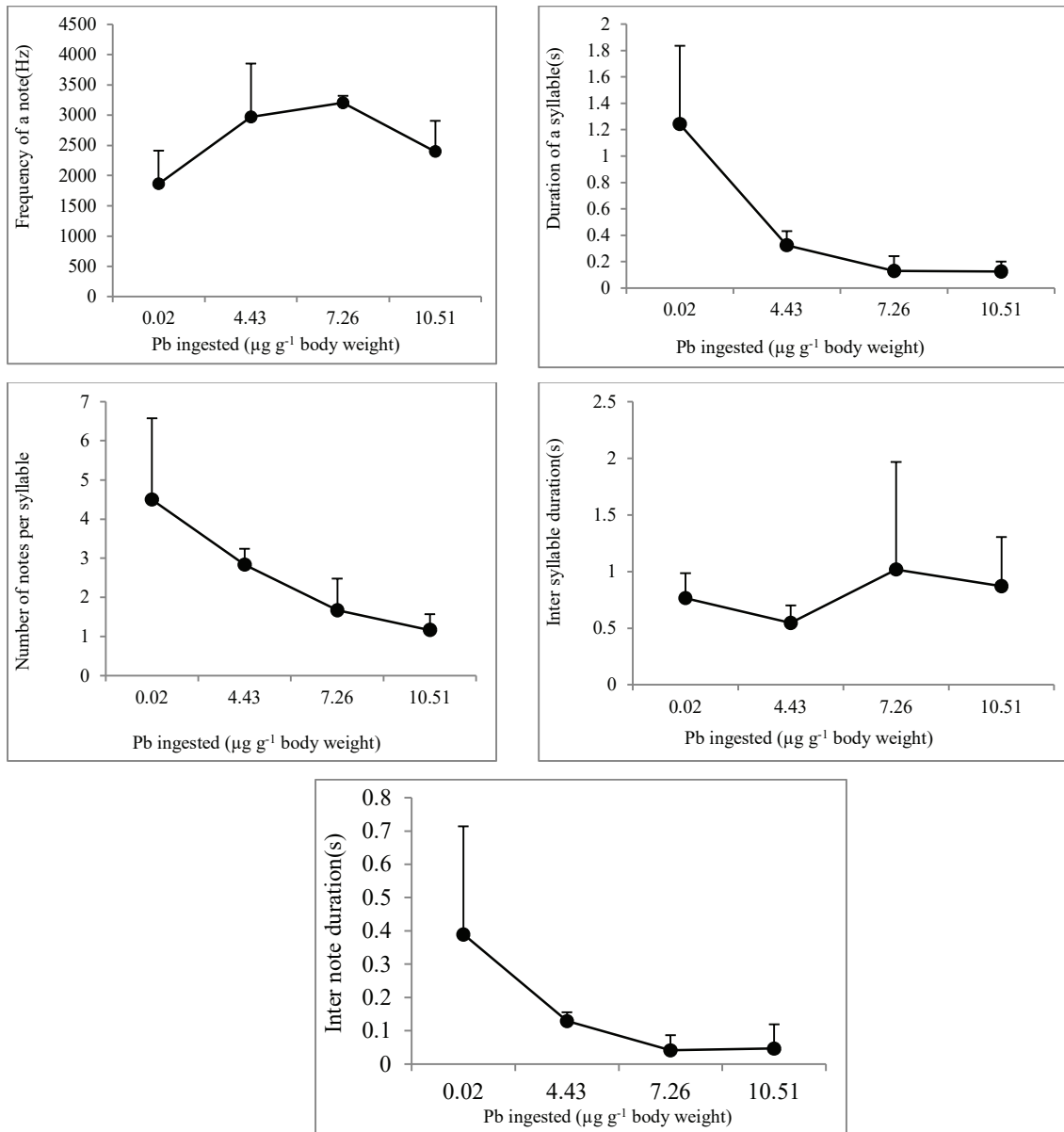


Figure 1: Five call parameters in the quail hatchlings exposed to three concentrations of Pb at the end of a 21-day trial ($n = 6$ sonograms per concentration). Amounts of metal ingested μg per g body weight were calculated using the pre-treatment body weights.

At day 5 there was no significant change in any of the five measured endpoints indicating that the nature of the calls remained unchanged following short-term exposure to Pb (Table 3). However, at day 21, except for the inter-syllable duration, significant changes were noted in the other four endpoints in the exposed birds compared to the control set (those that were not exposed). Significant directional trends were observed in three endpoints, *viz.*,

duration of a syllable, number of notes per syllable, and inter-note duration (Figure I; Table 3). For example, by day 21, the duration of a syllable had declined by 74% in hatchlings exposed to the lowest dose of Pb (ingested levels were $4.43 \mu\text{g g}^{-1}$) and by 90% in those exposed to the highest dose (ingested levels were $10.51 \mu\text{g g}^{-1}$). The number of notes per syllable also declined progressively with the increasing level of exposure to Pb, decreasing

Table 4: Results of the linear and non-linear regression analyses conducted between the exposure levels and the five call parameters at day 21 of the trial.

Parameter	Equation	F	p	R ² (%)
Frequency of notes <i>Non-linear</i>	$\text{Log Freq.} = 3.536 - 0.01729(\text{Log Pb}) - 0.1071(\text{Log Pb})^2$	6.28	0.01 ^a	37.4
Duration of a syllable <i>Linear</i>	$\text{Log Du. of a syll.} = - 0.5411 - 0.3608(\text{Log Pb})$	39.51	0.001 ^a	64.2
Notes per syllable <i>Linear</i>	$\text{Log Note. p. syll.} = - 0.3572 - 0.1657(\text{Log Pb})$	20.02	0.001 ^a	47.2
Inter-syllable duration <i>Non-linear</i>	$\text{Log Int.syll.Du.} = - 0.4445 + 0.146(\text{Log Pb}) - 0.1953(\text{Log Pb})^2$	0.92	0.41	8.1
Inter-note duration <i>Linear</i>	$\text{Log Int.note.Du} = 0.8074 - 0.1698(\text{Log Pb})$	15.66	0.001 ^a	51.5

by 37% at the lowest exposure dose and by 74% at the highest dose. Thus, at day 21 the syllables were shorter and the notes were fewer than those in the control. The linear dose-dependent trends for duration of syllable, number of notes per syllable, and inter-note duration were highly significant, with R² being between 47–64% (Table 4). Hormetic or biphasic responses were observed for the other two endpoints. In the case of call frequency low and moderate concentrations induced significantly different responses from those of the control, whereas no significant difference was noted between the frequency of those exposed to the highest concentration and those of the control (Table 4 and Figure 1).

It has been reported that anthropogenic changes in the natural environment could lead to alterations in communication signals of wild birds (Slabbekoorn & Peet, 2003). The present study provides evidence for the potential of Pb to induce changes in the vocal characteristics of a bird species. Specifically, the study demonstrated that dietary exposure of Japanese quail hatchlings to environmentally relevant levels of Pb could bring about changes in the nature of their calls measured through five standard endpoints.

Some of the responses observed in the present study are consistent with those reported by others in field studies. Gorissen *et al.* (2005) reported that male Great tits inhabiting a heavily polluted site near a smelter sang significantly less frequently (almost 35% less) and their songs had a significantly lower repertoire size (almost 30% less) than those of males only 4 km away from the smelter. Fields and Mitchell (2014) document that wrens and sparrows exposed to methyl mercury sang simpler and shorter songs than birds that were not exposed. These

observations could be taken as corresponding to the reduction in the number of syllables and the shortening of each syllable by incorporating fewer notes, in the calls of hatchlings that were exposed to Pb at day 21 of the trials in the present study. Dose-dependent trends were noted in the duration of a syllable, notes per syllable, and inter-note duration – the syllables were shorter and had fewer notes with increase in the exposure level. This is consistent with the findings of De Leon *et al.* (2013) that the song attributes of two passerines were linked to the load of PCBs to which they were exposed.

Fields and Mitchell (2014) also report that the songs of the birds exposed to methyl mercury had a lower pitch, but in the present study such a change was not seen. On frequency, which is responsible for pitch, a biphasic response (hormetic response) was observed. At low to moderate levels of exposure to Pb the calls were at a higher pitch, whereas at the highest levels of exposure calls were at a reduced pitch with the frequency not differing from those of the control hatchlings. Such biphasic responses were also seen in other endpoints. Several authors have reported such responses in parameters other than those of vocalization when birds are exposed to toxicants. A hormetic response for growth has been reported in chickens and ducks exposed to aflatoxins (Ostrowski-Meissner, 1984; Huff *et al.*, 1986). Harding (2008) found that, in Red-winged blackbirds, at high levels of selenium uptake, egg production was greater and the eggs were heavier than when the birds were exposed to lower levels. Similar egg growth stimulatory responses were noted for two species of songbirds and for Mallard ducks exposed to selenium (Stanley *et al.*, 1996; Ratti *et al.*, 2006). Hormetic responses in breeding success have been shown in

European blackbirds exposed to Pb (Fritsch *et al.*, 2019). Love *et al.* (2003) observed inverted U-shaped dose response curves for growth and adrenocortical hormones in captive American kestrels (*Falco sparverius*) after exposure to different PCBs.

Food deprivation has been shown to affect the song quality of the European starling (*Sturnus vulgaris*); when provided with a limited supply of food, songs were of shorter duration and less frequent (Buchanan *et al.*, 2003). Such effects are reported to be more severe in nestlings (Spencer *et al.*, 2003). In the present study, the Japanese quail hatchlings that were exposed to Pb, though showing no clear trend in the quantity of the food consumed, showed growth impairment, compared with the controls. This might suggest that the exposed birds experienced developmental stress. In studies on songbirds, Nowicki *et al.* (1998) have shown that in early life, developmental stress can have a deleterious effect on neural development, which may affect behaviour, life history strategies, and/or the development of secondary sexual signals. In males of the Great tit (*Parus major*) a reduced repertoire size at a heavy metal polluted site has been attributed to direct neurotoxic effects interfering with song system development or song learning (Gorissen *et al.*, 2005). It has been shown that, since brain tissue is costly to produce and maintain, it is likely that only birds that are healthy could meet the neurological demands required for learning songs (Garamszegi & Eens, 2004). Hence, as costs are likely to be highest during development, exposure to a heavy metal such as Pb can cause severe learning and memory deficits (Finkelstein *et al.*, 1998). It has been shown that Pb accumulates in bird brains and is reported to substitute for calcium even at minute concentrations, and that this affects protein kinase C resulting in the malfunctioning of neural excitation leading to memory loss in animals (Cid *et al.*, 2009; Jaishankar *et al.*, 2014). It is reported that another heavy metal, Cd, causes an abnormality in the size of neurons in the brain and the amounts of neurotransmitters, and that high doses lead to enlargement of brain cells (Gabol *et al.*, 2014). The neurotoxic impacts arising from heavy metal exposure are likely to be linear, *i.e.*, increased neurotoxicity at higher exposure levels. It is possible that such neurotoxic effects caused by Pb might have been responsible for some of the alterations in the nature of the call in the Japanese quail hatchlings exposed to Pb in the present study.

Systemic effects have also been implicated as a cause for observed changes in vocal characteristics of birds exposed to heavy metal contaminants. Devocalization

in falcons (*Falco cherrug*) that suffered from acute Pb poisoning has been attributed to narrowing of the lumen of the syrinx (Molnar *et al.*, 2008). The deposition of heavy metals in the syrinx and ventriculus in birds exposed to heavy metals has been linked to the flow of contaminated blood via branches of the carotid artery (Abdalla & King, 1976). The heavy metals Fe, Pb, Cd, and other inorganic and organic substances are said to be the probable cause of bronchi anthracosis associated with the narrowing of bronchi that would affect vocalization in ducks (Karadi & Al-Badri, 2018). Calabrese (2017) has documented that several physiological mechanisms have been cited as being responsible for different types of hormetic responses following exposure to a range of xenobiotics. Garamszegi and Eens (2004) report that intraspecific disparities observed in repertoire size, song length, and strophe length may be linked to brain space for a learned task. Hence, any or all of these factors combined might have led to the hormetic responses observed in some endpoints in our study.

The findings of the present study are important mainly because some of the noted changes in the nature of the calls were evident at environmentally relevant levels and over a limited period of exposure. The lowest levels of exposure corresponded to a level observed in rice grains in Sri Lanka. Through repeated ingestion of such material over a long period, birds would run the risk of acquiring quantities of Pb that are high enough to induce adverse impacts on vocalization. The present study is the first to experimentally test the relation between the level of heavy metal exposure and the magnitude of change in a range of call parameters. It was found that exposure to sublethal levels of Pb altered, to a considerable degree, the calls of Japanese quail hatchlings. Calls emitted by birds, as signals of different kinds, are linked to their survival. Therefore, changes induced by heavy metals, such as the shortening or dulling of calls, might, with time, lead to disruptions in bird communication, thereby affecting the long-term survival of the species. As suggested by Lackey (1994) and Suter *et al.* (1993), such alterations in vocalizations occurring in the wild could provide a snapshot of the integrity of an ecological system.

CONCLUSION

The present study has, for the first time, experimentally demonstrated the potential of the toxic heavy metal Pb to alter the nature of bird calls. In Japanese quail hatchlings subject to dietary exposure to Pb, the calls were shorter and contained fewer notes in comparison to those not exposed. Changes in calls were seen at the end of the

21-day trial period. Hormetic responses were noted for some of the endpoints. In the wild, such toxicity related endpoints could serve as an early warning of impending ecological change from chemical stress. In birds, vocalization patterns are relatively easily detected, and thus might function as a useful non-invasive tool for indicating heavy metal pollution in the environment. This in turn suggests that future studies must be more integrative and strive to document links between behavioural ecology and toxicology.

Conflict of interest

There are no financial or any other conflicts of interests.

Acknowledgement

Financial Assistance from the University of Colombo is acknowledged.

REFERENCES

- Abdalla M.A. & King A.S. (1976). The functional anatomy of the bronchial circulation of the domestic fowl. *Journal of Anatomy* **121**(3): 537.
- Ahuja S.D. (1990). *Quail Husbandry*. Indian Council of Agricultural Research, New Delhi, India.
- Buchanan K.L., Catchpole C.K., Lewis J.W. & Lodge A. (1999). Song as an indicator of parasitism in the sedge warbler. *Animal Behaviour* **57**(2): 307–314.
DOI: <https://doi.org/10.1006/anbe.1998.0969>
- Buchanan K.L., Leitner S., Spencer K.A., Goldsmith A.R. & Catchpole C.K. (2004). Developmental stress selectively affects the song control nucleus HVC in the zebra finch. *Proceedings of the Royal Society B: Biological Sciences* **271**(1555): 2381–2386.
DOI: <https://doi.org/10.1098/rspb.2012.2207>
- Buchanan K.L., Spencer K.A., Goldsmith A.R. & Catchpole C.K. (2003). Song as an honest signal of past developmental stress in the European starling (*Sturnus vulgaris*). *Proceedings of the Royal Society of London. Series B: Biological Sciences* **270**(1520): 1149–1156.
DOI: <https://doi.org/10.1098/rspb.2003.2330>
- Burger J. & Gochfeld M. (2000). Metal levels in feathers of 12 species of seabirds from Midway Atoll in the Northern Pacific Ocean. *Science of the Total Environment* **257**(1): 37–52.
DOI: [https://doi.org/10.1016/S0048-9697\(00\)00496-4](https://doi.org/10.1016/S0048-9697(00)00496-4)
- Calabrese E.J. (2017). Hormesis and homeopathy: a step forward. *Homeopathy* **106**(03): 131–132.
DOI: <https://doi.org/10.1016/j.homp.2017.07.002>
- Calandreau L., Favreau-Peigné A., Bertin A., Constantin P., Arnould C., Laurence A., Lumineau S., Houdelier C., Richard-Yris M.A., Boissy A. & Leterrier C. (2011). Higher inherent fearfulness potentiates the effects of chronic stress in the Japanese quail. *Behavioural Brain Research* **225**(2): 505–510.
DOI: <https://doi.org/10.1016/j.bbr.2011.08.010>
- Catchpole C.K. (1987). Bird song, sexual selection and female choice. *Trends in Ecology and Evolution* **2**(4): 94–97.
DOI: [https://doi.org/10.1016/0169-5347\(87\)90165-0](https://doi.org/10.1016/0169-5347(87)90165-0)
- Chowdhury M.J., McDonald D.G. & Wood C.M. (2004). Gastrointestinal uptake and fate of cadmium in rainbow trout acclimated to sub-lethal dietary cadmium. *Aquatic Toxicology* **69**(2): 149–163.
DOI: <https://doi.org/10.1016/j.aquatox.2004.05.002>
- Cid F.D., Gatica-Sosa C., Antón R.I. & Caviedes-Vidal E. (2009). Contamination of heavy metals in birds from Embalse la Florida (San Luis, Argentina). *Journal of Environmental Monitoring* **11**(11): 2044–2051.
DOI: <https://doi.org/10.1039/b906227k>
- De Leon S., Halitschke R., Hames R.S., Kessler A., DeVoogd T.J. & Dhondt A.A. (2013). The effect of polychlorinated biphenyls on the song of two passerine species. *PLoS One* **8**(9): e73471.
DOI: <https://doi.org/10.1371/journal.pone.0073471>
- Diyabalanage S., Navarathna T., Abeyundara H.T., Rajapakse S. & Chandrajith R. (2016). Trace elements in native and improved paddy rice from different climatic regions of Sri Lanka: implications for public health. *Springer Plus* **5**(1): 1–10.
DOI: <https://doi.org/10.1186/s40064-016-3547-9>
- Edens F.W., Benton E., Bursian S.J. & Morgan G.W. (1976). Effect of dietary lead on reproductive performance in Japanese quail, *Coturnix coturnix japonica*. *Toxicology and Applied Pharmacology* **38**(2): 307–314.
DOI: [https://doi.org/10.1016/0041-008X\(76\)90137-X](https://doi.org/10.1016/0041-008X(76)90137-X)
- Emadi M., Hadavi A., Ameri J. & Kermanshahi H. (2015). The effect of curcumin on acetaminophen-Induced toxicity on performance and some blood parameters of Japanese quail from 0-37 days of age. *Iran Journal of Applied Animal Sciences* **5**(1): 203–207.
- Fair J.M. & Myers O.B. (2002). The ecological and physiological costs of lead shot and immunological challenge to developing western bluebirds. *Ecotoxicology* **11**(3): 199–208.
DOI: <https://doi.org/10.1023/a:1015474832239>
- Fair J.M. & Ricklefs R.E. (2002). Physiological, growth, and immune responses of Japanese quail chicks to the multiple stressors of immunological challenge and lead shot. *Archives of Environmental Contamination and Toxicology* **42**(1): 77–87.
DOI: <https://doi.org/10.1007/s002440010294>
- Fields H. & Mitchell A. (2014). Wild birds' songs, feather colors changed by mercury contamination. Available at <https://www.nationalgeographic.com/news/2014/8/140828-bird-song-mercury-language-brain-science-winged-warning/>, Accessed 14 December 2019.
- Finkelstein M.E., Doak D.F., George D., Burnett J., Brandt J., Church M., Grantham J. & Smith D.R. (2012). Lead poisoning and the deceptive recovery of the critically

- endangered California condor. *Proceedings of the National Academy of Sciences* **109**(28): 11449–11454.
DOI: <https://doi.org/10.1073/pnas.1203141109>
- Finkelstein Y., Markowitz M.E. & Rosen J.F. (1998). Low-level lead induced neurotoxicity in children: an update on central nervous system effects. *Brain Research Reviews* **27**(2): 168–176.
DOI: [https://doi.org/10.1016/s0165-0173\(98\)00011-3](https://doi.org/10.1016/s0165-0173(98)00011-3)
- Fritsch C., Jankowiak Ł. & Wysocki D. (2019). Exposure to Pb impairs breeding success and is associated with longer lifespan in urban European blackbirds. *Scientific Reports* **9**(1): 1–11.
DOI: <https://doi.org/10.1038/s41598-018-36463-4>
- Gabol K., Khan M.Z., Khan M.U.A., Khan P., Fatima F., Siddiqui S., Jabeen T., Baig N., Iqbal M.A., Usman A. & Hashmi A. (2014). Induced effects of lead, chromium and cadmium on *Gallus domesticus*. *Canadian Journal of Pure and Applied Sciences* **8**(3): 3035–3042.
- Garamszegi L.Z. & Eens M. (2004). Brain space for a learned task: strong intraspecific evidence for neural correlates of singing behavior in songbirds. *Brain Research Reviews* **44**(2-3): 187–193.
DOI: <https://doi.org/10.1016/j.brainresrev.2003.12.001>
- Garamszegi L.Z., Möller A.P., Török J., Michl G., Péczely P. & Richard M. (2004). Immune challenge mediates vocal communication in a passerine bird: an experiment. *Behavioral Ecology* **15**(1): 148–157.
DOI: <https://doi.org/10.1093/beheco/arg108>
- Gayathri K.L., Shenoy K.B. & Hegde S.N. (2004). Blood profile of pigeons (*Columba livia*) during growth and breeding. *Comparative Biochemistry and Physiology Part A: Molecular and Integrative Physiology* **138**(2): 187–192.
DOI: <https://doi.org/10.1016/j.cbpb.2004.03.013>
- Gorissen L., Snoeijs T., Van Duyse E. & Eens M. (2005). Heavy metal pollution affects dawn singing behaviour in a small passerine bird. *Oecologia* **145**(3): 504–509.
DOI: <https://doi.org/10.1007/s00442-005-0091-7>
- Haig S.M., D'Elia J., Eagles-Smith C., Fair J.M., Gervais J., Herring G., Rivers J.W. & Schulz J.H. (2014). The persistent problem of lead poisoning in birds from ammunition and fishing tackle. *Ornithological Applications* **116**(3): 408–428.
DOI: <https://doi.org/10.1650/CONDOR-14-36.1>
- Hamidipour F., Pourkhabbaz H., Banaee M. & Javanmardi S. (2016). Bioaccumulation of lead in the tissues of Japanese quails and its effects on blood biochemical factors. *Iranian Journal of Toxicology* **10**(2): 13–21.
- Harding L.E. (2008). Non-linear uptake and hormesis effects of selenium in red-winged blackbirds (*Agelaius phoeniceus*). *Science of the Total Environment* **389**(2-3): 350–366.
DOI: <https://doi.org/10.1016/j.scitotenv.2007.09.026>
- Hoffman D.J., Pattee O.H., Wiemeyer S.N. & Mulhern B. (1981). Effects of lead shot ingestion on δ -aminolevulinic acid dehydratase activity, hemoglobin concentration, and serum chemistry in bald eagles. *Journal of Wildlife Diseases* **17**(3): 423–431.
DOI: <https://doi.org/10.7589/0090-3558-17.3.423>
- Huff W.E., Kubena L.F., Harvey R.B., Corrier D.E. & Mollenhauer H.H. (1986). Progression of aflatoxicosis in broiler chickens. *Poultry Science* **65**(10): 1891–1899.
DOI: <https://doi.org/10.3382/ps.0651891>
- Jaishankar M., Tseten T., Anbalagan N., Mathew B.B. & Beeregowda K.N. (2014). Toxicity, mechanism and health effects of some heavy metals. *Interdisciplinary Toxicology* **7**(2): 60–72.
DOI: <https://dx.doi.org/10.2478%2Fintox-2014-0009>
- Karadi H.K. & Al-Badri A.M. (2018). Histological and fluorescent microscope studies for evaluation carbon accumulation in trachea and bronchi of birds in polluted area in Wasit province. *Iraqi Journal of Veterinary Sciences* **32**(2): 135–141.
DOI: <http://dx.doi.org/10.33899/ijvs.2019.153839>
- Kumar A. (2003). Acoustic communication in birds. *Resonance* **8**(6): 44–55.
DOI: <https://doi.org/10.1007/BF02837868>
- Lackey R.T. (1994). Ecological risk assessment. *Fisheries, Bulletin of the American Fisheries Society* **19**(9): 14–18.
- Li M, Nabi G., Sun Y., Wang Y., Wang L., Jiang C., Cao P., Wu Y. & Li D. (2021). The effect of air pollution on immunological, antioxidative and hematological parameters, and body condition of Eurasian tree sparrows. *Ecotoxicology and Environmental Safety* **208**:111755.
DOI: <https://doi.org/10.1016/j.ecoenv.2020.111755>
- Love O.P., Shutt L.J., Silfies J.S., Bortolotti G.R., Smits J.E. & Bird D.M. (2003). Effects of dietary PCB exposure on adrenocortical function in captive American kestrels (*Falco sparverius*). *Ecotoxicology* **12**(1): 199–208.
DOI: <https://doi.org/10.1023/A:1022502826800>
- Marler P. (2004). Bird calls: their potential for behavioral neurobiology. *Annals of the New York Academy of Sciences* **1016**(1): 31–44.
DOI: <https://doi.org/10.1196/annals.1298.034>
- Merismon M., Budianta D., Napoleon A. & Hermansyah H. (2017). The insitu inactivation of the contaminated intensive paddy field of Pb and Cd using biochar and compost. *Ecology, Environment and Conservation* **23**(4): 143–148.
- Molnar L., Molnarova M., Legath J. & Vasko L. (2008). Environmental hazard of ingested lead shot in birds. *Zbornik Prednášok*, p. 60.
- Moore R.P., Robinson W.D., Lovette I.J. & Robinson T.R. (2008). Experimental evidence for extreme dispersal limitation in tropical forest birds. *Ecology Letters* **11**(9): 960–968.
DOI: <https://doi.org/10.1111/j.1461-0248.2008.01196.x>
- Nowicki S., Peters S. & Podos J. (1998). Song learning, early nutrition and sexual selection in songbirds. *American Zoologist* **38**(1): 179–190.
DOI: <https://doi.org/10.1093/icb/38.1.179>
- O'Reilly C. & Harte N. (2017). Pitch tracking of bird vocalizations and an automated process using YIN-bird. *Cogent Biology* **3**(1): 1322025.
DOI: <https://doi.org/10.1080/23312025.2017.1322025>
- Organization for economic co-operation and development (OECD) (1984). *205-Avian Dietary Toxicity Test*.

- Ostrowski-Meissner H.T. (1984). Biochemical and physiological responses of growing chickens and ducklings to dietary aflatoxins. *Comparative Biochemistry and Physiology Part C: Comparative Pharmacology* **79**(1): 193–204.
DOI: [https://doi.org/10.1016/0742-8413\(84\)90185-3](https://doi.org/10.1016/0742-8413(84)90185-3)
- Randall M. & Bolla G. (2008). Raising Japanese quail. *Primefacts* **602**: 1–5.
- Rathert T.Ç., Güven İ. & Üçkardeş F. (2017). Sex determination of Japanese quails (*Coturnix coturnix japonica*) using with zoometric measurements. *Turkish Journal of Agriculture - Food Science and Technology* **5**(9): 1002–1005.
DOI: <http://dx.doi.org/10.24925/turjaf.v5i9.1002-1005.1278>
- Ratti J.T., Moser A.M., Garton E.O. & Miller R. (2006). Selenium levels in bird eggs and effects on avian reproduction. *The Journal of Wildlife Management* **70**(2): 572–578.
DOI: [https://doi.org/10.2193/0022-541X\(2006\)70\[572:SLI BEA\]2.0.CO;2](https://doi.org/10.2193/0022-541X(2006)70[572:SLI BEA]2.0.CO;2)
- Rezende J.C.R., Sartori M.M.P., Sartori J.R., Ducatti C., Denadai J.C. & Pezzato A.C. (2017). Assessment of tissue development in fattening quails using the stable isotope technique. *Journal of Animal Physiology and Animal Nutrition* **101**(5): e427–e435.
DOI: <https://doi.org/10.1111/jpn.12624>
- Richard S., Land N., Saint-Dizier H., Leterrier C. & Faure J.M. (2010). Human handling and presentation of a novel object evoke independent dimensions of fear in Japanese quail. *Behavioural Processes* **85**(1): 18–23.
DOI: <https://doi.org/10.1016/j.beproc.2010.05.009>
- Richard F., Gigauri M., Bellini. G., Rojas O. & Runde A. (2021). Warning on nine pollutants and their effects on avian communities. *Global Ecology and Conservation* **32**: e01898.
DOI: <https://doi.org/10.1016/j.gecco.2021.e01898>.
- Sant'Ana M.G., Moraes R. & Bernardi M.M. (2005). Toxicity of cadmium in Japanese quail: Evaluation of body weight, hepatic and renal function, and cellular immune response. *Environmental Research* **99**(2): 273–277.
DOI: <https://doi.org/10.1016/j.envres.2005.06.003>
- Shafi M.M., Hussain L., Khan A.A., Ahmed S. & Ahmed M.S. (1984). Laboratory evaluation of 4-aminopyridine against house sparrow (*Passer domesticus*). *International Journal of Pest Management* **30**(3): 302–305.
DOI: <https://doi.org/10.1080/09670878409370897>
- Simmons L.W. & Zuk M. (1992). Variability in call structure and pairing success of male field crickets, *Gryllus bimaculatus*: the effects of age, size and parasite load. *Animal Behavior* **44**(6): 1145–1152.
DOI: [https://doi.org/10.1016/S0003-3472\(05\)80326-4](https://doi.org/10.1016/S0003-3472(05)80326-4)
- Simova-Curd S., Foldenauer U., Guerrero T., Hatt J.M. & Hoop R. (2013). Comparison of ventriculotomy closure with and without a coelomic fat patch in Japanese quail (*Coturnix coturnix japonica*). *Journal of Avian Medical Surgery* **27**(1): 7–13.
DOI: <https://doi.org/10.1647/2009-040>
- Slabbekoorn H. & Peet M. (2003). Birds sing at a higher pitch in urban noise. *Nature* **424**(6946): 267–267.
DOI: <https://doi.org/10.1647/2009-040>
- Spencer K.A., Buchanan K.L., Goldsmith A.R. & Catchpole C.K. (2003). Song as an honest signal of developmental stress in the zebra finch (*Taeniopygia guttata*). *Hormones and Behaviour* **44**(2): 132–139.
DOI: [https://doi.org/10.1016/S0018-506X\(03\)00124-7](https://doi.org/10.1016/S0018-506X(03)00124-7)
- Stanley Jr T.R., Smith G.J., Hoffman D.J., Heinz G.H. & Rosscoe R. (1996). Effects of boron and selenium on mallard reproduction and duckling growth and survival. *Environmental Toxicology and Chemistry* **15**(7): 1124–1132.
DOI: <https://doi.org/10.1002/etc.5620150717>
- Suter G.W.L., Barnthouse S.M., Bartell T., Mill D.M. & Paterson S. (1993). *Ecological Risk Assessment*. Lewis, Ann Arbor, Michigan, USA.
- Torres R. & Velando A. (2003). A dynamic trait affects continuous pair assessment in the blue-footed booby, *Sula nebouxii*. *Behavioral Ecology and Sociobiology* **55**(1): 65–72.
DOI: <http://dx.doi.org/10.1007/s00265-003-0669-1>
- Wijayawardhana D., Herath V. & Weerasinghe A. (2016). Heavy metal pollution in Sri Lanka with special reference to agriculture: a review of current research evidences. *Rajarata University of Sri Lanka Journal* **4**(1): 52–66.
- Wingfield J.C., Sapolsky R.M. (2003). Reproduction and resistance to stress: when and how. *Journal of Neuroendocrinology* **15**(8): 711–724.
- Zhou Y., Davis D.A. & Rhodes M.A. (2014). Comparative evaluation of copper sulfate and tribasic copper chloride on growth performance and tissue response in Pacific white shrimp (*Litopenaeus vannamei*) fed practical diets. *Aquaculture* **434**: 411–417.
DOI: <https://doi.org/10.1016/j.aquaculture.2014.09.004>

RESEARCH ARTICLE

Functional foods

Development of vacuum-dried powder and drinking yoghurt from soursop fruit (*Annona muricata* L.) and evaluation of their physico-chemical and functional properties

NI Ranaweera¹, RC Pitipanaarachchi², HMT Herath^{2*} and DVP Chandramali¹

¹ Department of Animal and Food Sciences, Faculty of Agriculture, Rajarata University of Sri Lanka, Puliyankulama, Anuradhapura, Sri Lanka.

² Food Technology Section, Modern Research and Development Complex, Industrial Technology Institute, 503A, Halbarawa Gardens, Malabe, Sri Lanka.

Submitted: 25 May 2021; Revised: 25 June 2021; Accepted: 25 February 2022

Abstract: Soursop (*Annona muricata* L.) is an underutilized seasonal climacteric fruit which exhibits many therapeutic and nutritive values. The objective of the present study was to develop soursop fruit powder and soursop incorporated drinking yoghurt and to evaluate their physico-chemical and antioxidant properties. Soursop fruit powder was developed by steam blanching of matured fresh cuts followed by vacuum drying at 60 °C for 6 hours. Soursop drinking yoghurt was developed by incorporating soursop pulp (15%, 20%, and 25% w/v) followed by selecting the best fruit content (*i.e.*, 20% w/v) based on the sensory evaluation trials. Titratable acidity, pH, total soluble solids, syneresis, and milk solid non-fat of selected soursop drinking yoghurt were 0.85%, 4.5, 16.3 °Brix, 29.3%, and 13.8%, respectively. The soursop drinking yoghurt (20% w/v) with added sucralose and sugar were separately compared with normal drinking yoghurt as a control. The drinking yoghurt with added sucralose was selected as the most preferable product based on the sensory attributes of odour, appearance, texture, taste, aftertaste, and overall acceptability. A significantly ($p < 0.05$) higher antioxidant potential in terms of total polyphenolic content, total flavonoids content, ferric reducing antioxidant power, and radical scavenging activities of 2,2'-azino-bis(3-ethylbenzothiazoline-6-sulphonic acid) and 2,2-diphenyl-1-picrylhydrazyl were shown in the soursop drinking yoghurt (14.13 ± 0.63 mgGAE/g, 3.39 ± 0.36 mgQE/g, 1.32 ± 0.30 mgTE/g, 30.1 ± 3.24 mgTE/g, and 25.67 ± 3.38 mgTE/g respectively) than in the vacuum-dried powder. The vacuum dried powder had a high content of protein (8.71%), crude fibre (4.28%) and ash (3.97%). Further study showed that the soursop drinking yoghurt is a potential source of

functional food, while soursop fruit powder is a good source of supplementary food.

Keywords: Antioxidant potential, drinking yoghurt, functional properties, soursop fruit, vacuum-dried powder.

INTRODUCTION

Soursop (*Annona muricata* L.) is an evergreen plant growing in tropical and subtropical regions, and belongs to the family *Annonaceae*. Those seasonal climacteric soursop fruits had a high rate of respiration and ethylene production during the ripening stage, leading to high perishability and post-harvest losses (Kader, 2005; Lagunju & Sandewa, 2018).

Soursop fruit is therapeutically very popular for its outstanding antioxidant properties throughout the world (Kaur & Kapoor, 2001; Villegas, 2002; Gyesei *et al.*, 2019) and has the ability to reduce tumour size, kill off breast cancer cells, and enhance the activity of the immune system (Fidianingsih & Handayani, 2015). It is a good natural remedy for diabetics by inhibition of α -amylase and α -glucosidase activities with minimal or no adverse side effects (Agu *et al.*, 2019). Recent research reported that *Annona muricata* L. fruit extract is used for the treatment of depression (Solanki *et al.*, 2020).

* Corresponding author (theja@iti.lk;  <https://orcid.org/0000-0001-6323-2384>)



Based on their remedial properties to many chronic diseases, soursop fruit can be used to generate varieties of value-added food products such as yoghurts, jams, fruit powders and beverages. Sinthiya and Poornima (2017) had developed several value added products from soursop such as fruit pulp concentrate, syrup, jam, and juice. It was reported that soursop nectar incorporated stirred yoghurt was developed by Dias and Jayasooriya (2017) and soursop incorporated set yoghurt was developed by Virgen-Ceceña *et al.* (2019). Further preparation and quality evaluation of soursop jelly was performed by Shashikala and Mahendran (2019). In most of the above studies, the functional properties or potential antioxidant properties had not been studied.

Although soursop fruits have many health promoting functional properties, consumption of fresh soursop fruit is low among the younger and adult generation, due to the time consumed for the peeling and seed removal process. Therefore there is a high potential for implementing the development of different attractive products to preserve soursop worldwide. The development of value added products like functional drinking yoghurt and vacuum-dried powder using soursop fruit may be considered as a timely solution for higher postharvest losses and its unavailability off-season.

Dehydration and drying is one of the most commonly used methods to prepare powders from fresh fruits and vegetables. Vacuum-drying is ideal for heat and oxygen-sensitive foods such as fruits and vegetables due to the advantage of removing moisture at low temperatures and minimizing the possibility of oxidation reactions (Wijewardana *et al.*, 2016; Ngamwonglumlert & Devahastin, 2018).

Drinking yoghurts are one of the fastest growing fermented products in the functional food market, because of their multi-nutrient content and health-promoting properties (Sun-Waterhouse *et al.*, 2012). The fermentation process is carried out by various characteristic bacterial cultures such as *Lactobacillus bulgaricus* and *Streptococcus thermophilus*. It has been showed that the incorporation of fresh or processed fruits (e.g., chokeberry, salal berry, water melon, cocoa) into regular drinking yoghurts enhanced the nutritional, functional, and antioxidant profile and sensory properties (Gonzalez *et al.*, 2011; Sengupta *et al.*, 2014; Nguyen & Hwang, 2016; Raikos *et al.*, 2019).

The objective of the present research study was to evaluate the feasibility of incorporating soursop fruit into regular drinking yoghurt and developing soursop powder by vacuum drying and evaluation of physico-chemical characteristics, antioxidants, and sensory properties of those products.

MATERIALS AND METHODS

Materials

Raw materials

Ripened soursop (*Annona muricata L.*) fruits were obtained from the local market at Malabe, Sri Lanka. Ultra Heat Treated (UHT) full cream fresh milk was purchased from a local supermarket in Malabe, and yoghurt cultures were obtained from Morison PLC, Colombo.

Chemicals and reagents

2,2'-Azino-bis(3-ethylbenzothiazoline-6-sulphonic acid), diammonium salt (ABTS), 1,1-diphenyl-2-picrylhydrazyl (DPPH), 6-hydroxy-2,5,7,8-tetramethylchroman-2-carboxylic acid (Trolox), gallic acid, 2,4,6-tripyridyl-s-triazine (TPTZ), potassium persulphate, ferric chloride, quercetin and Folin-Ciocalteu phenol reagent were purchased from Sigma-Aldrich, USA. All the other chemicals used were of analytical grade.

Preparation of vacuum-dried soursop powder

Soursop fruit powder was prepared by steam blanching followed by a vacuum drying technique as described by Bourdoux *et al.* (2016).

The edible portion of soursop fruit was cut into thin slices (2 cm x 2 cm) and dipped in 1% sodium meta bisulphite (SMS) solution. The pieces were steam blanched for 1 min and then were vacuum dried at 60 °C for 6 h using dehydrator (American Harvest, USA). The dried slices were ground using a pin mill (Munson cim-18-S316, Shanghai, China) to pass through 0.5 mm sieve size. Powdered samples were stored at 15 °C in airtight containers until assaying.

The recovery percentage of vacuum-dried powder was calculated using following equation.

Vacuum-dried recovery percentage =

$$\frac{\text{Weight of vacuum-dried powder}}{\text{Weight of edible portion}} \times 100$$

Preparation of soursop drinking yoghurt

The edible portion of the soursop fruit was obtained and ground well using a wet grinder (Prestige Deluxe LS 304, Bangalore, India). Three different formulae of drinking yoghurt were developed using the fruit content of soursop: 15%, 20%, and 25% (w/v) and other ingredients, *i.e.*, milk, sugar, and yoghurt culture. Ingredients required for each formula were put into a separate container and homogenized using a laboratory homogenizer (Pro 250 Scientific, Oxford, USA) at 3000 rpm for 10 min. The homogenized samples were pasteurized at 85°C for 15 min. The pasteurized samples were allowed to cool up to 42°C and the yoghurt culture was added to each sample. Samples were then incubated in an incubator (Memmert c1810, Munich, Germany) at 44°C for 3 h and 30 min until the samples reached a pH of 4.6. The incubated yoghurt samples were separately homogenized to break down the coagulum. The resulting drinking yoghurts were filled into previously autoclaved glass bottles (at 121°C for 20 min under the pressure of 15 psi) under a laminar air flow cabinet and hermetically sealed with lug cap. Bottled soursop drinking yoghurts were labelled and stored at 4°C in a refrigerator until use. After selecting the best soursop fruit content in drinking yoghurt using a sensory panel, the second trial was carried out to replace the sugar content in soursop drinking yoghurts by adding sucralose.

Sensory evaluation

Soursop incorporated drinking yoghurts with 3 different soursop fruit contents, 15%, 20% and 25% (w/v), were subjected to a sensory evaluation trial to select the most preferable soursop level. Thereafter, the sugar content of the drinking yoghurt with the most preferable level of soursop was replaced by adding 200 mg/kg of sucralose (*i.e.*, less than the maximum level of sucralose addition to milk based preparations, 400 mg/kg) according to Food (Sweeteners) Regulations published by Ministry of Health and Indigenous Medicine (2015). The sucralose and sugar-sweetened yoghurts were separately compared, with normal drinking yoghurt as the control, in another sensory evaluation trial. Both sensory evaluation trials

were conducted by using twelve trained panellists and the samples were evaluated in terms of colour, odour, appearance, texture, taste, aftertaste, and overall acceptability, using the nine point hedonic scale.

Determination of physico-chemical properties of drinking yoghurt

Determination of total soluble solids (TSS) content

The total soluble solids of drinking yoghurt samples was measured using a refractometer at room temperature (27°C) (Atago automatic1620, Fukaya-shi, Japan).

Determination of total solids-non-fat

The total solids-non-fat (SNF) of soursop drinking yoghurt was determined according to the following formula by Matela *et al.* (2019).

$$\text{Solids-non-fat \%} = \text{Total solids \%} - \text{Fat content \%}$$

The fat content of the drinking yoghurt samples was determined using Rose Gottlieb method as described in AOAC (2012).

The fat content was measured using the phase separation technique.

Briefly, a 10.0 g sample was extracted by a mixture of solvents (10 mL of 95% ethanol, 25 mL of diethyl ether, 25 mL of petroleum ether, and 0.88 mL of ammonia solution). The fat was extracted into the organic phase and solvent was removed under vacuum (200 mbar) at 40 °C using a rotor evaporator (Heidolph, Germany).

Titrateable acidity

The titrateable acidity of drinking yoghurt samples were measured according to the method described by Olugbuyiro (2011), and expressed as percentage acidity.

A 15 mL sample of the drinking yoghurt was titrated with 0.1 M sodium hydroxide using phenolphthalein as the indicator.

$$\text{Titrateable acidity\%} = \frac{\text{NaOH volume} \times \text{M} \times 90 \times 100}{\text{Volume of sample} \times 1000}$$

Where, M = Molar concentration of NaOH

pH of drinking yoghurt

The pH was measured on the same day of preparing the products according to AOAC, 2012, at room temperature (27 °C) using a digital pH meter (Ikmag rec-g, USA).

Syneresis of drinking yoghurt

The syneresis of drinking yoghurt was determined according to the method described by Vahedi *et al.* (2008). The following equation was used to determine the syneresis.

A 10 g sample of drinking yoghurt sample was placed on a filter paper resting on the top of a Buchner funnel. After 10 min of drainage under vacuum, the quantity of remaining yoghurt was weighted and syneresis was expressed as percentage of free whey.

Free whey (g/100g) =

$$\frac{(\text{Weight of initial sample} - \text{Weight of sample after filtration}) \times 100}{\text{Weight of initial sample}}$$

Proximate composition analysis of vacuum-dried soursop powder and soursop drinking yoghurt

Proximate composition of vacuum-dried soursop powder and soursop drinking yoghurt were determined according to the methods described in AOAC (2012) and SLS 824 (2018) respectively.

In brief, the moisture content of both vacuum-dried soursop powder and soursop drinking yoghurt was determined by oven drying at 105 °C for 5 h, applying a gravimetric principle, using a heating oven (Memmert, Schwabach, Germany). The fat content of the vacuum-dried soursop sample was determined by extraction at 150 °C for 2.5 h using petroleum ether (40–60 °C), using a Soxhlet extractor (C. Gerhardt GmbH & Co. KG, Schwabach, Germany) while the fat content of the soursop drinking yoghurt was determined as described in a previous section. The crude fibre content of the vacuum-dried soursop powder and soursop drinking yoghurt were determined using an acid/alkali digestion method, with a Fibretec hot extractor (Fibretec™M6 1020, Apeldoorn, Netherlands). The ash contents of vacuum-dried soursop powder and soursop drinking yoghurt were determined by a dry ashing method using a furnace (Lenton, Wales, England). The crude protein content of vacuum-dried soursop powder and soursop drinking yoghurt were determined by wet digestion followed by steam distillation using a Kjeldahl apparatus

(VELP Scientifica DK 20 and 139, Usmate, Italy). The percentage of carbohydrate (CHO) of the two products was determined using a mathematical equation as described by Matela *et al.* (2019).

$$\text{CHO \%} = 100 - (\text{ash} + \text{crude protein} + \text{crude fat} + \text{crude fibre} + \text{moisture}) \%$$

Total energy values of vacuum-dried soursop powder and soursop drinking yoghurt were determined by the Atwater method as described by Matela *et al.* (2019). The energy was measured in kilocalories/100 g.

$$\text{Energy value} = (\% \text{ CP} \times 4) + (\% \text{ CFT} \times 9) + (\% \text{ CHO} \times 4)$$

where, % CP = percentage crude protein, % CFT = percentage crude fat, % CHO = percentage carbohydrate

Determination of antioxidant potential

Sample preparation for the determination of antioxidant properties

Determination of antioxidant properties in fresh soursop fruit, vacuum-dried soursop powder and soursop drinking yoghurt was carried out according to the method as described by Agu and Okolie (2017).

A well-mixed fresh edible portion of soursop fruit (25.0 g) and vacuum-dried soursop powder (5.0 g) were separately shaken overnight using an orbital shaker (Ratek-ms 120, India) at 110 rpm with 4 times the sample weight of 80% ethanol. The ethanol was evaporated off in a rotary evaporator (Heidolph, Germany) at a temperature of 45 °C at 110 rpm. Ethanol free extracts were freeze-dried overnight at 20 °C. Freeze-dried extracts were collected into the Eppendoff tubes and refrigerated (4 °C) till samples were analysed for antioxidant properties.

Freshly prepared soursop drinking yoghurt (1 mL) was diluted with 9 mL of distilled water to prepare 1/10 dilution of the initial drinking yoghurt. The diluted yoghurt samples were directly used for the determination of antioxidant properties.

Total polyphenolic content

Total polyphenolic contents (TPC) of sample extracts were determined using the Folin-Ciocalteu reagent as described by Singleton *et al.* (1999).

In brief, each extract was diluted in distilled water

(2 mg/mL), and 20 μ L of diluted sample, 110 μ L of 10 times diluted Folin-Ciocalteu reagent and 70 μ L of 10% sodium carbonate (Na_2CO_3) solution were mixed in a well of a 96-well micro plate. After incubating for 30 min at $25 \pm 2^\circ\text{C}$, the absorbance was measured at 765 nm using a 96-well micro plate reader (SpectraMax Plus 384 Molecular Devices, USA) using gallic acid as the standard. The gallic acid standard solution (1 mg/mL) was prepared by dissolving 1 mg of gallic acid in 1000 μ L of distilled water and the standard series was prepared using half dilution.

TPC was expressed as mg gallic acid equivalents (GAE) / g of the sample on a dry weight basis.

Total flavonoid content

Total flavonoid content (TFC) of sample extracts were determined using the methods described by Pourmorad (2005).

In brief, each extract was diluted in methanol (2 mg/mL), and 100 μ L of diluted sample and 100 μ L of 2% aluminium chloride were added into a well of a 96-well micro plate. After incubating for 10 min at $25 \pm 2^\circ\text{C}$, the absorbance was measured at 415 nm using quercetin as the standard using micro plate reader (SpectraMax Plus 384 Molecular Devices, USA). The standard stock solution (1 mg/mL) was prepared by dissolving 1 mg of quercetin in 1000 μ L of methanol and the standard series was prepared by half dilution.

The results were expressed as mg quercetin equivalents (QE)/g of the sample on a dry weight basis.

Ferric reducing antioxidant power assay

Ferric reducing antioxidant power (FRAP) of sample extracts was performed according to the method described by Benzie and Szeto (1999).

In brief, 150 μ L of FRAP reagent [a mixture containing 300 mM of acetate buffer at pH 3.6, 10 mM 2,4,6-tripyridyl-s-triazine (TPTZ) in 40 mM HCl solution, and 20 mM $\text{FeCl}_3 \cdot 6\text{H}_2\text{O}$ in a ratio of 10:1:1 followed by incubation at 37°C for 10 min], 30 μ L acetate buffer and 10 μ L diluted sample (2 mg/mL) were transferred to a micro well. After incubating at $25 \pm 2^\circ\text{C}$ for 10 min, the absorbance was measured at 600 nm via 96-well micro plate reader (SpectraMax Plus 384 Molecular Devices, USA). The standard curve was plotted using half dilution series of the standard Trolox stock solution (1 mg/mL) which was prepared dissolving

1 mg of Trolox in 1000 μ L of Phosphate Buffer Saline (PBS).

The results were expressed as mg of Trolox equivalents (TE) /g of sample (dry weight basis).

DPPH radical scavenging activity

The DPPH radical scavenging activity of samples was performed according to the method described by Blois (1958).

In brief, 125 μ L of DPPH radical (20 mg/100 mL) and 50 μ L (2 mg/mL) of diluted sample were mixed in a well and incubated at $25 \pm 2^\circ\text{C}$ for 10 min. Absorbance was measured at 517 nm (SpectraMax Plus 384 Molecular Devices, USA). The stock standard solution was prepared by dissolving 1 mg of Trolox in 1000 μ L of PBS and standard series was prepared by half dilution.

Results were expressed as mg Trolox equivalent (TE)/g of the sample on dry weight basis.

ABTS radical scavenging activity

The ABTS radical scavenging activity of samples was determined according to the method described by Re *et al.* (1999).

40 μ L of seven times diluted ABTS stock solution (10 mg of ABTS in 2.5 mL of 2.5 mM potassium persulphate solution incubating at 37°C for 16 h in the dark), 110 μ L phosphate buffer and 50 μ L (2 mg/mL) of sample were incubated at $25 \pm 2^\circ\text{C}$ for 10 min. The absorbance was recorded at 734 nm using 96-well micro plate reader (SpectraMax Plus384 Molecular Devices, USA). The standard stock solution (1 mg/mL) was prepared by dissolving 1 mg of Trolox in 1000 μ L of PBS and then the standard series was prepared by half dilution.

Results were expressed as mg Trolox equivalent (TE)/g of the sample on a dry weight basis.

Statistical analysis

Completely Randomized Design (CRD) was used to analyse the parametric data of drinking yoghurt samples. Data was analysed using Analysis of Variance (ANOVA) in the Statistical Software Analysis (SAS) programme at 95% confidence interval and mean separation was conducted by the Least Significant Difference (LSD) method.

The data obtained for the two treatments of the most preferable fruit content and acceptability of sugar vs. artificial sweetener were statistically analysed by the Friedman method using MINITAB software at 95% confidence interval.

RESULTS AND DISCUSSION

Determination of edible portion of soursop fruit

Soursop fruit is comprised of the thorny pericarp, seeds, central pith, and the soursop pulp. Out of those parts, the fruit pulp is considered to be the edible portion, and hence the other parts of the fruit have to be removed. It was reported that soursop seeds contain annonaceous acetogenins, which cause neurotoxic effects on humans (Badrie & Schauss, 2010). Determination of recovery of edible portion is important in new product development activity in order to determine the production cost and wastage. The physical composition of soursop fruit in percentages were presented in Table 1.

Table 1: Composition of soursop fruit

Parts of the fruit	Composition (%)
Edible portion	71.5 ± 3.60
Peel	17.2 ± 1.21
Seeds	8.3 ± 0.8
Central pith	3.0 ± 0.6

Values are presented as mean ± standard deviations of three replicate measurements

According to the Table 1, the edible portion of soursop fruit was in accordance with the data reported in the previous study by Badrie and Schauss (2010), where the edible portion of an average soursop fruit is 67.5%, the amount of peel is 20%, and seeds and the central pith comprise 8.55% and 4% of the fruit, respectively.

Determination of vacuum-dried recovery percentage

The percentage recovery after vacuum drying will be an important factor in determining the feasibility of utilizing soursop powder in food industry.

According to the present study, the recovery percentage of soursop was 16.36 ± 0.83%. In the process of vacuum drying, a certain quantity of the fruit was

wasted due to the sticking of the soursop pulp onto the trays and when converting soursop into powder due to machinery losses.

Sensory evaluation of drinking yoghurts

The ideal fruit content of drinking yoghurts was evaluated with levels of soursop fruit content of 15% w/v, 20% w/v, and 25% w/v, using sensory attributes of odour, appearance, texture, taste, aftertaste, and overall acceptability, according to the nine point hedonic scale. Figure 1 shows the results obtained from the sensory evaluation with reference to varying fruit content. There was a significant difference ($p < 0.05$) in each sensory attribute; odour, appearance, texture, taste, aftertaste and overall acceptability.

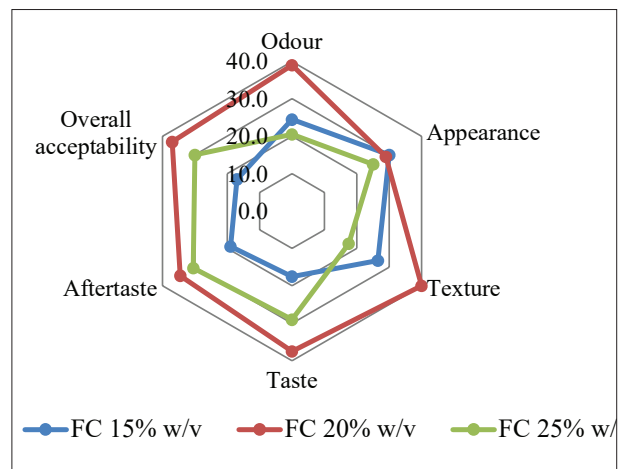


Figure 1: Sensory evaluation of soursop incorporated drinking yoghurts

The 20% w/v soursop incorporated drinking yoghurt showed the highest rank for odour, taste, texture, aftertaste, and overall acceptability while 15% w/v soursop incorporated drinking yoghurt showed the highest rank for appearance. The lowest acceptability regarding the odour, appearance and texture were recorded from 25% w/v soursop incorporated drinking yoghurt, due to the higher content of soursop pulp. It was seen that colour and thickness of the drinking yoghurt increased with increasing incorporation of soursop pulp. Based on the results, the 20% w/v soursop incorporated drinking yoghurt showed the highest overall acceptability in terms of all the attributes, and it was selected as the most preferable fruit content for soursop drinking yoghurt.

The second sensory evaluation trail for the preference of sugar vs sucralose was conducted based on the yoghurt with the best level of soursop incorporation (20% w/v). Sucrose added drinking yoghurt was carried out replacing the content of sugar by adding sucralose, 200 mg/kg, according to the Food (Sweeteners) Regulations published by Ministry of Health and Indigenous Medicine (2015). Soursop incorporated drinking yoghurt (20% w/v) with added sugar, soursop incorporated drinking yoghurt (20% w/v) with added sucralose, and drinking yoghurt without incorporation of soursop (0% w/v) with added sugar (control) were evaluated by means of sensory attributes of odour, appearance, texture, taste, aftertaste, and overall acceptability using the nine point hedonic scale. Figure 2 shows the results obtained from the sensory evaluation. There was a significant difference ($p < 0.05$) in all sensory attributes of odour, appearance, texture, taste, aftertaste, and overall acceptability.

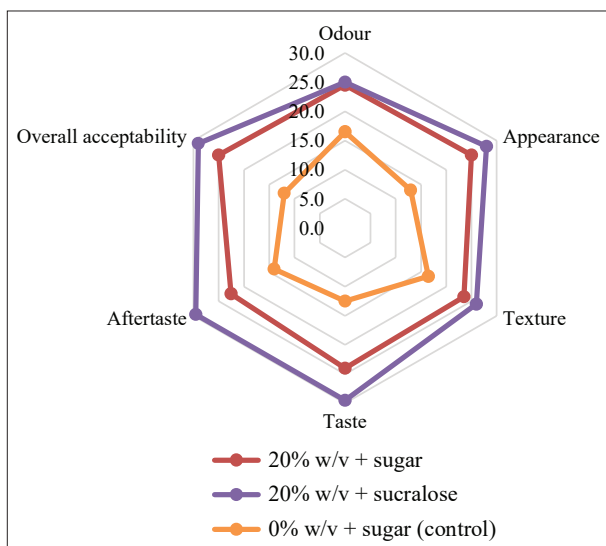


Figure 2: Sensory evaluation of the sugar added, sucralose added 20% Soursop incorporated drinking yoghurts and control drinking yoghurt

The 20% w/v soursop incorporated drinking yoghurt with added sucralose showed the highest ranks for odour, appearance, taste, texture, aftertaste and overall acceptability while control (0% w/v soursop) drinking yoghurt with added sugar showed the lowest ranks for all the attributes. Since soursop fruit is rich in polyphenols, it undergoes enzymatic browning easily and exhibits a pleasant cream colour with milk while the control drinking yoghurt prepared without adding soursop was pure white. In considering the taste, sucralose

added soursop drinking yoghurt achieved a higher rank than sugar added drinking yoghurts without bitter or objectionable aftertaste. Since sucralose has an excellent, intense taste profile the sweetness of sucralose inside the mouth was retained longer than the sweetness of sugar.

Even though 20% w/v soursop drinking yoghurt with added sucralose was selected as the most preferable drinking yoghurt, there are some limitations regarding sucralose which cause difficulty in commercializing. The higher price of sucralose and unknown health issues which may occur when overdosing are the main problems in commercializing sucralose added products. Therefore, sugar added 20% w/v soursop drinking yoghurt was selected as the best drinking yoghurt for further studies of functional and physico-chemical analysis, and it was compared with normal drinking yoghurt as a control.

Determination of physico-chemical properties of vacuum-dried soursop powder and drinking yoghurts

Proximate composition of vacuum-dried soursop powder

Proximate composition of moisture, crude fat, crude fibre, ash, crude protein and carbohydrates were determined and results are presented in Table 2.

Table 2: Proximate composition of vacuum-dried soursop powder, soursop incorporated drinking yoghurt and drinking yoghurt

Parameter	Soursop powder	Soursop drinking yoghurt	Control drinking yoghurt
Moisture (%)	4.04 ± 0.05	83.67 ± 0.31 ^b	84.67 ± 0.35 ^a
Fat (%)	1.86 ± 0.04	2.50 ± 0.03	3.43 ± 0.03 ^a
Crude fibre (%)	4.23 ± 0.03	0.14 ± 0.02 ^a	0.07 ± 0.01 ^b
Ash (%)	3.97 ± 0.04	1.04 ± 0.06 ^a	0.79 ± 0.02 ^b
Protein (%)	8.71 ± 0.04	2.96 ± 0.05 ^b	3.24 ± 0.03 ^a
Carbohydrates (%)	77.21 ± 0.06	9.70 ± 0.18 ^a	7.82 ± 0.23 ^b
Energy (kcal/100g)	360.42 ± 0.19	73.10 ± 1.07 ^a	75.26 ± 1.32 ^a

Values are represented in means ± standard deviations of three replicate measurements. Significant different was observed only between the soursop drinking yoghurt and control drinking yoghurt. Means with the same letters in the same row were not significantly different ($p < 0.05$).

According to the moisture content found in vacuum-dried soursop powder (4.04%), it had less moisture than the freeze-dried soursop powder ($8.68 \pm 0.07\%$), as described by Ceballos *et al.* (2012). Similar results were obtained, 4.33% and 4.02%, for the crude fibre and ash content, respectively, of the oven-dried soursop powder according to the study conducted by Badrie and Schauss (2010). In the same study by Badrie and Schauss (2010), the carbohydrate value of oven-dried soursop powder was found to be 84.82% and that value was comparatively higher than the carbohydrate content of vacuum-dried powder (77.21%).

A higher protein value could be observed in vacuum-dried soursop powder as shown in Table 2 when compared to the protein value in oven-dried soursop powder ($7.34 \pm 0.07\%$), developed by Badrie and Schauss (2010). The higher content of protein in vacuum-dried soursop powder may due to drying at a lower temperature ($60\text{ }^{\circ}\text{C}$) (Ngamwonglumlert & Devahastin, 2018). It was reported that the protein content of processed products derived from fresh fruits and vegetables is adversely affected by the temperature (Zhang *et al.*, 2016).

This phenomenon is due to the rate of the Maillard reaction at temperatures at or below $60\text{ }^{\circ}\text{C}$ becoming slower, so that amino acid nitrogens are hardly consumed in the Maillard reaction. With increasing temperature (above $60\text{ }^{\circ}\text{C}$), the rate of the Maillard reaction in food materials is accelerated, leading to a faster consumption of amino acid nitrogen; thereby the protein value of food becomes low. According to a study conducted by Wijewardana *et al.* (2016), vacuum drying was recommended as the most effective drying method to protect the chemical characteristics of fruit powders, compared to the other drying methods tested, such as sun drying, solar drying, freeze-drying, and oven drying.

Proximate composition of drinking yoghurts

Moisture, crude fat, crude fibre, ash, crude protein, and carbohydrates of both soursop drinking yoghurt and control drinking yoghurt are presented in Table 2.

As shown in Table 2, the moisture content of soursop drinking yoghurt was significantly lower ($p < 0.05$) than control drinking yoghurt. However, the soursop drinking yoghurt sample indicated a similar value for moisture content (83.69 ± 0.02) as reported by Virgen-Ceceña *et al.* (2019). The reason for the lower moisture content of soursop drinking yoghurt, compared with control

drinking yoghurt, was the significant increase ($p < 0.05$) in total solids of the soursop drinking yoghurt relative to control drinking yoghurt. Incorporation of fruit pulps, fruit pieces or fruit syrups into regular yoghurts resulted in higher total solid contents by lowering the moisture content of the product (Sengupta *et al.*, 2014).

The fat content of soursop drinking yoghurt was significantly lower ($p < 0.05$) than that of control drinking yoghurt while both drinking yoghurt samples were in accordance with Sri Lanka Standards (SLS 824, 2018). The fat content of soursop set yoghurt developed by Virgen-Ceceña *et al.* (2019) is comparatively higher (5.15 ± 0.24) than the fat content of soursop drinking yoghurt as shown in Table 2. Those changes may be due to the initial fat content of the cow's milk and the soursop fruits used (Jafarpour *et al.*, 2017).

The crude fibre content of the soursop drinking yoghurt according to Table 2 was significantly ($p < 0.05$) higher than control drinking yoghurt due to the incorporation of fibre rich soursop fruit pulp. A higher crude fibre content (3.13 ± 0.15) was observed in a coconut enriched drinking yoghurt prepared by Sengupta *et al.* (2014), compared to the soursop drinking yoghurt developed in this study.

According to Table 2, the soursop drinking yoghurt exhibited a significantly higher ($p < 0.05$) ash content than control drinking yoghurt due to the incorporation of mineral rich soursop fruit pulp. The total ash content of soursop incorporated set yoghurt developed by Sengupta *et al.* (2014) was comparatively lower (0.61 ± 0.05) than the value of soursop drinking yoghurt in the present study.

The protein content of the soursop drinking yoghurt exhibited a significantly lower value ($p < 0.05$) than the control drinking yoghurt due to the addition of gelatin into the control yoghurt as a stabilizer. However, the stabilizing effect in soursop drinking yoghurt is fulfilled by the pectin, which is naturally present in the soursop fruit (Wijesinghe *et al.*, 2018).

Energy value of stirred yoghurts developed by Dias and Jayasooriya (2017) using soursop juice and soursop nectar were higher than the value exhibited in soursop drinking yoghurt as shown in Table 2. The reason may due to the changes in carbohydrates, protein, and fat content in the final product (Sengupta *et al.*, 2014).

Evaluation of physico-chemical properties of drinking yoghurts

Titrateable acidity, pH, total soluble solids (TSS), milk solids non-fat (MSNF) and syneresis of both (20% w/v) soursop drinking yoghurt and control drinking yoghurt were determined once the products were prepared.

Titrateable acidity, pH, total soluble solids, syneresis, and milk solids non-fat of selected soursop drinking yoghurt were 0.85%, 4.5, 16.3 °Brix, 29.3%, and 13.8% respectively. According to the Sri Lanka standards, the minimum amount of MSNF required is 2.2% (w/w) and MSNF values obtained for both soursop drinking yoghurt and control drinking yoghurt satisfied the SLS requirement. The MSNF contents of soursop incorporated set yoghurt developed by Virgen-Ceceña *et al.* (2019) was comparatively lower (10.8%) than the value exhibited in the soursop drinking yoghurt developed in the present study. It may be due to the changes of the quantities of soursop pulp incorporated into the yoghurt.

Table 3: Physico-chemical properties of drinking yoghurts

Parameter	Soursop drinking yoghurt	Control drinking yoghurt
Total soluble solids (TSS) (°Bx)	16.33 ± 0.31 ^a	15.33 ± 0.35 ^b
Milk solids non-fat (MSNF)	13.83 ± 0.29 ^a	11.90 ± 0.36 ^b
Titrateable acidity (%)	0.85 ± 0.01 ^a	0.8 ± 0.02 ^b
pH	4.45 ± 0.01 ^b	4.52 ± 0.01 ^a
Syneresis (%)	29.33 ± 1.17 ^b	33.5 ± 1.04 ^a

Values represented are means ± standard deviations of three replicate measurements. Means with the same letters in the same row are not significantly different ($p < 0.05$)

The yoghurt starter culture (*Lactobacillus bulgaricus* and *Streptococcus thermophiles*) ferments milk sugar (lactose) to produce lactic acid which is essential for retaining the texture, taste, and shelf life of yoghurts in acidic environments to inhibit pathogen growth. Higher lactic acid content makes the yoghurts sour in taste and less palatable (Chandan & Kilara, 2013). Therefore, it is essential to maintain an optimum lactic acid content when developing a drinking yoghurt. The lactic acid content can be determined by measuring titrateable acidity of drinking yoghurts as shown in Table 3. The titrateable

acidity of both soursop drinking yoghurt and control drinking yoghurt are in accordance with the Sri Lanka standards where the range is defined as 0.8–1.25% (SLS 824, 1989). The titrateable acidity of soursop drinking yoghurt was significantly higher ($p < 0.05$) than control drinking yoghurt (Table 3). The titrateable acidity of soursop incorporated set yoghurt (0.70 ± 0.01) developed by Virgen-Ceceña *et al.* (2019) and that of soursop incorporated stirred yoghurt (0.68 ± 0.01) developed by Dias and Jayasooriya (2017) are less in value than that obtained for the soursop drinking yoghurt developed in the present study. This may be due to the acidity of the fruit, changes in the chemical composition of cow milk, and the fermentation conditions practised in developing the yoghurts.

The pH of the soursop incorporated drinking yoghurt exhibited a significantly lower value ($p < 0.05$) than control drinking yoghurt due to the inherent acidity of the soursop pulp. Espinosa *et al.* (2013) reported that just 3–4 days after harvesting of ripe soursop, malic acid increased by sevenfold, ascorbic acid increased by eleven fold and citric acid increased by three fold. Erkaya *et al.* (2012) reported that the amount of soursop pulp added and the fermentation process influenced both the pH and titrateable acidity of dairy products. According to SLS 824 (2018), drinking yoghurts should have a pH of 4.5, and both soursop incorporated yoghurt and control drinking yoghurt developed in this study complied with this standard.

Total soluble solids (TSS) of soursop drinking yoghurt and control drinking yoghurt exhibited a significant difference ($p < 0.05$). Brix value (20.85 ± 0.25) of soursop nectar incorporated stirred yoghurt developed by Dias and Jayasooriya (2017) was higher than the Brix value of soursop drinking yoghurt in the present study due to the fruit content and changes in chemical composition in milk (Calvacanti *et al.*, 2006).

Syneresis is the process of collecting whey on the surface of yoghurt and it is considered as a textural defect in yoghurt. As shown in Table 3, the soursop incorporated drinking yoghurt exhibited a significantly lower ($p < 0.05$) syneresis than the control drinking yoghurt. According to Vahedi *et al.* (2008), the reduction of syneresis in fruit incorporated yoghurts is due to absorption of unbound water molecules by fruit pulp. Further, the degree of homogenization, milk composition, type of culture, acidity resulting from the growth of bacterial cultures, and heat treatment of milk are also responsible for the occurrence of syneresis in yoghurt (Aswal *et al.*, 2012).

Determination of functional properties of fresh soursop fruit, vacuum-dried powder and drinking yoghurts

Determination of total polyphenolic content (TPC), total flavonoid content (TFC) and ferric reducing antioxidant power (FRAP) in soursop fruit and the products

TPC, TFC, and FRAP of fresh soursop fruit, vacuum-dried powder and the drinking yoghurts were determined and results are presented in both dry weight and fresh weight basis in Table 4.

Total polyphenolic content (TPC)

In the present study, comparisons were made only between fresh soursop fruit and the drinking yoghurts. According to Table 4 there was a significant difference ($p < 0.05$) in the TPC between the fresh fruit and the drinking yoghurts. The phenolic content of soursop drinking yoghurt had a significantly ($p < 0.05$) higher value than that of fresh soursop fruit and control. It was seen that when incorporating the fresh soursop

fruit (11.91 ± 1.80 mg GAE/g on dry weight basis) in developing the soursop drinking yoghurt, the TPC had increased to 14.13 ± 0.64 mg GAE/g. This increment may be due to the breakdown of soursop cell walls and subsequent activities of enzymes that lead to the liberation of bound polyphenolic compounds during fermentation (Adebo & Medina-Meza, 2020).

According to a study conducted by Adefegha *et al.* (2015), the TPC of fresh soursop fruit showed a lower value (4.30 ± 0.16 mg GAE/g) than the value in Table 4. According to Padmini *et al.* (2014), the TPC of fresh fruit pulp of the Sri Lankan *A. muricata* was reported as 0.22 mg/g, which was quite lower than the value obtained for the present study. The reason for those variations may be due to the differences in methodologies and geographical locations (Babbar *et al.*, 2011). The TPC of soursop incorporated set yoghurt developed by Virgen-Ceceña *et al.* (2019) had a lower value (2.43 ± 0.04 mg GAE/g of fresh weight) than the value obtained in the soursop incorporated drinking yoghurt developed in the present study. It may be due to the differences in the incorporated flesh weight of soursop fruit into the drinking yoghurt in both studies.

Table 4: TPC, TFC and FRAP contents of the fresh soursop fruit and the products

Product	TPC (mg GAE/g)		TFC (mg QE/g)		FRAP (mg TE/g)	
	DW basis	FW basis	DW basis	FW basis	DW basis	FW basis
Fresh soursop fruit	11.91 ± 1.80^b	1.85 ± 0.22^b	0.57 ± 0.12^b	0.09 ± 0.01^b	0.92 ± 0.03^b	0.15 ± 0.02^{ab}
Vacuum dried soursop powder	1.80 ± 0.09^c	1.73 ± 0.07^b	0.07 ± 0.01^b	0.07 ± 0.01^b	0.12 ± 0.01^d	0.12 ± 0.01^b
Control drinking yoghurt (0% soursop)	13.03 ± 0.88^{ab}	1.93 ± 0.10^b	0.66 ± 0.04^b	0.10 ± 0.05^b	0.51 ± 0.02^c	0.07 ± 0.00^c
Soursop drinking yoghurt (20% soursop)	14.13 ± 0.63^a	2.49 ± 0.09^a	3.39 ± 0.36^a	0.59 ± 0.14^a	1.32 ± 0.30^a	0.16 ± 0.00^a

Values are means \pm standard deviations of three replicate measurements. Means with the same letters in the same column are not significantly different ($p < 0.05$).

TPC- total polyphenolic content; TFC- total flavonoid content; FRAP- ferric reducing antioxidant power; FW- fresh weight; DW- dry weight

The TPC of fresh fruit was significantly reduced when developing vacuum-dried soursop powder. It was described by Pokorný and Schmidt (2001), that the heat treatment causes the reduction of antioxidant content by as much as 60%.

Total flavonoid content (TFC)

When comparing the TFC of drinking yoghurts, soursop drinking yoghurt gave the highest value ($p < 0.05$), even higher than the TFC value of the fresh soursop fruit.

As described by Kwak *et al.* (2007), the reason for the increase in TFC value is the production of aglycone isoflavone and malonylglycoside isoflavone compounds during fermentation. The TFC value of fresh soursop fruit (0.09 ± 0.01 mg QE/g) is slightly lower than the value reported by Adefegha *et al.* (2015) in the fresh fruit (1.00 ± 0.08 mg QE/g). The TFC value of soursop incorporated set yoghurt (0.32 mg QE/g) developed by Virgen-Ceceña *et al.* (2019) was lower than the value obtained in the present study (0.59 ± 0.14 mg QE/g) as shown in Table 4. The reason for such a change in TFC level may be the changes in the quantity of soursop fruit content incorporated into the yoghurt and the fermentation conditions (Kwak *et al.*, 2007).

Ferric reducing antioxidant power (FRAP)

Comparisons were discussed between fresh soursop fruit and the drinking yoghurts. According to the results obtained, the FRAP of soursop fruit is significantly lower ($p < 0.05$) than the FRAP of soursop drinking yoghurt. This suggests that consumption of soursop drinking yoghurt has more possibility in fighting cancer cells as a potent antioxidant than consuming soursop fruit. Further, the FRAP of fresh soursop fruit is significantly higher than that of the control drinking yoghurt which indicates that consuming soursop fruit is more beneficial than consuming regular drinking yoghurt with respect to ferric reducing antioxidant power. The FRAP of soursop drinking yoghurt is significantly higher than that of the control drinking yoghurt.

The FRAP values obtained in previous research cannot be compared with the present study due to the differences in the units used to express the results. The FRAP of vacuum-dried powder had a low value as presented in Table 4 due to the reduction of antioxidant compounds like polyphenols, tannins, coumarin,

flavones, and flavonoids at higher temperatures, as mentioned by Anaya Esparza and Montalvo-González (2020).

Determination of DPPH and ABTS radical scavenging activity

DPPH and ABTS radical scavenging activities of fresh soursop fruit, vacuum-dried powder and the drinking yoghurts were determined and presented in Table 5 in both wet and dry weight basis.

DPPH radical scavenging activity

The DPPH free radical method is an antioxidant assay based on electron-transfer activity that produces a violet coloured solution in ethanol. The antioxidant activity was expressed as the trolox equivalent and the sample extracts which showed high inhibitory activities in the screening study were studied for dose response relationship. The results were expressed as IC_{50} (μ g/mL), which is the concentration required to cause a 50% inhibition of DPPH activity (Garcia *et al.*, 2012).

Significant differences ($p < 0.05$) in DPPH radical scavenging activity could be observed between the fresh soursop fruit and drinking yoghurts. The DPPH radical scavenging activity of fresh soursop fruit has been significantly increased when incorporating into soursop drinking yoghurt. The enhancement of antioxidant activity of fresh produce due to the fermentation process was described by some researchers (Kwak *et al.*, 2007). Fermentation leads to release of phenolic acids and improved bio-accessibility and colonic metabolism of phenolic acids in fermentation (Verni *et al.*, 2019). According to a study conducted by Xu *et al.* (2020) the thermal drying of fruits and vegetables, including vacuum drying, results in a notable decrease in DPPH values.

Table 5: DPPH and ABTS radical scavenging activities of the fresh soursop fruit and the products

Product	DPPH radical scavenging activity		ABTS radical scavenging activity	
	mg TE/g	IC 50 (μ g/mL)	mg TE/g	IC 50 (μ g/mL)
Fresh soursop fruit	17.49 ± 1.01^b	360 ± 21^b	17.23 ± 0.38^b	321 ± 7^b
Vacuum dried soursop powder	0.919 ± 0.14^c	557 ± 17^a	2.0 ± 0.09^d	176 ± 6^c
Control drinking yoghurt (0% soursop)	15.28 ± 2.79^b	345 ± 25^b	9.50 ± 1.55^c	482 ± 24^a
Soursop drinking yoghurt (20% soursop)	25.68 ± 3.38^a	176 ± 18^c	30.15 ± 3.24^a	129 ± 11^c

Values are presented as mean \pm standard deviations of three replicate measurements. Means with the same letters in the same column are not significantly different ($p < 0.05$).

The radical scavenging rate at the concentration of a 50% inhibition (IC_{50}) was used as the indicator to evaluate the DPPH radical scavenging activity of fresh soursop and its products. The smaller the IC_{50} value, the higher the scavenging rate (Su *et al.*, 2017). It was seen that the significantly highest ($p < 0.05$) IC_{50} value was obtained in soursop drinking yoghurt (Table 5).

The DPPH radical scavenging activity of fresh soursop fruit (6.45 ± 0.07 mg TE/g) reported by Paz *et al.* (2015) was comparatively lower than the value obtained for the DPPH radical scavenging activity (Table 5). The reasons may be the varietal differences, soil conditions, maturity stage, and changes in the extraction method. The DPPH radical scavenging of soursop set yoghurt developed by Virgen-Ceceña *et al.* (2019) was lower (0.15 ± 0.09 mmol TE/g) than the DPPH radical scavenging activity of soursop drinking yoghurt studied in the present study. This may be due to the difference in quantity of the soursop incorporated. The IC_{50} value of control drinking yoghurt in relation to DPPH radical scavenging activity reported by Su *et al.* (2017) agrees with the IC_{50} value presented in Table 5. However, the DPPH radical scavenging activity assay has some limitations, such as steric hindrance, variability of DPPH radical interactions with other radicals, and the relations between antioxidants and DPPH (Xu *et al.*, 2020).

ABTS radical scavenging activity

Significant differences ($p < 0.05$) in ABTS radical scavenging activity were observed between the fresh soursop fruit and the drinking yoghurts. In comparison with the fresh fruit and the control drinking yoghurt, soursop fruit itself exhibited a significantly higher ($p < 0.05$) ABTS radical scavenging activity, due the presence of phyto-chemicals in the fruit. ABTS radical scavenging activity of soursop fruit had increased significantly ($p < 0.05$) when developing the soursop drinking yoghurt (Table 5) due to the fermentation process (Adebo & Medina-Meza, 2020). When comparing the two yoghurts, ABTS radical scavenging activity of soursop drinking yoghurt was significantly higher than the control drinking yoghurt. This is due to the incorporation of antioxidant rich soursop fruit pulp into regular drinking yoghurt followed by a fermentation process (Sah *et al.*, 2014).

CONCLUSION

According to the present study, the value added soursop drinking yoghurt could be developed by incorporating

fresh soursop fruit pulp into the regular drinking yoghurt. The soursop (20% w/v) incorporated drinking yoghurt with added sugar was chosen as the most feasible product and it showed acceptable physico-chemical and organoleptic properties with the best functional properties.

Acknowledgement

The authors acknowledge the Sri Lankan Treasury for granting financial support to the Industrial Technology Institute (Grant Number: TG19/169).

Competing interests

The authors have declared that there are no competing interests

REFERENCES

- Adebo O.A. & Medina-Meza I.G. (2020). Impact of fermentation on the phenolic compounds and antioxidant activity of whole cereal grains: A mini review. *Molecules* **25**(4): 927. DOI: <https://doi.org/10.3390/molecules25040927>
- Adefegha S.A., Oyeleye S.I. & Oboh G. (2015). Distribution of phenolic contents, antidiabetic potentials, antihypertensive properties and antioxidative effects of soursop (*Annona muricata* L.) fruit parts *in-vitro*. *Biochemistry Research International* 2015: 347673. DOI: <https://doi.org/10.1155/2015/347673>
- Agu K.C. & Okolie P.N. (2017). Proximate composition, phytochemical analysis and *in-vitro* antioxidant potentials of extracts of *Annona muricata* L. (Soursop). *Food Science and Nutrition* **5**(5): 1029–1036. DOI: <https://doi.org/10.1002/fsn3.498>
- Agu K.C., Eluehike N., Ofeimun R.O., Abile D., Ideho G., Ogedengbe M.O., Onose P.O. & Elekofehinti O.O. (2019). Possible anti-diabetic potentials of *Annona muricata* L. (soursop): inhibition of α -amylase and α -glucosidase activities. *Clinical Phytoscience* **5**(21): 1–13. DOI: <https://doi.org/10.1186/s40816-019-0116-0>
- Anaya Esparza L.M. & Montalvo-González E. (2020). Bioactive compounds of soursop fruit (*Annona muricata* L.). In: *Bioactive Compounds in Underutilized Fruits and Nuts* (eds. H.N. Murthy & V.A. Bapat), pp.175–189. Springer, Cham, Switzerland. DOI: https://doi.org/10.1007/978-3-030-30182-8_8
- AOAC (2012). *Official Methods of Analysis*. Association of Official and Analytical Chemists Washington DC, USA.
- Aswal P., Shukla A. & Priyadarshi S. (2012). Yoghurt: Preparation, characteristics and recent advancements. *Cibtech Journal of Bio-Protocols* **1**(2): 32–44.
- Babbar N., Oberoi H.S., Uppal D.S. & Patil R.T. (2011). Total phenolic content and antioxidant capacity of extracts

- obtained from six important fruit residues. *Food Research International* **44**(1): 391–396.
DOI: <https://doi.org/10.1016/j.foodres.2010.10.001>
- Badrie N. & Schauss A.G. (2010). Soursop (*Annona muricata* L.): composition, nutritional value, medicinal uses and toxicology. In: *Bioactive Foods in Promoting Health*. pp. 621–643. Academic Press, Orlando, USA.
DOI: <https://doi.org/10.1016/B978-0-12-374628-3.00039-6>
- Benzie I.F.F. & Szeto Y.T. (1999). Total antioxidant capacity of teas by the ferric reducing/antioxidant power assay. *Journal of Agricultural and Food Chemistry* **47**(2): 633–636.
DOI: <https://doi.org/10.1021/jf9807768>
- Blois M.S. (1958). Antioxidant determinations by the use of a stable free radical. *Nature* **181**: 1199–1200.
DOI: <https://doi.org/10.1038/1811199a0>
- Bourdoux S., Li D., Rajkovic A., Devlieghere F. & Uyttendaele M. (2016). Performance of drying technologies to ensure microbial safety of dried fruits and vegetables. *Comprehensive Reviews in Food Science and Food Safety* **15**(6): 1056–1066.
DOI: <https://doi.org/10.1111/1541-4337.12224>
- Calvacanti A.L., Oliveira K.F., Paiva P.S., Dias M.R., Costa S.K.P. & Vieira F.F. (2006). Determination of total soluble solids content (Brix) and pH in milk drinks and industrialized fruit juices. *Pesquisa Brasileira em Odontopediatria e Clínica Integrada* **6**(1): 57–64.
- Ceballos A.M., Giraldo G.I. & Orrego C.E. (2012). Effect of freezing rate on quality parameters of freeze dried soursop fruit pulp. *Journal of Food Engineering* **111**(2): 360–365.
DOI: <https://doi.org/10.1016/j.jfoodeng.2012.02.010>
- Chandan R.C. & Kilara A. (2013). *Manufacturing Yogurt and Fermented Milks*, 2nd edition, pp. 496. Wiley-Blackwell, New-Jersey, USA.
DOI: <https://doi.org/10.1002/9781118481301>
- Dias P.I. & Jayasooriya M.N. (2017). Enhancing the physicochemical and antioxidant properties of stirred yoghurt by incorporating soursop (*Annona muricata* L.). *International Journal of Life Sciences Research* **5**(1): 69–77.
- Erkaya T., Dağdemir E. & Şengül M. (2012). Influence of Cape gooseberry (*Physalis peruviana* L.) addition on the chemical and sensory characteristics and mineral concentrations of ice cream. *Food Research International* **45**(1): 331–335.
DOI: <https://doi.org/10.1016/j.foodres.2011.09.013>
- Espinosa I., Ortiz R.I., Tovar B., Mata M. & Montalvo E. (2013). Physiological and physicochemical behavior of soursop fruits refrigerated with methylcyclopropene. *Journal of Food Quality* **36**(1):10–20.
DOI: <https://doi.org/10.1111/jfq.12011>
- Fidianingsih I. & Handayani E.S. (2015). *Annona muricata* L. aqueous extract suppresses T47D breast cancer cell proliferation. *Universa Medicina* **33**(1): 19–26.
DOI: <https://doi.org/10.18051/UnivMed.2014.v33.19-26>
- Garcia E.J., Oldoni T.L.C., Alencar S.M.D., Reis A., Loguercio A.D. & Grande R.H.M. (2012). Antioxidant activity by DPPH assay of potential solutions to be applied on bleached teeth. *Brazilian Dental Journal* **23**(1): 22–27.
DOI: <https://doi.org/10.1590/s0103-64402012000100004>
- Gonzalez N.J., Adhikari K. & Sancho-Madriz M.F. (2011). Sensory characteristics of peach-flavored yogurt drinks containing prebiotics and synbiotics. *LWT-Food Science and Technology* **44**(1): 158–163.
DOI: <https://doi.org/10.1016/j.lwt.2010.06.008>
- Gyesi J.N., Opoku R. & Borquaye L.S. (2019). Chemical composition, total phenolic content and antioxidant activities of the essential oils of the leaves and fruit pulp of *Annona muricata* L. (Soursop) from Ghana. *Biochemistry Research International* **2019**: 4164576.
DOI: <https://doi.org/10.1155/2019/4164576>
- Jafarpour D., Amirzadeh A., Maleki M. & Mahmoudi M.R. (2017). Comparison of physicochemical properties and general acceptance of flavored drinking yogurt containing date and fig syrups. *Foods and Raw Materials* **5**(2): 546.
DOI: <https://doi.org/10.21603/2308-4057-2017-2-36-43>
- Kader A.A. (2005). Increasing food availability by reducing postharvest losses of fresh produce. *International Postharvest Symposium* **682**: 2169–2176.
DOI: <https://doi.org/10.17660/ActaHortic.2005.682.296>
- Kaur C. & Kapoor H.C. (2001). Antioxidants in fruits and vegetables—the millennium’s health. *International Journal of Food Science and Technology* **36**(7): 703–725.
DOI: <https://doi.org/10.1111/j.1365-2621.2001.00513.x>
- Kwak C.S., Lee M.S. & Park S.C. (2007). Higher antioxidant properties of Chungkookjang, a fermented soybean paste, may be due to increased aglycone and malonylglycosideisoflavone during fermentation. *Nutrition Research* **27**(11): 719–727.
DOI: <https://doi.org/10.1016/j.nutres.2007.09.004>
- Matela K.S., Pillai M.K., Ranthimo P.M. & Ntakatsane M. (2019). Analysis of proximate compositions and physicochemical properties of some yoghurt samples from Maseru, Lesotho. *Journal of Food Science and Nutrition Research* **2**: 245–252.
DOI: <https://doi.org/10.26502/jfsnr.2642-11000023>
- Ministry of Health and Indigenous Medicine (2015). FOOD ACT, No. 26 OF 1980, Food (Sweeteners) Regulations. The Gazette of the Democratic Socialist Republic of Sri Lanka, p. 7A.
- Ngamwonglumlert L. & Devahastin S. (2018). Microstructure and its relationship with quality and storage stability of dried foods. In: *Food Microstructure and Its Relationship with Quality and Stability*, pp. 139–159. Woodhead Publishing, UK.
DOI: <https://doi.org/10.1016/B978-0-08-100764-8.00008-3>
- Nguyen L. & Hwang E. (2016). Quality characteristics and antioxidant activity of yogurt supplemented with aronia (*Aronia melanocarpa*) Juice. *Preventive Nutrition and Food Science* **21**(4): 330–337.
DOI: <https://doi.org/10.3746/pnf.2016.21.4.330>
- Lagunju A. & Sandewa O. (2018). Comparative physicochemical properties and antioxidant activity of dietary soursop milk shake. *Beverages* **4**(2): 38–54.
DOI: <https://doi.org/10.3390/beverages4020038>
- Olugbuyiro J.A. (2011). Physico-chemical and sensory evaluation of market yoghurt in Nigeria. *Pakistan Journal of Nutrition* **10**(10): 914–918.

- DOI: <https://doi.org/10.3923/pjn.2011.914.918>
- Padmini S.M.P.C., Samarasekera R. & Pushpakumara D.K.N.G. (2014). Short Communication; Antioxidant capacity and total phenol content of Sri Lankan *Annona muricata* L. *Tropical Agricultural Research* **25**(2): 252–260. DOI: <https://doi.org/10.4038/tar.v25i2.8146>
- Paz M., Gúllon P., Barroso M.F., Carvalho A.P., Domingues V.F., Gomes A.M., Becker H., Longhinotti E. & Delerue-Matos C. (2015). Brazilian fruit pulps as functional foods and additives: Evaluation of bioactive compounds. *Food Chemistry* **172**: 462–468. DOI: <https://doi.org/10.1016/j.foodchem.2014.09.102>
- Pokorný J. & Schmidt S. (2001). Natural antioxidant functionality during food processing. In: *Antioxidants in Food: Practical Applications* (eds. J. Pokorny, N. Yanishlieva & M. Gordon), pp. 331–350. Woodhead Publishing, UK. DOI: <https://doi.org/10.1016/9781855736160.4.331>
- Pourmorad F., Hosseini-mehr S.J. & Shahabimajid N. (2005). Antioxidant Activity, phenol and flavonoids contents of some selected Iranian medicinal plants. *African Journal of Bio-Technology* **5**(11): 1142–1145.
- Raikos V., Ni H., Hayes H. & Ranawana V. (2019). Antioxidant properties of a yogurt beverage enriched with salal (*Gaultheria shallon*) berries and blackcurrant (*Ribes nigrum*) pomace during cold storage. *Beverages* **5**(1): 2–11. DOI: <https://doi.org/10.3390/beverages5010002>
- Re R., Pellegrini N., Proteggente A., Pannala A., Yang M. & Rice-Evans C. (1999). Antioxidant activity applying an improved ABTS radical cation decolorization assay. *Free Radical Biology and Medicine* **26**: 1231–1237. DOI: [https://doi.org/10.1016/s0891-5849\(98\)00315-3](https://doi.org/10.1016/s0891-5849(98)00315-3)
- Sah B.N.P., Vasiljevic T., McKechnie S. & Donkor O.N. (2014). Effect of probiotics on antioxidant and antimutagenic activities of crude peptide extract from yogurt. *Food Chemistry* **156**: 264–270. DOI: <https://doi.org/10.1016/j.foodchem.2014.01.105>
- Sengupta S., Chakraborty A. & Bhowal J. (2014). Production and evaluation of yogurt with water melon (*Citrullus lanatus*) juice. *Journal of International Academic Research for Multidisciplinary* **2**(5): 249–257.
- Shashikala G.G.A. & Mahendran T. (2019). Shelf life evaluation of soursop (*Annona muricata* L.) jelly without preservatives. *Proceedings of the 2nd International Symposium on Agriculture (ISA-2019)*, 9 January, Eastern University, Chenkalady, Sri Lanka, p. 132.
- Sinthiya R. & Poornima K. (2017). Value added products from annona fruit. *IOSR Journal of Environmental Science, Toxicology and Food Technology* **11**(8): 1–5.
- Singleton V.L., Orthofer R. & Lamuela-Raventos R.M. (1999) Analysis of total phenols and other oxidation substrates and antioxidants by means of Folin-Ciocalteu reagent. *Methods in Enzymology* **299**: 152–178. DOI: [https://doi.org/10.1016/S0076-6879\(99\)99017-1](https://doi.org/10.1016/S0076-6879(99)99017-1)
- SLS (1989). *SLS :824:Part2: Specifications for Fermented Milk Products*. Sri Lanka Standards Institute, Colombo, Sri Lanka.
- SLS (2018). *SLS:824: Part2: Methods of Tests for Fermented Milk Products*. Sri Lanka Standards Institute, Colombo, Sri Lanka.
- Solanki J., Mandaliya V.B. & George John J. (2020). Medical properties of *Annona muricata* extracts in various diseases. *Proceedings of 12th National Science Symposium on Recent Trends in Science and Technology*, 10 January. Rajkot, India, pp. 126–133.
- Su N., Ren L., Ye H., Sui Y., Li J. & Ye M. (2017). Antioxidant activity and flavor compounds of hickory yogurt. *International Journal of Food Properties* **20**(8): 1894–1903. DOI: <https://doi.org/10.1080/10942912.2016.1223126>
- Sun-Waterhouse D., Zhou J. & Wadhwa S.S. (2013). Drinking yoghurts with berry polyphenols added before and after fermentation. *Food Control* **32**: 450–460. DOI: <https://doi.org/10.1016/j.foodcont.2013.01.011>
- Vahedi N., Tehrani M.M. & Shahidi F. (2008). Optimizing of fruit yoghurt formulation and evaluating its quality during storage. *American-Eurasian Journal of Agricultural and Environmental Sciences* **3**(6): 922–927.
- Verni M., Verardo V. & Rizzello C.G. (2019). Review: How fermentation affects the antioxidant properties of cereals and legumes. *Foods* **8**(9): 362–383. DOI: <https://doi.org/10.3390/foods8090362>
- Villegas V.N. (2002). Breeding new fruit varieties in the Philippines. *Acta Horticulture* **575**: 273–277. DOI: <https://doi.org/10.17660/ActaHortic.2002.575.30>
- Virgen-Ceceña L.J., Anaya-Esparza L.M., Coria-Télez A.V., de Lourdes García-Magaña M., García-Galindo H.S., Yahia E. & Montalvo-González E. (2019). Evaluation of nutritional characteristics and bioactive compounds of soursop-yoghurt and soursop-frozen dessert. *Food Science and Biotechnology* **28**(5): 1337–1347. DOI: <https://doi.org/10.1007/s10068-019-00584-x>
- Wijesinghe J.A.A.C., Wickramasinghe I. & Saranandha K.H. (2018). Optimizing organoleptic properties of drinking yoghurt incorporated with modified kithul (*Caryotaurens*) flour as a stabilizer and evaluating its quality during storage. *Vidyodaya Journal of Science* **21**(1): 36–48. DOI: <http://doi.org/10.4038/vjs.v21i1.6066>
- Wijewardana R.M.N.A., Nawarathne S.B. & Wickramasinghe I. (2016). Effect of various dehydration methods on proximate composition and retention of antioxidants in different fruit powders. *International Food Research Journal* **23**(5): 2016–2020.
- Xu Y., Xiao Y., Lagnika C., Li D., Liu C., Jiang N., Song J. & Zhang M. (2020). A comparative evaluation of nutritional properties, antioxidant capacity and physical characteristics of cabbage (*Brassica oleracea* var. *Capitata* var. *L.*) subjected to different drying methods. *Food Chemistry* **309**: 124935. DOI: <https://doi.org/10.1016/j.foodchem.2019.06.002>
- Zhang X., Li N., Lu X., Liu P. & Qiao X. (2016). Effects of temperature on the quality of black garlic. *Journal of the Science of Food and Agriculture* **96**(7): 2366–2372. DOI: <https://doi.org/10.1002/jsfa.7351>

RESEARCH ARTICLE

Wind energy prediction

Development of wind energy prediction models using statistical, machine learning and hybrid techniques: a case study

P Ekanayake¹, O Panahatipola¹ and J Jayasinghe^{2*}

¹Department of Mathematical Sciences, Faculty of Applied Sciences, Wayamba University of Sri Lanka, Kuliyaipitiya, Sri Lanka.

²Department of Electronics, Faculty of Applied Sciences, Wayamba University of Sri Lanka, Kuliyaipitiya, Sri Lanka.

Submitted: 21 June 2021; Revised: 18 January 2022; Accepted: 25 March 2022

Abstract: This paper presents the development of statistical, machine learning, and hybrid models to predict the wind energy generation of a major wind farm in Sri Lanka named Nala Danavi. Regression based statistical techniques, namely, Multiple Linear Regression and Power Regression were applied to the input variables of wind speed and ambient temperature producing expressions for wind energy in terms of those weather indices. Similarly, the machine learning techniques of Support Vector Regression and Artificial Neural Network were applied in developing another set of wind energy prediction models. Unlike in the methods mentioned above, the Support Vector Machine was applied only to the past energy data. In contrast, a Vector Error Correction model was developed by using both wind energy and weather data. Further, time series modelling of wind energy data was performed to develop a Seasonal Autoregressive Integrated Moving Average model. The research was further extended to develop two hybrid prediction models by combining Support Vector Machine and Artificial Neural Network each with Seasonal Autoregressive Integrated Moving Average. The performance of all the models was assessed and compared in terms of the Coefficient of Determination, Root Mean Square Error, and the Mean Absolute Error. As per the results, all the models were highly accurate while the Support Vector Regression produced the most precise prediction model. The models developed in this research can be used to predict the wind energy generated at Nala Danavi wind farm using either the previous energy data or the projected weather data of the region.

Keywords: Correlation, neural networks, regression analysis, time series analysis, wind energy.

INTRODUCTION

Among all basic needs of human life today, the availability of an uninterrupted power supply has become indispensable due to the overwhelming dependence of every economic, educational, and social activity of people on electricity. The demand for electricity shall continue to increase in proportion to the growth of world population and other factors like urbanization and industrialization. With strong emphasis on ensuring a decarbonized environment for the future generation, the global energy bodies like the International Energy Agency (IEA) and the Global Wind Energy Council (GWEC) are insisting on the adoption of environmentally friendly renewable energy sources, and discouraging the use of power sources like thermal and fossil fuel that cause air pollution and ozone depletion leading to global warming. According to the World Energy Outlook (2018) by the IEA, the worldwide electricity consumption would increase by more than 25% within the next two decades. In this context, the environmental security will depend on the extent or the contribution made by clean energy sources like solar and wind power. Of these, the Global Wind Report (2019) by the GWEC reports that global wind power installations are gathering momentum with 60.4 GW of new input in 2019 alone due to its cost effectiveness compared to other renewable sources like bioenergy, tidal energy, hydro energy and

* Corresponding author (Jeevani@wyb.ac.lk;  <https://orcid.org/0000-0002-9266-8643>)



This article is published under the Creative Commons CC-BY-ND License (<http://creativecommons.org/licenses/by-nd/4.0/>). This license permits use, distribution and reproduction, commercial and non-commercial, provided that the original work is properly cited and is not changed in anyway.

solar photovoltaic energy. The annual increment of wind power capacity is reported to be around 30%, which has dominated the growth of other renewable energy sources during the past decade (Wang *et al.*, 2011; Zhao *et al.*, 2016). However, there is no shortage of challenges in extracting wind power to the main power grid from both onshore and offshore wind installations, due to the natural instability of weather around them.

The integration of wind power into a main grid also requires extra planning and management for balancing the power systems in the presence of the intermittence and volatility of wind power over various time scales (Foley *et al.*, 2010). The greatest impediment in the process of wind power assimilation to a main power grid is caused by fluctuations and uncertainties in wind speeds (Hanifi *et al.*, 2020), which set the stage for extensive research on discovering accurate wind power forecasting methods based on physical, statistical, machine learning and more recently hybrid techniques (Liu *et al.*, 2010; Shi *et al.*, 2012; Hanifi *et al.*, 2020). It has been pointed out that the risk of unpredictability in wind power penetration can be minimized with precise forecasting of wind speed and power generation (Chang, 2014). Wind speed is known to be affected by temperature, direction of wind, humidity, etc., as well as topographical and temporal features like terrain and particular time of the day/season. The demand for wind power forecasting over broad time scales is greater due to its advantages in planning unit commitment, dispatching, maintenance scheduling, and maximizing profits in power trade (Santhosh *et al.*, 2020).

The statistical models used in wind power forecasting have both advantages and disadvantages. Economical usage with convenience, accuracy in predictions over short-time scales (up to one day ahead), adaptation to the prevailing situation using auto-recursive mathematical algorithms, and the ability to provide average or peak wind speeds over such time scales are reported to be the advantages, while inaccurate predictions over long time periods (month or more ahead), need of a testing and tuning process to generate accurate predictions, and the assistance of site experts are reported to be the disadvantages (Lehr & Keeley, 2016). The Auto Regressive Moving Average (ARMA) is a widely used statistical model based on time series analysis (Chandra *et al.*, 2013). ARMA models, after being applied to wind speed and wind power output, have also shown that statistical modelling greatly improves wind forecasts compared to persistent forecasts (Milligan *et al.*, 2004). Taking the non-stationary wind speed into account and

using a Kalman Filter to estimate the time-varying model parameters, a linear autoregressive model was developed (Huang & Chalabi, 1995). Defining a particular state with the variables of wind speed, direction, and wind power, and determining the transition matrix using a maximum likelihood estimator based on multi-step transition data collected from a wind turbine in Portugal, a Markov Chain model also explained the wind speed and power probability density (Lopes *et al.*, 2012).

With the developments in the field of data science, researchers started to explore the potential of developing models based on machine learning for the prediction of wind energy generation and the performance of those models were compared with traditional statistical models. Having applied time series analysis on mean hourly wind speed data, a comparative study of several forecasting methods was conducted with ARMA, Feed Forward and Recurrent Neural Networks, Adaptive Neuro-Fuzzy Inference Systems (ANFIS), and Neural Logic Networks (NLN) (Sfetsos, 2000). As per the research findings of that study, neural network-based models outperformed ARMA. Yona *et al.* (2013) used historical wind speed data in a time series analysis using Neural Network, Auto Regression, and Kalman Filter to test wind power generation at a target time and their models predicted the power output based on wind forecasts. Using past power data and forecasts of wind speed and direction at a wind farm, a combination of Neural Networks and fuzzy logic techniques have also been applied to predict the wind power output (Sideratos & Hatzigiorgiou, 2007). In a review on different methods of wind power prediction, Agarwal *et al.* (2018) categorized statistical approaches into methods based on Neural Networks and models depending on time series. Though not generalized, they further pointed out that the performance of Neural Networks is usually higher than that of the time series models for most time scales. In another study, an ARMA statistical model and an Artificial Neural Network (ANN) model based on the Feed Forward Neural Network were used to forecast the wind power generation in Suthari, India while measuring the model accuracy in terms of the Mean Absolute Percentage Error (MAPE) and Mean Square Error (MSE) (Bhatt & Gandhi, 2019). Having used the normalization technique for better training performance and using the correlation coefficient to select inputs to the model, the ANN results were reported to be remarkably better than those produced by the statistical model. As per the literature, there is a high probability for techniques based on machine learning to outperform statistical approaches in the prediction of wind energy generation.

Apart from using statistical or machine learning techniques in isolation, several recent studies in the literature have highlighted the plausible dexterity of hybrid models for the prediction of wind power over conventional techniques (Shi *et al.*, 2012). A comprehensive study was carried out by Shi *et al.* (2012) to predict the hourly wind speed and power generation for five forecasting horizons using the hybrid methodology. In their work, the linear component of time series data was modelled by the ARIMA method and the nonlinear component by the ANN and Support Vector Machine (SVM) methods, to make up the two hybrid models: ARIMA-ANN and ARIMA-SVM. Having compared the results generated by the three single and two hybrid models, it was shown that the overall performance difference across all forecasting horizons remained under 5.5%. Due to this marginality of results, they concluded that hybrid models do not always yield the best predictions. Perusing the literature, it could be found that hybrid models were scarcely used for the wind energy prediction. In the meantime, hybrid modelling has been used in other fields too. Tseng *et al.* (2002) reported the development of a hybrid prediction model that comprised of Seasonal ARIMA (SARIMA) and the Back Propagation Neural Network models. Having combined the statistical ARIMA model with two Neural Networks, it was shown in a separate study that the hybrid model produced better results over each model applied separately (Hansen & Nelson, 2003). Voyant *et al.* (2012) used a pre-input layer selection method and combined an optimized multilayer perception with an ARMA model. They proved the reduction in the prediction error of the ANN-ARMA hybrid method and pointed out that their conclusions are consistent with renewable energy deployment too. In this context, this research focuses on the development of conventional statistical and machine learning models as well as hybrid models for the wind energy prediction.

Though the generation of wind power is increasing progressively in Sri Lanka, research on the operation of wind farms is in its infancy. Being a major generator of wind energy in Sri Lanka, the Nala Danavi wind farm should possess regular and accurate estimates of power generation capacity in order to manage its wind power contribution to the national grid. However, such estimates are complicated by volatile weather conditions in the region caused by changing wind speeds and other weather indices, which lead to inaccurate predictions. In this study, a comprehensive modelling package is developed to provide precise predictions of wind

energy based on either past wind energy and weather data or projected weather data for the future, so that wind power operators can make use of several options. As a previous study has not been undertaken for Nala Danavi with multiple modelling techniques, forecasting of wind energy generation at Nala Danavi wind farm in Sri Lanka is explored in this study comparatively using four statistical models: Multiple Linear Regression (MLR); Power Regression (PR); SARIMA; and Vector Error Correction (VEC), three machine learning models: Support Vector Regression (SVR); SVM; and ANN, and two hybrid models: SARIMA-SVR and SARIMA-ANN. Exploration of hybrid models shall be beneficial in determining whether they are in fact superior for predictions over the use of other techniques for coastal wind installations in Sri Lanka. The models to be identified as appropriate tools for Nala Danavi may be extended to other coastal wind farms in the island that exhibit similar weather patterns over longer periods of time.

MATERIALS AND METHODS

Study area and climatic data

Study area

The Nala Danavi wind farm is located in the Kalpitiya Peninsula in the Puttalam district (08°05'23"N 79°42'33"E) on the western coast of Sri Lanka (Figure 1a). The facility comprises of six turbines (model: Gamesa G58) with the rated power of 850 KW in each. The power curve of the wind turbines is shown in Figure 1b. The cut-in and cut-out wind speeds of the wind turbine are 3.0 m/s and 20.0 m/s respectively. The variation of monthly wind energy output during the period 2015–2020 is shown in Figure 2. The average monthly wind energy generation of the farm is 1112.9 MWh with minimum and maximum monthly energy generation of 125.2 MWh and 3037.8 MWh respectively. Further, an annual pattern of energy generation could be observed with a peak in the middle of each year (Figure 3a).

Wind energy generation zoomed into the daily values is illustrated in Figure 3b. The daily generation in most of the days from May to September varies between 50–100 MWh while it is lower than 40 MWh in other months. On average, about 77% of the annual energy generation is achieved during the period of the above five months as per the past data.

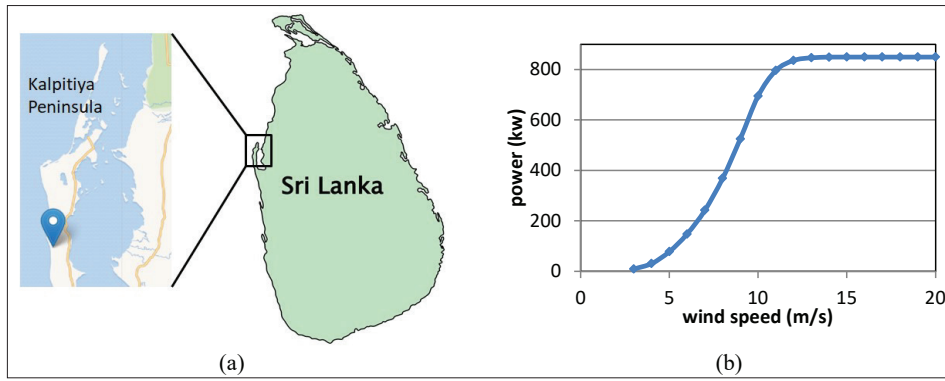


Figure 1: Wind turbines (a) location; (b) power curve

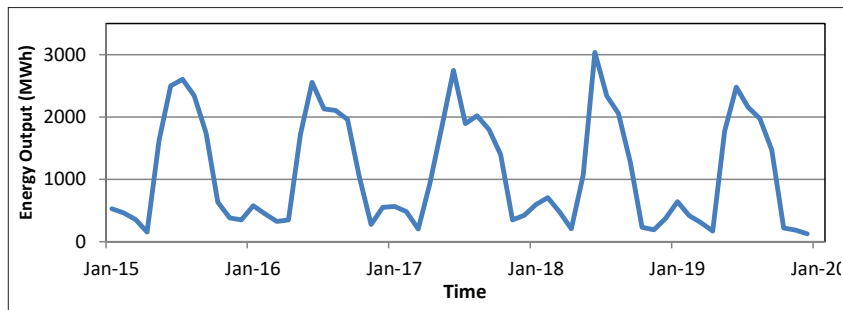


Figure 2: Variation of monthly wind energy output in the period: 2015–2020

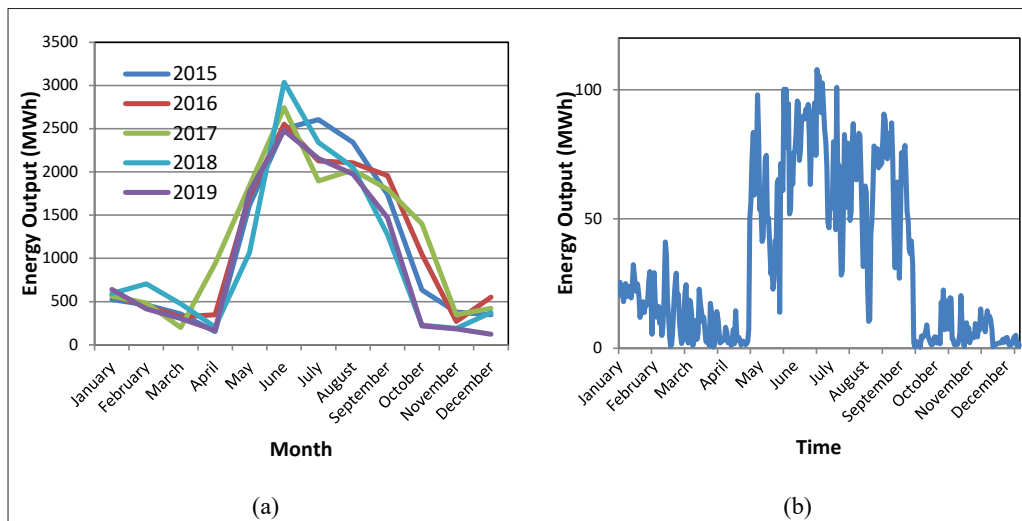


Figure 3: Variation of wind energy output (a) monthly data; (b) daily data

Climatic data

The climatic data of wind speed, wind direction, and the ambient temperature measured at the meteorological station located at the wind farm were obtained. The variation of monthly wind speed (Figure 4a) is similar to the variation of monthly energy generation, having speedy winds during the period from May to September annually. The average monthly wind speed varies between 10.7 m/s and 2.5 m/s, while the instantaneous wind speed varies between 0–18.7 m/s.

As per the plot of wind energy output with wind speed (Figure 5a), they are linearly correlated following the power curve of the wind turbines when the wind speed lies between 3–12 m/s. The monthly ambient temperature varies between 33.7 °C and 42.4 °C (Figure 4b). However, as per the data collected throughout the day, the ambient temperature varies between 25°C and 53 °C. As per the plot of wind energy output with ambient temperature (Figure 5b), the relationship is not very linear.

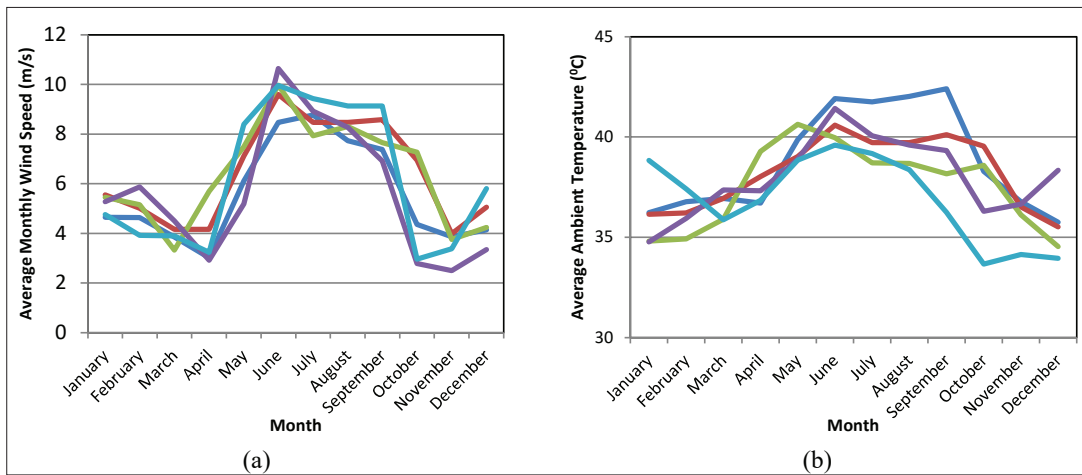


Figure 4: Variation of monthly climatic data (a) wind speed; (b) ambient temperature

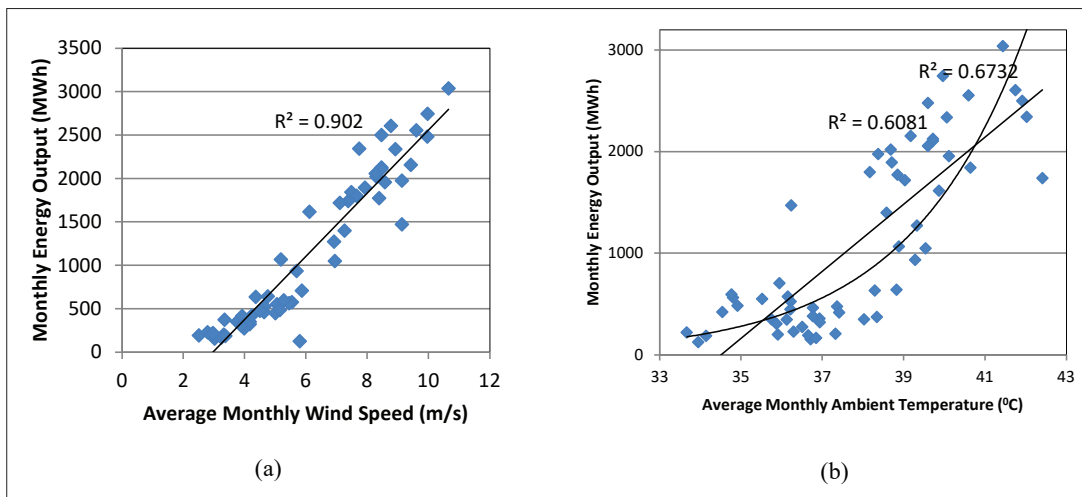


Figure 5: Variation of wind energy output with climatic factors (a) monthly wind speed; (b) monthly ambient temperature

Collinearity

The correlations between the variables were calculated in terms of the Pearson’s correlation (R) and the Spearman’s correlation (ρ), summarized in Figure 6.

It can be understood from the correlation values that a strong positive correlation exists between wind energy and wind speed. Further, the mediocre correlation values

between wind energy and ambient temperature are in agreement with the coherence between the patterns of monthly variation of the same weather indices seen in Figure 4. The wind energy generation depends on the wind direction as well. However, the rotor of the wind turbine rotates continuously based on the wind direction to harvest the maximum wind. Therefore, the wind direction was not considered as an input variable in this study.

Wind energy	1		
Ambient temperature	R= 0.82 $\rho = 0.79$	1	
Wind speed	R= 0.95 $\rho = 0.94$	R= 0.69 $\rho = 0.67$	1
	Wind Energy	Ambient Temperature	Wind Speed

Figure 6: Correlation between the wind energy and weather parameters

Prediction models

Multiple linear regression (MLR) model

The wind energy in MLR is expressed in terms of the wind speed (WS) and temperature (T) as follows:

$$\text{Energy} = \beta_0 + \beta_1 WS + \beta_2 T + \varepsilon \quad \dots(1)$$

where, β_0 is the intercept (a constant), β_1 and β_2 are the regression coefficients of the input variables, and ε is the random error under the assumption that it is normally distributed with mean zero and constant variance.

Power regression (PR) model

Unlike MLR, PR forms a nonlinear relationship in which the output is modelled in proportion to a power of the explanatory variables. Its expression is a power (polynomial) equation of the form of $y = ax^b$, where x has to be non-zero as follows:

$$\text{Energy} = a WS^b T^c \quad \dots(2)$$

where, a , b , and c are constants.

Seasonal autoregressive integrated moving average (SARIMA) model

ARIMA is one of the most widely used and recognized

statistical forecasting time series models. As the wind energy data demonstrate a seasonal pattern with a frequency of one year, a modified version of the ARIMA model called the SARIMA model was used in this research. The structure of the SARIMA model is presented in the form of SARIMA (p, d, q) (P, D, Q)_s, where, p, d, and q are non-seasonal terms and P, D, and Q are seasonal terms, which represent the order of the autoregressive process (P and p), the number of differencing (D and d), and the order of the moving average process (Q and q) respectively. The span of seasonality is indicated by s, which is 12 in this research study due to the use of monthly energy data with an annual pattern. The SARIMA model is expressed as (Haddad et al., 2019),

$$\phi_p(B)\Phi_P(B^s)W_t = \theta_q(B)\Theta_Q(B^s)Z_t \quad \dots(3)$$

where, Z_t is a purely random process and W_t is the transformation of the input variable (wind energy) X_t according to

$$W_t = \nabla_s^D \nabla^d X_t. \quad \dots(4)$$

Further, the model terms are expanded as follows.

$$\begin{aligned} \phi_p(B) &= 1 - \alpha_1 B - \alpha_2 B^2 - \dots - \alpha_p B^p \\ \Phi_P(B) &= 1 - \alpha_1 B^s - \alpha_2 B^{2s} - \dots - \alpha_P B^{Ps} \\ \theta_q(B) &= 1 + \beta_1 B + \beta_2 B^2 + \dots + \beta_q B^q \\ \Theta_Q(B) &= 1 + \beta_1 B^s + \beta_2 B^{2s} + \dots + \beta_Q B^{Qs} \end{aligned} \quad \dots(5)$$

In the development of the SARIMA model, the Box-Jenkins Method (Box & Jenkins, 1976) was used for identifying, estimating, and checking models. In the model identification process, several models were found suitable for time series modelling. The auto correlation function (ACF) and partial autocorrelation function (PACF) were applied to make the first guess on the orders (p, q, P, Q) of the ARIMA model, which is the initial tentative model. Using possible combinations of the orders, a set of suitable models was developed. Out of these models (combination of orders for the autoregressive and moving average), the model that generated the minimum Bayesian Information Criterion (BIC) value was selected for further analysis. The BIC is given by,

$$BIC = \ln(\hat{\sigma}_e^2) + \frac{2k \ln(n)}{n} \quad \dots(6)$$

where, n is the sample size, k is the number of estimated parameters, and $\hat{\sigma}_e^2$ is the error variance. A major advantage of this criterion is that it can effectively address the problem of overfitting.

Once the model is identified, the parameters need to be estimated and in principle the selected parameters should generate the lowest residual. This can be accomplished by using the Yule-Walker Estimation or the Maximum Likelihood Estimation. After estimating the parameters, the residuals should be checked to assess whether they are random and uncorrelated.

In order to test the selected model, the correlogram of the residuals was analysed and a global contrast was applied using the Ljung-Box statistic mentioned below.

$$Q^* = n \sum_{k=1}^L r_k^2(a) \quad \dots(7)$$

where, $r_k^2(a)$ is the autocorrelation coefficient of the residuals, n is the number of data points and L is the maximum delay considered (Shi *et al.*, 2012). In this study, all the data points were used to develop the model and 20% of data points were randomly selected for validation.

Based on the above technique, the data were tested using the Augmented Dickey Fuller Test and it was found that the data are stationary at the 5% significance level. Figure 7 shows the autocorrelation and partial autocorrelation values of the variable, wind energy, by k time periods apart called the lag.

As per the ACF and PACF plots (Figure 7), a model with the structure of SARIMA (2, 0, 1)(0, 0, 1)₁₂ was identified tentatively. The set of possible candidate models identified by modifying the tentative model is given in Table 1. The smallest BIC value could be obtained when the structure of the model is in the form of SARIMA (0, 0, 0)(0, 1, 1)₁₂.

The corresponding model can be given in the form of

$$\hat{X}_t = a + X_{t-12} + bZ_{t-12} \quad \dots(8)$$

where, a is a constant and b is the seasonal moving average parameter. In order to test the goodness of fit of the proposed SARIMA model, the correlogram of the residuals and Ljung-Box statistics were analyzed. According to the results, the residuals of the proposed model are not correlated.

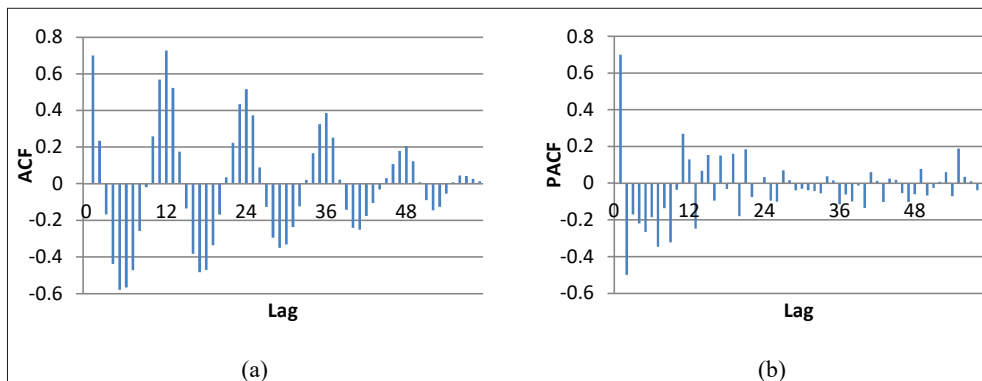


Figure 7: Correlation structure of wind energy (a) auto correlation function; (ACF) (b) partial autocorrelation function (PACF)

Table 1: BIC values of possible candidate models

Model structure	BIC
SARIMA(2,0,1)(0,0,1) ₁₂	12.4123
SARIMA(1,0,1)(0,0,1) ₁₂	12.5122
SARIMA(2,0,0)(0,0,1) ₁₂	12.4492
SARIMA(0,0,0)(0,1,1) ₁₂	11.4758
SARIMA(0,0,0)(1,1,0) ₁₂	11.8334

Vector error correction (VEC) model

A VEC Model, which is a special case of vector autoregression, was also used to predict the wind energy. It takes the form of

$$\Delta y_t = \alpha + \sum_{i=1}^p \beta_i \Delta y_{t-i} + \sum_{i=1}^p \gamma_i \Delta x_{t-i} + \sum_{i=1}^p \delta_i \Delta z_{t-i} + \sum_{i=1}^r \theta_i ECT_i + \varepsilon_t \quad \dots(9)$$

where, Δy_t is the first difference of the variable y_t (wind energy), α is a constant, β is the coefficient of the lags of differenced variable y_t , γ is the coefficient of the lags of differenced variable x (wind Speed), δ is the coefficient of the lags of differenced variable z (temperature), θ is the vector of cointegration relationships, ECT refers to the error correction terms derived from long run cointegration relationships, and ε_t are the serially uncorrelated random error terms with zero mean. Further, the summations are taken over the number of lags p and the rank of the cointegration (r).

80% of data were used to build the model and the remainder was used to validate the model. The Dickey-Fuller unit root test was used to check the stationarity of each variable. Lag order was determined by using the Akaike Information Criterion (AIC), Hannan–Quinn information Criterion (HQC), Schwarz Criterion (SC), and the Final Prediction Error (FPE) information criterion. A cointegration test was used to check whether there is a correlation between several time series in the long term. Further, the Johansen test was used to identify the rank of the cointegration. Seasonal variation was controlled by specifying the season as 12 since data demonstrated a seasonal variation.

After fitting the model, its adequacy was checked in terms of the serial correlation of residuals, heteroscedasticity in the residuals, and the normality of residuals by performing Portmanteau Test, Lagrange-

Multiplier test, and Jarque–Bera test respectively. Data were examined for stationarity using the Augmented Dickey Fuller test, which suggested that all the variables are stationary at 5% level of significance. The order of the model was chosen according to the information criteria and three out of four criteria favoured choosing the lag order 2, with AIC(n)=2, HQ(n) = 2, SC(n) = 1, and FPE(n) = 2. The trace of the Johansen test identified the rank of the cointegration as 1.

The model was built choosing lag $p = 2$ and the rank of cointegration $r = 1$ by specifying 12 seasonal dummies. After fitting the model, its adequacy was checked, and the results of the Portmanteau Test suggested that the error term is not serially correlated. Further, there was no heteroscedasticity as per the Auto Regressive Conditional Heteroscedasticity (ARCH) Lagrange-Multiplier test. The Jarque–Bera test suggested the normality of the residuals.

Support vector machine (SVM) and support vector regression (SVR) models

SVM is a versatile Supervised Learning Algorithm, which is used for classification as well as regression problems. SVR finds a linear hyper plane, which fits the multidimensional input vectors to output values. In this research, a single SVM model was used to classify monthly wind energy data, and the SVR predicts the monthly wind energy by regressing it on wind speed and temperature, using the support vector algorithms. The standard SVM to solve approximation problems is as follows,

$$f(x) = \sum_{i=1}^N (\alpha_i^* - \alpha_i) k(x_i, x) + b \quad \dots(10)$$

where, α_i^* and α_i are Lagrange multipliers and b is the displacement of bias. The kernel function $k(x_i, x)$ is the inner product of two elements of Hilbert space such that,

$$k(x_i, x) = \varphi(x_i)\varphi(x). \quad \dots(11)$$

where φ is the nonlinear mapping. The coefficients α_i^* and α_i have been obtained by minimizing the following regularized risk function:

$$R_{reg}[f] = \frac{1}{2} \|\omega\|^2 + C \sum_{i=1}^l L_\varepsilon(y) \quad \dots(12)$$

The term $\|\omega\|^2$ has been characterized as model complexity, C is a constant determining the trade-off, ε is the intensive loss function and $L_\varepsilon(y)$ is given by (Li et al., 2020)

$$L_\varepsilon(y) = \begin{cases} 0, & \text{for } |f(x) - y| < \varepsilon \\ |f(x) - y| - \varepsilon, & \text{otherwise.} \end{cases} \dots(13)$$

The kernel function used in this research is the Radial Basis Function (RBF),

$$k(x_i, x) = \exp(-\gamma||x_i - x||^2); \quad \gamma = 1/2\sigma^2 \dots(14)$$

The RBF kernel function was selected since the model trained by the RBF has a better overall performance than other kernel functions when there is no prior knowledge about the problems. In the SVM-based prediction models, the constant determining the trade-off (C) and kernel function parameter γ have a great effect on prediction results. The kernel function parameter γ is used to control the model complexity and the approximation error (Li *et al.*, 2020). A grid-search was done using 10-fold cross validation and the optimum values of C, γ and ε were selected based on the MSE. The grid selections of γ , C and ε were (1, 2, 3, 4, 5, ..., 100), (2⁻³, 2⁻², 2⁻¹) and (10⁻⁴, 10⁻³, 10⁻²) respectively. In this case too, 80% of data from the whole data set was extracted randomly to train the model and the remaining 20% was used to validate the model. Using the grid search, the final optimal parameters which minimized the MSE were found as C = 95, $\gamma = 0.125$ and $\varepsilon = 10^{-4}$ for SVM and C = 7, $\gamma = 0.125$ and $\varepsilon = 10^{-4}$ for SVR.

Artificial neural network (ANN)

The Feed-forward Neural Network architecture was trained by using the “neuralnet” function of the R package (Version 4.0.5), which is a network training function that updates weights and bias values during training. The input vector is presented by $Y_j = \{y_1, y_2, y_3, \dots, y_n\}$; W_{jk} ($j = 1, 2, 3, \dots, n; k = 1, 2, 3, \dots, m$) is the connection weight vector of the j nodes of the input layer to the k nodes of the hidden layer; X_k ($k = 1, 2, 3, \dots, m$) is the vector of k neurons in the hidden layer; W_k ($k = 1, 2, 3, \dots, m$) is the connection weights of the k nodes of the hidden layer to the output layer; and Y is the unit output vector for the neural network with one output neuron. Θ_k ($k = 1, 2, 3, \dots, m$) is the bias value of the hidden layer nodes and Θ is the bias value of the output layer.

The output of the hidden layer is determined by the formula

$$X_k = f(\sum_{j=1}^n W_{jk} Y_j + \Theta_k) \dots(15)$$

The output of the output layer is determined by the formula (Mapuwei *et al.*, 2020)

$$Y = f(\sum_{k=1}^m W_k X_k + \Theta), \dots(16)$$

where, f is the activation function for the hidden and output layers. Here, Logistic (Sigmoid) function was used as the activation function. When designing ANN, data were preprocessed before modelling. The data were normalized using the min-max normalization method in order to prevent saturation of hidden nodes before feeding into the neural network. Data were separated into two sets having 80% of data as the training set and the rest for testing. Supervised training with resilient backpropagation was used as the training algorithm with the threshold value of 0.01 for the training dataset.

Hybrid models

The performances of some forecasting methods such as ARIMA depend upon the linearity of data. Hybrid models, which have the capability to capture both linear and nonlinear characteristics, are thus believed to be a good strategy for time series forecasting. Hybrid models typically employ an ARIMA to model the linearity of data, while using an ANN or SVM for modelling the nonlinearity. In general, the concept of a hybrid model can be represented as follows (Shi *et al.*, 2012):

$$y_t = L_t + N_t, \dots(17)$$

where, L_t denotes the linear component and N_t , represents the non-linear component. First an ARIMA model was used to capture the linearity of the data and the non-linear techniques of SVM and ANN were used to capture the nonlinearity of the data.

In the SARIMA-SVM model, the SVM model was constructed to forecast the residuals of the established SARIMA models, and the parameter selection was done as per the same procedure in the single SVM modelling approach. Similarly, in the SARIMA-ANN model, ANN model dealt with the residuals and the FFNN model was developed using the residuals from the trained set, which is 80% of the residuals, and compared against observed data for the remaining test set. In the grid search of the SVM model for the errors established from SARIMA, the final optimal parameters which minimized the MSE were found as C = 2, $\gamma = 0.125$ and $\varepsilon = 10^{-4}$. The SARIMA-ANN hybrid model was developed using 5 hidden nodes.

Performance evaluation criteria

The coefficient of determination (R^2) describes the degree of collinearity between observed and predicted data. It indicates the proportion of the variance in observed data explained by the model. In the range from 0 to 1, higher R^2 values indicate less error variance. Typically, a prediction model with $R^2 \geq 0.5$ is considered acceptable (Mapuwe et al., 2020). Although widely used for the evaluation of prediction models, it is oversensitive to outliers. On the other hand, it is insensitive to additive and proportional differences between the observed and predicted data.

$$R^2 = \frac{(\sum_{i=1}^N (O_i - \bar{O})(P_i - \bar{P}_{mean}))^2}{\sum_{i=1}^N (O_i - \bar{O})^2 \sum_{i=1}^N (P_i - \bar{P}_{mean})^2} \quad \dots(18)$$

where O_i is the observed power generation, P_i is the predicted power generation, \bar{O} and \bar{P} are their means respectively, and N is the number of data points. R^2 provides a good measure of performance if the model to be fitted is linear but may not be an ideal goodness-of-fit statistic for nonlinear type of models. Another point of concern when using R^2 is that it tends to rise with the number of independent variables being considered, even if they may be redundant for the purpose.

The root mean square error (RMSE) is a commonly used metric for comparing model predictions with observed results. RMSE, which is expressed in the same units as the forecast variable, is of particular significance because of its property to attach a higher weightage to large errors which are unacceptable.

$$RMSE = \sqrt{\frac{\sum_{i=1}^N (P_i - O_i)^2}{N}} \quad \dots(19)$$

RMSE = 0 indicates a perfect fit and it increases with the variance of errors, the difference between predicted and observed values.

The Mean Absolute Error (MAE) is simply the average of absolute deviations of predicted values from the corresponding observed figures. Since it is the mathematical mean, the weightage attached to each deviation is the same, which is in contrast to the RMSE. Therefore, it is not susceptible to outliers in the data. MAE is determined using the following equation.

$$MAE = \frac{1}{N} \sum_{i=1}^N |O_i - P_i| \quad \dots(20)$$

As the above three metrics are capable of highlighting different characteristics, all of them were calculated to assess the performance of each statistical-, machine learning-, and hybrid-model employed in this study.

RESULTS AND DISCUSSION

Performance of the models

In the MLR- and PR-based models, the wind energy was expressed in terms of the wind speed (WS) and the ambient temperature (T) as follows.

$$E_{MLR} = -5333.5 + 281 WS + 125.5 T \quad \dots(21)$$

$$E_{PR} = 2.84 \times 10^{-7} WS^{1.71} T^{5.16} \quad \dots(22)$$

In the SARIMA model, the wind energy at time t ,

$$E_{t(SARIMA)} = -41.45 + E_{t-12} + Z_t + 0.7602Z_{t-12} \quad \dots(23)$$

where, Z_t denotes the forecast error at time t .

The variation of the predicted wind energy against the observed values corresponding to each prediction model is illustrated in Figure 8.

The performance of all the wind energy prediction models was compared in terms of the coefficient of determination, RMSE, and the MAE. As per the evaluation criteria, all the models are highly accurate. It can be clearly noticed that the two machine learning models of SVR and ANN, Figures 8(e) and 8(f), have produced the best linearity between the observed and predicted wind energies, as verified by the performance indicators in Table 2. This is closely followed by the performance of the three statistical techniques of MLR, PR and VEC whose scatter plots also show good agreement between observed and predicted values [Figures 8(a) and 8(b)]. All those five models have the common feature that weather indices of wind speed and ambient temperature were used as the input variables in modelling. The time series models, which are purely based on past wind energy data, also exhibit less error in terms of MAE and RMSE thus providing viable alternatives to the other prediction models. The single SVM model in which only the past energy data were used shows the least performance with the largest error which is also acceptable since it is a small portion of the energy.

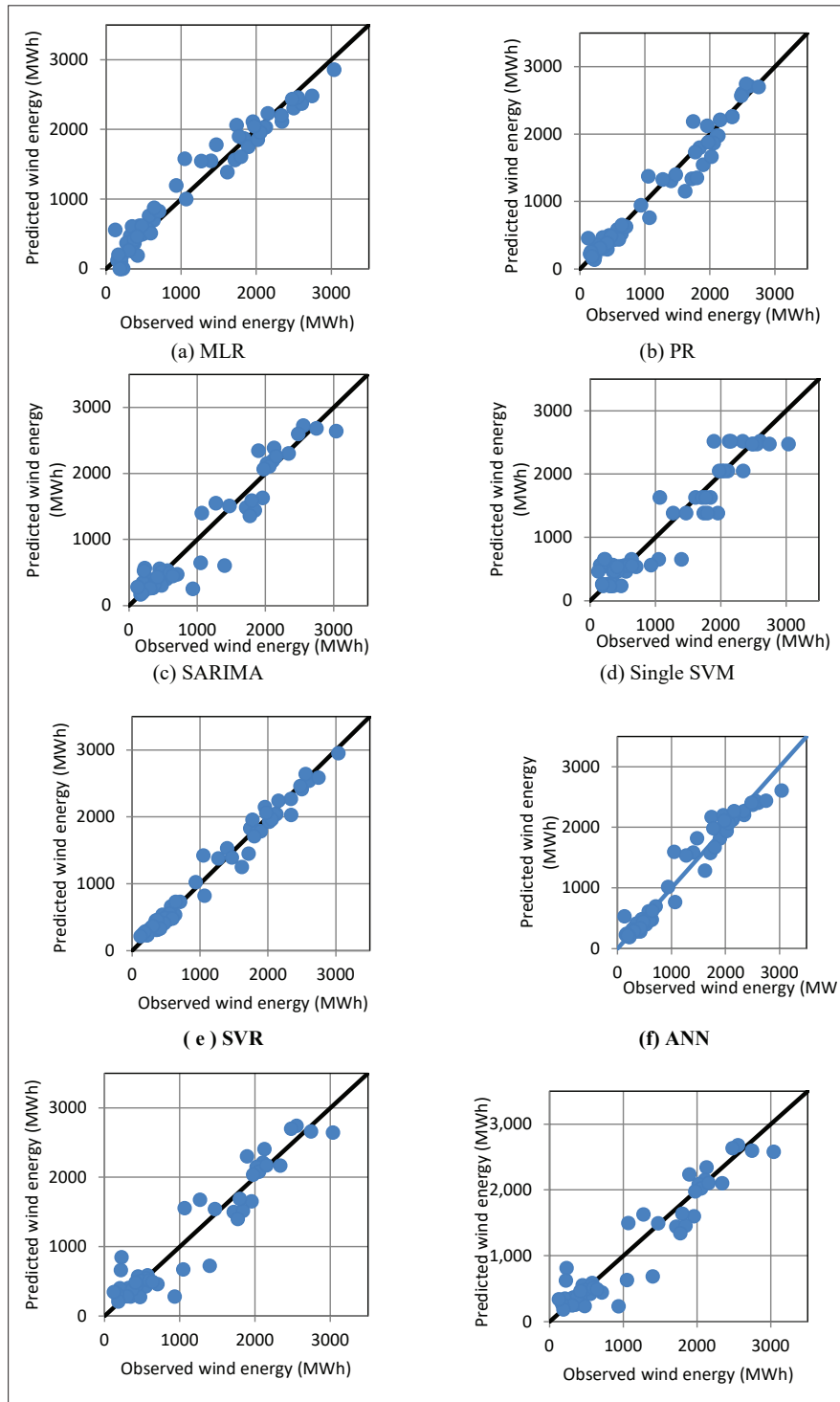


Figure 8: Scatter plots of predicted wind energy against the observed values with the line of best fit corresponding to each prediction model (a) MLR; (b) PR; (c) SARIMA; (d) Single SVM; (e) SVR; (f) ANN; (g) hybrid SARIMA-ANN; (h) Hybrid SARIMA-SVM

Table 2: Performance of the prediction models

	MAE	RMSE	R ²
SVR	77	133	0.98
ANN	123	173	0.96
MLR	142	177	0.95
PR	125	184	0.93
VEC	176	223	0.95
SARIMA	180	250	0.92
Single SVM	194	267	0.90
Hybrid SARIMA-SVM	190	264	0.91
Hybrid SARIMA-ANN	193	261	0.91

Subtle differences among model performances can be fathomed as the RMSE penalizes large prediction errors compared to MAE which is not sensitive to outliers. In this sense, SARIMA, SVM, and the two hybrid models indicate larger errors with their RMSE being 250 or more relative to the other models. More specifically within the former set of models, Figures 8(g) and 8(h) illustrate how points on graphs in hybrid models deviate more from the line of best fit relative to other models, implying some noteworthy errors in the hybrid models too. Further, of the two hybrid models, SARIMA-ANN performs slightly better than the SARIMA-SVM in terms of RMSE as their degree of collinearity denoted by R² is the same.

However, one may arrive at the opposite conclusion between the two hybrid models if judged by the MAE, as it is smaller in SARIMA-SVM. This is because MAE does not indicate the relative size of the error, which makes it difficult to distinguish large errors from small errors, since it is based on the ordinary mean value. As the model error magnitudes of SARIMA-SVM are unevenly distributed in the range from 0 to 790 MWh, it leads to an increase in the variance of the frequency distribution of error magnitudes. Therefore, the conclusion based on RMSE will be more appropriate than the contradictory one based on MAE. A similar clarification could be made to explain the different conclusions one may reach between the performances of the two models MLR and PR based on their corresponding metric values in Table 2. As the error magnitudes in both MLR and PR range from 2.5 to 785 MWh, more attention should be paid to the metric which attaches more weight to large errors, *i.e.*, the RMSE. Further, since PR is not a linear model, R² may not precisely project its performance as it is not the best goodness-of-fit statistic for non-linear type of regression models.

Looking at PR and VEC performances in terms of MAE and RMSE, PR is obviously the better model, but one may conclude the other way round if only the R² is used as the performance indicator. But R² is not the appropriate metric for model comparison here because in the VEC model, not only the wind speed and temperature, but also the past values of wind energy were used for modelling, and therefore the higher number of independent variables considered in VEC could well be the reason for yielding a higher R².

Considering the above analysis and if there is a contradiction for a choice based on MAE and RMSE, choosing the models indicated by RMSE is more appropriate in this research as the errors in all the models are not distributed evenly. Despite the slight differences within the model sub groups clarified above, machine learning models have outperformed other models for wind energy predictions at the Nala Danavi wind farm, which may be generalized to other coastal wind farms in the island exhibiting an annual pattern of weather and energy data similar to those in this study, and further, regression approaches like MLR, PR, and VEC, which use environmental factors, also lead to good prediction results.

Discussion

According to the performance of the models, SVR (R² = 0.98) and ANN (R² = 0.96) with very low error outperform the statistical and hybrid models. The superiority of SVR and ANN is achieved due to the non-linearity facilitated by machine learning and the use of weather indices as inputs in modelling. The statistical models of MLR, PR, and VEC, which used the same modelling approach, are also highly accurate with R² ≥ 0.93. In contrast, the models which used only the past energy data in modelling yielded 0.92 ≥ R² ≥ 0.90. These results indicate that developing prediction models based on the weather indices is more suitable. However, prediction of wind energy requires weather data to be projected, which needs additional work. Therefore, when the future weather data are unavailable, SARIMA, Single SVM, Hybrid SARIMA-SVM or Hybrid SARIMA-ANN models can be used.

Further to the detailed statistical analysis on the delicate differences among the models carried in the previous section, the overall performance of the present work was also compared with some similar studies reported in recent literature which are summarized in Table 3.

Table 3: Comparison of prediction models applied on wind farms

Reference	Country	Modelling techniques	Performance of the best model
Chen and Folly (2018)	South Africa	ANN, ANFIS, ARMA	RMSE = 5.6% MAE = 3.8%
Sfetsos (2000)	Greece	ARIMA, Linear Neural Network, back propagation NN, Levenberg Marquardt NN, RBF, Elman Recurrent Neural Network, ANFIS, (NLN), hybrid Logic Rules+ NLN	RMS error 4.89% better than the persistent method
Yona <i>et al.</i> (2013)		Auto Regressive, Kalman Filter, Neural Network	MAE = 68.732
Dupré <i>et al.</i> (2020)	France	ANN, ARMA	$\Delta_{RMSE} = 0.1\%$
Tena Garcia <i>et al.</i> (2019)	Mexico	ANN, ARMA	MAE = 0.060 MSE = 0.079
Biswas <i>et al.</i> (2021)	US	ARIMA, Random Forest (RF), Bagging Classification & Regression Trees (BCART), ARIMA-RF, ARIMA-BCART	Boosted the prediction accuracy by 32%
Ekanyake <i>et al.</i> (2021)	Sri Lanka	ANN, MLR, PR	R = 0.97 RMSE = 109 Bias = -0.0003 Nash = 0.98
Zafirakis <i>et al.</i> (2019)	Greece	ANN, SVR	R ² = 99.52% index of agreement = 99.71%

As understood from the comprehensive literature survey, only a few research studies have explored the efficacy of several wind energy prediction models falling under different categories. This research is unique in the context that nine types of statistical, machine learning, and hybrid techniques are applied with a comparison among them, and the best modelling options were proposed for wind energy prediction at a major wind farm in Sri Lanka. More importantly, the performances of the best models developed in this research are comparable to those of the models proposed by researchers on wind farms located in other countries.

CONCLUSION

As the prediction of wind power generation has been identified as extremely useful in managing power grids, this study focused on presenting prediction models for a key wind farm installation in Sri Lanka in the context of promoting clean energy sources. A total of nine models

developed by applying statistical-, machine learning-, and hybrid-techniques were used with five years of data on wind energy, wind speed, and ambient temperature since commissioning of the wind farm. In general, all the models showed very high accuracy measured in terms of the MAE, RMSE, and R². Nevertheless, the difference in model performance of the three categories (statistical-, machine learning-, and hybrid-techniques) shall provide flexibility in choosing an appropriate model for a given situation depending on the availability of weather data. Due to the capacity in dealing with nonlinearity of data, the SVR model, which uses machine learning techniques, turned out to be the most accurate for predicting the wind energy when the weather data are available as inputs.

As indicated by the next higher values of R² and lower error measures of MAE and RMSE, the statistical models of MLR, PR, and VEC could also be used as either substitutes or alternatives for predicting wind energy within the same context of data availability. However, all

the above models require weather data to be forecast first, based on which the wind energy is predicted. The other machine learning model of SVM, the time series model of SARIMA, and the two hybrid models of SARIMA-SVM and SARIMA-ANN can also be used for wind energy prediction in the event that future weather data are not available for some reason. The better accuracy of the single models over the hybrid models used in this study reinforced the findings of some previous studies that hybrid models do not always produce the best predictions for wind speed and power generation over the single forecasting models. Therefore, the results of this study also challenge the plausible opinion reported in some literature that hybrid modelling is superior to using individual modelling techniques. Rather, the findings of this study provide enough evidence to conclude that modelling techniques making the optimum use of past weather data would be the most appropriate for wind energy prediction at the Nala Danavi wind farm in Sri Lanka.

Conflicts of interest statement

The authors declare that they have no conflicts of interest.

Acknowledgement

Authors are thankful to LTL Holdings (Pvt) Ltd. and Ceylex Renewables (Pvt) Ltd. for providing data.

REFERENCES

- Agarwal P., Shukla P. & Sahay K.B. (2018). A review on different methods of wind power forecasting. *Proceedings of the 2018 International Electrical Engineering Congress*, 7–9 March, Krabi, Thailand, pp. 1–4.
DOI: <https://doi.org/10.1109/IEECON.2018.8712262>
- Bhatt G.A. & Gandhi P.R. (2019). Statistical and ANN based prediction of wind power with uncertainty. *Proceedings of the 3rd International Conference on Trends in Electronics and Informatics*, 23–25 April, Tirunelveli, India, pp. 622–627.
DOI: <https://doi.org/10.1109/ICOEI.2019.8862551>
- Biswas A.K., Ahmed S.I., Bankefa T., Ranganathan P. & Salehfar H. (2021). Performance analysis of short and mid-term wind power prediction using ARIMA and hybrid models. *2021 IEEE Power and Energy Conference at Illinois (PECI)*, 01–02 April, Urbana, Illinois, USA, pp. 1–7.
DOI: <https://doi.org/10.1109/PECI51586.2021.9435209>
- Box G.E.P. & Jenkins G. (1976). *Time Series Analysis: Forecasting and Control*, pp. 575. Holden-Day, Inc., San Francisco, CA, USA.
- Chandra D.R., Kumari M.S. & Sydulu M. (2013). A detailed literature review on wind forecasting. *Proceedings of 2013 International Conference on Power, Energy and Control, (ICPEC)*, 6–8 February, Dindigul, India, pp. 630–634.
DOI: <https://doi.org/10.1109/ICPEC.2013.6527734>
- Chang W.Y. (2014). A literature review of wind forecasting methods. *Journal of Power and Energy Engineering* 2(04): 161–168.
DOI: <https://doi.org/10.4236/jpee.2014.24023>
- Chen Q. & Folly K.A. (2018). Wind power forecasting. *IFAC-Papers OnLine* 51(28): 414–419.
DOI: <https://doi.org/10.1016/j.ifacol.2018.11.738>
- Dupré A., Drobinski P., Alonzo B., Badosa J., Briard C. & Plougonven R. (2020). Sub-hourly forecasting of wind speed and wind energy. *Renewable Energy* 145: 2373–2379.
DOI: <https://doi.org/10.1016/j.renene.2019.07.161>
- Ekanayake P., Peiris A.T., Jayasinghe J.M. & Rathnayake U. (2021). Development of wind power prediction models for Pawan Danavi wind farm in Sri Lanka. *Mathematical Problems in Engineering* 2021: 4893713.
DOI: <https://doi.org/10.1155/2021/4893713>
- Foley A.M., Leahy P.G. & McKeogh E.J. (2010). Wind power forecasting and prediction methods. *Proceedings of the 9th International Conference on Environment and Electrical Engineering*, 16–19 May, Prague, Czech Republic, pp. 61–64.
DOI: <https://doi.org/10.1109/EEEIC.2010.5490016>
- Global Wind Energy Council (2020). *Global Wind Report 2019*. Global Wind Energy Council, Brussels, Belgium.
- Haddad M., Nicod J., Mainassara Y.B., Rabehasaina L., Al Masry Z.A. & Péra M. (2019). Wind and solar forecasting for renewable energy system using SARIMA-based model. *International conference on Time Series and Forecasting*, 25–27 September, Gran Canaria, Spain, pp. 599–610.
- Hanifi S., Liu X., Lin Z. & Lotfian S. (2020). A critical review of wind power forecasting methods - past, present and future. *Energies* 13(15): 3764.
DOI: <https://doi.org/10.3390/en13153764>
- Hansen J.V. & Nelson R.D. (2003). Time-series analysis with neural networks and ARIMA-neural network hybrids. *Journal of Experimental and Theoretical Artificial Intelligence* 15(03): 315–330.
DOI: <https://doi.org/10.1080/0952813031000116488>
- Huang Z. & Chalabi Z.S. (1995). Use of time-series analysis to model and forecast wind speed. *Journal of Wind Engineering and Industrial Aerodynamics* 56(02-03): 311–322.
DOI: [https://doi.org/10.1016/0167-6105\(94\)00093-S](https://doi.org/10.1016/0167-6105(94)00093-S)
- Lehr J.H. & Keeley J. (2016). *Alternative Energy and Shale Gas Encyclopedia*, 1st edition, John Wiley & Sons, USA.
DOI: <https://doi.org/10.1002/9781119066354>
- Li L.L., Zhao X., Tseng M.L. & Tan R.R. (2020). Short-term wind power forecasting based on support vector machine with improved dragonfly algorithm. *Journal of Cleaner*

- Production* **242**(05): 118447.
DOI: <https://doi.org/10.1016/j.jclepro.2019.118447>
- Liu H., Tian H., Chen C. & Li Y. (2010). A hybrid statistical method to predict wind speed and wind power. *Renewable Energy* **35**(08): 1857–1861.
DOI: <https://doi.org/10.1016/j.renene.2009.12.011>
- Lopes V.V., Scholz T., Estanqueiro A. & Novais A. Q. (2012, May). On the use of Markov chain models for the analysis of wind power time-series. *Proceedings of the 11th International Conference on Environment and Electrical Engineering*, 18–25 May. Venice, Italy, pp. 770–775.
DOI: <https://doi.org/10.1109/EEEIC.2012.6221479>
- Mapuweii T.W., Bodhlyera O. & Mwambi H. (2020). Univariate time series analysis of short-term forecasting horizons using artificial neural networks: the case of public ambulance emergency preparedness. *Journal of Applied Mathematics* **2020**(02): 1–11.
DOI: <https://doi.org/10.1155/2020/2408698>
- Milligan M., Schwartz M.N. & Wan Y.H. (2003). Statistical wind power forecasting for US wind farms. *Proceedings of the 17th Conference on Probability and Statistics in the Atmospheric Sciences*, 11–15 January, American Meteorological Society Annual Meeting Seattle, Washington, USA.
- Santhosh M., Venkaiah C. & Vinod Kumar D.M.V. (2020). Current advances and approaches in wind speed and wind power forecasting for improved renewable energy integration: A review. *Engineering Reports* **2**(06): 1–20.
DOI: <https://doi.org/10.1002/eng2.12178>
- Sfetsos A. (2000). A comparison of various forecasting techniques applied to mean hourly wind speed time series. *Renewable Energy* **21**(01): 23–35.
DOI: [10.1016/S0960-1481\(99\)00125-1](https://doi.org/10.1016/S0960-1481(99)00125-1)
- Shi J., Guo J. & Zheng S. (2012). Evaluation of hybrid forecasting approaches for wind speed and power generation time series. *Renewable and Sustainable Energy Reviews* **16**(05): 3471–3480.
DOI: <https://doi.org/10.1016/j.rser.2012.02.044>
- Sideratos G. & Hatzigiorgiou N.D. (2007). An advanced statistical method for wind power forecasting. *IEEE Transactions on Power Systems* **22**(01): 258–265.
DOI: <https://doi.org/10.1109/TPWRS.2006.889078>
- Tena García J.L., Cadenas Calderón, E., González Ávalos, G., Rangel Heras E. & Mbikayi Tshikala A. (2019) Forecast of daily output energy of wind turbine using SARIMA and nonlinear autoregressive models. *Advances in Mechanical Engineering* **11**(2): 1–15.
DOI: <https://doi.org/10.1177/1687814018813464>
- Tseng F.M., Yu H.C. & Tzeng G.H. (2002). Combining neural network model with seasonal time series ARIMA model. *Technological Forecasting and Social Change* **69**(01): 71–87.
DOI: [https://doi.org/10.1016/S0040-1625\(00\)00113-X](https://doi.org/10.1016/S0040-1625(00)00113-X)
- Voyant C., Muselli M., Paoli C. & Nivet M.L. (2012). Numerical weather prediction (NWP) and hybrid ARMA/ANN model to predict global radiation. *Energy* **39**(01): 341–355.
DOI: <https://doi.org/10.1016/j.energy.2012.01.006>
- Wang X., Guo P. & Huang X. (2011). Energy procedia a review of wind power forecasting models. *Energy Procedia* **12**: 770–778.
DOI: <https://doi.org/10.1016/j.egypro.2011.10.103>
- Yona A., Senjyu T., Toshihisa F. & Kim C.H. (2013). Very short-term generating power forecasting for wind power generators based on time series analysis. *Smart Grid and Renewable Energy* **4**(02): 181–186.
DOI: <https://doi.org/10.4236/sgre.2013.42022>
- Zafirakis D., Tzanes G. & Kaldellis J.K. (2019) Forecasting of wind power generation with the use of artificial neural networks and support vector regression models. *Energy Procedia* **159**: 509–514.
- Zhao Y., Ye L., Li Z., Song X., Lang Y. & Su J. (2016). A novel bidirectional mechanism based on time series model for wind power forecasting. *Applied Energy* **177**(C): 793–803.
DOI: <https://doi.org/10.1016/j.apenergy.2016.03.096>

GUIDANCE TO CONTRIBUTORS

GENERAL INFORMATION

Scope

The Journal of the National Science Foundation of Sri Lanka publishes the results of research in all aspects of Science and Technology. It is open for publication of Research Articles, Reviews, Research Communications and Correspondence.

Categories of manuscripts

Research Articles: Research Articles are papers that present complete descriptions of original research. Research Articles should include an Abstract, Keywords, Introduction, Methodology, Results and Discussion, Conclusion and Recommendations where relevant. References should be prepared according to the “Guidelines for the preparation of manuscripts”. Maximum length of the article should be limited to 25 pages with a word count of 10,000 including references, figures and tables. Any articles above this limit will be returned.

Reviews: Reviews are critical presentations on selected topics of Science or Technology. They should be well focused and organized and avoid general “textbook” style. As reviews are intended to be critical presentations on selected topics, reviewers need to have had substantial leadership in research supported by a publication track record in the areas covered by the review. A person/s wishing to submit a Review Article should obtain prior approval from the Editorial Board by submitting a concise summary of the intended article, along with a list of the author’s publications in the related area (jnsf@nsf.gov.lk). Maximum length of the article should be limited to 40 pages with a word count of 12,000 including references, figures and tables. Any articles above this limit will be returned.

Research Communications: Research Communications are intended to communicate important new findings in a specific area of limited scope that are worthy of rapid dissemination among the scientific community. Authors are required to provide a statement justifying the suitability of the submission for a Research Communication. The article should include an Abstract, Keywords, Introduction, Methodology, Results & Discussion, Conclusion and References. Maximum length of the article should be limited to 10 pages with a word count of 2,500 including references, figures and tables. Any articles above this limit will be returned.

Correspondence: Correspondence will be accepted regarding one or more articles in the preceding four issues of the Journal, as well as Letters to the Editor. Articles covering important scientific events or any other news of interest to scientists, reviews of books of scientific nature, articles presenting views on issues related to science and scientific activity will also be considered. Publication will be made at the discretion of the Editor-in-Chief. Maximum length of the article should be limited to 05 pages with a word count of 1,500 including references, figures and tables. Any articles above this limit will be returned.

SUBMISSION OF MANUSCRIPT

Authors submitting articles to the JNSF should first create an account in the Sri Lanka Journals Online System (<https://jnsfsl.sljol.info/>). All manuscripts in MS Word format must be electronically submitted to the journal’s online platform at <https://jnsfsl.sljol.info/submit/start/>. Submissions via emails are not encouraged. Please make sure that no author information is mentioned in the article submitted. The names and details of affiliations of all authors and contact information of the corresponding author must be fed into the system during the online submission process. Authors (at least the corresponding author) are required to provide their personal, validated ORCID ID (by obtaining an ORCID ID from <https://orcid.org/>) when submitting the manuscript. No change to the authors or order of authors will be accepted after the submission. All those who have made significant contributions should be listed as co-authors. The corresponding author should ensure that all contributing co-authors are included in the author list and have approved the final version of the paper and have agreed to its submission for publication.

All submissions should be in English. If the manuscript conforms to the guidelines specified, the date received will be the date that the manuscript was submitted to the online system.

Submissions are accepted for processing on the understanding that they will be reviewed and that they have not been submitted for publication elsewhere (including publication as a full paper or extended abstract as a part of Conference Proceedings). The JNSF does not accept manuscripts that have already been submitted to pre-print servers.

Suggesting potential reviewers by authors

The authors may suggest up to three names of referees when submitting their manuscript, in the Cover Letter space provided at the bottom of the page in the first stage of online submission. Referees should not be from the institution where the work was carried out and should not have been co-authors in previous publications. The address, institutional affiliation and e-mail of the suggested referees should be supplied. Please note that the JNSF is not bound to select all or any of the suggested referees for sending the manuscript for reviewing

Authorship

All authors designated as authors should be eligible for authorship. Those who have made a substantial contribution to the concept or design of the work; or acquisition, analysis or interpretation of data are recognized as Authors.

The corresponding author should be prompt and ensure adherence to timelines when responding to requests, queries and recommendation of reviewers conveyed by or on behalf of the Editor-in Chief and Editorial Board.

Supplementary materials

Any experimental data necessary to evaluate the claims made in the paper but not included in the paper should be provided as supplementary materials. Supplementary materials will be sent to the reviewers and published online with the manuscript if accepted. The supplementary materials should conform to Journal guidelines and should be uploaded as separate files. Authors should number Supplementary Tables and Figures as, for example, 'Supplementary Table S1'. Refer to each piece of supplementary material at the appropriate point(s) in the main article. Supplementary Materials may include description of the materials and methods, controls, or tabulated data presented in Tables or Figures, and programming codes.

Peer review

The manuscripts submitted to the JNSF will initially be screened by the Editorial Board and, if suitable, will be referred to at least two subject experts in the relevant field. The peer-review process of the JNSF is double-blind.

When revision of a manuscript has been requested, the revised manuscript should be submitted on or before the stated deadline. If the revised manuscript is not received on time, the manuscript will not be processed further. The authors' response to the comments of referees should be tabulated with the comment, response and the line number/s for reference. The decision of the Editorial Board shall be final.

Accepted papers are subject to editing. The date of acceptance will be the date when the Editorial Board has decided it to be acceptable for publication.

Article publication fee and complementary copies

A publication fee of US\$ 150 will be levied for each manuscript other than where the corresponding author is affiliated to a Sri Lankan Institute, to cover the publication cost.

A complimentary copy of the Journal issue carrying the respective article will be supplied to each of the authors.

Authors' declaration

When an article is accepted for publication, the authors are required to submit the Authors' Declaration signed by all the authors.

Copyright

Articles in JNSF are published under the Creative Commons License CC-BY-ND. This license permits use, distribution and reproduction of articles for commercial and non-commercial purposes, provided that the original work is properly cited and is not changed in anyway. The copyright of the article is with the National Science Foundation of Sri Lanka. Therefore, authors are requested to check with institution's copyright and publication policy before submitting an article to the JNSF. Authors secure the right to reproduce any material that has already been published or copyrighted elsewhere. When an article is accepted for publication, the authors are required to submit the Transfer of Copyright document signed by all the authors.

Post-publication corrections

The Editorial Board reserves the right to take action on publishing an erratum or corrigendum. If serious errors are identified in a published article, the Journal may consider a retraction or publishing a correction.

STRUCTURE OF MANUSCRIPT

Manuscript

The manuscript should be free of errors and prepared in single column, using double-spaced text of Times New Roman 12 font throughout with line numbers, leaving at least 2 cm margins on both sides, and liberal spacing at the top and bottom of each page. Pages should be numbered consecutively.

a. Style

The paper should be written clearly and concisely. The style of writing should conform to scholarly writing. Slang, jargon, unauthorized abbreviations, abbreviated phrasings should not be used. In general, the impersonal form should be used. Poor usage of language will result in rejection of the manuscript during initial screening.

b. Layout

Manuscripts other than review articles should be generally organized as follows: Title, Abstract, Keywords, Introduction, Methodology, Results and Discussion, Conclusions and Recommendations (where relevant), Acknowledgements and References. Pages should be arranged in the following order:

Title page should include the title of manuscript, and no author information should be mentioned in the title page. If a major part of the research has been published as an abstract in conference proceedings, it should be cited as a footnote on the title page. Authors must also indicate the **general and specific research area** of the manuscript in the title page. In order to highlight the significance of the manuscript, authors are required to provide the following highlights in brief. (1) Why was this study conducted? (2) What are the new findings? (3) Possible applications of the findings. Please limit your answers to 25-30 words for each.

Title: Should accurately and concisely reflect the contents of the article.

Running title: Should be a shortened title (limited to a maximum of 50 characters) that could be printed at the top of every other page of the Journal article.

Abstract: Should be between 200 - 250 words for full length articles and written as a single paragraph. It should not contain any references and should be able to stand on its own. It should outline objectives and methodology together with important results and conclusions. A Review Article should carry a summary of not more than 300 words.

Keywords: Include a maximum of six keywords, which may include the names of organisms (common or scientific), methods or other important words or phrases relevant to the study.

Introduction: This should state the reasons for performing the work with a brief review of related research studies in the context of the work described in the paper. Objectives of the study should be clearly stated.

Materials and Methods: This section should give the details of how you conducted your study. New methods may be described in detail with an indication of their limitations. Established methods can be mentioned with appropriate references. Sufficient details should be included to allow direct repetition of the work by others. Where human subjects are involved, they should be referred to by numbers or fictitious names. A paper reporting the results of investigations on human subjects or on animals must include a statement to the effect that the relevant national or other administrative and ethical guidelines have been adhered to, and a copy of the ethical clearance certificate should be submitted. Methods of statistical analyses used should be mentioned where relevant.

Results and Discussion: Results: the results should be concisely and logically presented. Repetition of the same results in figures, tables or text should be avoided.

Discussion: data essential for the conclusions emerging from the study should be discussed. Long, rambling discussions should be avoided. The discussion should deal with the interpretation of results. It should logically relate new findings to earlier ones. Unqualified statements and conclusions not completely supported by data should be avoided.

Molecular sequence data, such as gene or rDNA sequences, genome sequences, metagenomic sequences etc. must be deposited in a public molecular sequence repository, such as GenBank, that is part of the International Nucleotide Sequence Database Collaboration (INSDC). The accession numbers obtained must be cited in the text, Table or on Figures of phylogenetic trees of the manuscript.

Conclusion: The conclusion should be brief, highlight the outcomes of the study and should be aligned with the objectives of the study. It should not contain references.

Conflict of interest statement: All authors should include a statement on conflict of interest disclosing any financial or other substantive conflicts of interest that may be construed to influence the results or interpretation of their research. All sources of financial support for the project should be disclosed.

Acknowledgement: Should be brief and made for specific scientific, financial and technical assistance only. If a significant part of the research was performed in an institution other than in those indicated by the authors' affiliations given in the title page, this fact should be acknowledged. All those who have made substantial contribution to the research but do not qualify to be authors should be acknowledged.

References :

All research work of other authors, when used or referred to or cited, should be correctly acknowledged in the text and in the References.

Citing references in the text:

- References to the literature must be indicated in the text and tables as per the Author-Year System, by the author's last name and year, in parenthesis (i.e. Able, 1997) or (Able & Thompson, 1998).
- Citation to work by more than two authors should be abbreviated with the use of *et al.* (i.e. Able *et al.*, 1997).
- Multiple publications by the same first author in the same year should be coded by letters, (i.e. Thompson, 1991a; b).
- Multiple citations should be made in chronological order and separated by a semi-colon, (i.e. Zimmerman *et al.*, 1986; Able *et al.*, 1997).
- Reference to unpublished work, work in preparation or work under review should be cited in italics as (*unpublished data*) or, with the author's initials and surname given; such works should not be included in the Reference section.
- Personal communications may be mentioned in the text with the date of communication as (*Personal communication*, 2 June 2000).

List of references:

- The list of References should be arranged in alphabetical order based on the last name of the first author.
- Names of all the authors should be given except when there are more than 10 authors. When there are more than 10 authors, only the name of the first author can be given followed by *et al.*
- All the initials of the author must be given after the last name and the year of publication should follow in parentheses.
- This should be followed by the full title of the referred publication.
- When journal articles are listed, the journal name should be given in full and in italics and followed by the volume number in bold type, issue number in parentheses and then the inclusive pages.
- Where there are several publications by the same author(s) and published in the same year they should be differentiated by adding a lower-case letter after the year. When books are listed, the order should be: author(s), year, book title, volume number, edition, pagination/ inclusive pages, publisher and place of publication. The book title should be in italics. When sections of a book are listed, the order should be: author(s) of chapter, year, title of the section, title of the book, edition, inclusive pages, publisher and place of publication.
- Digital object identifiers (DOIs) should be included for all references where available.
- References should only be cited as 'in press' if the paper has been accepted for publication.

Examples of correct forms of references are given below.

Journal Articles

Boutin C. & Harper J.L. (1991). A comparative study of the population dynamics of five species of *Veronica* in natural habitats. *Journal of Ecology* 79(01): 199 – 221.

DOI: <https://doi.org/10.2307/2260793>

Books

Burnham K.P. & Anderson D.R. (2002). *Model Selection and Multimodal Inference*, 2nd edition, pp. 488. Springer Science and Business Media, Inc., New York, USA.

Book Chapters

Hinrichsen R.A. & Holmes E.E. (2009). Using multivariate state-space models to study spatial structure and dynamics. In: *Spatial Ecology* (eds. R.S. Cantrell, C. Cosner & S. Ruan), pp. 145 – 166. CRC/ Chapman Hall, Florida, USA.

DOI: <https://doi.org/10.1201/9781420059861.ch8>

Edited Books

Kimati H., Amorim L., Rezende J.A.M., Bergamin Filho A. & Camargo L.E.A. (eds.) (2005). *Manual de Fitopatologia*, volume 2. Doenças das Plantas Cultivadas, 4th edition. Ceres, São Paulo, Brazil.

Conference Papers

Weaver D. (2002). Implementation of a learning management system using an integrated approach to professional development. In: Winds of change in the sea of learning. *Proceedings of the 19th Annual Conference of the Australasian Society for Computers in Learning and Tertiary Education (ASCILITE)* (eds. A. Williamson, C. Gunn, A. Young & T. Clear), volume 2, Auckland, New Zealand, 8-11 December. Unitec Institute of Technology, Auckland, New Zealand, pp. 711-720.

Agency Publications

U.S. Census Bureau (2009). *World Population: 1950 – 2050*. U.S. Census Bureau, Washington DC, USA.

Department of Health (2008). *Health Inequalities: Progress and Next Step* (pdf). Department of Health, London, UK. Available at http://PublicationsPolicyAndGuidance/DH_08_5307, Accessed 9 June 2008.

Other

Robinson L.J. (2003) Spatial scale and depletion models of farmland birds in a fragmented landscape. *PhD thesis*, University of Reading, Reading, UK.

Efford M.G. (2008). Density 4.3: software for spatially explicit capture-recapture. Available at <http://www.otago.ac.nz/density>, Accessed 15 March 2009.

Abbreviations and Symbols: Unless common, these should be defined when first used, and not included in the abstract. The SI System of units should be used wherever possible. If measurements were made in units other than SI, the data should be reported in the same units followed by SI units in brackets, e.g. 5290 ft (1610 m).

Formulae and Equations: Equations should be typewritten and quadruple spaced. They should be started on the left margin and the number placed in parentheses to the right of the equation.

Nomenclature: Scientific names of plants and animals should be printed in italics. In the first citation, genus, species and authority must be given. e.g. *Borassus flabellifer* Linn. In latter citations, the generic name may be abbreviated, for example, *B. flabellifer* L.

Tables and figures: Tables and Figures should be clear and intelligible and kept to a minimum, and should not repeat data available elsewhere in the paper. Any reproduction of illustrations, tabulations, pictures etc. in the manuscript should be acknowledged.

Tables: Tables should be numbered consecutively with Arabic numerals and placed at the appropriate position in the manuscript. If a Table must be continued, a second sheet should be used and all the headings repeated. The number of columns or rows in each Table should be minimized. Each Table should have a title, which makes its general meaning clear, without reference to the text. All Table columns should have explanatory headings. Units of measurement, if any, should be indicated in parentheses in the heading of each column. Vertical lines should not be used and horizontal lines should be used only in the heading and at the bottom of the table. Footnotes to Tables should be placed directly below the Table and should be indicated by superscript lower case italic letters (^{*a*}, ^{*b*}, ^{*c*}, etc.).

Figures: All illustrations are considered as figures, and each graph, drawing or photograph should be numbered consecutively with Arabic numerals and placed at the appropriate position in the manuscript. Any lettering to appear on the illustrations should be of a suitable size for reproduction and uniform lettering should be used in all the Figures of the manuscript. Scanned figures or photographs should be of high quality (**300 dpi**), to fit the proportions of the printed page (12 × 17 cm). Each figure should carry a legend so that the general meaning of the figure can be understood without reference to the text. Where magnifications are used, they should be stated.

Units of measurement

Length: km, m, mm, μ m, nm

Area: ha, km², m²

Capacity: kL, L, mL, μ L

Volume: km³, m³, cm³

Mass: t, kg, g, mg, μ g

Time: year(s), month(s), wk(s), d(s), h, min, s

Concentration: M, mM, N, %, g/L, mg/L, ppm

Temperature: °C, K

Gravity: x g

Molecular weight: mol wt

Others: Radio-isotopes: 32P

Radiation dose: Bq

Oxidation-reduction potential: rH

Hydrogen ion concentration: pH